MAGMA GENESIS AND COMPOSITION OF THE SLAB-DERIVED FLUIDS BENEATH THE SE MARIANA INTRAOCEANIC ARC, WESTERN PACIFIC

Julia Ribeiro

MAGMA GENESIS AND COMPOSITION OF THE SLAB-DERIVED FLUIDS BENEATH THE SE MARIANA INTRAOCEANIC ARC, WESTERN PACIFIC

by

Julia M. Ribeiro

APPROVED BY SUPERVISORY COMMITTEE:

Robert J. Stern , Chair

John S. Oldow

William I. Manton

Elizabeth Anthony

A mes parents, pour leur soutien et leur présence pendant toutes ces épreuves endurées.

A toi, Brahim, merci d'avoir partagé mes joies et mes peines.

Merci d'être là.

Ils ont dit, tu vas devenir fou à poursuivre tes rêves.

J'ai dit, ils sont fous ceux qui ne les suivent pas.

MAGMA GENESIS AND COMPOSITION OF THE SLAB-DERIVED FLUIDS BENEATH THE SE MARIANA INTRAOCEANIC ARC, WESTERN PACIFIC

by

JULIA M. RIBEIRO, MS

DISSERTATION

Presented to the Faculty of

The University of Texas at Dallas

in Partial Fulfillment

of the Requirements

for the Degree of

DOCTOR OF PHILOSOPHY IN

GEOSCIENCES

THE UNIVERSITY OF TEXAS AT DALLAS

August 2013

ACKNOWLEDGEMENTS

I would like first to thank my family who supported me for all these years, before and during my graduate studies. Many thank to my friends (Chun, Gabriel, Diana,…), for the friendships, for the fun and the support during my stay here in the US; to Jim and Margaret Gayles, for their kindness, for opening their house every Friday and making me feel like home (Jim, tu resteras à jamais dans mes pensées); to Peggy and Bo, for the many discussions we had about life, and I am so happy to see your family growing; to Mrs. Hazards, for having me in her home for 6 months during my trip in Rhode Island, and who definitely made my trip more fun! Thank you for helping me to know better that side of America; to Warren, for all the fun discussions we had; and to the many others I forgot. Many thanks to Bob, for taking me on those wonderful Mariana expeditions and getting me work on this very exciting project. I wanted to work on a great project about petrology and geochemistry of subduction-related lavas, associated with a slab tear; and I did it! Merci d'avoir rendu mon rêve réalité. Many to Julie White from ISSO and to the ISSO people for helping me with any international issues during my stay and for looking after Nala while I was oversea. And finally, many thanks to Amanda and Lila for helping me out with the formatting of this dissertation.

April 2013

MAGMA GENESIS AND COMPOSITION OF THE SLAB-DERIVED FLUIDS BENEATH THE SE MARIANA INTRAOCEANIC ARC, WESTERN PACIFIC

Publication No. _____

Julia M. Ribeiro, PhD
The University of Texas at Dallas, 2013

Supervising Professor: Dr. Robert J. Stern

Subduction zones are places where one hydrated oceanic plate goes underneath another plate, and releases its fluids into the overlying mantle wedge. Slab-derived fluids play a key role in subduction zone processes. They serpentinize the cold forearc mantle at shallow depths; and deeper, they trigger hydrous mantle melting beneath the arc volcanoes and sometimes at backarc basin (BAB) spreading center. Examining the composition of arc and BAB magmas helps understanding genesis of subduction-related magmas, nature and composition of their mantle sources and slab-derived fluids. However, investigating such processes at shallow subduction zones is challenging, because the cold forearc mantle generally does not melt. Here, I investigate an unusual region in the southernmost Mariana convergent margin in the Western Pacific, near the Challenger Deep. The SE Mariana forearc stretched to accommodate opening of the southernmost Mariana Trough ~5Ma ago, opening the SE Mariana forearc rift (SEMFR) and causing seafloor spreading ~2.7–3.7Ma ago. The subducted slab beneath SEMFR deepens from

<50km to ~100km, thus studying SEMFR lavas provides a unique opportunity to understand shallow subduction processes. By examining the major and trace element composition, the Pb-Nd-Sr isotopic ratios and the volatile contents (H_2O, CO_2, Cl, S, F) of SEMFR basalts, associated glassy rinds and olivine-hosted melt inclusions (Ol-MI) collected during three cruises (YK08-08, YK10-12, TN273), I show that:

(i) SEMFR lavas were produced by adiabatic decompression melting of depleted asthenospheric BAB-like mantle at ~30±6.6 km depth and 1224±40^{o}C;

(ii) Ol-MI represent hydrous melts trapped by forearc mantle olivines. Xenocrysts were entrained with SEMFR basalts during ascent;

(iii) SEMFR mantle flowed from the forearc towards the arc volcanoes and was metasomatized by shallow aqueous fluids;

(iv) SEMFR shallow fluids are more aqueous than the fluids released beneath the Mariana arc and Mariana BAB;

(v) the aqueous slab-derived fluids and the volatile fluxes are greatest at ~50–100km slab depth, suggesting that the minerals from the subducting plate mostly broke down beneath the arc to release their fluids.

Such results provide new insights into shallow subduction processes, as previous studies showed that volatile fluxes and aqueous slab-derived fluids should increase toward the trench.

TABLE OF CONTENTS

LIST OF FIGURES

LIST OF TABLES

CHAPTER 1

INTRODUCTION

Oceanic plate is created at mid-ocean ridges, where its crust begins to hydrate by hydrothermal circulation and seawater alteration. This crust is slowly covered by sediments. Hydrated and sedimented oceanic plate goes underneath another plate at a subduction zone, and sinks into the hot asthenospheric mantle to release its fluids into the mantle wedge, which partially melts to form magmas that erupt at arc volcanoes. Subduction zones are thus key features of the solid Earth system, as they are the locus of many fundamental processes: formation of island arcs, which ultimately form continental crust, recycling of the oceanic lithosphere, fluxing of fluids and volatiles from the surface into the mantle and back to the surface through arc volcanism, explosive volcanism, economic ore deposits, and intense earthquakes that extend to much greater depths than anywhere else in Earth (Figure 1.1). There are ~ 55 000 km of convergent margins, and 80% of these occur around the Pacific Ocean.

Subduction zones are destructive margins, where the plate boundary between the upper plate and the downgoing plate is defined by a deep trench (Figure 1.2). Subduction zones are associated with many arc volcanoes (Figure 1.1) that generally develop ~ 100 km above the subducting plate (Figure 1.2). Between the trench and the arc volcanoes is a region known as the forearc.

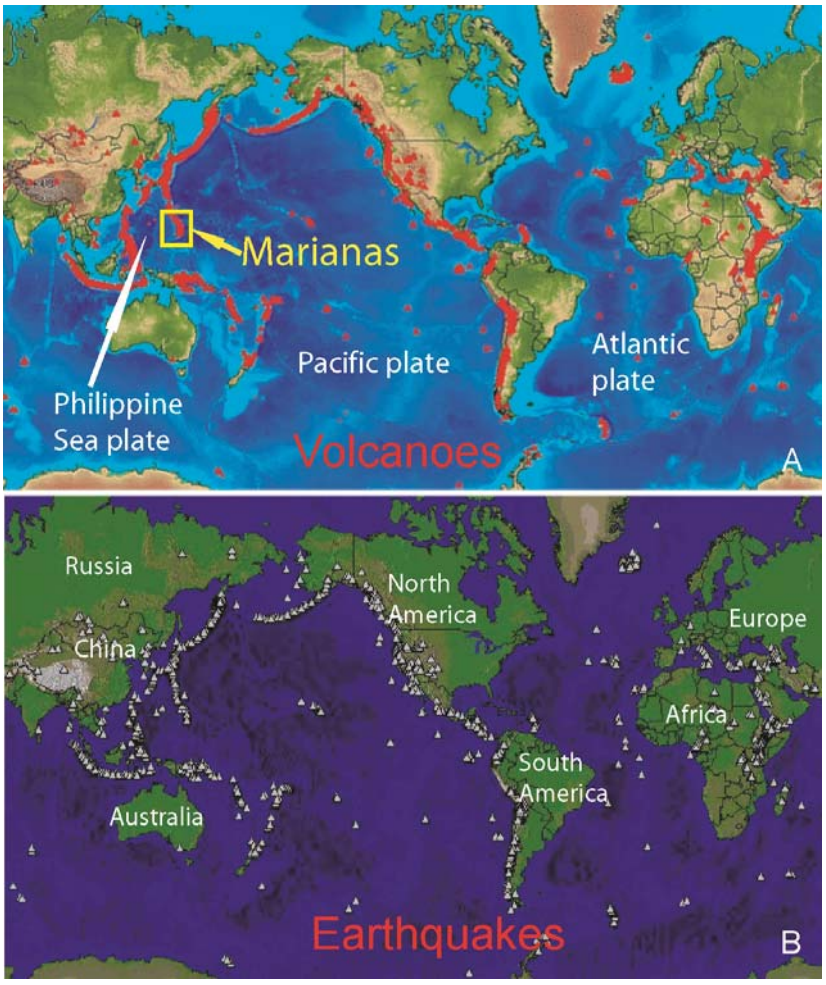

Figure 1.1. World map centered on the Pacific Ocean showing (A) arc volcanism (red triangles) and (B) seismic activity (white triangles denote earthquakes) associated with subduction zones. Most subduction zones occur around the Pacific Ocean (Ring of Fire), where oceanic plates are subducted beneath other plates. The yellow box highlights the Mariana convergent margin in the Western Pacific, where the Pacific plate subducts beneath the Philippine Sea plate. Maps are from www.volcano.si.edu and www.hsv.com.

Forearcs are generally ~ 100 – 200 km wide (Figure 1.2) and generally are produced when subduction zones first form. Forearcs can also accumulate eroded materials from the arc volcanoes and from neighborhood continents ands can be accretionary or non-accretionary, depending on how much sediment is supplied to the trench, which generally reflects proximity to continent-derived sediments. Behind the arc volcanoes lies the backarc region, typically ~ 250 –

300 km from the trench (Figure 1.2). Backarc regions can be under compression or extension, depending on the slab downdip (extension for slab downdip > 51°, and compression for slab downdip < 31°). Convergent margins in the western Pacific are generally extensional, forming backarc basins (BABs). BABs form by seafloor spreading, and the Mariana Trough (of interest here) is an outstanding example of a BAB (Figure 1.2-1.3).

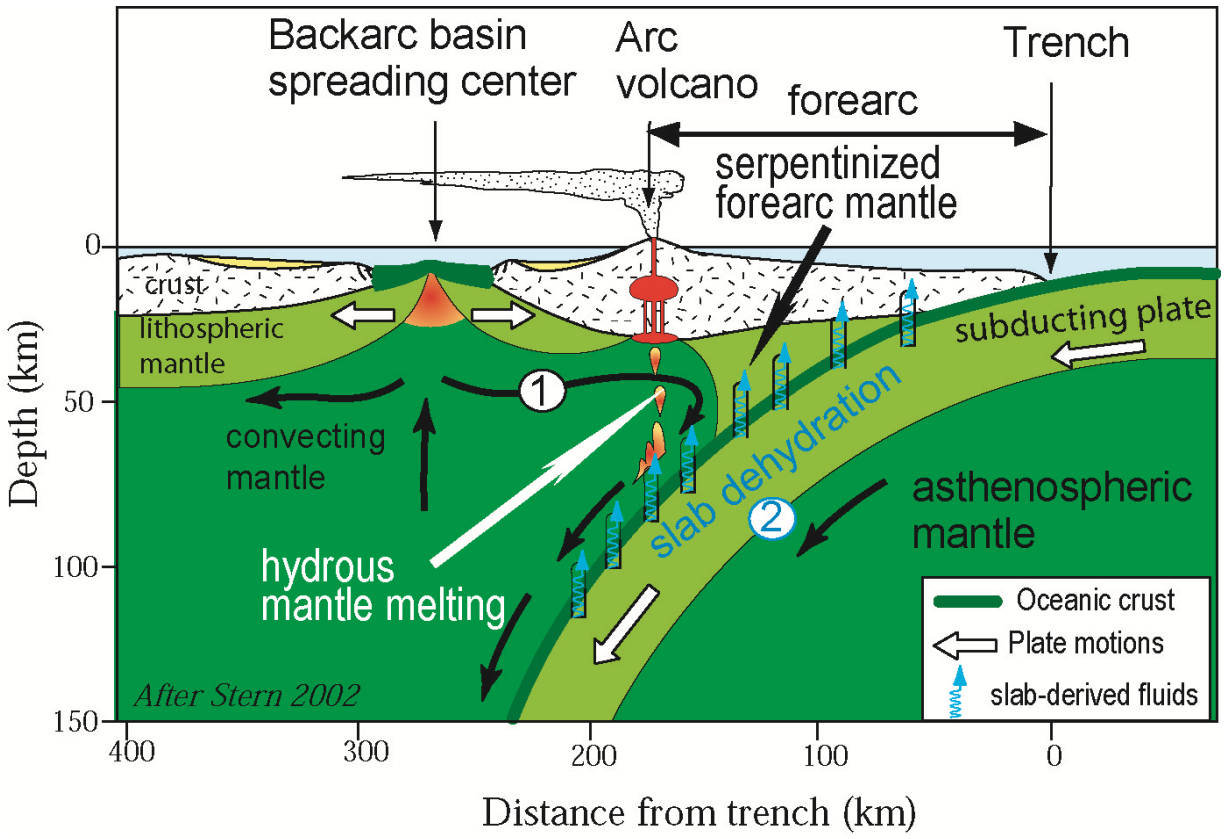

Figure 1.2. Sketch of a typical subduction zone with non-accretionary forearc and a backarc basin spreading center, such as the Mariana arc. (1) The mantle flows from the backarc basin spreading center (thick black arrows) towards the forearc; and formation of BAB melts and then arc lavas successively deplete the flowing mantle, resulting in a highly depleted mantle beneath the forearc. (2) The downgoing plate releases its fluids into the mantle wedge as subduction proceeds. The slab-derived fluids serpentinize the mantle wedge beneath the forearc, and they trigger hydrous mantle melting beneath the arc, resulting in intense volcanic activity.

As the downgoing plate subducts beneath the upper plate, the hydrated downgoing slab releases its fluids, which rise up into the overlying mantle wedge (Figure 1.2). The fluids are first released from the subducting plate by compaction and then by metamorphic reactions, so that the minerals carrying volatiles (H_2O, Cl, S, F, Cl, B, CO_2) and fluid-mobile elements (e.g. Ba, Cs, Rb) to depth lose their water-rich (aqueous) fluids. At shallow depths, these fluids released from dehydrating the subducting plate serpentinize the cold forearc mantle wedge, and at greater depths trigger hydrous melting beneath the arc volcanoes and beneath the BAB spreading center, resulting in hydrous lavas (Figure 1.2). Composition of the slab-derived fluids evolves with increasing slab depth, and the composition of these fluids is preserved in the composition of arc and BAB lavas. The aqueous fluids become less hydrous with depth, as the subducted minerals lose their volatiles and fluid-mobile elements (FMEs), until sediment melts and supercritical fluids (volatiles and melts are mixed as a single phase) are produced at depth ≥ 100 km. The mantle wedge also changes as a result of subduction-related processes because formation of backarc basin and arc magmas successively depletes the mantle flowing toward the trench (Figure 1.2), resulting in more depleted mantle beneath the forearc.

This dissertation focuses on the nature, the composition and the evolution of subdution-related magmas, their mantle source and their subduction components (i.e., slab-derived fluids), using an unusual region in the SE Mariana convergent margin in the Western Pacific (Figure 1.1, 1.3). I investigated fresh, basaltic pillowed lavas and lavas flows that erupted 2.7 – 3.7 Ma ago in the SE Mariana forearc rift (SEMFR). SEMFR formed in late Miocene time to accommodate stretching of the SE Mariana Trough. SEMFR extends from Mariana arc volcanoes to the trench

(Figure 1.3). The subducted slab beneath SEMFR deepens from < 50 km depth beneath SE SEMFR to ~100 km depth beneath NW SEMFR, so studying these igneous rocks provides a unique opportunity to understand fluids released from the shallow part of the subducting slab. Such a perspective on shallow fluids is not seen in many other subduction zones.

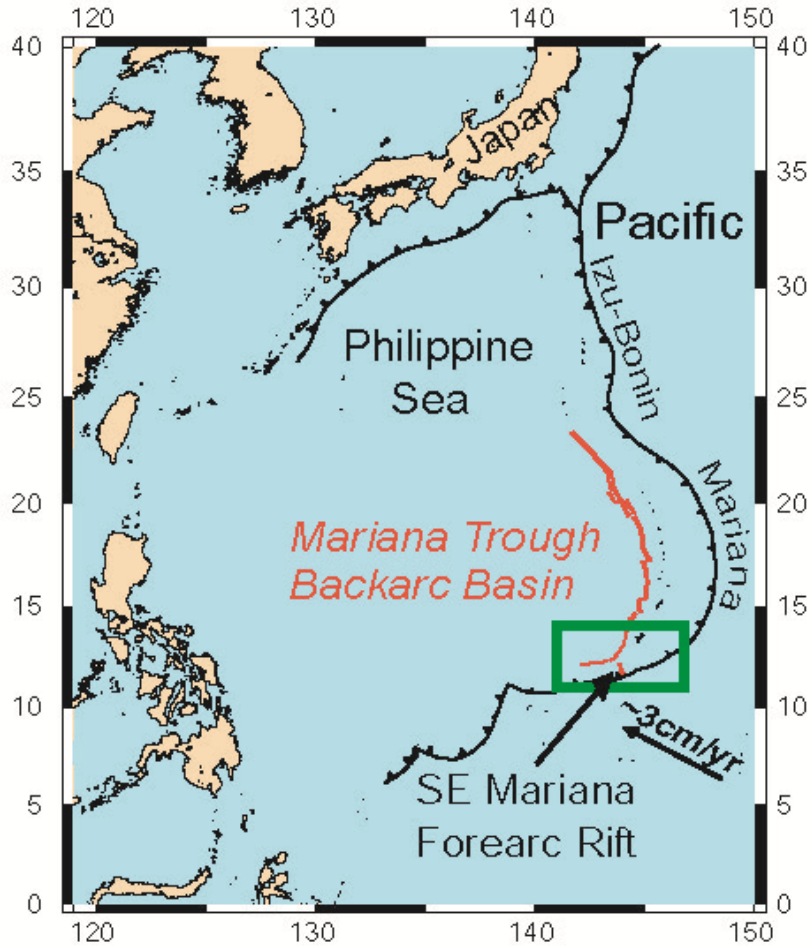

Figure 1.3. Map of the Izu-Bonin-Mariana (IBM) convergent margin. The Pacific plate subducts beneath the Philippine Sea plate along the IBM trench (black line with triangles), resulting in the Mariana Trough backarc basin spreading center (in red). The green rectangle highlights the area of interest, the SE Mariana convergent margin, where the Mariana trench curves from N-S to nearly E-W. This is also the location of Earth's greatest deep, the Challenger Deep. The SE Mariana Forearc Rift (SEMFR), the focus of this research project, is located at the southern end of the SE Mariana Intraoceanic arc, where the convergence vector (~ 3 cm/yr) is nearly orthogonal to the trench, as denoted by the black arrow.

Keys questions that are addressed in this dissertation are:

1) How can magmas be produced beneath the forearc, in a region that is usually underlain by a cold serpentinized mantle wedge that does not melt?
2) What do these magmas tell us about the composition of the mantle and the fluids released at shallow depths in the subduction zone?
3) How do the mantle and the slab-derived fluids evolve with increasing slab depth (i.e., increasing distance to the trench)?
4) Are the fluids released beneath the shallow part of the subducting plate more hydrous (water-rich) than are the deeper slab-derived fluids released beneath the arc volcanoes and the BAB spreading center?

This dissertation is divided into four chapters, focusing on answering these key questions to better understand the magma genesis, the mantle processes and the composition of the slab-derived fluids at shallow subduction zones:

- Chapter one is this introduction. It gives general background about this research project along with the key points that will be further developed.

- The second chapter is based on seafloor investigations by two research cruises (YK0808 and YK1012) carried out aboard Japanese research vessels and research submarine Shinkai 6500 in 2008 and 2010. It describes the geology, the magma genesis and the geodynamic evolution of the SEMFR by using bathymetric maps, backscatter image and high resolution images and movies of the seafloor. I also describe the petrography and

mineralogy of the collected samples, and report major elements analyses and ^{40}Ar-^{39}Ar ages. The purpose of this chapter is (i) to give a geological background on the SE Mariana Intraoceanic Arc to better understand its geodynamic evolution, and (ii) to address the genesis of the SEMFR lavas in the forearc region. I show that stretching of the Eocene forearc lithosphere brought new input of hot asthenospheric mantle, allowing hydrous mantle melting to occur above the very shallow part of the subducting slab, resulting in SEMFR lavas. I also propose a geodynamic model for the evolution of the SE Mariana convergent margin, along with a petrogenetic model for SEMFR. This first manuscript is now in press in the peer-reviewed journal *Island Arc* (Ribeiro *et al.*, in press).

- The third chapter is based on samples collected during YK0808 and YK1012, but also a cruise of US research vessel R/V TN273 Thomas Thompson in Dec. 2011-Jan. 2012. This chapter presents major, trace element analyses and Nd-Sr-Pb isotopic ratios of SEMFR lavas (whole rock and glassy rinds), SE Mariana Trough lavas and SE Mariana arc lavas, and I use these new data to address the following key points: (i) what do SEMFR magmas tell us about shallow subduction and mantle processes? And (ii) how do the mantle and the slab-derived fluids evolve with increasing slab depth? One important aspect to consider in this chapter is the alteration effect on the whole rock, as this can change the composition of the fluid markers (such as Rb and Cs). Therefore, this chapter mostly focuses on the composition of the fresh glassy rind to track the shallow subduction components. I show that: (i) the slab-derived fluids beneath SEMFR are

composed of aqueous fluids and sediment melts, perhaps inherited from the mantle source; (ii) contributions of the aqueous fluids and sediment melts increase towards the arc volcanoes, demonstrating that the fluid-mobile elements (FMEs: Cs, Rb, Ba) are mostly released from the slab at ~ 50 – 100 km depth; and finally, (iii) the SEMFR mantle source is less depleted than generally found for forearc mantle (Figure 1.1), suggesting that less depleted mantle was added to the region beneath SEMFR. This second manuscript has been submitted to the peer-reviewed journal *Geochemistry, Geophysics, Geosystems*, and it is now under review (Ribeiro *et al.*, submitted).

- The fourth chapter focuses on the composition and the evolution with slab depth of the shallow aqueous fluids released from the subducting plate. Because magmas generally lose their volatiles (e.g., CO_2, H_2O, S) as magmas erupt on the seafloor, I studied small (30 - 200 microns) pockets of glass trapped in early-formed minerals (olivines), known as olivine-hosted melt inclusions (OL-MI). Ol-MI were analyzed by using two micro-analytical techniques: Laser-Ablation Inductively Coupled Mass Spectrometry (LA-ICP-MS) and Secondary Ion Mass Spectrometry (SIMS). In this chapter, I report volatile, major, and trace element contents of SEMFR Ol-MI, and I compare their composition to that of the host glassy rinds, which preserves the composition of the lava at the time of eruption. I discovered that SEMFR Ol-MI are the most depleted and primitive basaltic melts sampled in the Mariana Intraoceanic Arc. These Ol-MI represent hydrous melts trapped by olivine xenocrysts from the forearc mantle. This is the first time that such Ol-MI in equilibrium with the highly depleted forearc lithosphere were recovered at

subduction zones, and they thus provide unique and valuable insights into the composition of the shallow aqueous fluids released from the shallow part of the subducting plate beneath forearcs. Shallow slab-derived fluids are thought to be the most aqueous fluids (enriched in FMEs and volatiles) relative to the deeper aqueous slab-derived fluids released beneath the arc volcanoes. Undegassed SEMFR Ol- MI and host basaltic glassy rinds record the highest volatile and FME fluxes in the whole Mariana intraoceanic system, indicating that the fluids released beneath forearcs are the most hydrous. However, the volatile and the FME fluxes also show a SE-NW compositional gradient, demonstrating that the minerals from the subducting plate carrying volatile and FMEs (serpentinite, phengite, barite, chlorite) mostly broke down ~ 50 – 100 km slab depth to release most their aqueous fluids beneath the arc volcanoes. This manuscript will be submitted to the peer-reviewed journal *Earth and Planetary Science Letters*.

CHAPTER 2

GEODYNAMIC EVOLUTION OF A FOREARC RIFT IN THE SOUTHERNMOST MARIANA ARC

2.1 ABSTRACT

The southernmost Mariana forearc stretched to accommodate opening of the Mariana Trough backarc basin in late Neogene time, erupting basalts now exposed in the SE Mariana Forearc Rift (SEMFR) 3.7 – 2.7 Ma ago. Today, SEMFR is a broad zone of extension that formed on hydrated, forearc lithosphere and overlies the shallow subducting slab (slab depth < 30 – 100 km). It comprises NW-SE trending subparallel deeps, 3 - 15 km wide, that can be traced ≥ ~ 30 km from the trench almost to the backarc spreading center, the Malaguana-Gadao Ridge (MGR). While forearcs are usually underlain by serpentinized harzburgites too cold to melt, SEMFR crust is mostly composed of Pliocene, low-K basaltic to basaltic andesite lavas that are compositionally similar to arc lavas and backarc basin (BAB) lavas, and thus defines a forearc region that recently witnessed abundant igneous activity in the form of seafloor spreading. SEMFR igneous rocks have low Na_8, Ti_8, and Fe_8, consistent with extensive melting, at ~ 30 ± 6.6 km depth and 1224 ± 40^{o}C, by adiabatic decompression of depleted asthenospheric mantle metasomatized by slab-derived fluids. Stretching of pre-existing forearc lithosphere allowed BAB-like mantle to flow along SEMFR and melt, forming new oceanic crust. Melts interacted with preexisting forearc lithosphere during ascent. SEMFR is no longer magmatically active and post-magmatic tectonic activity dominates the rift.

2.2 INTRODUCTION

Forearcs are cold regions above subduction zones that lie between the trench and the magmatic arc. They can be accretionary or non-accretionary depending on the amount of sediments carried into the trench (Lallemand, 2001, Stern, 2002). Non-accretionary forearcs, such as that of the Marianas, are of special interest as they preserve a record of the first lavas erupted in association with subduction initiation (Ishizuka *et al.*, 2011, Reagan *et al.*, 2010, Stern and Bloomer, 1992). Forearc lithosphere is underlain by the cold, subducting plate that releases its hydrous fluids into the upper mantle wedge, resulting in exceptionally cold (< 400^{o}C; (Hulme *et al.*, 2010)) and serpentinized mantle lithosphere that rarely melts (Hyndman and Peacock, 2003, Rüpke *et al.*, 2004, Van Keken *et al.*, 2002, Wada *et al.*, 2011). The occurrence of cold, serpentinized forearc mantle beneath the Mariana forearc is demonstrated by eruption of serpentinite mud volcanoes (Hulme et al., 2010, Mottl *et al.*, 2004, Savov *et al.*, 2007, Savov *et al.*, 2005, Wheat *et al.*, 2008) and serpentinized peridotite outcroppings on the inner trench slope (Bloomer and Hawkins, 1983, Ohara and Ishii, 1998). Serpentinized mantle beneath the forearc has also been imaged by geophysical surveys (Tibi *et al.*, 2008). Ultramafic rocks from the upper mantle wedge found as clasts in mud volcanoes and on the inner trench slope mostly consist of harzburgite, residues of mantle melting (Parkinson and Pearce, 1998, Savov et al., 2007, Savov et al., 2005) that are chemically distinct from the more fertile, backarc basin (BAB) peridotites (Ohara *et al.*, 2002). Such highly depleted, forearc mantle can melt in association with early-arc volcanism to generate boninites (Reagan et al., 2010, Stern and Bloomer, 1992). Decompression melting of more fertile mantle to form tholeiitic basalts near the trench also has been documented during the first stage of subduction initiation. These lavas have MORB-like compositions and have been termed

forearc basalts (FABs) reflecting their subduction-related origin and location in modern forearcs (Reagan et al., 2010).

In the Izu-Bonin-Mariana (IBM) intraoceanic system, most forearc lavas are Eocene - Oligocene in age and younger forearc lavas are unusual (Ishizuka et al., 2011, Reagan et al., 2010, Stern and Bloomer, 1992). Here, we document the first record of Pliocene forearc lavas from the southernmost Mariana convergent margin, indicating that the mantle can melt beneath forearcs long after subduction initiation. These low-K lavas are tholeiitic basalts generated from BAB-like asthenospheric mantle during seafloor spreading in the Southeast Mariana Forearc Rift (SEMFR), which is a broad zone of deformation (~40 km wide and ~ 60 km long), extending from the trench to near the BAB spreading center. SEMFR today overlies a shallow subducting Pacific slab (≤ 50 - 100 km deep; (Becker, 2005)).

This paper presents a first report on the geology and tectonic evolution of the SEMFR. We present bathymetry, summarize the results of bottom traverses, and provide petrologic, major element geochemical data and $^{40}Ar/^{39}Ar$ ages of igneous rocks sampled during two JAMSTEC research cruises. These data are used to characterize SEMFR lavas and to address when, where, and how SEMFR lavas were generated, and to determine sources of the magmas, and conditions of melting. Addressing these issues helps us better understand how such melts were produced in a cold forearc, and allows us to develop a geodynamic model to constrain the geodynamic evolution of the S. Mariana forearc. In this manuscript, we show that SEMFR lavas have BAB-like geochemical and petrographic features; and opening of the Southernmost Mariana Trough

allowed adiabatic decompression melting of BAB-like asthenospheric mantle in the forearc to produce SEMFR lavas 3.7 – 2.7 Ma ago.

2.3 GEODYNAMIC SETTING

The Mariana intraoceanic arc system is the southern third of the IBM convergent margin. It is generally associated with a sediment-starved forearc ~ 200 km wide (Fryer *et al.*, 2003, Kato *et al.*, 2003), submarine and subaerial volcanoes of the active magmatic arc (Baker *et al.*, 2008), and a BAB with a spreading axis that generally lies ~ 250 – 300 km from the trench (Stern *et al.*, 2003). Mariana geodynamic evolution was influenced by collisions with buoyant oceanic plateaus (Ogasawara Plateau in the north and Caroline Ridge in the south). These resisted subduction, stimulating backarc extension to open the Mariana Trough between the collisions (Wallace *et al.*, 2005).

The arc magmatic front almost intersects the southern end of the BAB spreading center south of 13^{o}N (Figure 2.1B, (Fryer et al., 2003)). These features are about 100 – 150 km from the trench, whereas to the north the BAB spreading axis lies ~250 – 300 km from the trench and is separated from the magmatic arc by 50 - 100 km (Fryer *et al.*, 1998, Stern et al., 2003).

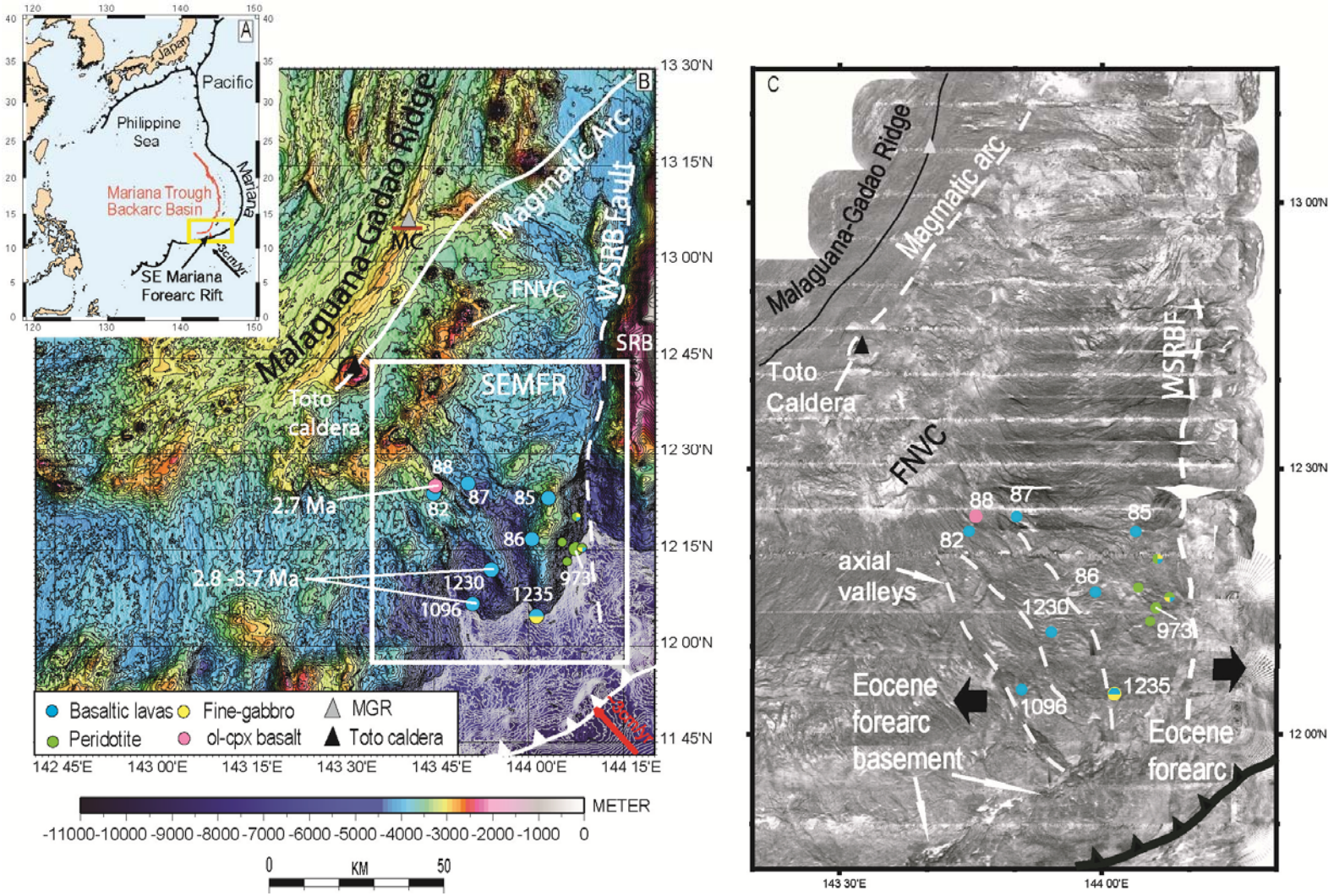

Figure 2.1. Locality maps. A) Izu-Bonin-Mariana intraoceanic arc system. The IBM magmatic arc generally lies ~ 200 km from the trench and the Mariana Trough backarc basin spreading center generally lies ~ 300 km from the trench.

The arrows represent Pacific-Mariana convergence vectors from (Kato et al., 2003). Yellow box shows the area of B. B) Bathymetric map of the southernmost Mariana arc-backarc basin system. Southward, the magmatic arc (white line) approaches the Malaguana-Gadao spreading ridge, both of which lie unusually close (~110 km) to the trench. Location of the Malaguana-Gadao spreading ridge is from (Martinez *et al.*, 2000). Filled colored circles show locations of YK06-12, YK08-08 Leg 2 and YK10-12 Shinkai dives and YK08-08 Leg 2 YKDT deep-tow cameras; the small circles show the locations of dredge site D27 (Bloomer and Hawkins, 1983), Shinkai 6500 dives158 and 159 (Fryer, 1993) and dredge sites KH98-1D1 and KH98-1D2 (Sato and Ishii, 2011); triangles show the locations of KR00-03 Leg 2 Kaiko dives in Toto caldera and Malaguana-Gadao Ridge. Note that Kaiko dive 164 is near the magma chamber (MC) identified by (Becker *et al.*, 2010). The white box shows the approximate region encompassed by SEMFR. The dashed white line shows the position of the W. Santa Rosa Bank (WSRB) Fault which separates older rocks of the Santa Rosa Bank (SRB) from the SEMFR younger rocks. The red numbers are $^{40}Ar - ^{39}Ar$ radiometric ages. Map generated with GMT (Smith and Wessel, 1990, Wessel and Smith, 1995a, Wessel and Smith, 1998, Wessel and Smith, 1995b) by using a compilation from the University of New Hampshire / Center for Coastal and Ocean Mapping / Joint Hydrographic Center (Gardner, 2006, Gardner, 2007, Gardner, 2010). C) Sidescan sonar (HMR1) image of the S. Mariana convergent margin (Fryer et al., 2003) with the location of traverses by JAMSTEC submersibles during YK06-12, YK08-08 Leg 2, YK10-12 and KR00-03 Leg 2 cruises. Dark areas have high backscatter, whitish corresponds to low backscatter. The SEMFR, the Malaguana-Gadao Ridge (MGR) and Toto caldera are dominated by high backscatter, indicating that the oceanic crust or lightly sedimented basement is exposed. White dashed line denotes SEMFR axial deeps, ridges lie between the valleys. Black arrows show the opening of SEMFR (Martinez and Stern, 2009). FNVC (Fina-Nagu Volcanic Chain) represents the arc volcanoes.

The magmatic arc appears to have been reorganized recently, as evidenced by a complex bathymetric high with multiple nested calderas – an inferred paleo-arc (the Fina-Nagu Volcanic Chain, FNVC, in Figure 2.1B) where no hydrothermal activity was observed (Baker et al., 2008) and calderas are covered with sediments (Figure 2.1C) - SE of and parallel to the modern magmatic arc (e.g. Toto caldera). The southern Mariana Trough has a well-defined spreading ridge, the Malaguana-Gadao Ridge (MGR), with a well-developed magma chamber and several hydrothermal vents (Baker et al., 2008, Becker et al., 2010, Kakegawa *et al.*, 2008). Because the subducted Pacific plate lies ~ 100 km beneath it, the MGR melt source region captures hydrous fluids usually released beneath arc volcanoes, enhancing mantle melting and resulting in an

inflated ridge morphology that is unusually robust for the Mariana Trough backarc basin, in spite of an intermediate spreading rate (< 65 mm/yr; (Becker et al., 2010, Fryer et al., 1998, Martinez et al., 2000)). More rapid extension along the MGR might also enhance decompression melting (Becker et al., 2010).

The southernmost Mariana convergent margin is underthrust by a narrow slab of Pacific plate (traceable to ~ 250 km depth; (Gvirtzman and Stern, 2004)), torn N-S at ~ 144°15'E (Fryer et al., 1998, Gvirtzman and Stern, 2004). Analogue experiments show that short, narrow subducted slabs trigger toroidal (around the slab edge) and poloidal (underneath the slab tip) asthenospheric mantle flows that generate rapid slab rollback and trench retreat relative to the upper plate (Funiciello *et al.*, 2003, Funiciello *et al.*, 2006, Schellart *et al.*, 2007). These conditions lead to weak coupling of the subducting plate with the overriding plate, stimulating rapid deformation of the overriding plate (i.e., the southern Mariana Trough) and may be responsible for the very narrow forearc that defines the southern Mariana margin west of the W. Santa Rosa Bank Fault (Figure 2.1B, (Gvirtzman and Stern, 2004)). The unusual tectonic situation of the southernmost Mariana convergent margin has also affected magmagenesis. Sub-forearc mantle usually is too cold to melt (Van Keken et al., 2002), so that slab-derived fluids only lead to serpentinization (Hyndman and Peacock, 2003, Wada et al., 2011). Instead, the dynamic tectonic setting of the southern Marianas results in mantle melting much closer to the trench than is normally observed.

2.4 GEOLOGY AND MORPHOLOGY OF THE SOUTHEAST MARIANA FOREARC RIFT

Most of the IBM convergent margin is underlain by lithosphere that formed after subduction began ~52 Ma (Ishizuka et al., 2011, Reagan et al., 2010). In the southernmost Marianas, Eocene forearc lithosphere was stretched in late Neogene time to accommodate opening of the Mariana Trough BAB; part of this extension is localized along the SEMFR (Martinez and Stern, 2009). The morphological expression of the SEMFR is apparent over a region ~ 40 km wide and at least 60 km long. SEMFR is composed of broad southeast-trending deeps and ridges (Figure 2.1B), each 50 to 60 km long and 3 to 15 km wide, which opened nearly parallel to the trench axis. These rifts can be traced from the Mariana Trench almost to the MGR (Appendix Figure 2.A1). Eastward, the SEMFR is bounded by a N-S fault, the W. Santa Rosa Bank fault (WSRBF, Figure 2.1B; (Fryer et al., 2003)), which separates thick crust of the broad Eocene forearc to the north and east (including that beneath Santa Rosa Bank) from the deeper and narrower forearc of the S. Marianas - including SEMFR - to the west. WSRBF also appears to overlie a tear in the subducted slab (Fryer et al., 2003, Gvirtzman and Stern, 2004). The WSRBF is taken to be the eastern boundary of the SEMFR because it does not have the same NNE-SSW trend as the three SEMFR deeps (Figure 2.1B), and the forearc is significantly older to the east (Reagan et al., 2010). SEMFR overlies the shallow part of the slab (≤ 50 km deep, (Becker, 2005)) and is situated in a region with numerous shallow (crustal) earthquakes, (Martinez and Stern, 2009) signifying active deformation.

We studied SEMFR by interpreting swathmapped bathymetry and previously published HMR-1 sonar backscatter imagery (Martinez et al., 2000). The region is characterized by high sonar backscatter, indicating little sedimentary cover (Figure 2.1C). This was confirmed by Shinkai 6500 manned submersible and YKDT deep-tow camera / dredge seafloor studies. Appendix Table 2.A1 summarizes the position and lithologies encountered during these dives (Figure 2.1B). Most dives recovered basalt. In addition, deeper crustal and upper mantle lithologies, e.g. diabase, fine-grained gabbros and deformed peridotites, were recovered near the WSRBF (Appendix Figure 2.A7 and 2.A8). Similar lithologies are also reported by previous studies of the area (Bloomer and Hawkins, 1983, Fryer, 1993, Michibayashi *et al.*, 2009, Sato and Ishii, 2011). Based on relief, the SEMFR can be subdivided along strike into NW, central, and SE sectors. SEMFR relief is ruggedest in the SE sector near the trench, where it is intensely faulted and affected by landsliding, with abundant talus slopes of fragmented basaltic lavas (Figure 2.2A, C, D and Appendix Figures 2.A5 to 2.A8). The central SEMFR is less faulted, with more outcrops and less talus, but still has many steep talus slopes and faulted lava flows. The NW SEMFR, nearest the MGR, has gentler relief, with better-preserved pillow lava outcrops (Figure 2.2B, E and Figures 1.A9, 1.A10). We did not recover samples of Paleogene forearc crust in the SEMFR, although this is common to the NE and west, indicating that SEMFR is floored by young, tectonized oceanic crust. Our bottom observations along with the absence of parallel magnetic fabrics in the SEMFR (Martinez et al., 2000) suggest that the SEMFR is no longer a site of active volcanism.

Toto caldera (Figure 2.1B) and part of the MGR near the NW limit of the SEMFR were studied during ROV Kaiko Dives 163 and 164 (R/V Kairei cruise KR00-03 Leg 2, Figure 2.1B). Toto caldera, which may be part of the immature magmatic arc, is mostly covered by talus of fresh lava fragments with a whitish coating, perhaps bacteria or sulfur-rich precipitate (Appendix Figure 2.A14), derived from the active Nakayama hydrothermal site (Gamo *et al.*, 2004, Kakegawa et al., 2008). The MGR seafloor is mostly composed of fresh, well-preserved pillow lavas alternating with aa and solidified lava lake (Becker et al., 2010), along with active hydrothermal vents (Appendix Figure 2.A15) indicating ongoing magmatic activity. Figure 2.1C shows high sonar backscatter for Toto caldera and around the MGR, indicating hard rock (fresh lava) exposures and thin sediments, consistent with seafloor seen in dive videos.

2.5 METHODS

Igneous rock samples were collected during two cruises YK08-08 Leg 2 (Shinkai 6500 manned submersible dive 1096) in 2008 and YK10-12 (Shinkai 6500 dives 1230, 1235 and Yokosuka deep-tow camera dredge (YKDT) 85, 86, and 88) in 2010. Representative, fresh samples were selected onboard for petrographic and geochemical studies. Information from Kaiko ROV dives 163 and 164 (R/V Kairei cruise KR00-03 Leg 2 in 2000) is also included. High-resolution videos of the seafloor generated during dives were reviewed during and after the cruises (see Appendix 2.A for more details). GMT (Smith and Wessel, 1990; Wessel and Smith, 1995b, a, 1998) was used to compile SEMFR bathymetric data, including swathmapping results from these cruises and those of (Gardner, 2006, 2007, 2010). Maps were imported into ArcGIS to generate bathymetric cross sections perpendicular to the strike of SEMFR (Appendix Figure 2.A1).

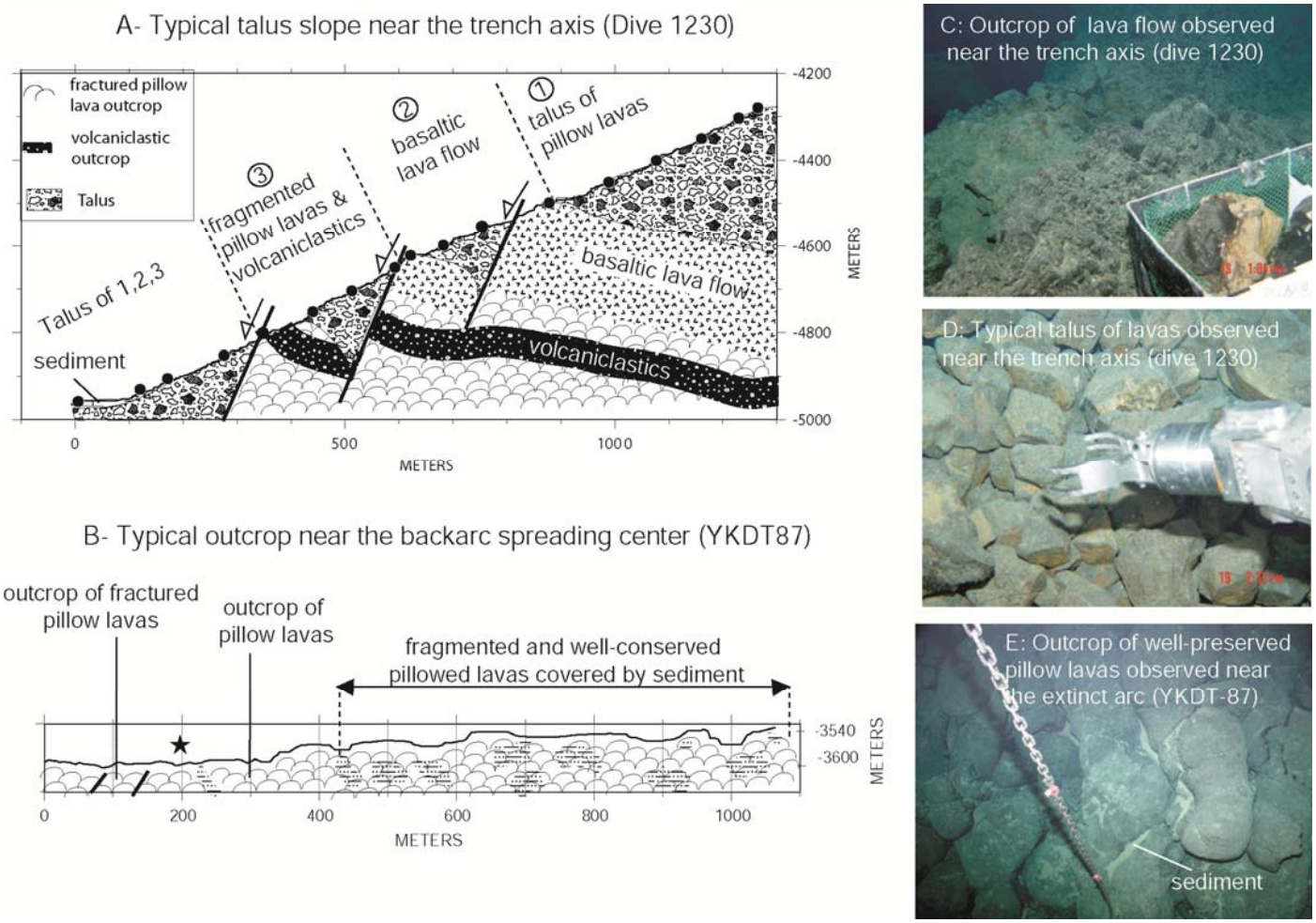

Figure 2.2. Typical bottom profiles of SEMFR encountered during seafloor traverses. A) near the trench axis (Shinkai 6500 dive 1230) and B) near the Fina-Nagu Volcanic Chain (YKDT-87). Near the trench, SEMFR flanks are dominated by steep talus slopes of lava fragments with few exposures of tilted and faulted lava flows. Talus and outcrops are covered by thin pelagic sediment. Near the Fina-Nagu Volcanic Chain (FNVC), SEMFR relief is smoother with better-preserved pillow lava outcrops covered by thin sediment. Photographs of the typical seafloor observed near the trench (C, D) and near the FNVC (E). Black star in B) shows the beginning of YKDT deep-tow camera dredging.

Igneous rock samples were analyzed, using procedures reported in Appendix 2B. For major element analyses, fresh sample chips containing as few phenocrysts as possible were hand-picked and powdered in an alumina ball mill. Whole rock chemical analyses for Shinkai dive 1096 samples were carried out on Philips PW1404 X-Ray fluorescence (XRF) spectrometer at the Geological Survey of Japan/AIST. External errors and accuracy are < 2%. Whole rock chemical analyses for other samples were performed at University of Rhode Island by fusion – dissolution of glass beads; and analyses were conducted using a Ultima-C Jobin Yvon Horiba Inductively Coupled Plasma Atomic Emission Spectroscopy (ICP-AES) at Boston University. Glass beads were generated by melting 400 ± 5 mg of lithium metaborate ($LiBO_4$) flux with 100 ± 5 mg of ignited sample powder at 1050^{o}C for 10 min. Molten beads were dissolved in 5% nitric acid to achieve a final dilution factor of ~4000 (Kelley *et al.*, 2003). Calibration curves for ICP-AES data yield $r^2 \geq 0.999$, reproducibility of replicate analyses are ≤ 3% rsd for each element, and major element oxides sum to 99 ± 1 wt%. Replicates of samples analyzed by ICP-AES and XRF yield averaged reproducibility < 4% rsd for each element. Results are reported in Table 2.1. For mineralogical chemistry analyses, 50-micron-thick polished thin sections were prepared for 16 samples. These were analyzed using the Cameca SX-50 electron microprobe at University of Texas at El Paso. Multiple point analyses give a mean value with 1σ precision ≤ 1 wt% for each selected mineral.

Four samples were dated by step-heating ^{40}Ar-^{39}Ar at the Geological Survey of Japan/AIST on a VG Isotech VG3600 noble gas mass spectrometer fitted with a BALZERS electron multiplier. Further details of procedures are reported in Appendix 2.B.

2.6 RESULTS

2.6.1 Rock description:

Here we outline the principal petrographic and mineralogical features of igneous rocks sampled from the SEMFR, Toto caldera and MGR. Method for sample description is reported in Appendix 2.C and detailed sample descriptions are in Appendix 2.D. SEMFR lavas are mostly aphyric (< 1% phenocrysts) and sparsely phyric (1 – 5% phenocrysts) basalts and basaltic andesites, indicating eruption at near-liquidus temperatures. These are microporphyritic pillows or massive flows, with thin, microcrystallite-rich glassy rims (1 – 11mm of fresh, translucent to dark brown glass), thin (≤ 1 mm) Mn coat, and negligible alteration (Figure 2.3). Pillow lavas are vesicular despite being collected at ~ 6000 – 3000 m, indicating that these magmas contained significant volatiles. In contrast, basalt flows are more crystalline and less vesicular. Embayed phenocrysts indicate disequilibrium, perhaps due to magma mixing. Pillowed lavas sampled in the NW (YKDT-88) contain larger crystals (≥ 0.5 mm) of clinopyroxene and olivine set in a finely microcrystalline olivine-rich groundmass (Figure 2.3). Similar olivine-rich lavas were not sampled elsewhere in the SEMFR. Diabase and fine-grained gabbros were also recovered near the WSRB fault (Shinkai 6500 dive 1235; Figure 2.3B, D). These might represent the lower crust of SEMFR (dyke complex and gabbro layer). Pillow lavas from MGR are very fresh, with translucent glassy rinds. Lavas are vesicular, cryptocrystalline andesites with a glassy groundmass and <1% plagioclase microlites. Lava flows from Toto caldera are vesicular, sparsely phyric to aphyric, fine-grained to cryptocrystalline basaltic andesites.

2.6.2 Major element and mineral compositions:

SEMFR lavas are fresh basalts and basaltic andesites, with 50.4 to 57 wt% SiO_2 (data reported in Table 2.1 are adjusted to 100% total on an anhydrous basis; Figure 2.4A). In terms of normative compositions, all lavas are quartz tholeiites. These define a low-K to medium-K suite, with K_2O < 1 wt%. Lava compositions cluster along the tholeiitic – calc-alkaline boundary on a plot of FeO*/MgO vs. SiO_2 (Figure 2.4B; (Miyashiro, 1974)), or along the medium-Fe / low-Fe boundary (Arculus, 2003). Lavas recovered during Shinkai 6500 dive 1096 and 1230 and YKDT-86 and -88 are relatively primitive, with whole-rock Mg# (= atomic Mg * 100 / (Mg + Fe)) > 65 (Figure 2.4C). Other SEMFR samples are significantly more fractionated, with Mg# = 49 - 63. A mean composition of SEMFR lavas is reported in Table 2.1. MGR and Toto caldera lavas are mostly andesites (SiO_2 = 55 – 61.7 wt%, with K_2O < 0.5 wt% and Mg# = 32 – 53). None of the studied lavas are boninitic (MgO > 8 wt%, SiO_2 > 52 wt%, TiO_2 < 0.5 wt%; (Le Bas, 2000)). Toto caldera lavas plot within the compositional field of southernmost Mariana volcanic arc lavas (SMA: 13°10'N – 11°N, (Fryer et al., 1998, Kakegawa et al., 2008, Stern *et al.*, in press)), suggesting that Toto caldera belongs to the SMA. Toto caldera samples also cluster along the tholeiitic – calc-alkaline boundary. In contrast, MGR lavas are tholeiitic (high-Fe) basaltic andesites and andesites ((Kakegawa et al., 2008, Pearce et al., 2005); Figure 2.4A, B). The Fe enrichment of the MGR lavas (Figure 2.4B) suggests that their parental magmas contain less water, inhibiting early crystallization of Fe-oxides.

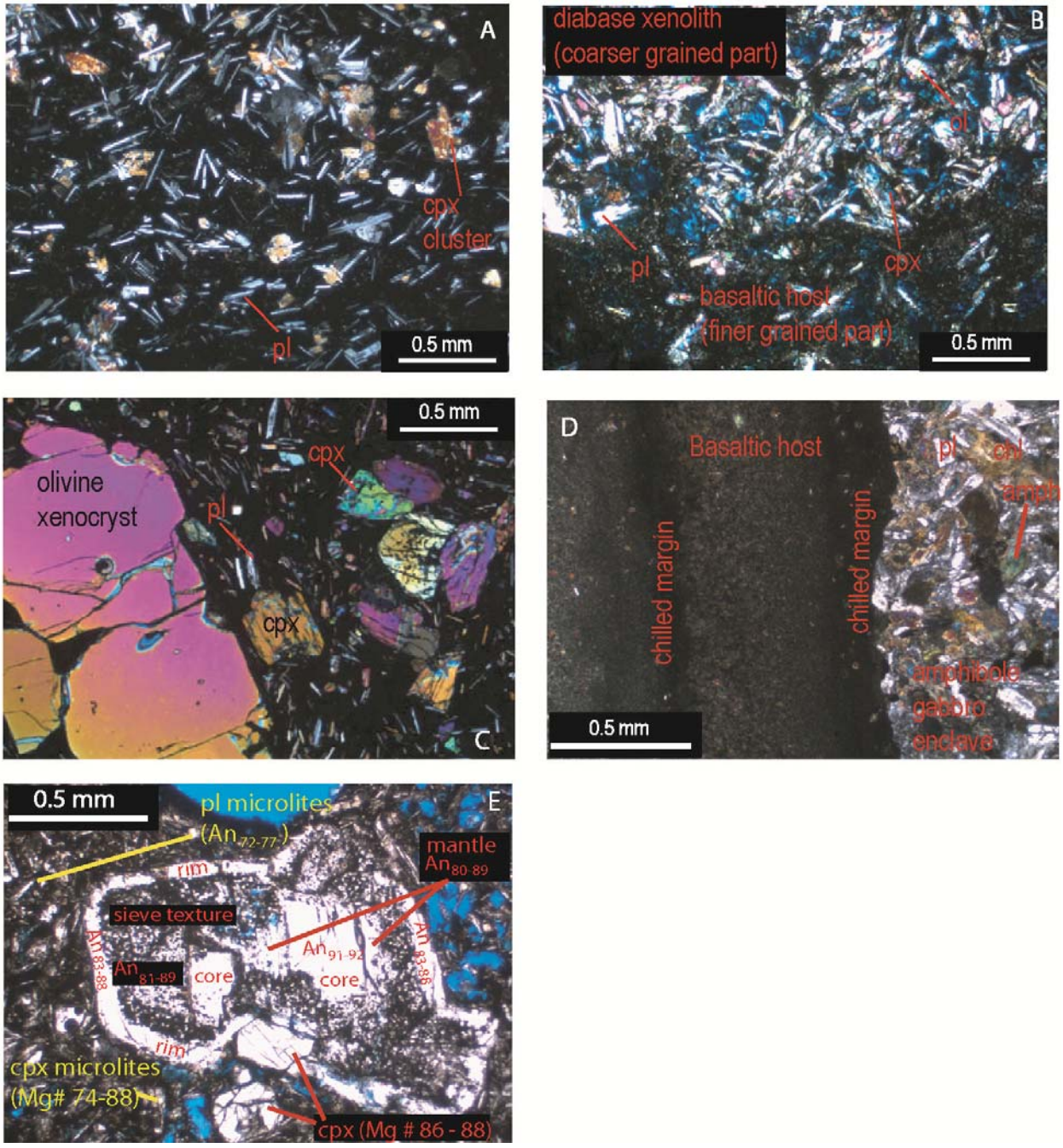

Figure 2.3. Photomicrographs of SEMFR lavas and fine gabbro. A) Typical microporphyritic olivine – clinopyroxene basalt (sample 1230-R2) with microlitic groundmass and microphenocrysts of plagioclase (pl) and clinopyroxene (cpx). B) Fine-grained diabase xenolith (sample 1235-12) hosted by microcrystalline basalt (finer grained part to left). The diabase contains Mg-rich olivine (Fo_{89}), Mg-rich clinopyroxene (Mg# ≥ 80) and normally zoned Ca-rich plagioclase (≥ 0.1 mm). In contrast, the basaltic host is more fractionated, with Fe-rich olivine

(Fo_{85-86}) and Mg-rich clinopyroxene microphenocrysts (≥ 0.1 mm). Clinopyroxene in the groundmass (< 0.1 mm) are Mg-poor and coexist with Ca-poor plagioclase microlites. Clinopyroxenes in the diabase exhibit oscillatory and reverse zoning. The boundary between the two textural realms is straight, suggesting that basalt magma picked up solidified diabase. See Appendix 2D for more details. C) Olivine – clinopyroxene basalt from YKDT-88 containing large olivine xenocrysts surrounded by olivine-rich groundmass. D) Photomicrograph of cryptocrystalline plagioclase basalt from Shinkai dive 1235 (sample 1235-R8) hosting an amphibole gabbro xenolith (chl: chlorite, amph: amphibole). The contact between gabbro and basalt is an irregular chilled margin, suggesting that the basalt picked up solid pieces of gabbro. A second chilled margin is observed inside the basalt, suggesting multiple magmatic injections in the basalt. E) Photomicrograph of plagioclase (pl) xenocryst observed in the Shinkai dive 1230 (sample 1230-R17). The core of the plagioclase is well-preserved and exhibits An_{91-92} content. The mantle exhibits An_{80-89} and is mostly resorbed (sieve-texture) due to the interaction plagioclase – melt. The rim is well-preserved and is An_{83-88}. Plagioclase microlites have lower An content (An < 80 %). Larger, Mg-rich clinopyroxenes (cpx) occur near the An-rich plagioclase xenocrysts (Mg # = 86 – 88), while the clinopyroxenes microlites exhibit higher range in Mg# (74 – 88). Such An-rich plagioclases are observed in the arc crust. See Appendix 2.D for details.

In Figure 2.4A, MGR lavas do not plot along the SEMFR fractionation trend, and their similar K_2O content suggests that MGR and SEMFR lavas interacted with similar arc-like slab-derived fluids. FABs (Reagan et al., 2010) are low-K to medium-K basalt to basaltic andesites that plot within the tholeiitic and calc-alkaline fields (Figure 2.4A, B); and SEMFR plot along the FAB fractional trend (Figure 2.4C, D). All lavas from the southernmost Marianas suggest fractionation controlled by plagioclase, clinopyroxene ± olivine crystallization trend (Figure 2.4C, F).

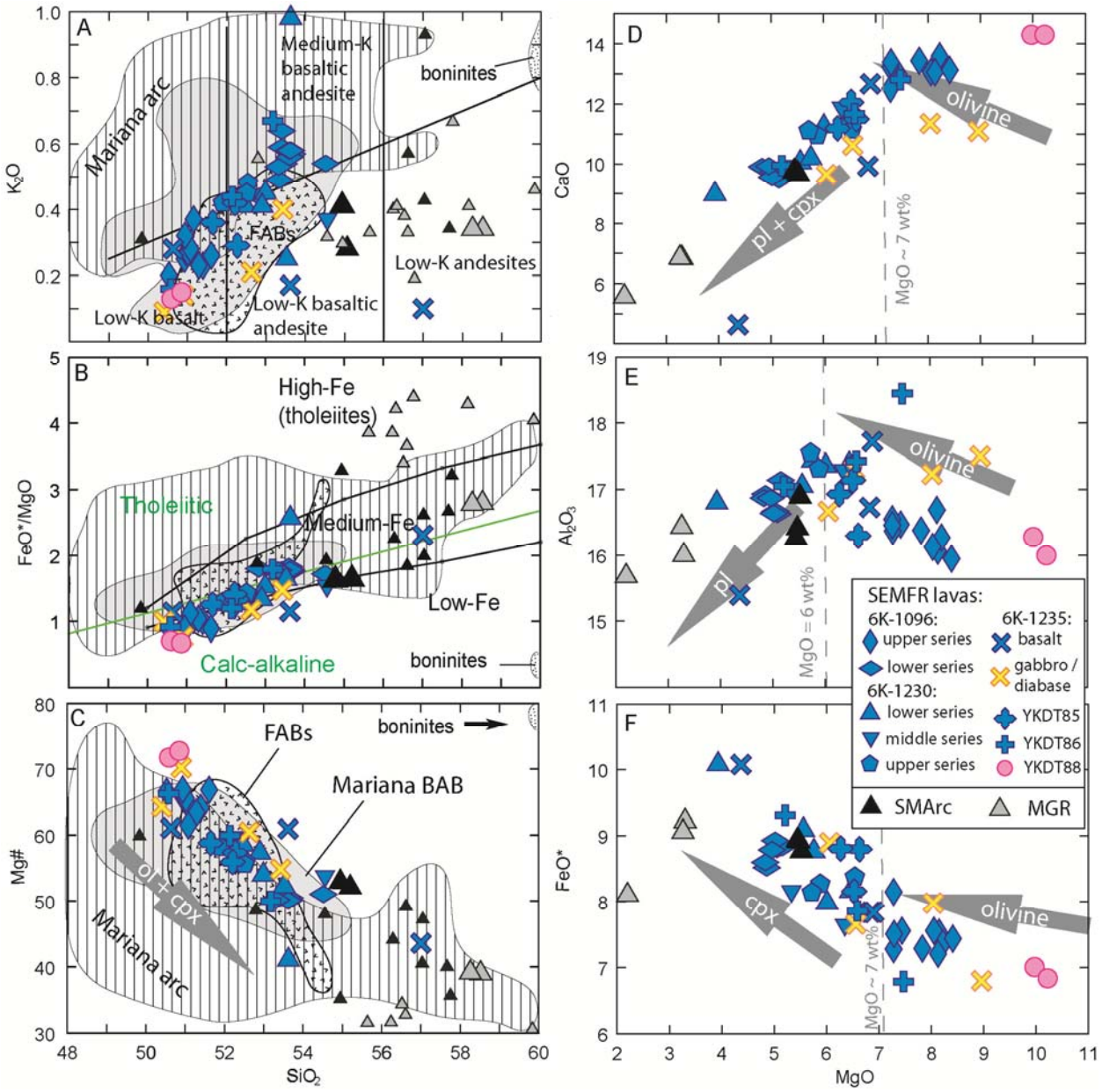

Figure 2.4. Major element compositional characteristics of SEMFR, MGR, Eocene forearc basalts (FABs; (Reagan et al., 2010)), S. Mariana Arc lavas (SMA, 13°10'N – 11°N). All data recalculated to 100% anhydrous. A) Potash-silica diagram (Peccerillo and Taylor, 1976), showing that SEMFR lavas are low-K basalts to medium-K basaltic andesites. The grey field represents Mariana Trough BAB lavas (14°N – 20°N, (Gribble *et al.*, 1996, Hawkins *et al.*, 1990, Kelley and Cottrell, 2009, Pearce et al., 2005)) and the hatched field represents Mariana Arc lavas (Kelley and Cottrell, 2009, Kelley *et al.*, 2010, Pearce et al., 2005, Shaw *et al.*, 2008, Stern

et al., 2006, Wade *et al.*, 2005). The small grey triangles are Malaguana-Gadao Ridge (MGR) data from (Kakegawa et al., 2008, Pearce et al., 2005). The small black triangles are data from SMA volcanoes (Kakegawa et al., 2008, Stern et al., in press). Larger grey triangles denote MGR and larger black triangles denote Toto samples reported in this manuscript. The field for boninites is from (Reagan et al., 2010). Note that SEMFR lavas mostly plot in field of Mariana Trough BAB lavas. B) FeO*/MgO vs SiO_2 diagram for medium-Fe, medium-Fe, high-Fe discrimination (Arculus, 2003); green line discriminates between tholeiitic and calk-alkaline lavas (Miyashiro, 1974).C) Mg# vs SiO_2 and D) CaO, E) Al_2O_3, F) FeO* plotted against MgO for SEMFR, MGR, and Toto caldera. When plagioclase starts crystallizing, it produces a hinge in the liquid line of descent (LLD) of Al_2O_3. The hinge in Al_2O_3 is observed at MgO = 6 wt%; and the kink in CaO and FeO* is observed at MgO ~ 7 wt%. Therefore. primitive lavas are identified with MgO ≥ 7 wt%, following the method of (Kelley et al., 2010). Arrows represent fractionation trends. Ol : olivine, pl : plagioclase, cpx : clinopyroxene. We used the same method as for SEMFR lavas (MgO ≥ 7 wt%) to filter the Mariana arc and Mariana Trough lavas.

SEMFR basalts and basaltic andesites contain olivine, clinopyroxene, and plagioclase. Results for representative mineral composition are listed in Appendix Tables 2.D1 to 2.D4 and summarized in Table 2.2. Mineral compositions correlate with whole rock chemical compositions (Figure 2.5A, B and Appendix 2.E). Near-primitive (Mg# ≥ 60), olivine-rich SEMFR lavas (Shinkai dive 1096, upper series and YKDT-88) contain Mg-rich olivines (Fo_{86-88}) in equilibrium with Mg-rich clinopyroxene (Mg# = 83 – 91) and anorthitic plagioclase (An ≥ 80). In contrast, fractionated (Mg# < 60) lavas have Fe-rich olivine (Fo_{75-84}) coexisting with two kinds of clinopyroxene (endiopside – diopside with Mg # ≥ 80 and augite with Mg# < 80) and plagioclase (An ≥ 80 and An < 80). Reverse and oscillatory zoning is only observed in more fractionated plagioclase (An < 80 in the core), suggesting magma mixing perhaps in a magmatic reservoir. Fine-grained gabbro and diabase have Mg-rich clinopyroxenes (Mg# ≥ 60) coexisting with more albitic plagioclase (An ≤ 70). Toto caldera and MGR andesites contain clinopyroxene and plagioclase that are more fractionated than those in SEMFR lavas (Appendix Figure 2.D1). Olivine xenocrysts (≥ 0.5 mm) enclosing chromium spinel are common in primitive lavas

(Figure 2.5D). The olivine xenocryst – spinel assemblage ($Fo_{89-92;}$ Cr# (= 100 * Cr / (Cr +Al)) = 47 – 73) plots in the mantle array of (Arai, 1994) and are similar to those of SE Mariana forearc mantle peridotite (Cr# > 50 and Fo_{90-92}, (Ohara and Ishii, 1998)), suggesting that these xenocrysts are samples of forearc mantle (Figure 2.5C).

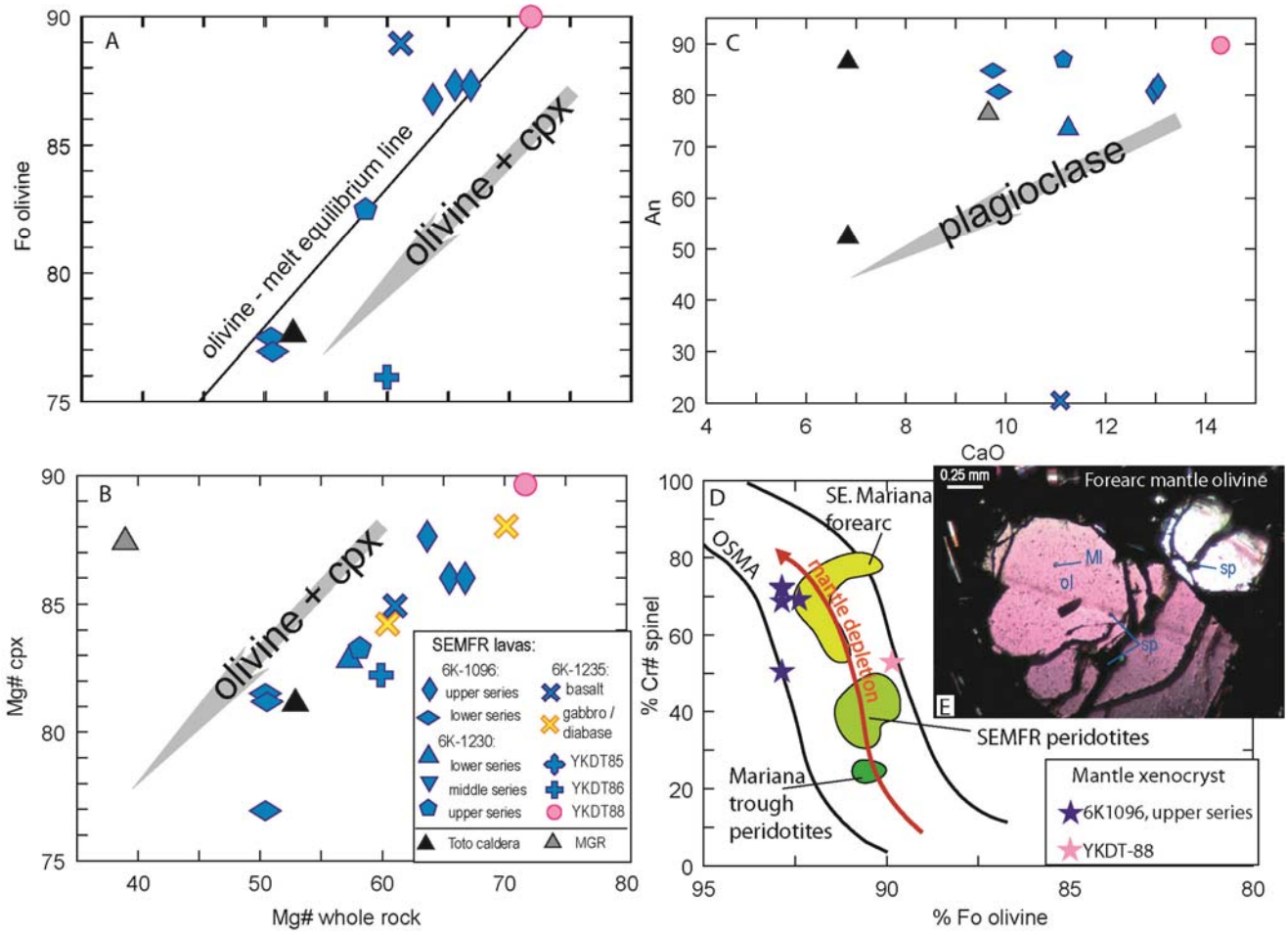

Figure 2.5. Variation of A) olivine Fo and B) clinopyroxene Mg# composition with whole rock Mg#. C) Variation of An content of plagioclase core with whole rock CaO (wt%) content. Olivine, clinopyroxene and plagioclase are mostly in equilibrium with their host rock. Fractional crystallization (grey arrow) removes Mg-rich minerals from the residual melt which precipitates increasingly Fe-rich minerals. The olivine-liquid equilibrium line is calculated from experimental data of (Roeder and Emslie, 1970) with K_D olivine – melt = 0.3 and $Fe^{3+}/Fe_T = 0.17$ (Kelley and Cottrell, 2009). C) Olivine – spinel Mantle Array (OSMA) diagram of (Arai, 1994).

Cr# of spinel inclusions and Fo content of host olivine xenocrysts in Shinkai dive 1096 upper series (blue star) and in YKDT-88 lavas (pink stars) plot within OSMA. Cr# are means for each spinel inclusion and reported with the Fo content of their olivine host. Their Cr# ≥ 50 is similar to that of the southern Mariana forearc peridotite (Ohara and Ishii, 1998); whereas BAB peridotites have Cr# < 30 (Ohara et al., 2002). SEMFR peridotites (Michibayashi et al., 2009, Sato and Ishii, 2011) have Cr# and Fo contents intermediate between southern Mariana forearc peridotites and Mariana Trough BAB peridotites (Ohara et al., 2002). D) Large xenocryst of anhedral olivine (ol) with Fo_{90-92} hosting chromium spinel (sp) and melt inclusions (MI) from Shinkai dive, 1096 upper series (sample 1096-R21).

2.6.3 ^{40}Ar-^{39}Ar ages:

Four SEMFR samples (2 samples from Shinkai 6500 dive 1096, 1 sample each from Shinkai 6500 dive 1230 and YKDT-88) were dated by step-heating ^{40}Ar-^{39}Ar (Figure 2.6 and Table 2.1). Initial ^{40}Ar/^{36}Ar for these samples (290 - 295) is nearly atmospheric (^{40}Ar/^{36}Ar $_{atmosphere}$ = 298.6), indicating that negligible radiogenic ^{40}Ar was inherited. Dated samples from dive 1096 samples include one from each of the lower (1096-R2) and upper series (1096-R16) lavas. These gave indistinguishable plateau ages of 3.5 ± 0.4 Ma (lower series 1096-R2) and 3.7 ± 0.3 Ma (upper series 1096-R16). Shinkai dive 1230 and YKDT-88 gave slightly younger ages, respectively of 2.8 ± 0.5 Ma and 2.7 ± 0.3 Ma. SEMFR ^{40}Ar-^{39}Ar ages indicate that seafloor spreading occurred in Pliocene time (Figure 2.1B), and suggests that SEMFR seafloor youngs toward the MGR.

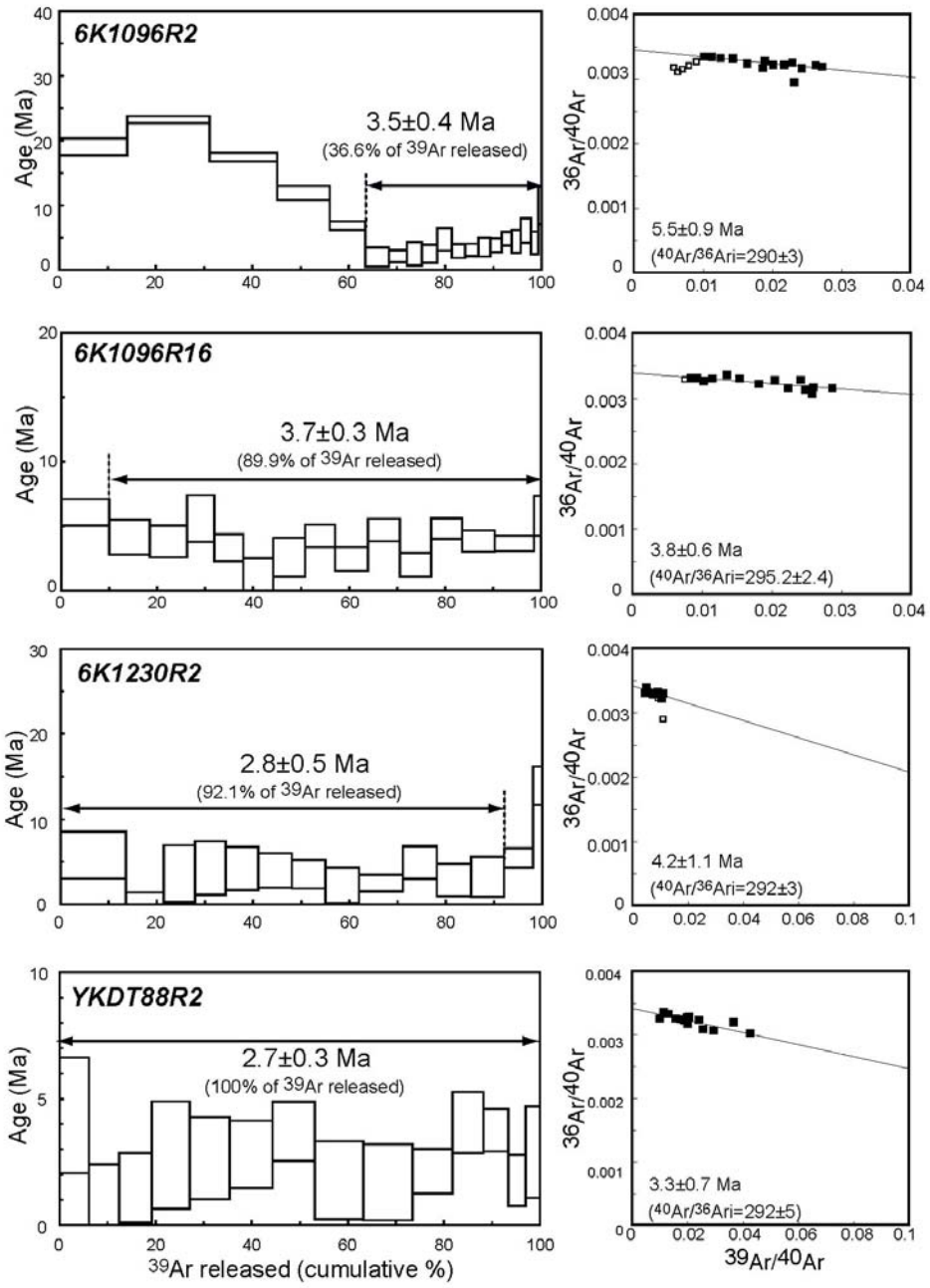

Figure 2.6. The $^{40}Ar/^{39}Ar$ age spectra with $^{36}Ar/^{40}Ar$ vs $^{39}Ar/^{40}Ar$ plot for samples from the SEMFR.

Table 2.1. Example of major element (wt%) compositions of SEMFR lavas. Mg# [= atomic $(Mg^{2+} * 100) / (Mg^{2+} + Fe^{2+})$] was calculated assuming all the iron is Fe^{2+} on anhydrous basis. Samples with MgO < 8 wt% were corrected on anhydrous basis by using the equations of (Klein and Langmuir, 1987) for Na_8 and Fe_8, and (Taylor and Martinez, 2003) for Ti_8. See text for details. fg: fine-grained, ol: olivine, pl: plagioclase, cpx: clinopyroxene. Complete data set is provided in a joined excel file.

Sample No.	1096-R2*	1096-R3	1096-R4	1096-R7	1096-R8	1096-R11	1096-R12	1096-R15	1096-R16	1096-R17
IGSN	SEMFR JMR000011	SEMFR JMR000012	SEMFR JMR000013	SEMFR JMR000016	SEMFR JMR000017	SEMFR JMR00001A	SEMFR JMR00001B	SEMFR JMR00001D	SEMFR JMR00001E	SEMFR JMR00001F
Method	-	XRF	XRF	XRF	XRF	XRF	XRF	XRF	XRF	XRF
Sample description	pillow lava	pillow basalt	pillow basalt	pillow basalt	pillow basalt	pillow basalt	pillow basalt	pillowed ol basalt	pillowed ol basalt	pillowed ol basalt
SiO2	-	52.50	52.73	52.60	52.58	52.57	52.45	50.56	50.52	50.69
TiO2	-	0.97	0.98	0.97	0.96	1.01	0.96	0.69	0.67	0.66
Al2O3	-	16.34	16.64	16.55	16.36	16.31	16.60	16.28	15.94	16.29
FeO	-	8.73	8.38	8.44	8.64	8.75	8.65	7.47	7.47	7.25
MnO	-	0.16	0.14	0.15	0.15	0.15	0.15	0.13	0.13	0.13
MgO	-	5.00	4.78	4.74	4.95	4.92	4.88	7.35	8.08	7.79
CaO	-	9.60	9.69	9.71	9.56	9.36	9.76	12.81	13.09	13.36
Na2O	-	3.31	3.33	3.30	3.28	3.30	3.33	2.27	2.14	2.14
K2O	-	0.53	0.56	0.57	0.55	0.57	0.52	0.36	0.25	0.27
P2O5	-	0.11	0.11	0.11	0.11	0.12	0.11	0.08	0.07	0.07
total	-	98.22	98.27	98.06	98.09	98.04	98.37	98.82	99.20	99.46
%LOI										
Mg#	-	50.52	50.42	50.05	50.56	50.04	50.14	63.68	65.85	65.70
Na8								2.09	2.16	2.09
Ti8								0.62	0.67	0.64
Fe8								6.62	7.53	7.00
40Ar-39Ar ages (Ma)	3.5 ± 0.4								3.7 ± 0.3	
T(°C)								1221	1219	1212
P(GPa)								0.85	0.82	0.78

Table 2.2. Overview of mean mineral compositions in basalts from each dive in the SEMFR for a subset of samples. Complete data set is provided in a joined excel file. C : core, m : mantle, st : sieve texture, r : rim, gr: groundmass, * : minerals in 1235-R12 observed in the microcrystallized basalt, while the other 1235-R12 analyses refer to minerals in the diabasic xenolith. Numbers in italics represent reverse zoning. Bold numbers represent minerals with oscillatory zoning. NA: Not analyzed. MGR: Malaguana-Gadao Ridge, SEMFR: S.E. Mariana Forearc Rift.

Sample #	Lilithology	Location	olivine xenocrysts		olivine		feldpspars						clinopyroxene			
			Fo>= 90		Fo	stdev	An > 80	stdev	80 > An > 60	stdev	An < 60	stdev	Mg# > = 80	stdev	Mg# < 80	stdev
1096-R21	upper series primitive basalt	SEMFR	c: 92.6 r: 92.3 r: 87.6	0.3 0.5 1.7	c: 87.2 r: 86.5	0.5 0.4	c: 81.7 r: 81.0	1.1 0.1					c: 86.0 r: 86.9	1.7 0.8		
1096-R15	upper series primitive basalt	SEMFR			c: 86.8 r: 85.7	1.1 1.2	c: 80.7 r: 81.2	1.3 0.6					c: 87.6 r: 87.6	0.9 0.5		
1096-R8	lower series andesitic basalt	SEMFR			c: 76.9 r: 76.46	2.1 1.0	*c: 84.7* *r: 87.7*	*0.3* *0.1*	c: 67.9 r: 68.5	3.3 1.6			c: 81.2 r: 79.2	0.9 1.3	c: 76.8 r: 76.6	2.4 3.0
1096-R4	lower series andesitic basalt	SEMFR			c: 77.5 r: 76.6	1.6 0.4	*c: 80.6* *m: 86.8* *r: 83.4*	*2.0* *0.4* *0.4*	c: 67.3 r: 67.4	2.1 1.9			c: 81.5 r: 82.8	0.6 0.4	c: 76.9 r: 77.9	1.7 1.4
1230-R14	lower series basalt	SEMFR			NA				73.5	3.2			*c: 82.8* *r: 83.7*	*1.2* *0.3*	78.6	0.8
1230-R17	middle series basalt	SEMFR			NA		c:91.3 m:84.5 st: 85.7 r: 86.4	0.4 3.8 2.9 1.8	74.8	2.1			85.0	2.2	75.6	1.4

2.7 DISCUSSION

2.7.1 Genesis of SEMFR lavas:

Compositions of lavas and their minerals record the conditions of magma genesis and evolution; nd from this, important tectonic information can be gleaned (e.g. (Klein and Langmuir, 1987)). Incompatible elements such as K_2O, Na_2O and TiO_2 are concentrated in the melt as mantle melting or crystal fractionation proceeds. The first melt fraction is enriched in these elements and so concentrations anti-corrrelate with fraction of melting, or "F" (Kelley *et al.*, 2006, Kelley et al., 2010, Klein and Langmuir, 1987a, Taylor and Martinez, 2003). In addition, K_2O contents in convergent margin magma sources are strongly affected by subduction-related metasomatism (e.g. K-h relationship, (Dickinson, 1975, Kimura and Stern, 2008)), therefore this element is generally not used to monitor F. FeO contents in basalts also contain petrogenetic information. In basaltic systems, deeper melts are progressively enriched in iron (Klein and Langmuir, 1987). Therefore, the Na_2O, TiO_2 and FeO contents of lavas are good proxies for the degree and depth of melting. However, estimating the extent and depth of partial melting requires primitive lavas with compositions in equilibrium with their mantle source; consequently, Na_2O, TiO_2 and FeO contents are commonly corrected for olivine fractionation in order to infer their Na_8, Ti_8 and Fe_8 contents (Na_2O, TiO_2 and FeO contents calculated at MgO = 8 wt%).The Na_8 of N-MORBs anti-correlates with Fe_8, indicating that melting is greater if it begins deeper (Figure 2.7A; (Arevalo Jr. and McDonough, 2010, Klein and Langmuir, 1987)). Subduction-related melting is somewhat different because melting extents are enhanced by water (Gribble et al., 1996, Kelley et al., 2006, Taylor and Martinez, 2003). BAB magma sources often are affected by subducted water and are

characterized by more melting at shallower depth than MORBs, so that Na_8 increases with Fe_8 (Figure 2.7A; (Kelley et al., 2006, Taylor and Martinez, 2003)). BAB and arc lavas have distinct geochemical signatures (Figure 2.7A), resulting from elements dissolved in fluids derived from the subducting slab that are involved in magma genesis. Arc lavas have lower Na_8, Ti_8, Fe_8 content at higher K_2O/TiO_2 because they formed by high degrees of melting at greater depths in the presence of slab-derived fluids. In contrast, BAB lavas have higher Na_8, Ti_8, Fe_8 content at lower K_2O/TiO_2, as they were generated at shallower depth by adiabatic mantle decompression, with less involvement of slab-derived fluids.

To investigate SEMFR magmagenesis (i.e. whether SEMFR lavas were produced in a BAB-like and / or in a arc-like magmagenetic settings), we calculated Na_8, Ti_8 and Fe_8 contents for these lavas. Plots of Al_2O_3, CaO and FeO* against MgO (Figure 2.4D-F) show that the kink in Al2O3 _indicating the beginning of plagioclase crystallization_ is observed at MgO = 6 wt%; and the hinge in CaO and FeO* _ indicating the beginning of plagioclase fractionation_ is observed at MgO ~ 7 wt%. Therefore, data were filtered to exclude highly fractionated samples with MgO < 7 wt% that crystallized olivine, clinopyroxene and plagioclase on their LLD (Figure 2.4D-F), following the method described in (Kelley et al., 2006, Kelley et al., 2010). The least fractionated samples with 7 - 8 wt% MgO, which fractionated olivine only (Figure 2.4D-F), were then corrected to 8% using the equations of (Klein and Langmuir, 1987) for Na_8 and Fe_8, and (Taylor and Martinez, 2003) for Ti_8 . These are listed in Table 2.1 (mean SEMFR $Na_8 = 1.99 \pm 0.40$ wt% (1 std. dev.); mean $Ti_8 = 0.60 \pm 0.11$ wt%;. mean $Fe_8 = 6.91 \pm 0.54$ wt%). The Na_8 , Fe_8 and Ti_8 contents of SEMFR lavas are slightly lower than those observed for N-MORBs (Arevalo

Jr. and McDonough, 2010), indicating higher degrees of mantle melting produced shallower. SEMFR lavas have similar Ti_8 and Na_8 contents at lower Fe_8 than FABs; and they plot in the compositional overlap between Mariana arc lavas and the Mariana BAB lavas, with homogeneous, low Na_8 and Ti_8 contents varying little with Fe_8 content (Figure 2.7A - B), suggesting a roughly constant degree and depth of mantle melting. These lavas were produced by extensive melting (≥ 15%) of shallow mantle (~ 25 ± 6.6 km, see section 6.2). The K_2O/TiO_2 (proxy for the total subduction input; (Shen and Forsyth, 1995)) of SEMFR lavas is higher that of FABs and plot between the arc – BAB compositional fields (Figure 2.7C - D), well above N-MORBs, further demonstrating a subduction component in SEMFR magma genesis. Negative correlations of Ti_8 and Fe_8 with K_2O/TiO_2 show that subduction input increases with extent of partial melting and decreases with melting depth (Kelley et al., 2006, Kelley et al., 2010, Taylor and Martinez, 2003). Only lavas from YKDT-88, collected closest to the FNVC (Figure 2.1B), do not fit on SEMFR trends, with lower Na_8 and Ti_8 at similar Fe_8 contents. Their Ti8 and Na8 values are lower than those of Mariana arc lavas (Figure 2.7), suggesting that YKDT-88 lavas were produced by more mantle melting and / or melting of a more depleted mantle source at similar depth compared to other SEMFR magmas.

The above inference that SEMFR lavas are similar to back-arc basin basalts (BABB) can be checked by examining mineral compositions, because arc basalts and BABBs have distinct An-Fo relationships (Stern, 2010). Arc basalts contain more Fe-rich olivine with more An-rich plagioclase compared to BABB, MORB, and OIB (Ocean Island Basalt) because high water content in arc magmas delays plagioclase but not olivine crystallization (Kelley et al., 2010,

Stern, 2010), resulting in higher CaO and FeO contents in the melt when plagioclase starts crystallizing.

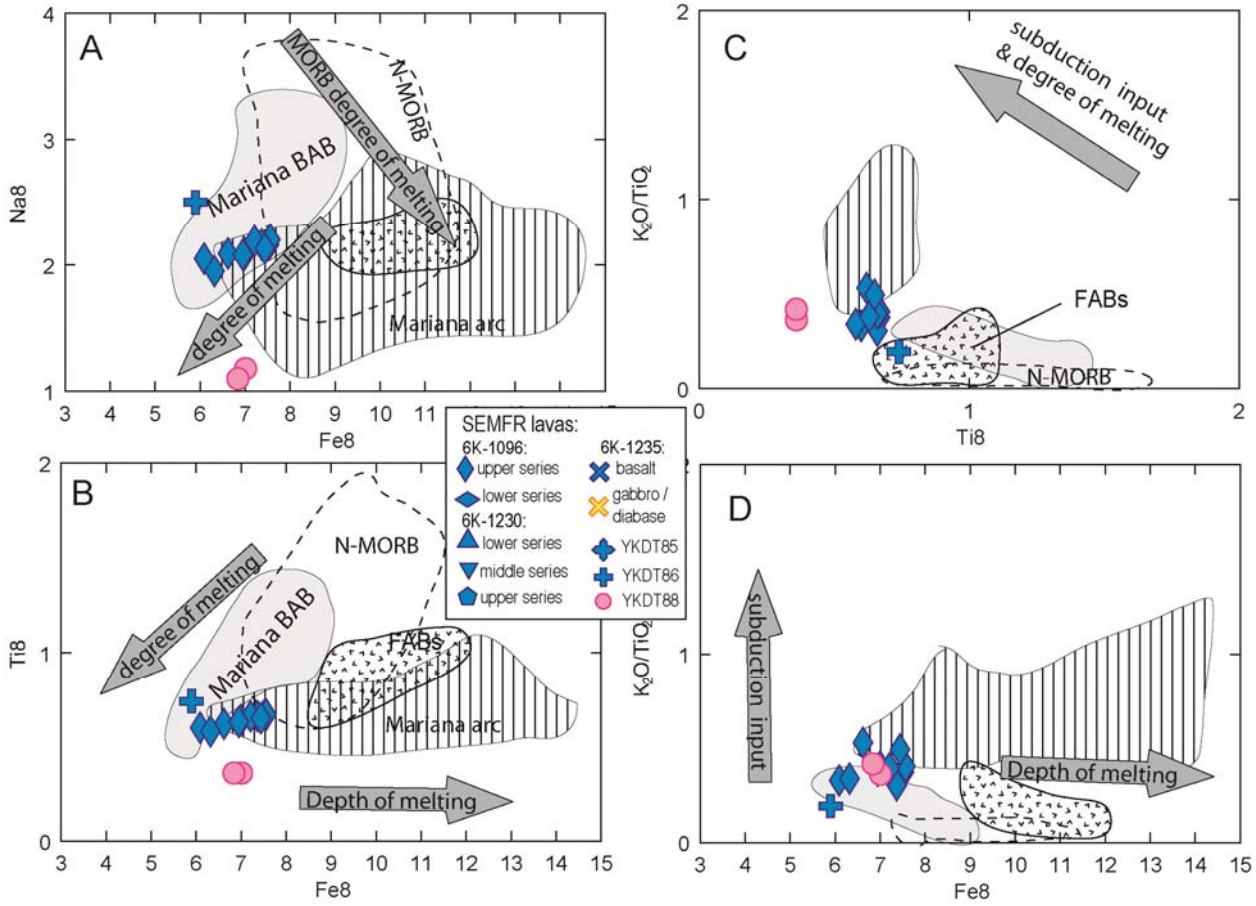

Figure 2.7. Diagrams showing variations in A) Na_8, B) Ti_8, D) K_2O/TiO_2 versus Fe_8 and C) K_2O/TiO_2 versus Ti_8. Na_8 and Ti_8 are proxies for the fraction of mantle that is melted, Fe_8 is a proxy for the depth of mantle melting (Klein and Langmuir, 1987, Pearce et al., 2005), and K_2O/TiO_2 is a proxy for the subduction input. The grey field represents Mariana Trough BAB lavas ($14^oN - 20^oN$, (Gribble et al., 1996, Hawkins et al., 1990, Kelley and Cottrell, 2009, Pearce et al., 2005)) and the hatched field represents Mariana arc lavas (Kelley et al., 2010, Pearce et al., 2005, Shaw et al., 2008, Stern et al., 2006, Wade et al., 2005, Kelley and Cottrell, 2009). The FABs field is from (Reagan et al., 2010). The negative correlation of Na_8 with Fe_8 of N-MORBs (grey arrow; (Arevalo Jr. and McDonough, 2010)) shows that more magma is produced when melting begins deeper. The grey arrow with black outline shows the Na_8-Ti_8-Fe_8 correlation for subduction-related lavas. In contrast, SEMFR lavas have Na_8 and Ti_8 contents content slightly varying with Fe_8 indicating little variation in the melting depth. Low Ti_8 and Na_8 relative to MORB suggest that SEMFR melts are produced from an unusually depleted mantle or reflect unusually high degrees of melting, or both.

In contrast, BABBs, formed largely by adiabatic decompression mantle melting, have Fo-An relationships essentially indistinguishable from those of MORB and OIB (Figure 2.8A). Accordingly, we can discriminate arc basalts from BABBs based on An and Fo contents of the plagioclase – olivine assemblages. Figure 2.8A shows that most SEMFR lavas plot within the BABB compositional field, consistent with observations from Na_8, Ti_8, and Fe_8 discussed in the previous section. A few samples also plot within the arc compositional field, strongly suggesting that BAB-like (i.e. adiabatic decompression melting) and arc-like (i.e. wet mantle melting) conditions of magmagenesis coexist beneath SEMFR. We propose that SEMFR magmas formed by adiabatic decompression of fertile asthenospheric mantle (BAB-like mantle) strongly metasomatized by slab-derived fluids, enriching the melt in water and sometimes delaying plagioclase fractionation.

2.7.2 Pressure and temperature of mantle melting:

The P-T conditions of mantle melting, recorded by primary melts in equilibrium with the mantle beneath SEMFR, were calculated from major element compositions of basalts with MgO ≥ 7 wt% ((Kelley et al., 2010); Figure 2.4D-F and section 6.1 for more details on the filtering) by using the geothermobarometer of (Lee et al., 2009), based on Si, Mg and water contents of primitive magmas. The estimated P-T conditions are those of the last melt in equilibrium with the mantle or a mean value of the P-T conditions of polybaric, fractional pooled melts recorded along a melting column (Kelley et al., 2010).

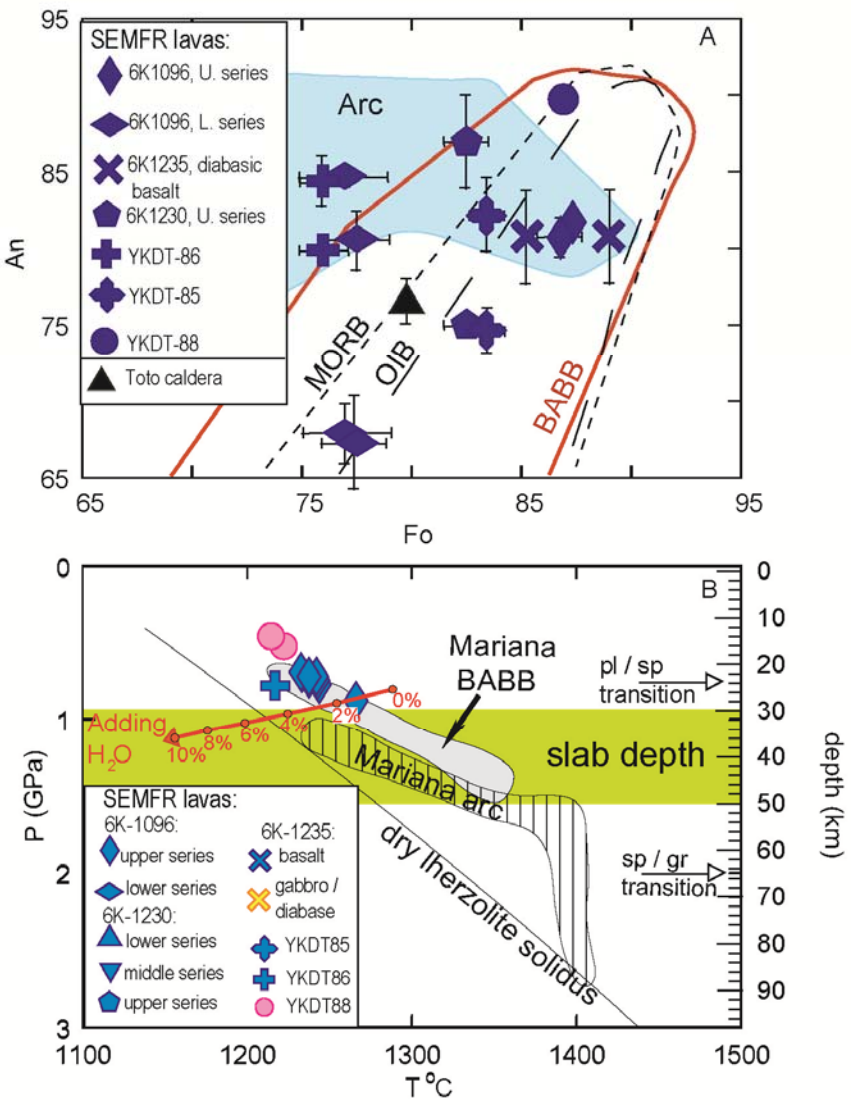

Figure 2.8. A) Composition ranges for coexisting olivine Fo – plagioclase An in intraoceanic arc lavas (blue field) and BABB (red outline) after (Stern et al., 2006). Arc basalts have more calcic plagioclase in equilibrium with more Fe-rich (Fo_{70-85}) olivine compared to MORB (short dashed outline), OIB, and BABB (long dashed outline). The plagioclase-olivine relationships of SEMFR lavas generally plot in the BABB-MORB-OIB field. The black triangle denotes a Toto caldera sample. B) Pressure and potential temperature of hydrous mantle melting estimated using procedure of (Lee et al., 2009) of SEMFR primitive lavas with MgO ≥ 7 wt%. We used an equilibrium mantle with composition of Fo90. Also shown are Mariana Trough basaltic glasses (Gribble et al., 1996, Kelley and Cottrell, 2009, Pearce et al., 2005) and the Mariana arc lavas with analyzed water contents (Kelley et al., 2010, Shaw et al., 2008). The water content was set to 1.5 wt% (mean water content of the Mariana Trough lavas with H_2O > 1 wt% (Kelley and Cottrell, 2009)) for BABBs when not analyzed. The solidus is from (Katz *et al.*, 2003). We used

$Fe^{3+}/Fet = 0.17$ for SEMFR and Mariana Trough BABBs, $Fe^{3+}/Fet = 0.25$ for Mariana arc lavas (Kelley and Cottrell, 2009) and Fo90 for the equilibrium mantle. We used the same method as for SEMFR lavas (MgO ≥ 7 wt%) to filter the Mariana arc and Mariana Trough lavas.

SEMFR lavas are compositionally similar to BABBs and,FABs (Reagan et al., 2010) have low Ba/La (< 20) like BABBs, we therefore used BAB-like oxidation state ($Fe^{3+}/Fe_T = 0.17$) and water content (1.5 wt%) for SEMFR, FABs and Mariana Trough lavas; and $Fe^{3+}/Fe^T = 0.25$ and H_2O ~ 3 wt% for Mariana arc magmas (Gribble et al., 1996, Kelley and Cottrell, 2009, Kelley et al., 2010, Pearce et al., 2005, Shaw et al., 2008). We also used lherzolitic BAB-like mantle source (Fo_{90}; (Kelley et al., 2006)) to estimate the P-T conditions of SEMFR mantle melting. SEMFR whole rock compositions indicate melting pressures of 0.6 – 1.0 GPa (± 0.2 GPa) and temperatures of 1192 – 1242^{o}C (± 40^{o}C), with a mean of 0.8 ± 0.2 GPa (~ 26 ± 6.6 km) and 1212 ± 40^{o}C (Figure 2.8B). This is consistent with melting just above the present subducting slab (~ 30 – 50 km depth), although we do not know the position of the subducting slab at 2.7 – 3.7 Ma, when SEMFR melts were generated. Mariana Trough BABBs (Gribble et al., 1996, Kelley and Cottrell, 2009, Pearce et al., 2005) reflect similar P-T conditions of mantle melting (0.7 – 1.5 ± 0.2 GPa, 1243 – 1360 ± 40^{o}C; mean melting depth ~ 33 ± 6.6 km). In contrast, Mariana arc lavas (Kelley et al., 2010, Shaw et al., 2008) and FABs (Reagan et al., 2010) show higher P-T conditions of mantle melting (1 – 3.5 ± 0.2 GPa, 1247 - 1562 ± 40^{o}C for the arc lavas; and 1.0 – 2.0 ± 0.2 GPa, 1296 - 1424 ± 40^{o}C for FABs). These results suggest that SEMFR lavas and Mariana Trough BABBs were similarly generated by adiabatic decompression of shallow asthenospheric mantle (~ 30 – 35 ± 6.6 km). In contrast, arc lavas and FABs record deeper and hotter mantle melting conditions (Kelley et al., 2010). This leads to the further deduction that SEMFR lavas formed by BABB-like seafloor spreading at 2.7 to 3.7 Ma.

2.7.3 Geodynamic evolution of the Southeastern Mariana Forearc Rift:

Investigations of the petrography and geochemistry of SEMFR lavas reveal that i) SEMFR lavas are petrographically and compositionally similar to Mariana Trough BABB; ii) SEMFR melts interacted with the pre-existing forearc lithosphere and picked up some forearc mantle olivines, indicating rapid ascent; iii) magmatic activity (2.7 – 3.7 Ma) formed SEMFR oceanic crust by seafloor spreading (no Eocene forearc basement has been recovered from the SEMFR); iv) SEMFR primitive basalts formed by decompression melting at 30 km depth and 1224^{o}C, like that associated with the Mariana Trough backarc basin, suggesting similar formation; and v) lack of evidence for recent igneous and hydrothermal activity, except near MGR and Toto caldera, indicates that the presently-observed NNW-SSE trending relief formed during post-magmatic rifting (< 2.7 Ma).

SEMFR is a rift with no morphological expression of large arc-like volcanoes, like those of the Mariana arc. SEMFR lavas are vesicular with K_2O contents (Figure 2.4A) and K_2O/TiO_2 ratios that are similar to MGR and other Mariana Trough BAB lavas (Figure 2.7C, D). They also have similar P-T conditions of magma genesis, demonstrating that they formed by adiabatic decompression of BAB-like mantle metasomatized by slab-derived fluids. These observations raise a fundamental question: were SEMFR lavas produced by seafloor spreading in the backarc basin or in the forearc? The southernmost Mariana convergent margin has reorganized rapidly since its collision with the Caroline Ridge, suggesting that SEMFR lavas were produced by different geological settings that what exists today. From the location of SEMFR adjacent to the trench, it is clear that these lavas formed in the forearc.

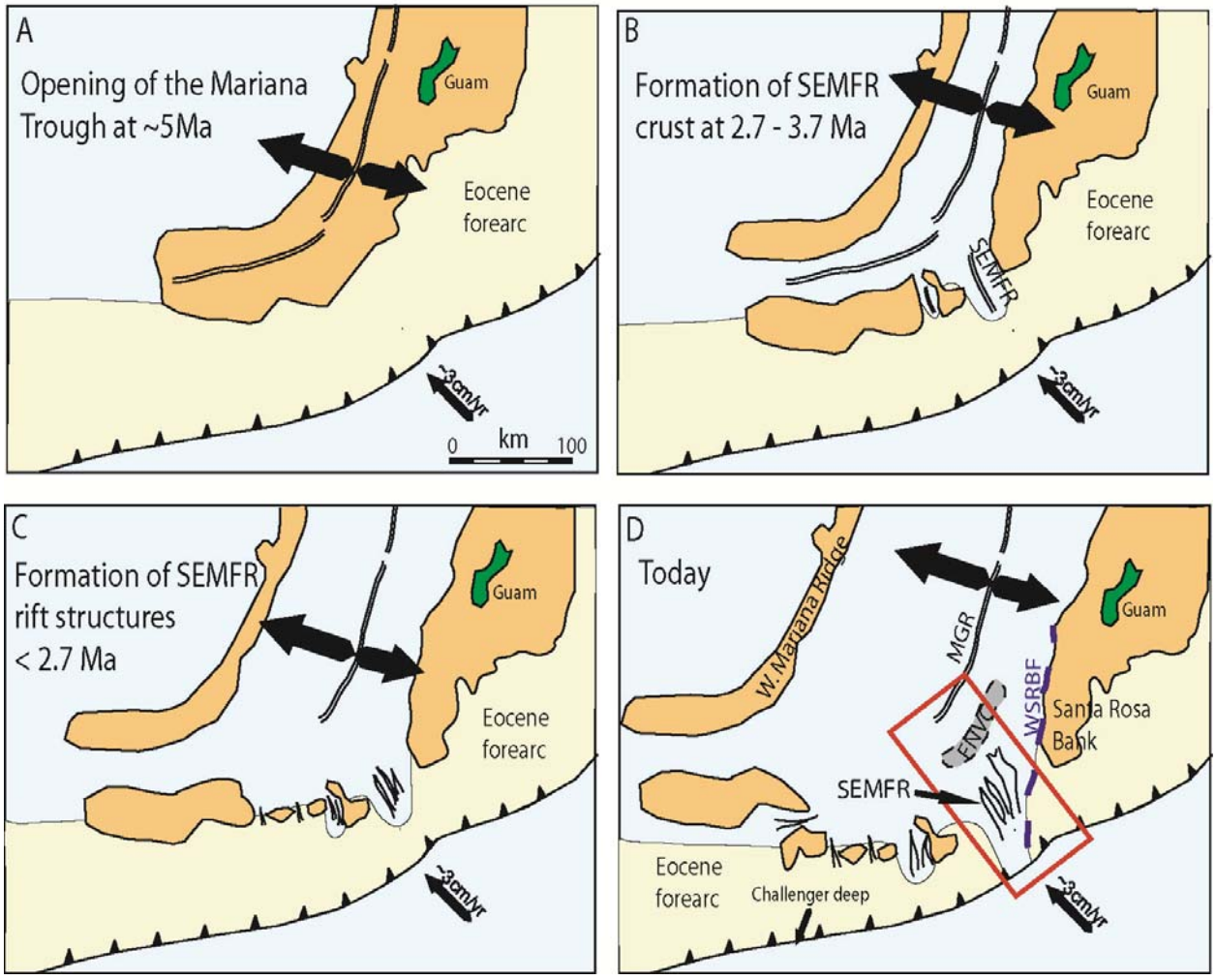

Figure 2.9. Geodynamic evolution of SEMFR. A) The Mariana Trough is opening ~ 5 Ma ago. B) Spreading of the Mariana Trough rifts the arc lithosphere and forms SEMFR by stretching the forearc crust 2.7 – 3.7 Ma ago. We speculate that SEMFR is a spreading center with intense magmatic activity. C) Post-magmatic deformation of SEMFR occurred < 2.7 Ma ago, and intensely deformed the Eocene forearc crust. D) Today, SEMFR is no longer magmatically active and amagmatic extension dominates the rift. Eocene forearc is eroded with opening of the S. Mariana Trough; and actual position of the forearc is based on R/V Yokosuka YK08-08 Leg 2 and YK10-12 cruise reports (Ohara *et al.*, 2010, Ohara *et al.*, 2008). The red box highlights the area of Figure 2.10.

We propose a geodynamic model for the southernmost Mariana arc, in which SEMFR formed to accommodate opening of the southernmost Mariana Trough (Figure 2. 9A, B and Figure 2.10A-C). Rupturing the forearc lithosphere allowed asthenospheric mantle to flow into the forearc and

to melt by adiabatic decompression under hydrous conditions 2.7 – 3.7 Ma ago; and origin of SEMFR mantle (i.e. from the backarc basin, the arc or a slab window) is still under investigation. Some SEMFR melts picked up fragments of pre-existing forearc mantle during ascent, demonstrating that SEMFR lavas formed long after subduction initiation. Post-magmatic activity (< 2.7 Ma ago) shapes the S. Mariana forearc lithosphere (Figure 2.9C) and formed the NNW-SSE trending rifts of SEMFR, as we know it today (Figure 2.9D and Figure 2.10D).

2.8 CONCLUSIONS

Two important conclusions can be drawn from this study: i) SEMFR magmas formed by adiabatic decompression in the southernmost IBM forearc, usually underlain by cold, serpentinized harzburgitic mantle that rarely melts (Reagan et al., 2010); instead ii) SEMFR lavas were produced by melting of fertile asthenospheric mantle metasomatized by slab-derived fluids, long after subduction initiation, allowing development of a forearc lithosphere. Our results show that the southernmost Mariana forearc stretched to accommodate opening of the Mariana Trough to form the SEMFR, allowing hydrated, asthenospheric mantle to flow into the forearc and to produce new oceanic crust ~ 2.7 – 3.7 Ma ago. SEMFR lavas formed by adiabatic decompression of depleted backarc mantle at ~ 30 ± 6.6 km depth and 1224 ± 40^{o}C. SEMFR at 2.7-3.7 Ma was likely a ridge-like spreading center, where the slab-derived fluids enhanced mantle melting beneath the forearc. Today, SEMFR is no longer magmatically active and amagmatic extension shapes its morphology.

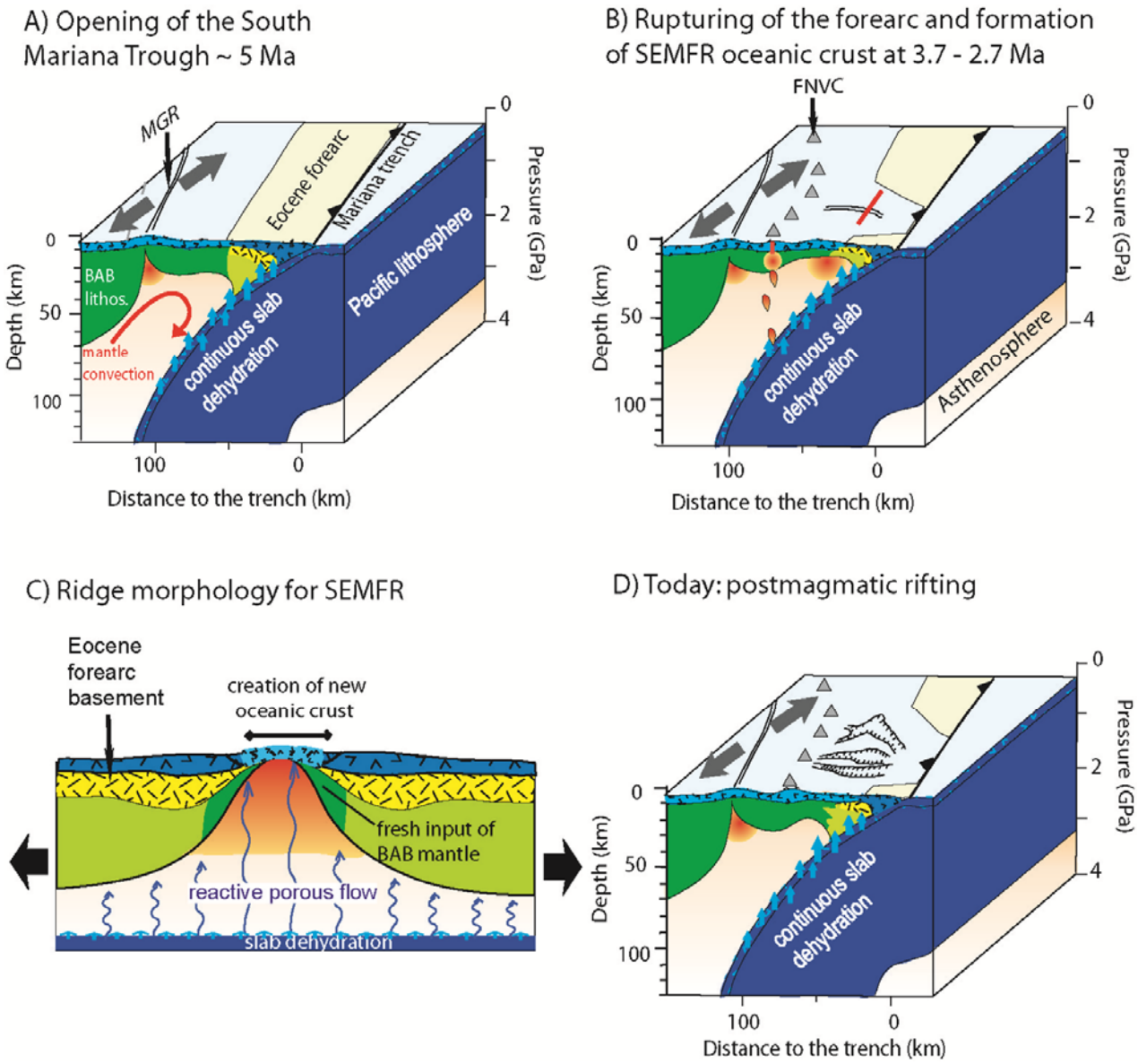

Figure 2.10. 3D model of geodynamic evolution of the SEMFR. The cross section is drawn from the area highlighted by a red box in Figure 2.9. The subducting slab is drawn after the tomographic images of (Miller *et al.*, 2006a). BAB lithos.: backarc basin lithosphere. A) Opening of the S. MarianaTrough, the Malaguana-Gadao Ridge (MGR), strectches the pre-existing Eocene forearc lithosphere ~ 5 Ma ago. B) Rupturing of the forearc allow mantle melting, creating new SEMFR oceanic crust ~ 2.7 – 3.7 Ma ago. C) Continuous dehydration of the shallow downgoing slab controlled SEMFR magmatic activity, and SEMFR had ridge morphology (A). D) Today, post-magmatic rifting dominates SEMFR.

2.9 ACKNOWLEDGEMENTS

We thank JAMSTEC for providing Kaiko samples and related videos, Teruaki Ishii, Stuart Murchison, Katsuyoshi Michibayashi, Warren Lieu, John S. Oldow and the reviewers for their help and their insightful comments. Many thanks to the R/V Yokosuka crew for their efforts work during YK08-08 Leg 2 and YK10-12 cruises. This research was supported by NSF grant 0961352 to RJS. This is UTD Geosciences Contribution # 1246.

APPENDIX 2A

DESCRIPTION OF THE DIVES

The SEMFR is composed of 3 broad rifts that converge and shoal northwestwards. These are called rifts 1, 2 and 3 from west to east. These are 50 to 56 km long (Tables 2A.1 to 2A.2 for more details). The depth and width of the rift valleys vary along strike, 3.6 to 8.2 km deep and 3 to 15 km wide (Figure 2A.1). Outcrops generally consist of faulted, fresh pillow lavas with crystallite-rich glassy rind, lava flows and volcaniclastics. Only on the western flank of the WSRB fault were deeper crustal lithologies –diabase, fine-grained gabbros and deformed peridotites - recovered (Figure 2A.4 and 2C.8; (Bloomer and Hawkins, 1983, Fryer, 1993, Michibayashi et al., 2009, Sato and Ishii, 2011).

Table 2A.1. Longitude and latitude of the dives in the SEMFR, MGR and Toto caldera with their depth and trench distance.

Location	Cruise	Shinkai dive / Deep tow YKDT/ Kaiko ROV	Latiitude start of dive	Longitude start of dive	Latiitude end of dive	Longittude end of dive	depth (m) max.	depth (m) min.	Δ depth (m)	distance from trench (± 5 km)	Samples collected
SEMFR	YK08-08 LEG 2	Shinkai dive 1096	12°06.63 N	143°51.15 E	12°06.73 N	143°51.88 E	6077	5414	663	40	basaltic pillows
SEMFR	YK10-12	Shinkai dive 1230	12°11.36 N	143°54.19 E	12°11.91 N	143°54.60 E	4958	4280	678	45	basalts
SEMFR	YK10-12	Shinkai dive 1235	12°04.22 N	144°00.73 E	12°04.91 N	144°01.20 E	6478	5861	617	26	basalts & gabbros
SEMFR	YK10-12	YKDT 82	12°25.00 N	143°50.00 E	12°25.43 N	143°49.51 E	4169	3911	258	68	no samples
extinct arc	YK10-12	YKDT 83	12°29.00 N	143°35.00 E	12°29.00 N	143°35.56 E	3052	2968	84	82	no samples
extinct arc	YK10-12	YKDT 84	12°24.60 N	143°32.50 E	12°25.61 N	143°33.11 E	3482	2658	824	78	basaltic pillows
SEMFR	YK10-12	YKDT 85	12°23.00 N	144°03.00 E	12°23.21 N	144°03.83 E	3090	2577	513	56	basaltic pillows
SEMFR	YK10-12	YKDT 86	12°16.50 N	143°59.70 E	12°16.64 N	144°00.39 E	4050	3454	596	44	basaltic pillows
SEMFR	YK10-12	YKDT 87	12°22.60 N	143°44.70 E	12°23.09 N	143°45.03 E	3630	3536	94	68	no samples
SEMFR	YK10-12	YKDT 88	12°24.20 N	143°45.70 E	12°24.45 N	143°45.99 E	3475	3342	133	70	basaltic pillows
SEMFR	YK06-12	Shinkai dive 973	12°14.55 N	144°07.81 E	12°14.96 N	144°06.81 E	6469	5957	512	36	peridotites
MGR	KR00-03 LEG 2	Kaiko dive 164	13°06.18 N	143°41.55 E	13°06.27 N	143°41.45 E	2920	2908	12	141	andesitic pillows
Toto	KR00-03 LEG 2	Kaiko dive 163	12°42.92 N	143°32.12 E	12°42.80 N	143°32.38 E	3044	3006	38	108	andesites

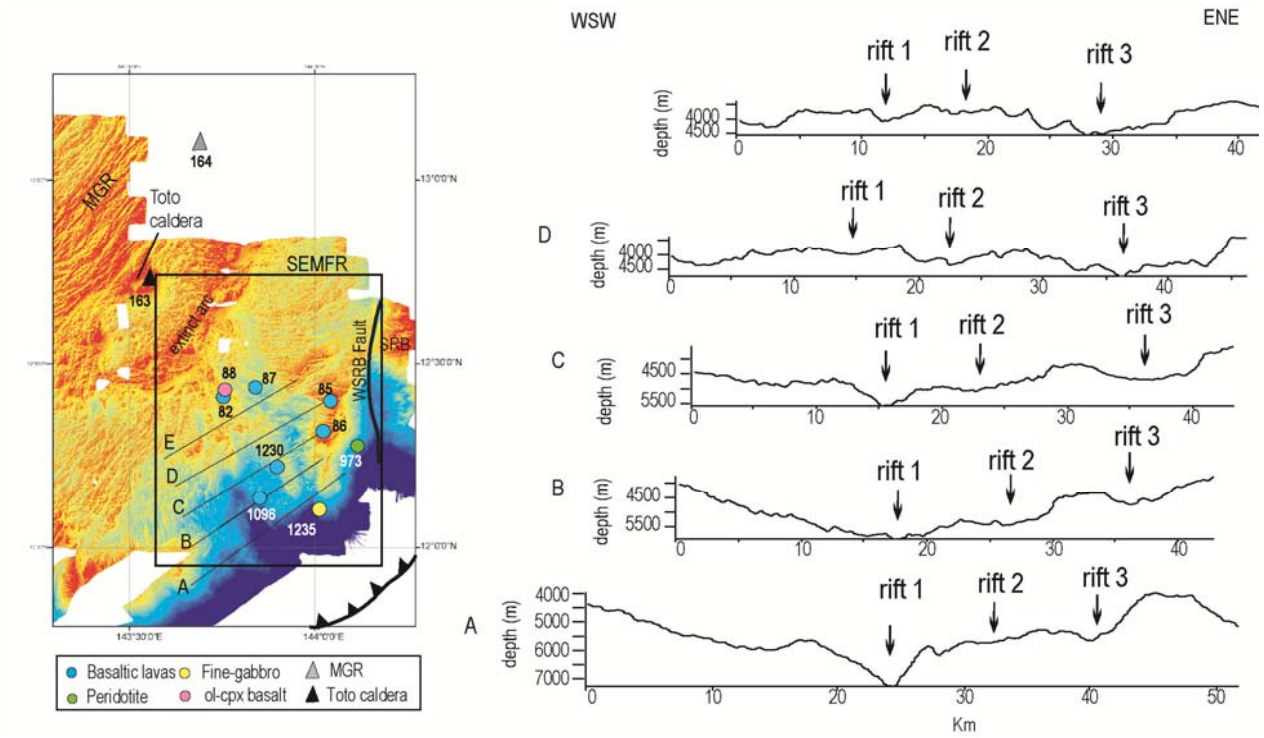

Figure 2A.1. Cross-sections of SEMFR rifts 1, 2 and 3 from the trench (A) to MGR (E). Note change in depth and width of the axial valleys, highlighted by a red line, along SEMFR axis, and reported in Table 2A.2. Rift 1 is the deepest of the three, while rift 2 and especially rift 3 are better developed near the MGR. The map was generated by S. Merle using GMT (Smith and Wessel, 1990, Wessel and Smith, 1995a, Wessel and Smith, 1998, Wessel and Smith, 1995b), with a resolution of 100 m, using sonar multibeam data from Mariana cruises since 2001 (NOAA compilation) and by using a compilation from the University of New Hampshire / Center for Coastal and Ocean Mapping/Joint Hydrographic Center (Gardner, 2006, Gardner, 2007, Gardner, 2010). Maps were then imported under ArcGIS, in the projected coordinate system Mercator WGS 1984, to generate cross-sections. The map was artificially illuminated at 31^{o} NNW to highlight relief. MGR: Malaguana-Gadao ridge; SRB: Santa Rosa Bank. The black rectangle encompasses the SEMFR region. Thick black line shows the position of the W. Santa Rosa Bank (WSRB) Fault. The circle shows the location of the YK06-12, YK08-08 LEG 2 and YK10-12 Shinkai dives and YK08-08 LEG 2 camera deep tow, the triangle shows the location of KR00-03 Leg 2 Kaiko dives in Toto caldera (163) and Malaguana-Gadao Ridge (164).

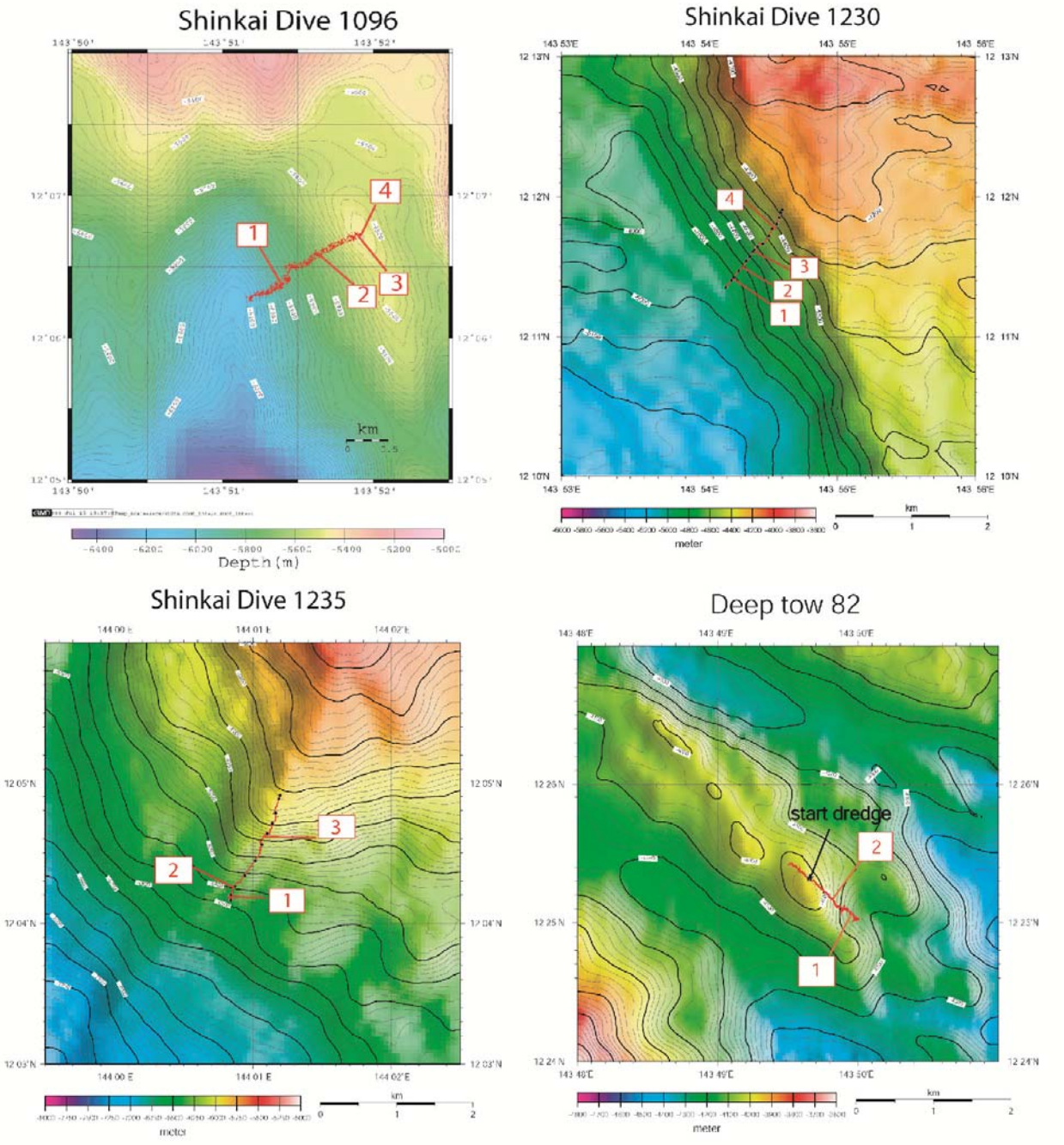

Figure 2A.2. Dive tracks (red line) of Shinkai dives 1096, 1230 and 1235 and deep tow camera 82. Locations of the dives are reported in the manuscript (Figure 2.1B). The red boxes with a number correspond to the location of the bottom pictures in the bathymetric profiles. The star represents the beginning of the dredge. The maps have been realized on-board with GMT (Smith and Wessel, 1990, Wessel and Smith, 1995b, Wessel and Smith, 1995a, Wessel and Smith, 1998) by using sonar multibeam data YK10-12 and YK08-08 LEG 2.

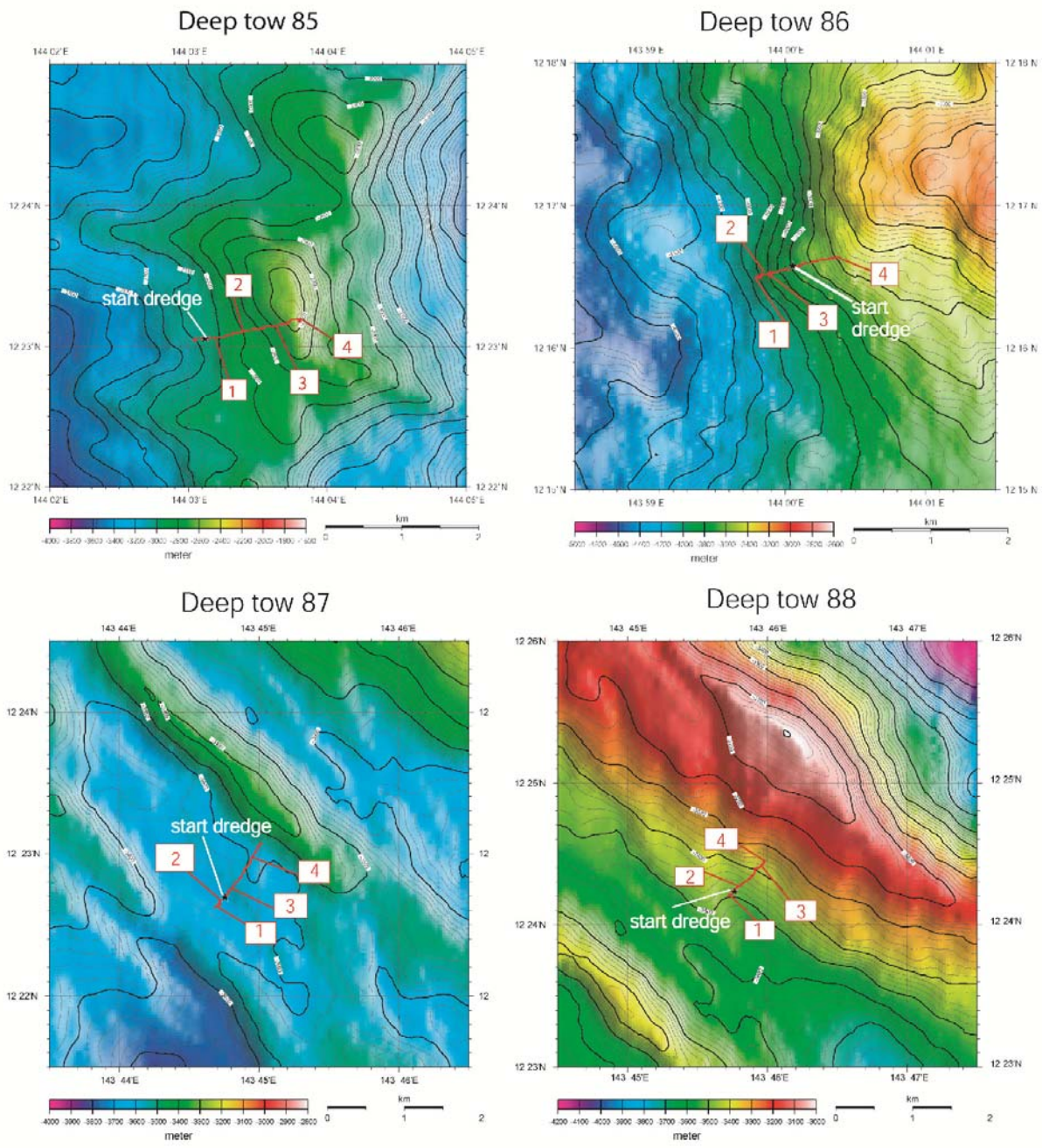

Figure 2A.3. Dive tracks (red line) of YKDT 85, 86, 87 and 88. Locations of the dives are reported in the manuscript (Figure 2.1B). The red boxes with a number correspond to the location of the bottom pictures in the bathymetric profiles. The star represents the beginning of the dredge. The maps have been realized on-board by F. Martinez with GMT (Smith and Wessel, 1990, Wessel and Smith, 1995b, Wessel and Smith, 1995a, Wessel and Smith, 1998) by using sonar multibeam data from YK10-12.

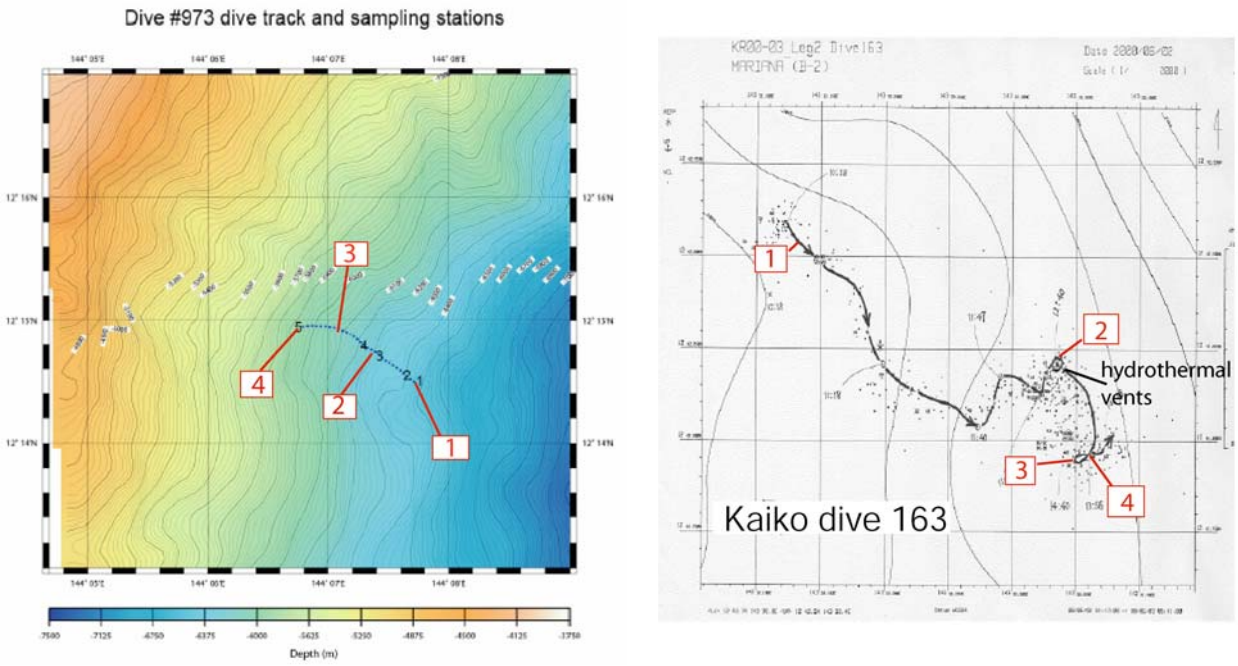

Figure 2A.4. Dive tracks (red line) of Shinkai dive 973 from YK06-12 cruise report and Kaiko dive 163 (black line) from KR00-03 Leg 2 cruise report. Locations of the dives are reported in the manuscript (Figure 2.1B). The red boxes with a number correspond to the location of the bottom pictures in the bathymetric profiles.

2.A.1 SEMFR:

The SEMFR was investigated by the manned submersible Shinkai 6500 and the YKDT with mini-dredges in 2006, 2008 and 2010 on board of the Yokosuka. Shinkai dives 1096, 1230 and 973 were performed in the vicinity of the trench. Details are reported in Tables 2A.1 to 2A.2.

Table 2A.2. Variation of the width and depth (km) of the three SEMFR rifts along axis.

	width (km)	length (km)	min. depth (m)	max. depth (m)	Δ depth (m)
Rift 1	16.4	50 - 56	3600	8200	4600
Rift 2	8	54	3600	7000	3400
Rift 3	4.8	56	4000	7000	3000
SEMFR	31 - 41	56 - 59	3600	8200	4600

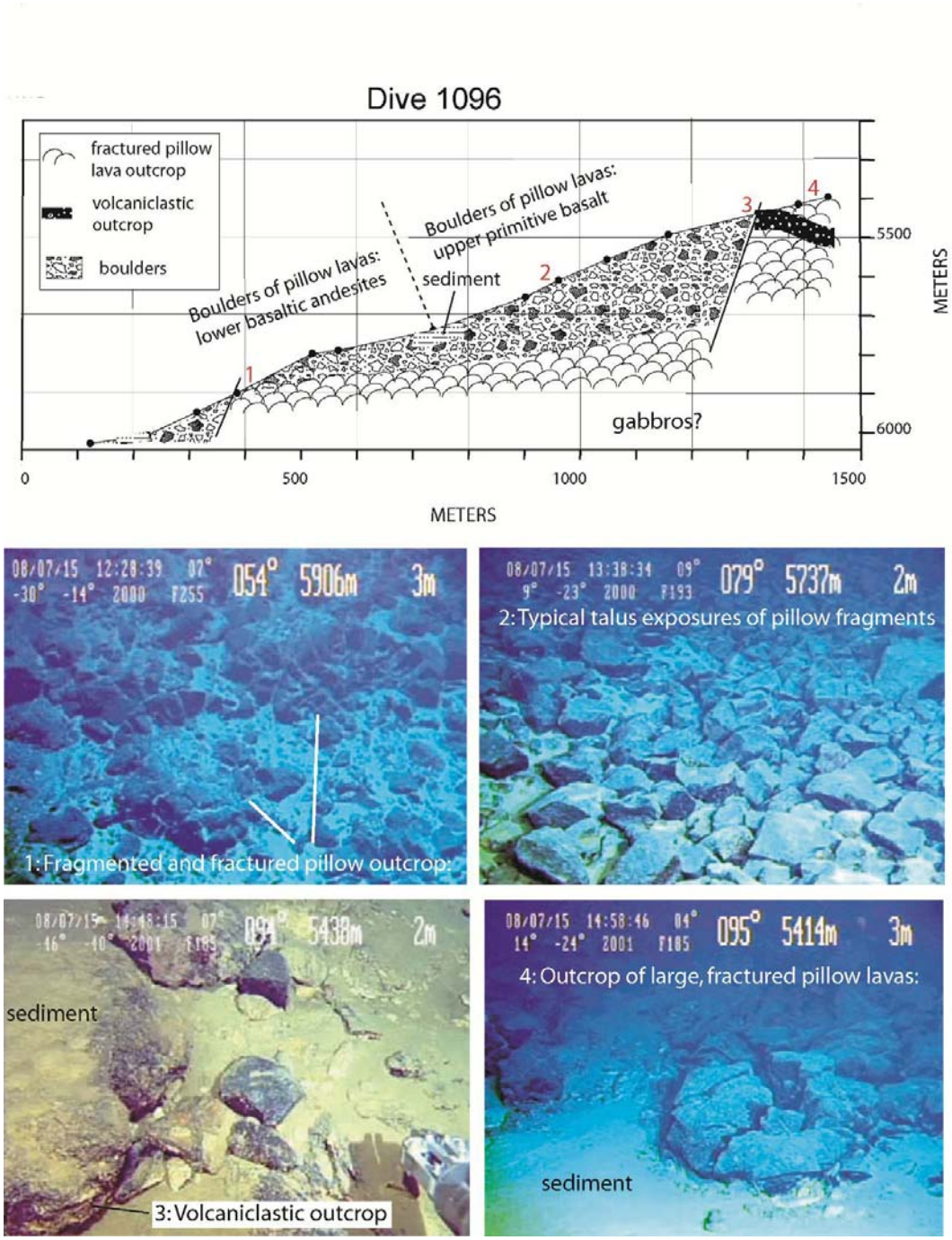

Figure 2A.5. Interpreted bathymetric profile of the eastern flank of rift 1 traversed during Shinkai dive 1096, located near the trench. Locations of the bottom pictures are reported in red on the bathymetric profile. Two distinct suites of pillow lavas were identified, based on abundance of olivine phenocrysts, an olivine-poor lower series (6077 – 5797 m) and an upper series richer in olivine (5737 – 5414 m). An outcrop of volcaniclastics was observed at 5429 m. Note the steep flanks of the rift near the trench. Profile has been realized under ArcGIS.

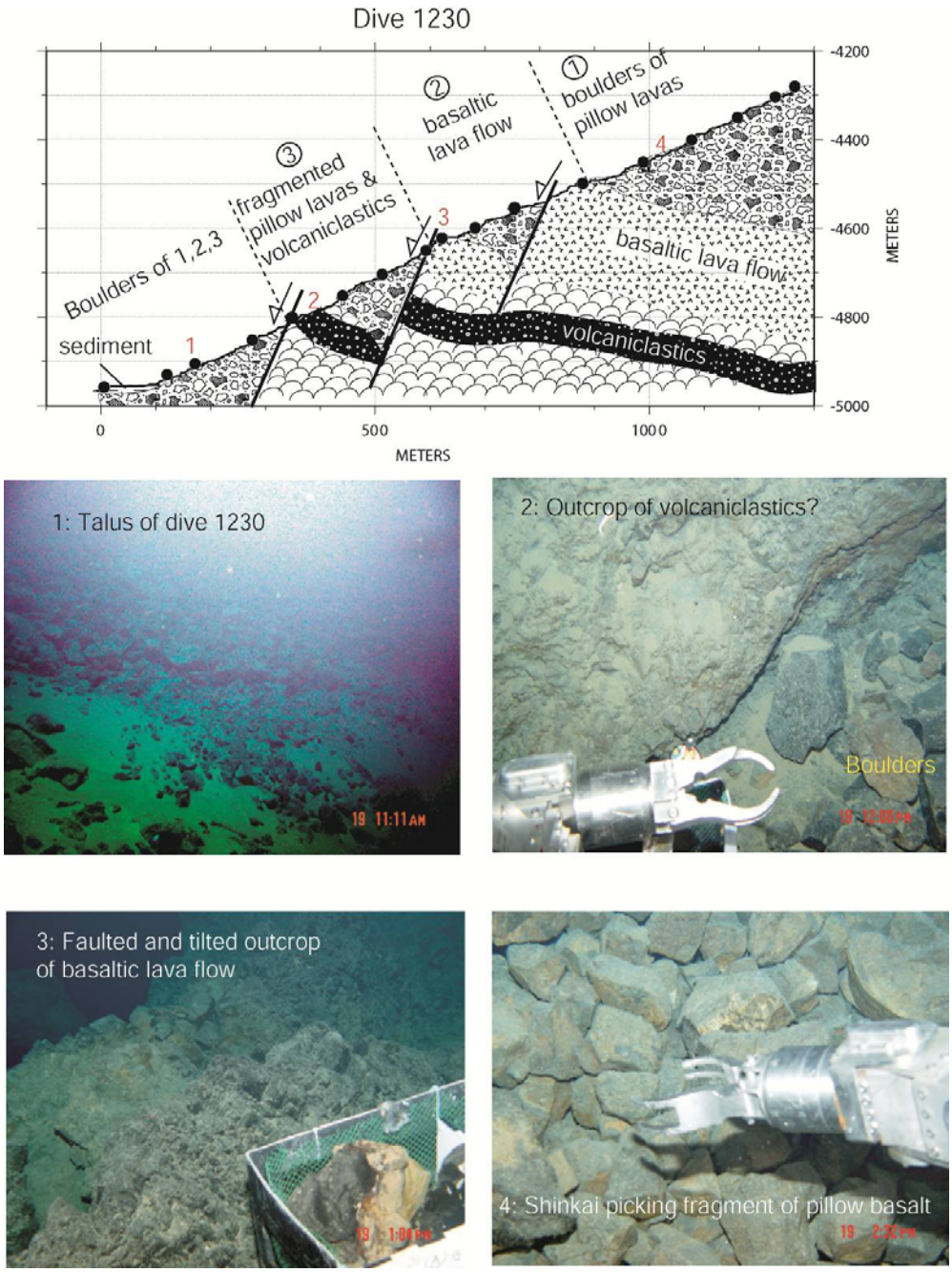

Figure 2A.6. Interpreted bathymetric profile of the eastern flank of rift 2 traversed during Shinkai dive 1230 (near the trench). Locations of the bottom pictures are reported in red on the bathymetric profile. This dive mostly traversed a talus slope composed of large fragments of pillow lava, lava flow and volcaniclastics. The rift flank is very steep and faulted. Profile has been realized on-board by F. Martinez with GMT (Smith and Wessel, 1990, Wessel and Smith, 1995b, Wessel and Smith, 1995a, Wessel and Smith, 1998) by using sonar multibeam data from YK10-12.

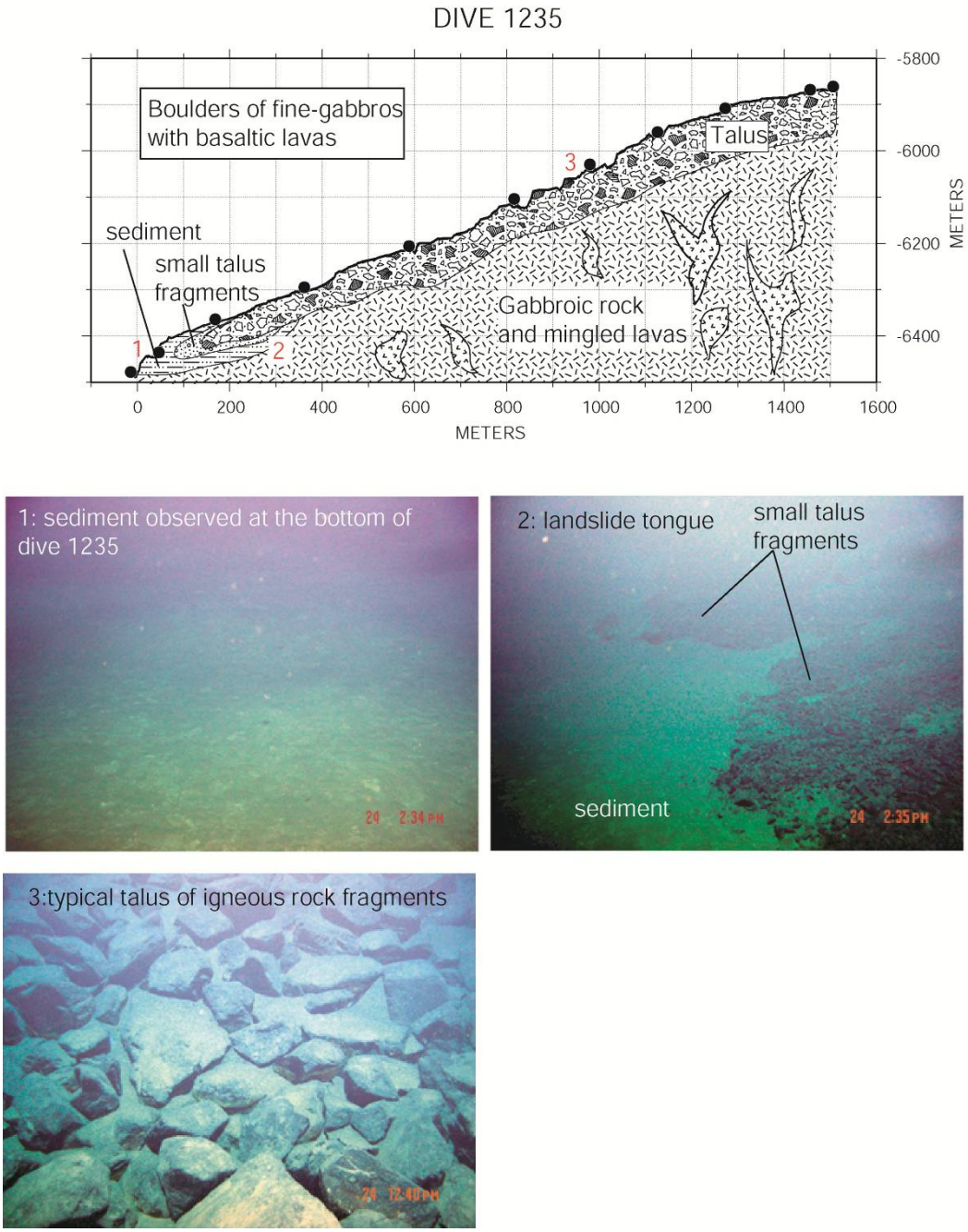

Figure 2A.7. Interpreted bathymetric profile of the eastern flank of rift 3 traversed during Shinkai dive 1235. Locations of the bottom pictures are reported in red on the bathymetric profile. Talus slope exhibits fragments of basaltic lava flows, fine-grained gabbros and diabases. Boulders become well-sorted to form landslide tongues. Faulting and landsliding shapes the rift flanks near the trench. Profile has been realized on-board by F. Martinez with GMT (Smith and Wessel, 1990, Wessel and Smith, 1995a, Wessel and Smith, 1998, Wessel and Smith, 1995b) by using sonar Multibeam data from YK10-12.

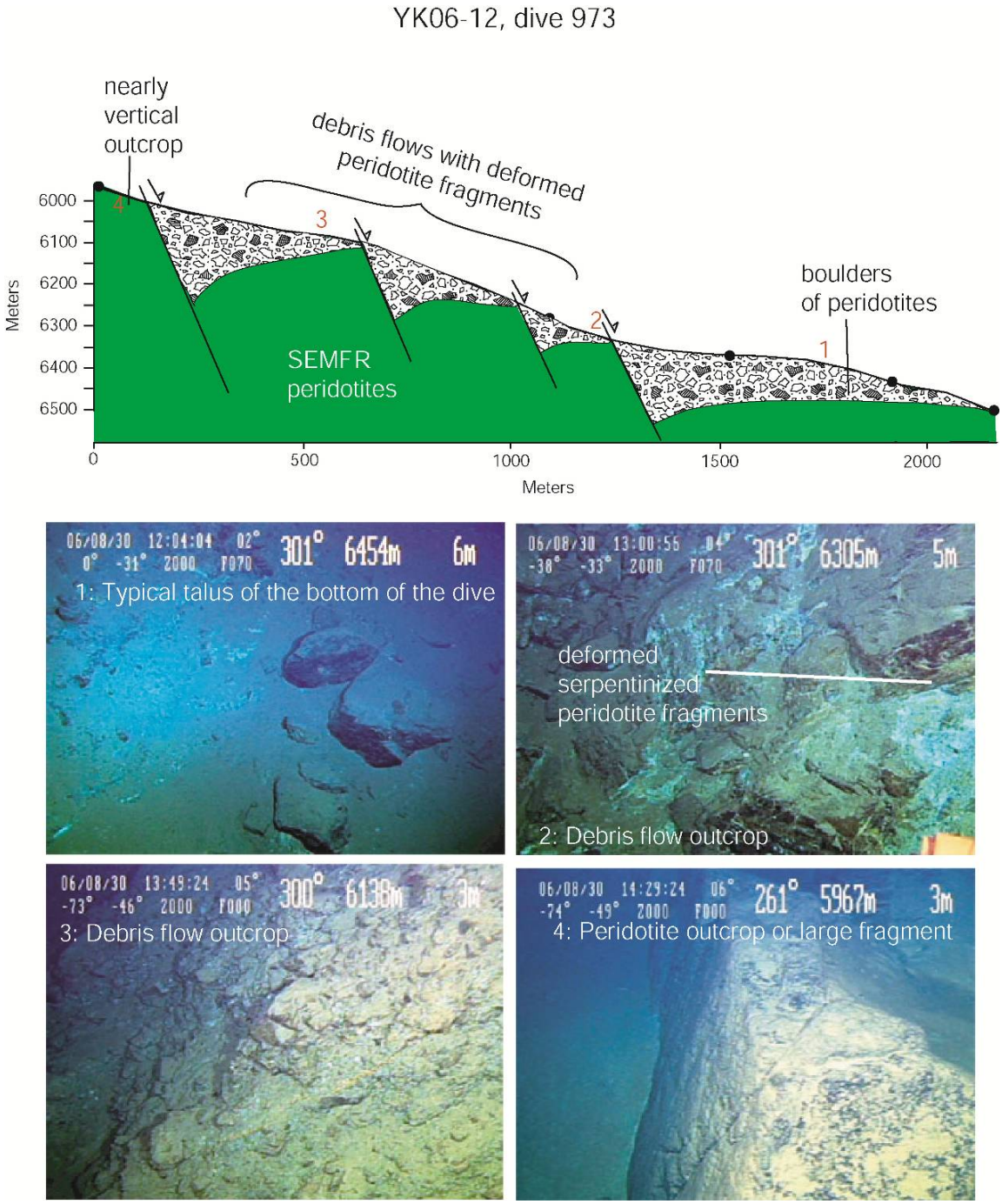

Figure 2A.8. Interpreted bathymetric profile of the eastern flank of rift 1 traversed during Shinkai dive 973, located near the trench axis. Locations of the bottom pictures are reported in red on the bathymetric profile. This dive occurred near the W. Santa Rosa Bank fault and traversed slope covered by angular peridotites fragments and thin sediments. Sub-vertical, faulted and tilted outcrop of grayish, altered peridotites occur nears the top of dive. Profile has been realized under ArcGIS.

Shinkai dive 1096 traversed the eastern flank of rift 1, ~ 40 ± 5 km from the trench axis. Pillow lavas were identified by their rounded shape when well-preserved or "piece of pie" shape when fragmented, along with shipboard observations of a glassy rinds (Figure 2A.2 and 2A.5). Two distinct suites of pillow lavas were identified, based on abundance of olivine phenocrysts, an olivine-poor lower series (6077 – 5797 m) and an upper series richer in olivine (5737 – 5414 m). Larger pillow fragments were observed in the depth range occupied by each series, suggesting proximity to outcrops of highly fractured pillow lavas found at 5906 m (lower series) and at 5414 m (upper series). The upper outcrop was heavily covered by volcaniclastic sediments and an outcrop of volcaniclastics was observed at 5429 m. 28 samples were collected during this dive.

Shinkai dive 1230 was performed along the steep eastern flank of rift 2, ~ 45 ± 5 km from the trench axis (Figure 2A.2 and 2A.5). This dive mostly traversed a talus slope composed of large fragments of pillow lava, lava flow and volcaniclastics. 33 samples were recovered from this dive. Outcrops of volcaniclastics (4752 m) and tilted and faulted outcrops of basaltic lava flows (4599 m and 4451 m) were observed (Figure 2A.2 and 2C.6). 3 series were identified in Shinkai dive 1230, based on their plagioclase abundances and their texture: lower plagioclase-rich basalt (4752 – 4599 m deep), middle plagioclase-rich diabasic basalt (4599 – 4451 m deep) and upper plagioclase-poor basalt (> 4451 m depth).

Shinkai dive 1235 was performed along the eastern flank of rift 3, ~ 26 km from the trench axis (Figure 2A.2 and 2A.7). 617 m of talus slope exhibiting fragments of basaltic lava flows, fine-grained gabbros and diabases were observed. Boulders become well-sorted to form landslide tongues. All the talus slopes and outcrops observed in those 3 dives were partially covered by volcaniclastic sediment. 25 samples were collected during Shinkai dive 1235.

Shinkai dive 973 (~ 36 km from the trench) is the easternmost dive in the region of interest. This dive recovered peridotite and has been described by (Michibayashi et al., 2009). This dive occurred near the W. Santa Rosa Bank fault (Figure 2.1B) and traversed slope covered by angular peridotites fragments and thin sediments. Upslope, sediments are less abundant and partially cover outcrops of debris flow (from 6329 m to 6006 m deep) with peridotite fragments (Figure 2A.4 and 2A.8). Sub-vertical, faulted and tilted outcrop of grayish, altered peridotites occur nears the top of dive. Dive 973 recovered altered and deformed peridotites, named SEMFR peridotites. We suggest that peridotites were deformed, exhumed, and later fragmented to form steep talus slopes at the base of faulted outcrops.

Shoaler parts of SEMFR were investigated using YKDT with mini-dredge. YKDT-85 and YKDT-86 were performed on the prominent N-S ridge to the east of rift 3 (Figure 2.1C). YKDT-85 was on the summit of the ridge; while YKDT-86 was along the west-facing slope to the top of the ridge. Seafloor videos of YKDT-85 and YKDT-86 show steep escarpments dominated by prismatic lava flows (Figure 2A.3, 2A.9 and 2A.10). The bottom was covered by decimeter-scale, subangular to subrounded fragments of lava flows. During YKDT-85, the size of talus fragments increased upslope, consistent with proximity to outcrops of lava flows interbedded with volcaniclastics, also observed in YKDT-86 (Figure 2A.10). The top of the ridge studied during YKDT85 and YKDT-86 is composed of basaltic cobbles with glassy rinds. We only sampled basaltic cobbles from the top of the ridge during both mini-dredges.

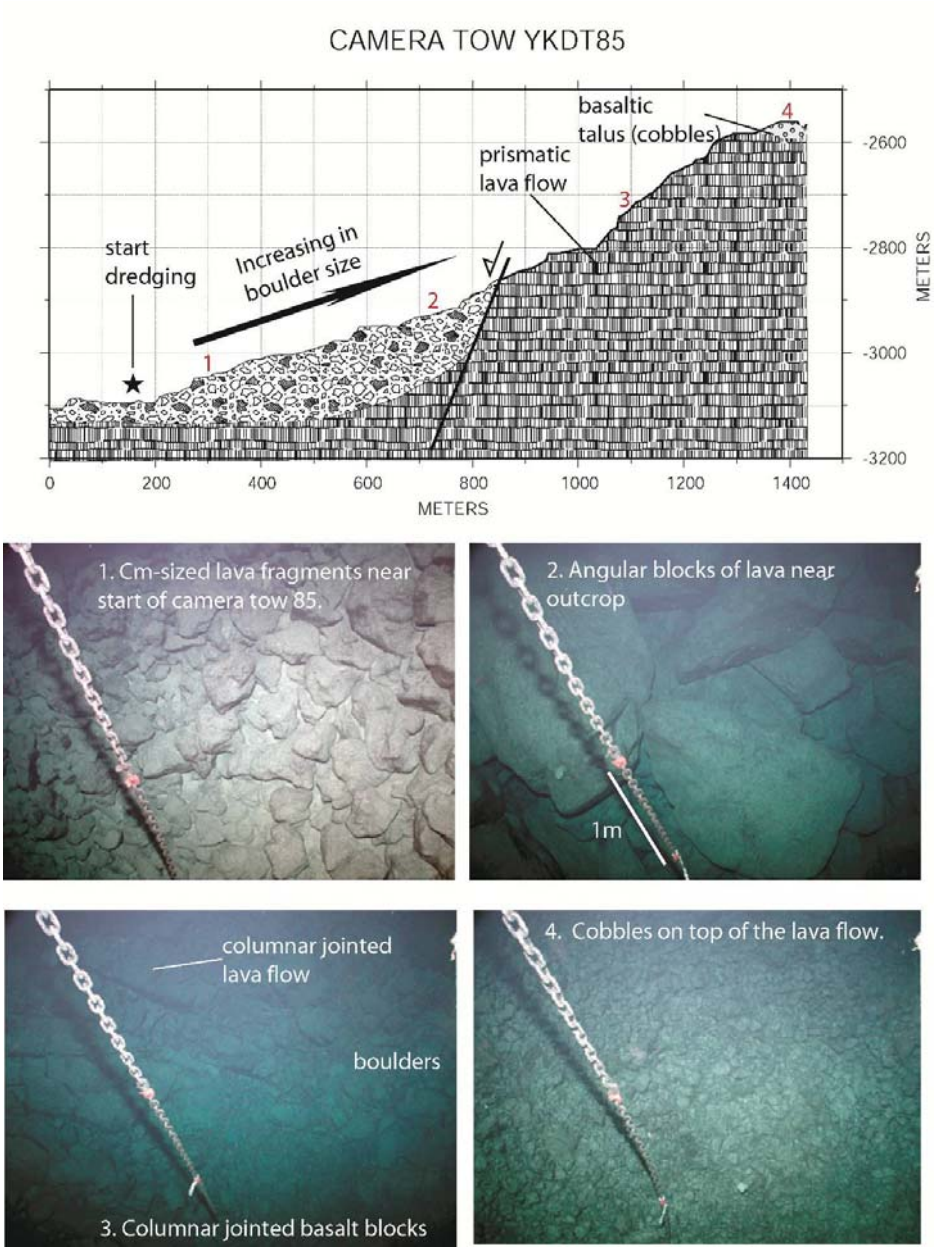

Figure 2A.9. Interpreted bathymetric profile of the summit of ridge on the eastern side of rift 3 traversed during YKDT-85 with the deep-tow camera. The dive is located in the central part of SEMFR. Locations of the bottom pictures are reported in red on the bathymetric profile. The star represents the beginning of the dredge. The size of talus fragments increased uslope, consistent with proximity to outcrops of lava flows interbedded with volcaniclastics. The top of the ridge is covered of basaltic cobbles. Note that the outcrops are well-preserved and faulted. Profile has been realized on-board by F. Martinez with GMT (Smith and Wessel, 1990, Wessel and Smith, 1995b, Wessel and Smith, 1995a, Wessel and Smith, 1998) by using sonar Multibeam data from YK10-12.

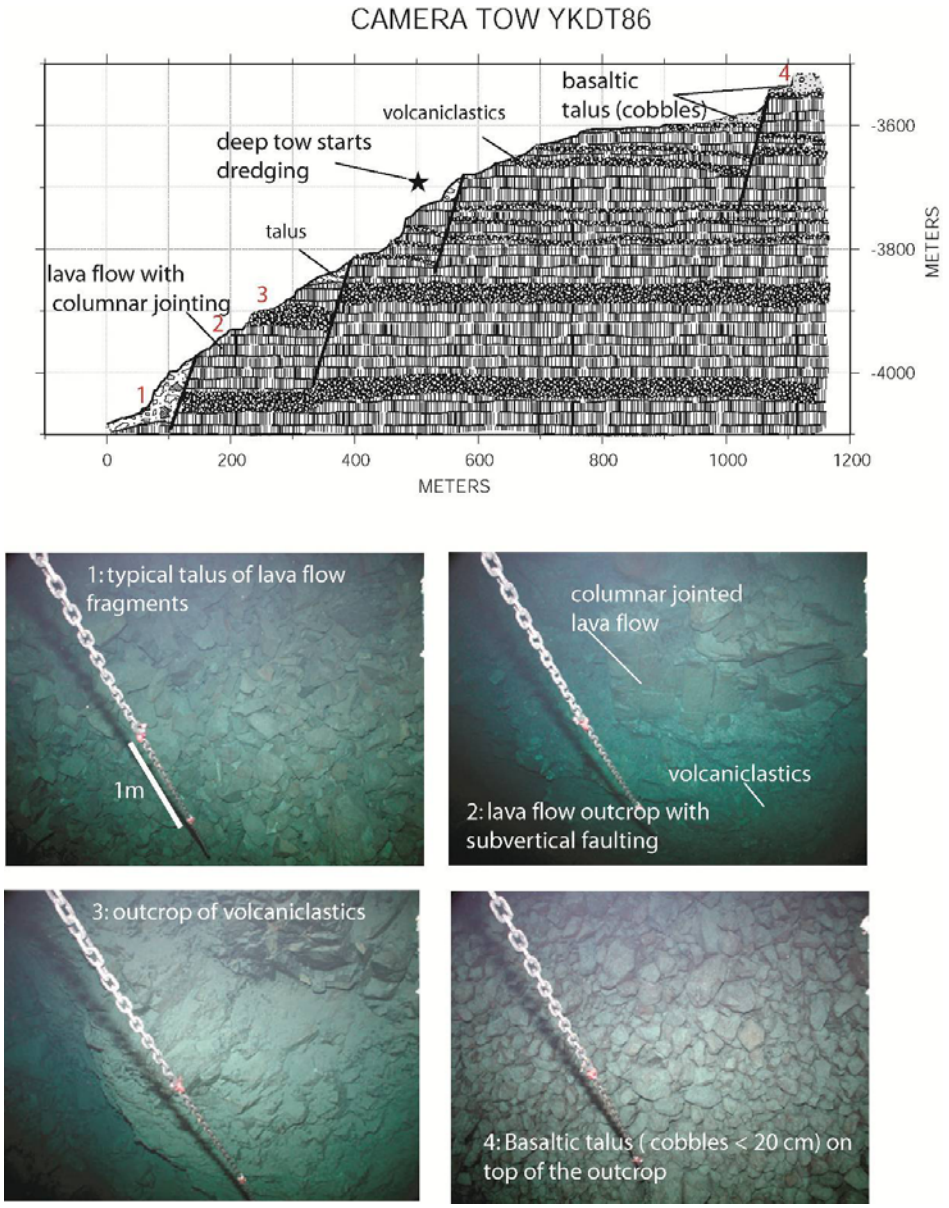

Figure 2A.10. Interpreted bathymetric profile of the eastern flank of ridge of rift 3 (central part of SEMFR) traversed during YKDT-86. Locations of the bottom pictures are reported in red on the bathymetric profile. The star represents the beginning of sampling with the dredge. The bottom was covered by lava fragments. Outcrops of lava flows alternating with volcaniclastics were mostly observed during the dive. The top of the dive was covered of basaltic cobbles. It is difficult to discriminate whether the lava flows alternate with the volcaniclastics or if only large pieces of lava fragments are mixed within the volcaniclastics. Profile has been realized on-board by F. Martinez with GMT (Smith and Wessel, 1990, Wessel and Smith, 1995b, Wessel and Smith, 1995a, Wessel and Smith, 1998) by using sonar Multibeam data YK10-12.

The northwestern, shoalest part of SEMFR near the BAB spreading center was studied during YKDT-82, YKDT-87 and YKDT-88 (~ 70 km from the trench axis). YKDT-87 examined the axial valley of rift 3 (Figure 2.1B). There was relatively subdued relief for this dive, in comparison to the steep outcrops observed closer to the trench. YKDT-87 is mostly composed of fractured and well-preserved pillow lavas with a thin sediment cover (Figure 2A.3 and 2A.12). YKDT-82 was performed on the summit of a ridge between rifts 2 and 3 (Figure 2.1B). Video examination showed that the ridge is composed of fractured pillow lavas alternating with lava flow outcrops (Figure 2A.2 and 2A.12). No samples were recovered during YKDT-87 and YKDT-82. YKDT-88 is the closest site to the extinct arc (Figure 2.1B). The deep-tow camera traversed the eastern flank of rift 2 (Figure 2A.3 and 2A.13). The traverse encountered seafloor with subdued relief covered by pillow lava fragments. The summit of the ridge revealed outcrops of fractured pillow lavas. These lavas have large phenocrysts of olivine and pyroxene not observed elsewhere. As the whole, the northern part of SEMFR is smoother with better preserved outcrops.

2.A.2 Toto caldera and Malaguana-Gadao Ridge:

Kaiko dive 163 traversed the north-facing flank of the Toto caldera. Video examination showed that the bottom of the Toto caldera (3044 m) was covered by basaltic cobbles, hyaloclastite and volcaniclastic sediment (Figure 2A.4 and 2A.14). The caldera wall is mostly composed of vesicular basaltic clasts with a whitish coating, perhaps bacteria or sulfur-rich. Few sedimented areas were observed along the caldera wall. White ‘smoke’ was observed during most of the dive; this is related to the Nakayama hydrothermal site at 2931 m depth (Gamo et al., 2004).

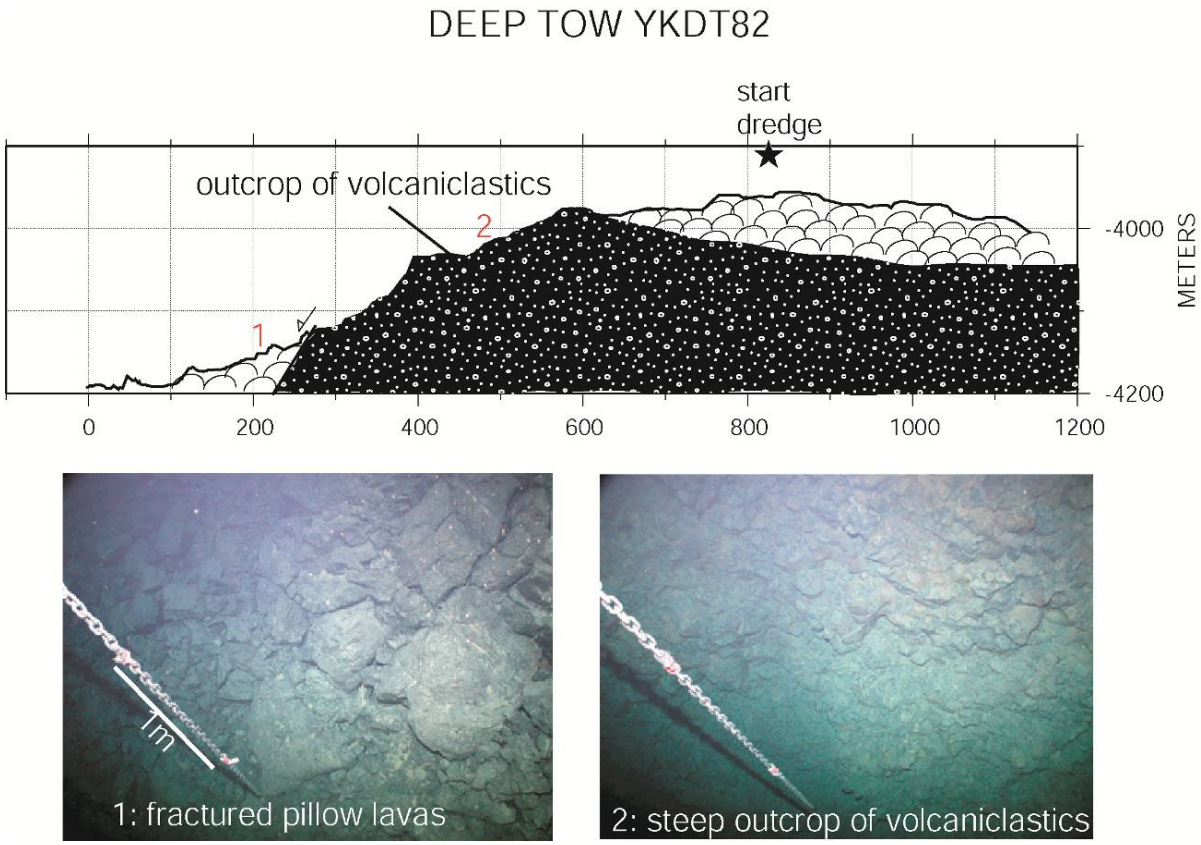

Figure 2A.11. Interpreted bathymetric profile of YKDT-82 (near the extinct arc), performed on the summit of a ridge between rifts 2 and 3. The ridge is composed of fractured pillow lavas alternating with lava flows. The relief is much smoother than it is near the trench. Locations of the bottom pictures are reported in red on the bathymetric profile. The star represents the beginning of the dredge. Profile has been realized on-board by F. Martinez with GMT (Smith and Wessel, 1990, Wessel and Smith, 1995b, Wessel and Smith, 1995a, Wessel and Smith, 1998) by using sonar Multibeam data from YK10-12.

Hydrothermal vents were associated with shimmering water and abundant fauna (Galatheids, tube worms, worms, shrimp, and anemones). Near the end of the dive, a crater with volcaniclastic outcrop and breccia was identified. White hydrothermal plumes escaped from the bottom of the crater. These observations are consistent with observations of other submarine arc volcanoes in the region, where fresh pillowed and sheeted lavas with venting sites and abundant fauna were identified (Kakegawa et al., 2008). Detailed study about the hydrothermal fluid from the vents is reported in (Gamo et al., 2004).

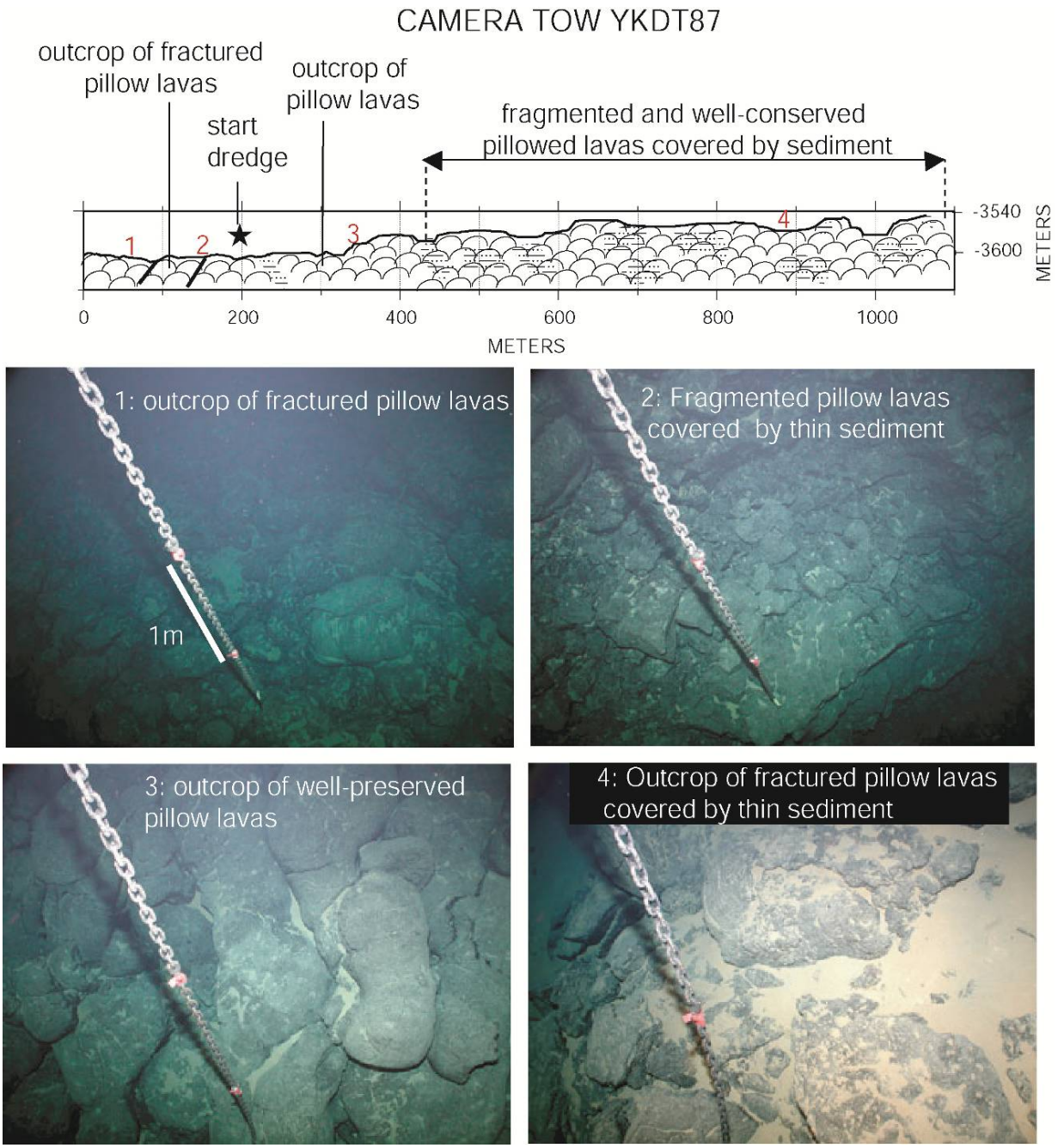

Figure 2A.12. Interpreted bathymetric profile of the axial valley of rift 3 traversed during YKDT-87 (near the extinct arc). YKDT-87 is mostly composed of fractured and well-preserved pillow lavas with a thin sediment cover. The relief is relatively smooth, in comparison with the steep flanks observed near the trench. Locations of the bottom pictures are reported in red on the bathymetric profile. The star represents the beginning of the dredge. Profile has been realized on-board by F. Martinez with GMT (Smith and Wessel, 1990, Wessel and Smith, 1995b, Wessel and Smith, 1995a, Wessel and Smith, 1998) by using sonar Multibeam data YK10-12.

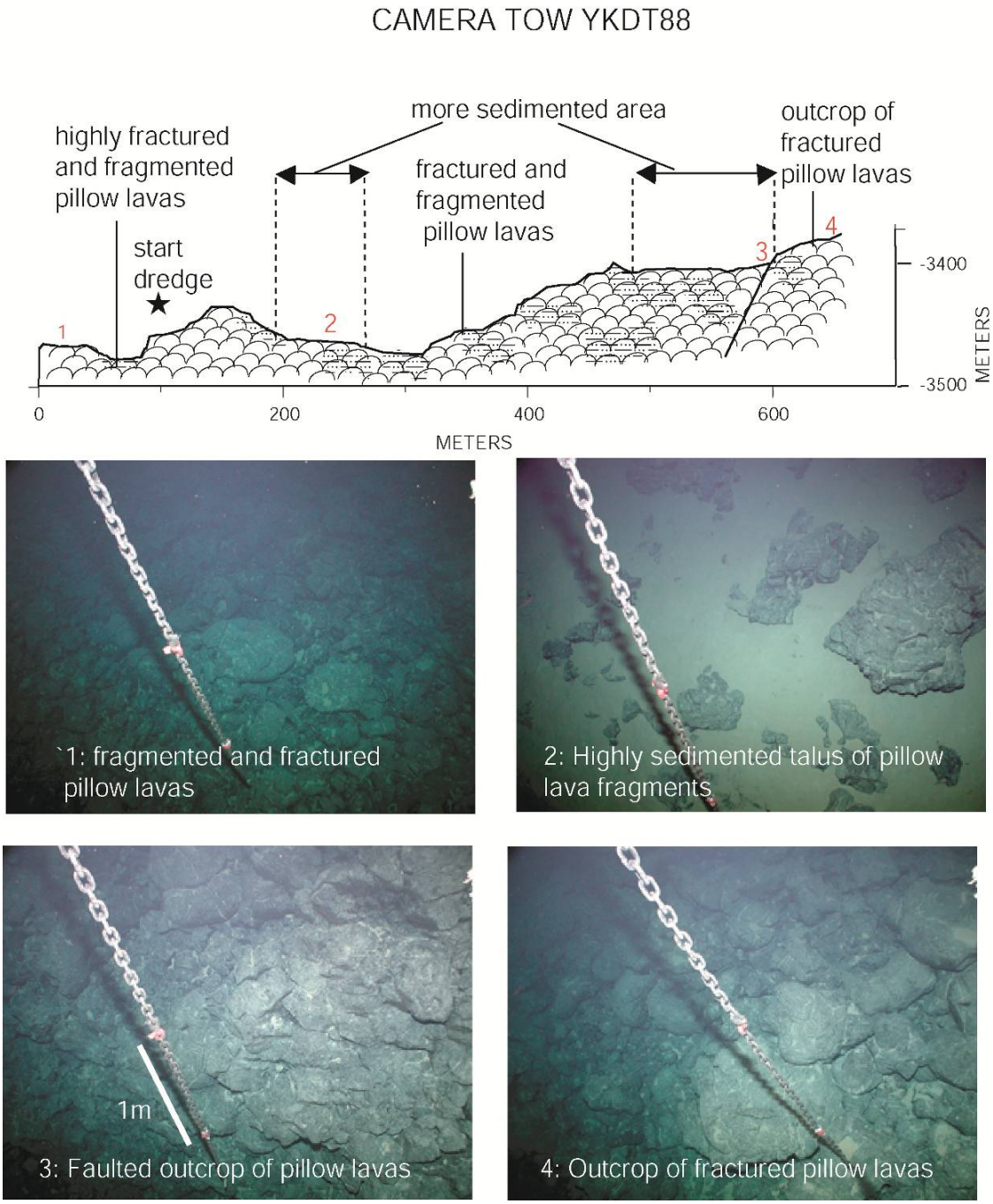

Figure 2A.13. Interpreted bathymetric profile of the eastern flank of ridge of rift 2 performed during YKDT-88, near the extinct arc. Seafloor has subdued relief covered by pillow lava fragments. The summit of the ridge revealed outcrops of fractured pillow lavas. Locations of the bottom pictures are reported in red on the bathymetric profile. The star represents the beginning of the dredge. Profile has been realized on-board by F. Martinez with GMT (Smith and Wessel, 1990, Wessel and Smith, 1995b, Wessel and Smith, 1995a, Wessel and Smith, 1998) by using sonar Multibeam data from YK10-12.

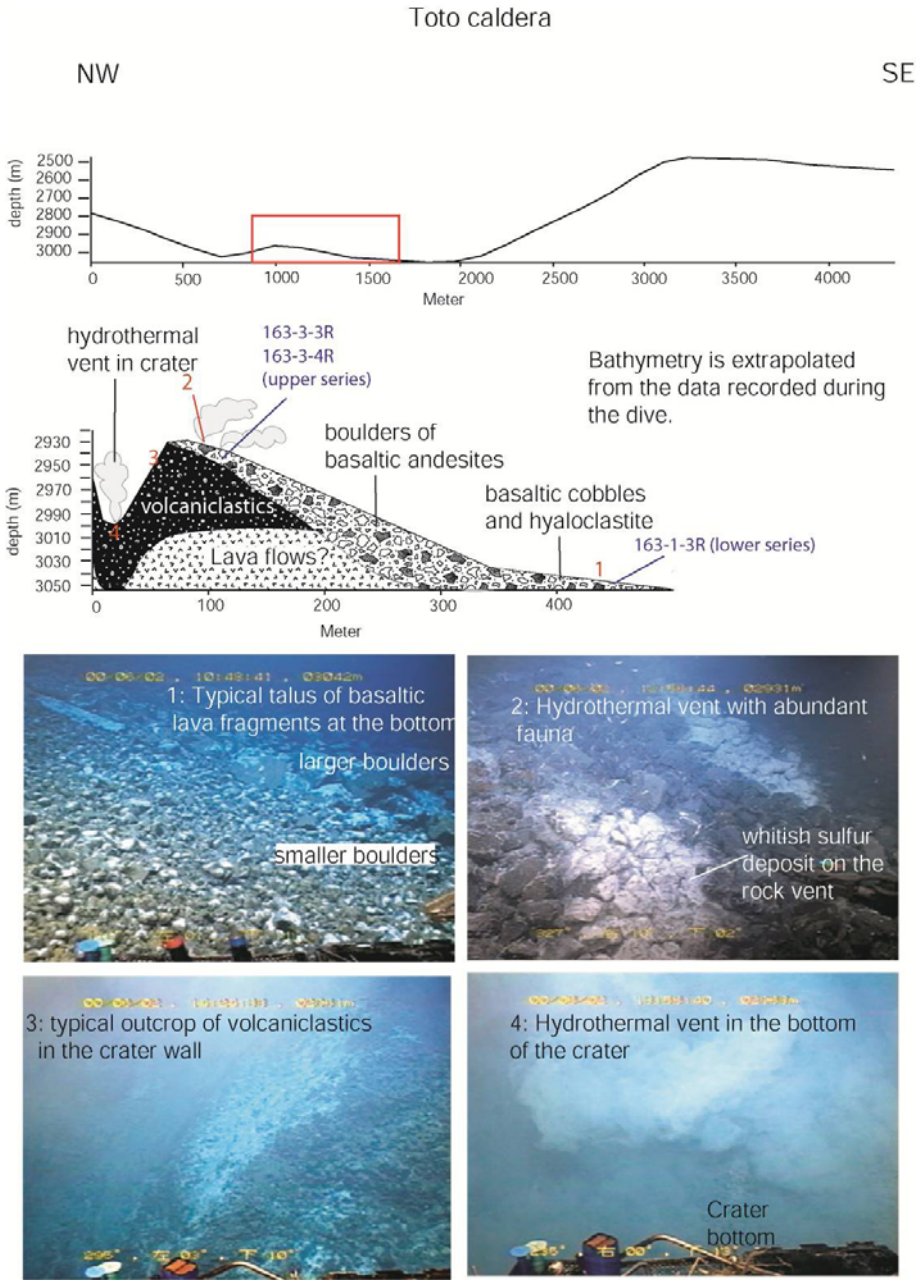

Figure 2A.14. Interpreted bathymetric profile of Toto caldera performed during Kaiko dive 163. The bottom of the caldera was covered by basaltic cobbles, hyaloclastite and volcaniclastic sediment. The caldera wall is mostly composed of vesicular basaltic clasts with a whitish coating. The Nakayama hydrothermal site, at 2931 m depth, is associated with abundant fauna. A crater with volcaniclastic outcrop, breccia and white hydrothermal plumes were observed near the end of the dive. Locations of the bottom pictures are reported in red on the bathymetric profile. Profile has been realized under ArcGIS. Locations of the analyzed samples for major elements are in blue.

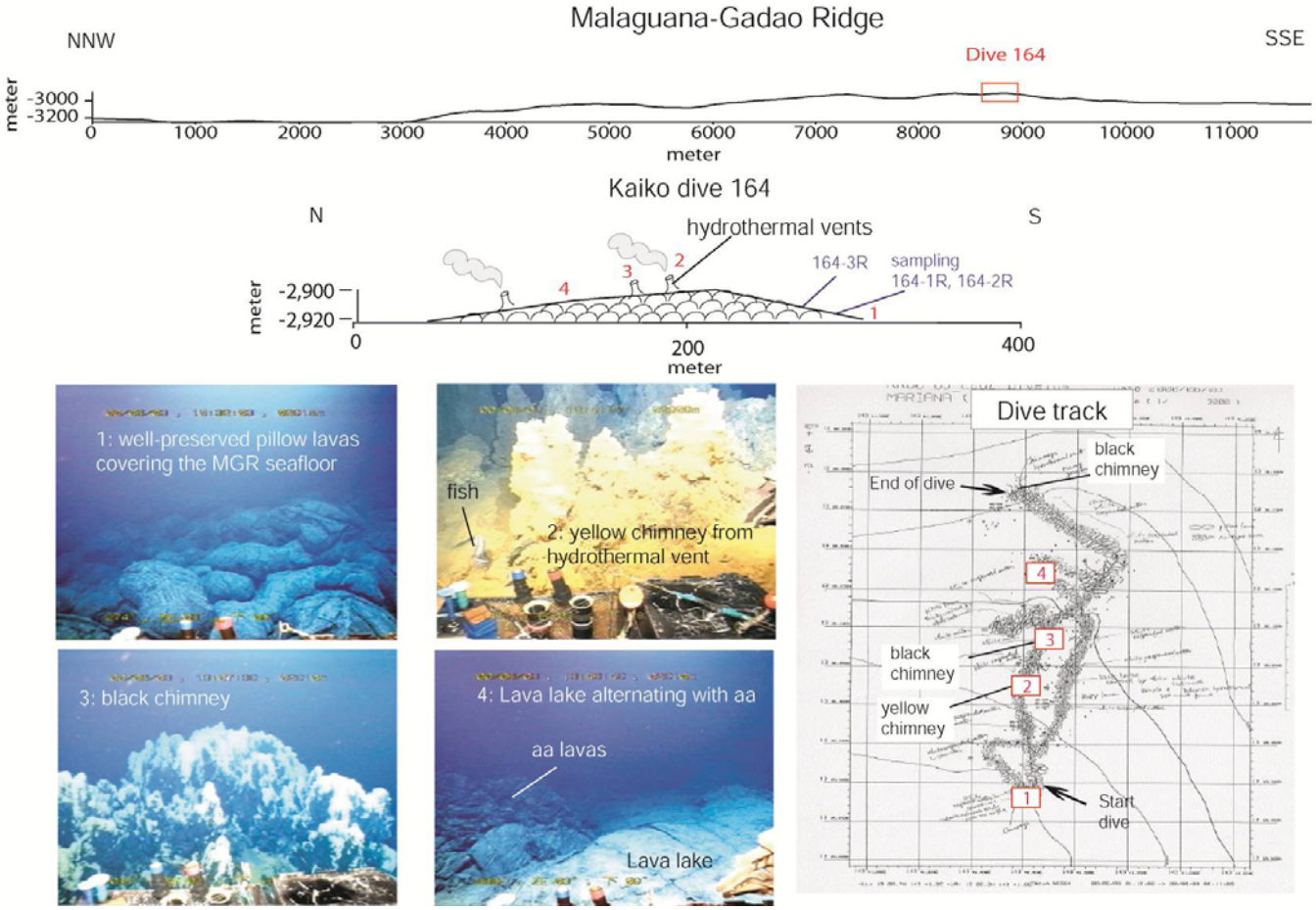

Figure 2A.15. Interpreted bathymetric profile along the Malaguana-Gadao Ridge performed during Kaiko dive 164, near the 13°N magmatic chamber (Becker et al., 2010). Seafloor has a smooth and flat relief, covered by fresh, well-preserved pillow lavas alternating with aa and smooth lava lake. Three hydrothermal sites, with yellow and black chimneys, were observed at 2908 m and 2910 m deep along with fauna. Locations of the bottom pictures are reported in red on the bathymetric profile. Profile has been realized under ArcGIS. The red boxes with a number on the dive track (from KR00-03 LEG 2 cruise report) correspond to the location of the bottom pictures in the bathymetric profiles. Locations of the analyzed samples for major elements are in blue.

Kaiko dive 164 investigated the ridge crest of the Malaguana-Gadao Ridge near 13^{o}N. The submersible mostly encountered fresh, well-preserved pillow lavas alternating with aa and smooth lava lake (Figure 2A.15). Pillow lavas of the Malaguana-Gadao Ridge were also reported by (Becker et al., 2010). The seafloor here is smooth and flat. Lava stratification and lava pillars were locally identified, suggesting collapse of a lava lake. Few fish, anemone and sponge were observed with white hydrothermal plumes as hydrothermal vent chimneys were approached. Three hydrothermal sites, with yellow and black chimneys, were observed at 2908 m and 2910 m deep.

APPENDIX 2B

SAMPLE SELECTION AND ANALYTICAL TECHNIQUES

2.B.1 Sample selection:

28 samples (3 sediments and 25 pillow lavas) were collected during cruise YK08-08 LEG 2 (Shinkai dive 1096) in 2008, and 112 igneous rocks were collected during cruise YK10-12 (Shinkai dives 1230, 1235 and YKDT-88, 85, 86) in 2010 (Figure 2A.1, 2A.14, 2A.15). 12 peridotites were also collected in SEMFR during cruise YK06-12 (Shinkai dive 973) and described in (Michibayashi et al., 2009). Only igneous samples were selected for further study. 73 were selected onboard based on representativeness and freshness. 71 thin sections were examined. Samples were then selected on a basis of freshness (≤ 2 % visibly altered phases), stratigraphic position and presence of glass. Where all the samples from the same dive had more than 2% alteration (e.g. Shinkai Dive 1235 gabbros), we selected the least altered for geochemical analyses. Glassy rinds were observed under the microscope and selected, based on size. When several geological units were observed in a single dive, we selected between 2 to 4 samples for analyses. 50-micron-thick doubly polished thick sections were prepared for 13 samples for electron microprobe work. 42 samples were selected for whole rock major element analyses. Four samples were also analyzed for $^{40}Ar/^{39}Ar$ ages. In addition to samples collected by Shinkai 6500 and YKDT, 9 samples from cruise KR00-03 LEG 2 (Kaiko dives 163 and 164) were also studied. The 9 samples were examined petrographically and 5 were analyzed for major

element compositions. 1 sample from Kaiko dive 164 and 2 samples from Kaiko dive 163 were selected for microprobe analyses.

2.B.2 Rock analyses:

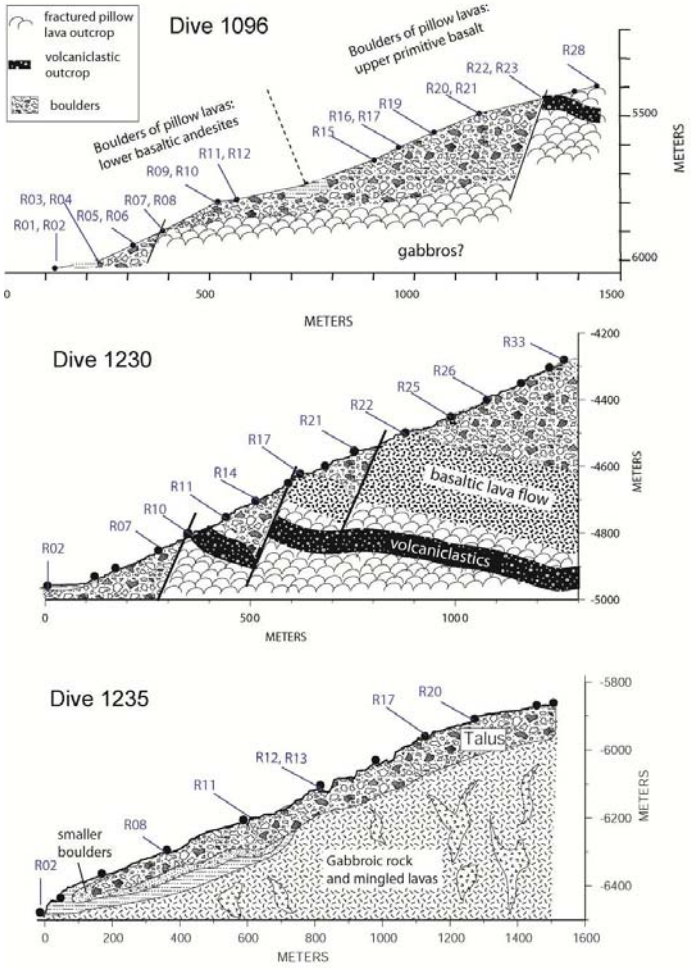

Figure 2B.1. Location of the analyzed samples (in blue), for major elements during this study, on the bathymetric profiles of the Shinkai dives 1096, 1230 and 1235. Profiles have been realized by F. Martinez with GMT (Smith and Wessel, 1990, Wessel and Smith, 1995b, Wessel and Smith, 1995a, Wessel and Smith, 1998) by using sonar multibeam data from YK10-12. Analyzed sample numbers are reported in blue.

Analytical work for major elements for dive 1096 (YK08-08 LEG 2 cruise) was completed for 15 pillow lavas at Geological Survey of Japan / AIST, following techniques described in (Ishizuka *et al.*, 2009). Glass beads were prepared by fusing 0.5 mg of sample powder with lithium tetraborate flux and analyzed by X-ray fluorescence (XRF) using a Philips PW1404 spectrometer for whole rock major element analyses. Standards (JB1A, JB2, BHVO2, BCR2) were made with the same procedure and analyzed daily. External errors and accuracy are < 2%. Standards JB2, JB3, BHVO2 were analyzed daily.

27 samples from the YK10-12 cruise and 5 samples from KR00-03 LEG 2 cruise were prepared at the University of Rhode Island following the method of (Kelley et al., 2003). Samples were polished with sand paper to remove saw marks, sonicated with deionized water to remove sediment, and dried before crushing with a ceramic jaw crusher. Fresh sample chips containing few phenocrysts were picked to remove alteration, and powdered with high-purity alumina ball mill. Samples were ignited into high-purity alumina crucibles at ~ 100^{o}C in a furnace for ~ 1h and at 950^{o}C for 45 min to remove the bounded water. 400 ± 5 mg of lithium metaborate ($LiBO_4$) flux with 100 ± 5 mg of ignited sample powder were heated at 1050^{o}C for 10 min, forming glass beads dissolved in 50 mL 5% HNO_3, and then in 212 mL 5% HNO_3. Sample is diluted 4040 times in 5% HNO_3. Standards (W2, BIR1, BHVO1, DNC1, JB3) and one blank were prepared following the same procedures as the samples. W2 was used as the drift corrector. One set of 10 unknowns, 4 USGS standards, one drift corrector and one blank were analyzed with the Ultima-C Jobin Yvon Horiba ICP-AES at Boston University, set up following the conditions described in (Kelley et al., 2003). The blank was analyzed at the beginning and the

end of each sample set. The drift corrector was analyzed every 3 to 4 samples. Calibration curves yield $r \geq 0.999$, averaged reproducibility of replicate analyses are < 2% rsd for each element but for P_2O_5 and K_2O (≤ 3% rsd), and major element oxide sum to 99 ± 1 wt%. Replicates of samples analyzed by ICP-AES and XRF yield averaged reproducibility < 4% rsd for each element.

2.B.3 Mineral analyses:

Major element content were analyzed on a Cameca SX-50 electron microprobe at the University of Texas at El Paso using a 15 kV accelerating voltage with a 20 nA beam intensity and a 5 micron diameter beam. Analyses were performed by using the operating software SX50, recently upgraded to SX RAY N50 on Solaris 2. This software operates nearly like a SX100. Calibrations were performed every day using the Smithsonian standards. Standards were analyzed every day to monitor accuracy and precision. Mineral analyses with major oxides summing to 100 ± 1.5 wt% were preserved. However, when few analyses were present, we accepted a sum that ranged within 98 wt% to 101.99 wt%. Repeated analyses of a sample give a mean value with $1\ \sigma \leq 1\%$. However, when mean had $1\ \sigma > 2\%$, the analysis was not averaged. In that case, we considered that the compositional variation of the grain was real and not related to the technique. Means of the standards give a precision ≤ 1 wt%.

2.B.4 ^{40}Ar – ^{39}Ar method:

Ages of 4 pillow lavas (1096-R2, 1096-R16, 1230-R2, and YKDT88-R2) were measured at the $^{40}Ar/^{39}Ar$ dating facility at the Geological Survey of Japan/AIST, using step-heating procedure

(Figure 2A.1). Argon isotopes were measured on a VG Isotech VG3600 noble gas mass spectrometer fitted with a BALZERS electron multiplier. Details of procedures are reported in (Ishizuka et al., 2009). Sample irradiation was done at the JMTR, JRR3 and JRR4 reactors (Ishizuka, 1998). Fast neutron fluxes in these reactors were about 6.7×10^{12} n/cm^2 s, 1.4–1.7×10^{12} n/cm^2 s and 5.9×10^{12} n/cm^2 s, respectively. Sanidine from the Fish Canyon Tuff (FC3) was used for the flux monitor and assigned an age of 27.5 Ma (Lanphere and Baadsgaard, 2001).

A continuous Ar ion laser (Coherent INNOVA310: for analysis No. U05xxx and U06xxx) and CO_2 laser (NEWWAVE MIR10-30: for analysis No. U07xxx and U08xxx) were used for sample heating. Correction for interfering isotopes was achieved by analyses of $CaFeSi_2O_6$ and $KFeSiO_4$ glasses irradiated with the samples. The blank of the system including the mass spectrometer and the extraction line was 7.5×10^{-14} ml STP for ^{36}Ar, 2.5×10^{-13} ml STP for ^{37}Ar, 2.5×10^{-13} ml STP for ^{38}Ar, 1.0×10^{-12} ml STP for ^{39}Ar and 2.5×10^{-12} ml STP for ^{40}Ar. The blank analysis was done every 2 or 3 step analyses.

All errors for ^{40}Ar/^{39}Ar results are reported at one standard deviation. Errors for ages include analytical uncertainties for Ar isotope analysis, correction for interfering isotopes and J value estimation. An error of 0.5% was assigned to J values as a pooled estimate during the course of this study. Plateau ages were calculated as weighted means of ages of plateau-forming steps (Figure 2.6), where each age was weighted by the inverse of its variance. Age plateaus were determined following the definition by (Fleck *et al.*, 1977). Inverse isochrons were calculated

using York's least-squares fit, which accommodates errors in both ratios and correlations of errors (York, 1969).

APPENDIX 2C

METHODOLOGY FOR DESCRIBING THE SAMPLES

This section of the manuscript documents the method used to describe the sampled rocks, based on the petrographic atlas of (MacKenzie *et al.*, 1982), the experiments of (Lofgren, 1974) and the methodology of (Teagle *et al.*, 2006). Volcanic and plutonic rocks were characterized and named based on their mineral abundances and grain size. Rock names were refined with chemical analyzes. Mineral and vesicle abundances were microscopically estimated using Photoshop (Teagle et al., 2006). Grain size was measured under a microscope and by taking pictures of thin sections. Rocks were defined as follow: coarse grained (cg: 5 – 30 mm), medium grained (mg: 1 – 5 mm), fine grained (fg: 0.5 – 1 mm), microcrystalline (mx: 0.1 – 0.5 mm), cryptocrystalline (cx < 0.1 mm), to keep petrographic consistency observed between the series of each dive. Rocks were classified according to their vesicle proportions as: not vesicular (< 1% vesicles), sparsely vesicular (1 – 5%), moderately vesicular (5 – 20% vesicles) and highly vesicular (> 20% vesicles). Igneous rocks are also classified according to their degree of crystallinity as holohyaline (100% glass), hypocrystalline (glass and minerals) and holocrystalline (100% minerals), and according to their degree of alteration as fresh (<2% alteration minerals), slightly altered (2 – 5 %), moderately altered (5 – 20%), highly altered (> 20%).

In the next paragraph we define the vocabulary that we used in this manuscript to describe the samples, because different definitions, sometimes contradictory, are available. The purpose here

is not to redefine igneous textures but to describe samples consistently. Crystal shapes are described as euhedral (the characteristic crystal shape is clear), subhedral (crystal has some of its characteristic faces) and anhedral (crystal lacks characteristic faces). To describe the interstitial material between feldspar laths, we used the terms: intersertal texture, where glass or alteration material occupies the interstices, and intergranular texture, where olivine and / or pyroxenes are between the plagioclase laths. We also used the terms ophitic (olivine or pyroxene partially enclose plagioclase), subophitic (plagioclase partially enclose olivine or pyroxene) and poikilitic (larger crystals totally enclose smaller crystals) to describe larger crystals that enclose smaller grains. Magmatic flow textures are described as trachytic when plagioclase laths are subparallel. Subtrachytic texture is a poorly-defined subparallel arrangement of plagioclase. Dykes (≥ 5cm) and veins (< 5 cm) define any features that crosscut the rock. Sieve texture refers to minerals which contains glass and crystal in a channelway-like arrangement due to resorption or rapid cooling. Some crystals show kink banding (lattice dislocation due to solid-state deformation) in their core with possible mineral dislocation (crystal defect or irregularity in the crystal) and mineral recrystallization in smaller, polygonal and equigranular grains. Xenocryst refers to a larger foreign crystal included in the host rock.

2.C.1 Volcanic rocks:

Igneous rocks are classified as volcanic rocks when they are holohyaline, hypocrystalline or mineral abundances < 100%. Rocks were further classified by abundances of primary phenocrysts. The least abundant minerals are used to name the rock. For example, basalt with 30% plagioclase, 5% olivine, 10% clinopyroxene and 2% orthopyroxene is named

orthopyroxene – olivine basalt. Basalts are mafic hypocrystalline rocks with matrix grain sizes ranging from cryptocrystalline to fine-grained. Pillow lavas are dark, basaltic rocks with a curved glassy rind. Diabasic texture refers to rocks sparsely to highly vesicular with mineral abundances ≥ 50%. Diabases are not porphyritic.

In holohyaline and hypocrystalline rocks, glass was described as fresh (translucent to amber in transmitted polarized light and isotropic in cross-polarized light), dark (due to abundant microlites), spherulitic (glass with microlites forming spheroidal bodies), variolitic (glass with microlites with a fan-like arrangement), and altered. Porphyritic or microporphyritic texture refers to phenocrysts or microphenocrysts surrounded by groundmass of smaller crystals (microlites) and glass. In microporphyritic rocks, we use the term of microphenocrysts (0.1 - 1 mm) instead of phenocrysts (≥ 1mm), while microlites are < 0.1 mm (Lofgren, 1974). In volcanic rocks, crystals can be described as skeletal (crystal showing a high proportion of voids filled with glass or groundmass), dendritic (needle-like crystals) or embayed (holes in crystals filled with glass or groundmass). These textures suggest that crystals grew during rapid cooling or quenching, or were resorbed due to interaction with surrounding melt. Skeletal and dendritic crystals are common in pillow lavas. Glomeroporphyritic texture refers to clusters of phenocrysts, generally stripped off the magmatic conduits. Some volcanic rocks show a dark, microcrystalline material with spherulitic microlites of plagioclase and are rich in vesicles, called segregation vesicles, which represent solidified residual melt that migrated into vesicles (Smith, 1969). Felty texture refers to phenocrysts or microlites that have random orientation. Diktytaxitic

texture is used for rocks that contain vesicles in which phenocrysts, especially plagioclase, protrude.

2.C.2 Plutonic rocks:

Plutonic rocks are holocrystalline (100% crystals). To describe the general crystal shape in the rock, we use the terms equigranular (principal minerals have the same range in size) and inequigranular (the principal minerals have different grain size). Subequigranular refers to intermediate texture between equigranular and inequigranular. Minerals usually develop intersertal and intergranular textures that go along with ophitic and subophitic textures. Minerals can also be embayed, as in volcanic rocks. We use the term dolerite for fine- to medium-grained, sparsely to non vesicular mafic intrusive rock. This term is the U.S. equivalent of diabase, used in Europe and in Japan. Doleritic texture is used for mafic rocks with texture intermediate between intergranular and ophitic (Cordier *et al.*, 2005, Teagle et al., 2006). Similarly, granular texture is used for mafic rocks with texture intermediate between ophitic and equigranular. Seriate texture refers to crystals with random orientation.

Gabbros are classified based on their modal mineralogy after (Teagle et al., 2006, Le Maitre *et al.*, 1989), as follows: olivine- or orthopyroxene-bearing gabbro (1-5 % olivine or orthopyroxene), olivine gabbro (> 5% olivine), gabbronorite (> 5% orthopyroxene), troctolitic gabbro (5 - 15% olivine), ferrogabbro (> 5% Fe-Ti oxides). In some gabbros, secondary green amphibole and chlorite replace pyroxene due to low grade metamorphism. When the amphibole proportions are > 20%, we use the term amphibolite gabbro.

APPENDIX 2D

PETROGRAPHIC DESCRIPTION AND MINERALOGY OF THE SAMPLES

SEMFR is floored overwhelmingly by relatively fresh mafic lavas and shallow intrusives, often from talus derived from steep fractured outcrops. The SEMFR mafic suite comprises mostly aphyric and sparsely phyric basalts and basaltic andesites. These are pillows or massive flows, with thin glassy rims and negligible alteration.

2.D.1 Lavas and plutonic rocks from SEMFR:

SEMFR pillow lavas and talus fragments have a thin (≤ 1 mm) Mn coat. All lavas are composed of microphenocrysts of skeletal olivine, dendritic plagioclase and euhedral to subhedral clinopyroxene (Figure 2.3A). Lava can be felty, diktytaxitic, intergranular and / or intersertal with subtrachytic texture and some segregation veins. Samples are vesicular despite being collected at ~ 6000 – 3000 m, indicating that these magmas contained significant volatiles. Discrete glomerocrysts consisting of olivine, clinopyroxene and plagioclase are set in a microlitic groundmass composed of the same mineral assemblages and interstitial dark brown devitrified glass. Discrete microphenocrysts of plagioclase with variolitic to spherulitic texture are observed. Embayment, ophitic, subophitic and poikilitic textures with small plagioclase needle rim are observed in olivine and clinopyroxene, especially in pillowed lavas of Shinkai dive 1096. These textures indicate that the melt was in disequilibrium with the phenocrysts

during magma crystallization. Discrete plagioclase needles in the groundmass show variolitic to spherulitic textures. Pillow lavas generally show a thin glassy rim (1 – 11 mm), composed of translucent to dark brown glass with microcrystallites, testifying to quenching during submarine eruption.

Pillow lavas are fresh to slightly altered and sparsely to moderately vesicular. They are fine-grained to microcrystalline microporphyritic olivine – clinopyroxene basalt. Mineral abundances vary between series, and generally range within 1 – 20 % clinopyroxene, ≤ 5 – 10 % olivine and 5 – 40% plagioclase. Petrographic series were identified in some dives, based on texture and mineral proportions. Shinkai dive 1096 is divided into an olivine-rich (1 – 4 % olivine) upper series and an olivine-poor (≤ 2 % olivine) lower series (Figure 2A.4). Shinkai dive 1230 is composed of three petrographic series (Figure 2A.5): a pillowed, plagioclase-poor upper series (5 – 20 % plagioclase) and a pillowed, plagioclase-rich lower series (5 – 40 % plagioclase) that are separated by a diabasic, plagioclase-rich middle series (40 – 75% plagioclase). YKDT-85 and 86 collected centimeter-scale cobbles (Figure 2A.8 and 2C.9) of fine-grained microporphyritic to diktytaxitic olivine - clinopyroxene basalt with millimeter-scale glassy rind. The basaltic clasts exhibit similar petrographic features to SEMFR pillow lavas. In contrast, YKDT-88 pillowed lavas contain larger crystals (≥ 0.5 mm) of clinopyroxene and olivine set in a finely microcrystalline (< 0.5 mm) olivine-rich (5 – 10%) groundmass. Olivine-rich lavas like those of YKDT-88 were not sampled elsewhere in the SEMFR. Shinkai dive 1235 igneous rocks are mostly talus fragments of non vesicular basalts, diabase and fine-grained gabbros. Lava flows are composed of cryptocrystalline basalt, microcrystallized olivine basalt hosting a xenolith of fine-

grained diabase (Figure 2.3B), and cryptocrystalline microporphyritic plagioclase basalt with a centimeter-scale xenolith of altered, fine-grained amphibole gabbro (Figure 2.3B & D). Fine-grained gabbro and diabase contain 22 – 35 % clinopyroxene, 50 – 60 % plagioclase, 1 - 5% Fe-Ti oxides, 5 – 15% chlorite and < 1 – 2% actinolite, indicating metamorphism to lower greenschist facies.

Microphenocrysts and phenocrysts were analyzed using the electron microprobe at UT El Paso to get representative analyses of mineral compositions in each dive. Complete analytical results for representative mineral composition are listed in Tables 2D.1 to 2D.4 and summarized in Table 2.2. SEMFR basalts exhibit similar compositional ranges for plagioclase, olivine and clinopyroxene. Near-primitive (Mg# > 60), olivine-rich SEMFR lavas (Shinkai dive 1096, upper series and YKDT-88) contain Mg-rich olivines (Fo_{86-88}) in equilibrium with Mg-rich clinopyroxene (Mg# = 83 – 91) and anorthitic plagioclase (An ≥ 80). In contrast, the more fractionated lavas have Fe-rich olivine (Fo_{75-84}) coexisting with Mg-poor (Mg# < 80) and Mg-rich clinopyroxenes (Mg# ≥ 80), and Ca-rich (An ≥ 80) and Ca-poor plagioclase (An < 80). Fine-grained gabbros and diabase from Shinkai Dive 1235 have Mg-rich clinopyroxenes coexisting with more albitic plagioclases (An ≤ 70). The microcrystallized olivine basalt with diabase xenolith (sample 1235-R12, Figure 2.3B) contain Mg-rich olivine (Fo_{89}), Mg-rich clinopyroxene, and normally zoned Ca-rich plagioclase (≥ 0.1 mm) in the coarser diabase (Figure 2D.1). In contrast, the basaltic host is more fractionated, with Fe-rich olivine (Fo_{85-86}) and Mg-rich clinopyroxene microphenocrysts (≥ 0.1 mm); whereas clinopyroxene in the groundmass (< 0.1 mm) are Mg-poor and coexist with Ca-poor plagioclase microlites. Clinopyroxenes in the

diabase exhibit oscillatory and reverse zoning. Shinkai Dive 1230 (middle series) contains larger (> 1 mm), zoned plagioclase (core of An_{91-92}, sieve-textured mantle of An_{81-88} and rim of $An_{83-87;}$ Figure 2.3E), which composition contrasts with that of smaller, less anorthitic plagioclases (≤ 0.2 mm, An_{72-77}) in equilibrium with the melt. The xenocrystic plagioclase is surrounded by larger Mg-rich clinopyroxenes (> 0.2 mm, Mg# = 86 – 88). Its An-rich core has arc-like composition (Figure 2.8; (Stern, 2010)) that perhaps reflects arc-like hydrous mantle melting.

In summary, SEMFR lavas can be subdivided into pillow basalts and basalt flows. Pillow lavas are vesicular with microporphyritic textures and a quenched, microcrystalite-rich glassy rind (fresh, translucent to dark brown glass), indicating they erupted underwater at near-liquidus conditions. In contrast, basalt flows are more crystallized and less vesicular. Two kinds of plagioclase (An ≥ 80 and An < 80) and clinopyroxene (endiopside – diopside with Mg # > 80 and augite with Mg# < 80) are common. The more fractionated samples from Shinkai Dives 1230 and YKDT-86 contain both compositions of plagioclase and clinopyroxene in individual grains, which may have reverse, normal or oscillatory zoning. Reverse and oscillatory zonings are only observed in plagioclase with a core of An < 80, and these suggest magma replenishment perhaps in a magmatic reservoir. Shinkai dive 1235 lavas exhibit similar ranges in compositions of olivine, clinopyroxene and in the more anorthitic plagioclase (An > 60) to other SEMFR lavas. However, Shinkai dive 1235 lavas also contain albitic plagioclase (An < 50) possibly related to hydrothermal alteration.

Olivine xenocrysts (≥ 0.5 mm) enclosing chromium spinel are common in the upper series of Shinkai dive 1096 and in YKDT-88 (Figure 2.5C, D). Olivine xenocrysts of the Shinkai dive 1096 exhibit Fo_{92} in their cores and Fo_{87-92} in their rims. They host chromium spinel with Cr# (= 100 x Cr / (Cr +Al)) = 50 – 73. Mantle xenocrysts of YKDT-88 have lower Fo content (Fo_{89-91} core and Fo_{89-90} rim) in equilibrium with lower chromium content in the spinel (Cr# = 47 – 56). This large compositional range in Cr# is observed in single spinel grain of Shinkai Dive 1096 and YKDT-88. The olivine – spinel assemblage of the olivine xenocrysts plots in the mantle array of (Arai, 1994) and are similar to those of the SE Mariana forearc mantle peridotite (Cr# > 50 and Fo_{90-92}, (Ohara and Ishii, 1998)), consistent with the interpretation that they are forearc-like mantle xenocrysts (Figure 2.5C). In contrast, the SEMFR mantle peridotite (Shinkai dive 973; (Michibayashi et al., 2009)) exhibits lower spinel Cr# and Fo contents (Cr# < 50, Fo_{90-91}). Only one assemblage olivine – spinel of Shinkai dive 1096 and the assemblage of YKDT-88 (Cr# ~ 50) have mean spinel compositions that are intermediate between the S.E. Mariana forearc mantle and the BAB-like SEMFR mantle.

2.D.2 Lavas from the Toto caldera and the S. Mariana backarc spreading center:

Lavas from Toto caldera (Kaiko dive 163) are fresh, vesicular, fine-grained to cryptocrystalline, microporphyritic basaltic andesites (≤ 1% microphenocrysts). They contain sulfides in vesicles and smell strongly of sulfur, consistent with their proximity to hydrothermal vents. Two petrographic suites were identified: olivine-poor, lower series and olivine-rich, upper series.

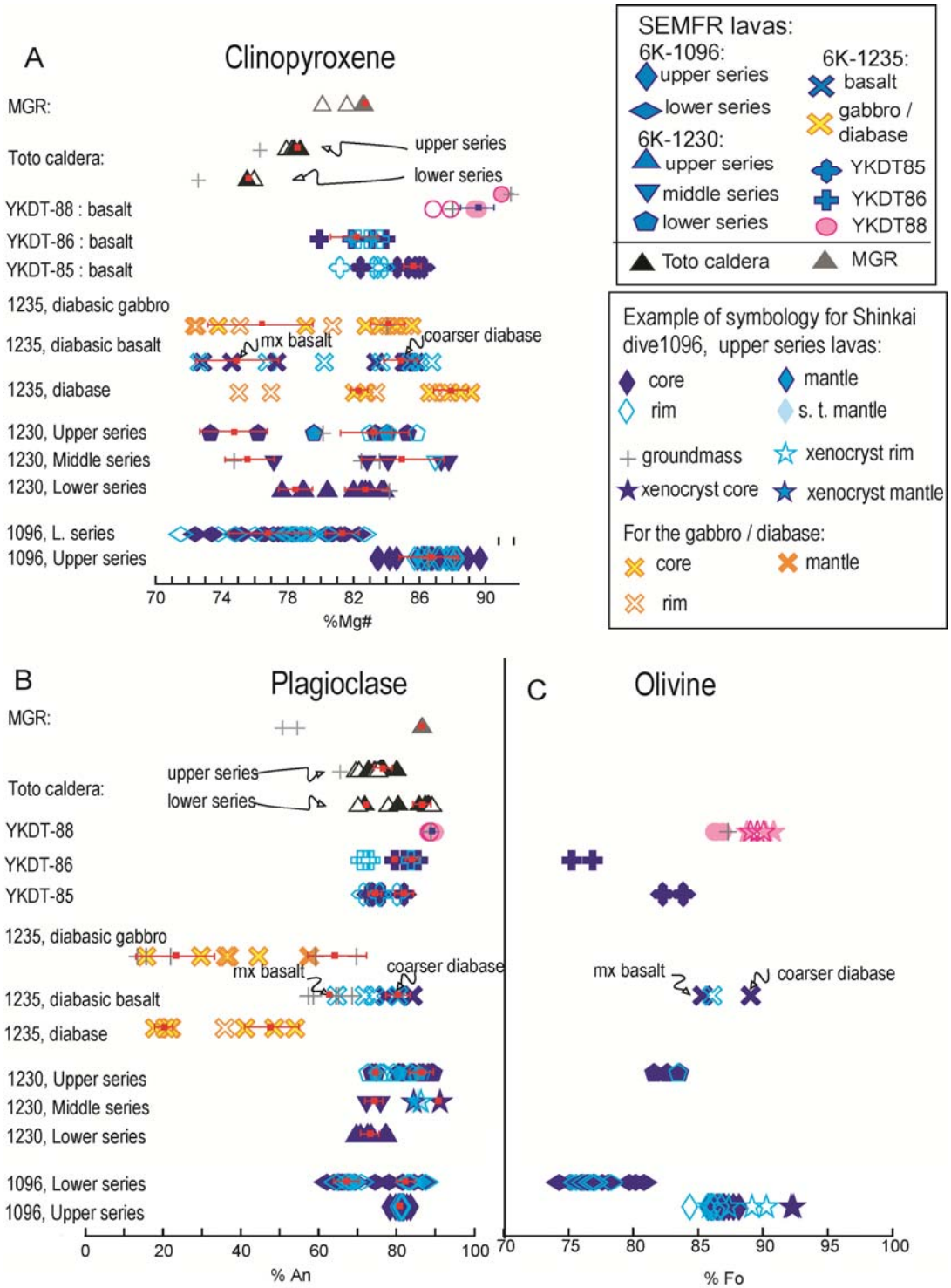

Figure 2D.1. SEMFR mineral compositions. A) Clinopyroxene, B) plagioclase and C) olivine. Red squares are mean chemical composition of mineral cores with error bar of 1 standard deviation (see Table 2.2 for details). Filled dark blue symbols denote mineral cores, empty light blue symbols denote rims, light blue symbols with a dark blue contour are mantle of zoned

minerals, light blue symbols are sieve textured (s. t.) mantle of zoned minerals and black crosses represent the groundmass. For YKDT-88, filled pink circles denote cores, empty pink circles denote rims, blue squares are mean composition with error bars. Stars denote xenocrysts. For Shinkai Dive 1235 microgabbro and diabase, filled yellow crosses denote cores, empty orange crosses denote rims. For Shinkai dive 1235 diabasic basalt, arrows indicate compositions of coarser diabasic xenolith and microcrystallized (mx) basaltic host. Black triangles represent samples from Toto caldera; grey triangles denote samples from the Malaguana-Gadao Ridge (MGR). Filled triangles denotes core and empty triangles denote rim. See text for details.

The lower series, sampled near the bottom of the dive, is characterized by cryptocrystalline groundmass, Mg-poor clinopyroxene, and < 1% microphenocrysts of An-rich plagioclase with oscillatory zoning. In contrast, the diktytaxitic and porphyritic upper series, sampled near the hydrothermal vents, has microphenocrysts of < 1% skeletal olivine (Fo_{80}), ≤ 1% Mg-rich clinopyroxene and ≤ 1% normally zoned, An-poor plagioclase. The groundmass has less anorthitic plagioclase and Mg-poor clinopyroxenes. Pillow lavas from the Malaguana-Gadao Ridge (Kaiko dive 164) are fresh, cryptocrystalline microporphyritic plagioclase basalts (< 1 % plagioclase) with translucent glassy rinds. Lavas are mostly composed of Ca-poor plagioclase microlites (An_{50-54}); while rare An-rich plagioclase (An_{86}) and Mg-rich clinopyroxene glomerocrysts (~ 0.5 mm) are observed in some sections (e.g. 164-3R); while the plagioclase microlites in the groundmass are An-poor (An_{50-54}). The mineral composition of Toto caldera lavas and MGR lavas are within the compositional range of SEMFR lavas, although they lack olivine (Figure 2D.1). Occurrence of two mineral compositional groups in both Toto and MGR lavas, without significant compositional overlap, strongly suggests magma mixing. Also, the microphenocrysts / glomerocrysts have more Mg-rich clinopyroxenes and more An-rich plagioclases than the microlites, suggesting that they were picked up from a more mafic melt.

Table 2D.1. Example of representative mean clinopyroxene composition for Shinkai dive 1096, sample R4. Mg# = (Mg2+ x 100) / (Mg2+ + Fe2+). All the iron is considered as Fe2+. cpx: clinopyroxene. n: number of analyses realized. Wo: wollastonite, En : enstatite, Fs: ferrosilite. Complete mineral analyses are provided in joined excel files.

.

SEMFR	cpx					cpx				cpx				cpx	
1096-R4	Mg# < 80					Mg# < 80				Mg# < 80				Mg# < 80	
Number of analyses	n=2	1σ	n=1	n=2	1σ	n=2	1σ	n=2	1σ	n=7	1σ	n=2	1σ	n=2	1σ
	mantle		core	rim		core		rim		core		rim		core	
SiO2	50.46	0.27	48.92	50.93	0.02	49.40	0.26	50.76	0.26	49.44	1.57	51.76	0.74	51.51	1.72
TiO2	0.64	0.05	1.02	0.64	0.05	0.89	0.03	0.65	0.03	0.93	0.35	0.50	0.21	0.54	0.27
Al2O3	3.63	0.48	5.12	3.29	0.34	3.99	0.05	3.58	0.05	4.98	1.62	2.38	1.01	2.52	1.40
FeO	8.10	1.09	9.80	8.64	0.42	8.96	0.17	8.05	0.17	8.20	0.47	8.36	0.65	8.42	0.23
MnO	0.21	0.04	0.24	0.26	0.03	0.26	0.04	0.21	0.04	0.22	0.04	0.26	0.03	0.29	0.04
MgO	15.82	0.54	15.20	16.38	0.67	15.29	0.36	15.75	0.36	15.89	1.69	17.49	0.73	17.16	1.42
CaO	20.47	1.80	19.19	19.84	1.07	20.37	0.32	20.65	0.32	20.29	1.61	19.41	0.32	18.91	1.03
Na2O	0.22	0.01	0.25	0.23	0.02	0.25	0.00	0.22	0.00	0.25	0.05	0.21	0.02	0.19	0.06
K2O	0.01	0.01	0.00	0.02	0.01	0.01	0.00	0.02	0.00	0.01	0.01	0.01	0.00	0.00	0.00
Total	99.67	0.41	99.78	100.27	0.34	99.46	0.46	99.94	0.46	100.30	0.46	100.46	0.07	99.60	0.70
Si	1.87	0.02	1.81	1.87	0.00	1.84	0.00	1.87	0.00	1.81	0.05	1.89	0.02	1.90	0.04
Ti	0.02	0.00	0.03	0.02	0.00	0.02	0.00	0.02	0.00	0.03	0.01	0.01	0.01	0.01	0.01
Al	0.16	0.02	0.22	0.14	0.01	0.17	0.00	0.16	0.00	0.22	0.07	0.10	0.04	0.11	0.06
Fe2	0.25	0.03	0.30	0.27	0.01	0.28	0.00	0.25	0.00	0.25	0.01	0.26	0.02	0.26	0.00
Mn	0.01	0.00	0.01	0.01	0.00	0.01	0.00	0.01	0.00	0.01	0.00	0.01	0.00	0.01	0.00
Mg	0.87	0.03	0.84	0.90	0.04	0.85	0.02	0.87	0.02	0.87	0.09	0.95	0.04	0.94	0.07
Ca	0.81	0.07	0.76	0.78	0.04	0.81	0.02	0.82	0.02	0.80	0.07	0.76	0.01	0.75	0.05
Na	0.02	0.00	0.02	0.02	0.00	0.02	0.00	0.02	0.00	0.02	0.00	0.01	0.00	0.01	0.00
K	0.00	0.00	0.00	0.00	0.00	0.00	0.00	0.00	0.00	0.00	0.00	0.00	0.00	0.00	0.00
Sum	4.00	0.00	4.00	4.00	0.00	4.00	0.00	4.00	0.00	4.00	0.00	4.00	0.00	4.00	0.00
Mg#	77.74	1.74	73.45	77.17	0.14	75.25	0.10	77.72	0.10	77.48	1.11	78.83	1.99	78.39	0.94
Wo	41.95	3.52	39.98	40.19	2.32	41.88	0.93	42.27	0.93	41.64	4.06	38.60	0.01	38.34	2.96
En	45.10	1.73	44.08	46.15	1.70	43.74	0.75	44.87	0.75	45.24	3.72	48.40	1.22	48.35	2.90
Fs	12.95	1.80	15.94	13.66	0.62	14.39	0.17	12.87	0.17	13.11	0.54	13.00	1.22	13.31	0.06
Sum	100.00	0.00	100.00	100.00	0.00	100.00	0.00	100.00	0.00	100.00	0.00	100.00	0.00	100.00	0.00

Table 2D.2. Example of representative mean plagioclase composition for Shinkai dive 1235, sample R11. n: number of analyses realized. An: anorthite, Ab : albite, Or: orthoclase, pl : plagioclase, fp : feldpspar. Complete mineral analyses are provided in joined excel files. n: number of analyses realized. An: anorthite, Ab : albite, Or: orthoclase, pl : plagioclase, fp : feldpspar. Complete mineral analyses are provided in joined excel files.

SEMFR	60>An>20 Anorthitic	60>An>20	60>An>20	60>An>20 Anorthitic	An < 20 Albitic	An < 20 Albitic	An < 20
1235-R11	pl	Anorthitic pl		pl	pl	pl	Albitic pl
Number of analyses	n=1	n=1 rim	n=1 core	n=1	n=1	n=1	n=1
SiO2	54.40	59.38	57.47	55.70	62.65	63.83	63.10
TiO2	0.02	0.00	0.01	0.01	0.00	0.00	0.00
Al2O3	28.35	26.04	26.77	27.80	23.57	22.65	23.30
FeO	1.05	0.75	0.79	0.76	0.51	0.59	0.54
MgO	0.00	0.00	0.00	0.00	0.00	0.00	0.00
MnO	0.00	0.00	0.05	0.01	0.01	0.00	0.03
CaO	11.31	7.57	8.69	10.26	4.61	3.71	4.60
Na2O	5.31	7.42	6.85	5.98	8.91	9.30	9.08
K2O	0.02	0.07	0.05	0.03	0.12	0.15	0.15
Total	100.49	101.24	100.70	100.57	100.38	100.22	100.79
Si	2.45	2.62	2.56	2.49	2.77	2.82	2.77
Ti	0.00	0.00	0.00	0.00	0.00	0.00	0.00
Al	1.50	1.35	1.40	1.47	1.23	1.18	1.21
Fe2	0.04	0.03	0.03	0.03	0.02	0.02	0.02
Mg	0.00	0.00	0.00	0.00	0.00	0.00	0.00
Mn	0.00	0.00	0.00	0.00	0.00	0.00	0.00
Ca	0.54	0.36	0.41	0.49	0.22	0.18	0.22
Na	0.46	0.64	0.59	0.52	0.76	0.80	0.77
K	0.00	0.00	0.00	0.00	0.01	0.01	0.01
Sum	5.00	5.00	5.00	5.00	5.00	5.00	5.00
An	53.97	35.90	41.09	48.59	22.10	17.90	21.70
Ab	45.91	63.71	58.61	51.23	77.24	81.27	77.47
Or	0.11	0.39	0.30	0.17	0.67	0.83	0.83
Sum	100.00	100.00	100.00	100.00	100.00	100.00	100.00

Table 2D.3. Example of mean olivine composition of Shinkai Dive 1096 lavas, sample R4. Fo: Fosterite content of the measured olivine. n: number of analyses realized. Ol: olivine. Complete mineral analyses are provided in joined excel files.

1096-R4 SEMFR	ol			ol				ol	ol				ol			
Number of analyses	n=3 core	1 σ	n=1 rim	n=2 rim	1 σ	n=2 core	1 σ	n=1	n=2 rim	1 σ	n=2 core	1 σ	n=3 rim	1 σ	n=2 core	1 σ
SiO2	38.49	0.14	38.19	38.09	0.28	38.02	0.56	37.89	38.27	0.48	39.09	0.15	38.02	0.04	38.69	0.16
TiO2	0.01	0.01	0.00	0.02	0.01	0.03	0.01	0.03	0.01	0.01	0.00	0.00	0.02	0.01	0.00	0.00
Al2O3	0.02	0.01	0.02	0.01	0.02	0.04	0.01	0.00	0.03	0.00	0.04	0.00	0.01	0.02	0.04	0.02
FeO	21.12	0.38	21.64	21.73	0.41	21.77	0.12	21.44	21.13	1.20	18.12	0.04	21.52	0.33	20.54	0.02
MnO	0.38	0.02	0.35	0.39	0.04	0.31	0.06	0.42	0.35	0.07	0.30	0.03	0.35	0.01	0.38	0.02
MgO	40.29	0.22	39.52	40.51	0.57	40.19	0.00	40.91	40.58	1.44	43.54	0.43	40.50	0.09	41.81	0.51
Total	100.60	0.31	100.03	101.05	0.11	100.65	0.74	100.97	100.62	0.61	101.37	0.44	100.75	0.27	101.79	0.56
Si	0.99	0.01	0.99	0.97	0.01	0.98	0.01	0.97	0.98	0.00	0.98	0.00	0.97	0.00	0.98	0.00
Ti	0.00	0.00	0.00	0.00	0.00	0.00	0.00	0.00	0.00	0.00	0.00	0.00	0.00	0.00	0.00	0.00
Al	0.00	0.00	0.00	0.00	0.00	0.00	0.00	0.00	0.00	0.00	0.00	0.00	0.00	0.00	0.00	0.00
Fe2	0.45	0.01	0.47	0.46	0.01	0.47	0.00	0.46	0.45	0.03	0.38	0.00	0.46	0.01	0.43	0.00
Mn	0.01	0.00	0.01	0.01	0.00	0.01	0.00	0.01	0.01	0.00	0.01	0.00	0.01	0.00	0.01	0.00
Mg	1.54	0.01	1.53	1.54	0.02	1.54	0.01	1.56	1.55	0.03	1.63	0.01	1.55	0.00	1.57	0.01
Ca	0.01	0.00	0.01	0.01	0.00	0.01	0.00	0.01	0.01	0.00	0.01	0.00	0.01	0.00	0.01	0.00
Sum	3.00	0.00	3.00	3.00	0.00	3.00	0.00	3.00	3.00	0.00	3.00	0.00	3.00	0.00	3.00	0.00
Fo	76.96	0.33	76.21	76.54	0.55	76.43	0.14	76.93	77.09	1.67	80.82	0.21	76.74	0.23	78.08	0.24
Fa	22.63	0.33	23.40	23.04	0.59	23.23	0.08	22.62	22.53	1.59	18.86	0.18	22.88	0.24	21.52	0.21
Te	0.41	0.03	0.38	0.42	0.04	0.34	0.06	0.45	0.38	0.08	0.32	0.03	0.38	0.01	0.40	0.03
Sum	100.00	0.00	100.00	100.00	0.00	100.00	0.00	100.00	100.00	0.00	100.00	0.00	100.00	0.00	100.00	0.00

Table 2D.4. Example of representative mean spinel composition for the primitive sample 1096-R21. n: number of analyses realized. Mg# = (Mg2+ x 100) / (Mg2+ + Fe2+), Cr# = (Cr x 100) / (Cr + Al). Fe2+ and Fe3+ proportions are calculated by stoechiometry. Complete mineral analyses are provided in joined excel files.

1096-R21	spinel hosted by ol	1δ	spinel hosted by ol		1δ	spinel hosted by ol	1δ	spinel hosted by ol		1δ	spinel hosted by ol	
Number of analyses	n=3		n=1	n=2		n=2		n=1	n=3		n=1	n=1
SiO2	0.00	0.00	0.00	0.00	0.00	0.00	0.00	0.00	0.00	0.00	0.00	0.00
TiO2	0.35	0.00	0.27	0.24	0.00	0.29	0.07	0.29	0.25	0.05	0.23	0.29
Al2O3	15.68	0.17	15.80	13.66	0.30	16.00	0.85	13.95	25.99	2.57	13.20	14.50
Cr2O3	52.43	0.44	53.67	56.07	0.05	52.38	0.08	54.09	39.43	2.73	54.96	52.99
FeO	15.22	0.07	15.14	14.79	0.12	15.51	0.11	18.09	16.27	1.06	19.95	18.82
MnO	0.24	0.01	0.24	0.26	0.02	0.22	0.10	0.40	0.19	0.02	0.35	0.32
MgO	15.79	0.16	16.72	16.21	0.13	16.46	0.46	13.61	17.52	0.51	12.46	13.30
Total	100.48	0.33	101.88	101.27	0.34	100.90	0.96	100.47	99.69	0.43	101.20	100.30
Si	0.00	0.00	0.00	0.00	0.00	0.00	0.00	0.00	0.00	0.00	0.00	0.00
Ti	0.01	0.00	0.01	0.01	0.00	0.01	0.00	0.01	0.01	0.00	0.01	0.01
Al	0.57	0.01	0.56	0.50	0.01	0.58	0.02	0.52	0.90	0.08	0.49	0.54
Cr	1.29	0.01	1.28	1.37	0.01	1.27	0.02	1.35	0.92	0.07	1.37	1.32
Fe2	0.40	0.00	0.38	0.38	0.01	0.40	0.01	0.48	0.40	0.03	0.53	0.50
Fe3	0.00	0.00	0.00	0.00	0.00	0.00	0.00	0.00	0.00	0.00	0.00	0.00
Mn	0.01	0.00	0.01	0.01	0.00	0.01	0.00	0.01	0.00	0.00	0.01	0.01
Mg	0.73	0.01	0.75	0.74	0.00	0.75	0.01	0.64	0.77	0.01	0.59	0.63
Sum	3.00	0.00	3.00	3.00	0.00	3.00	0.00	3.00	3.00	0.00	3.00	3.00
CALCULATED CHARGE	7.88	0.00	7.86	7.87	0.00	7.85	0.00	7.88	7.83	0.02	7.87	7.87
Fe2+	0.27	0.01	0.24	0.25	0.00	0.25	0.01	0.35	0.23	0.02	0.40	0.36
Fe3+	0.12	0.00	0.14	0.13	0.00	0.15	0.00	0.12	0.17	0.02	0.13	0.13
Mg#	72.91	0.56	75.87	74.87	0.31	75.10	1.10	64.42	77.01	1.60	59.45	63.23
Cr#	69.17	0.39	69.50	73.36	0.41	68.73	1.17	72.23	50.48	4.17	73.64	71.03
Fe2+*100/(Fe2+ + Mg)	27.09	0.56	24.13	25.13	0.31	24.90	1.10	35.58	22.99	1.60	40.55	36.77
Fe3+/Fet	0.31	0.01	0.37	0.34	0.00	0.37	0.01	0.26	0.43	0.02	0.24	0.27
Fe2+/Fe3+	2.20	0.13	1.67	1.91	0.00	1.68	0.10	2.86	1.35	0.12	3.16	2.74

APPENDIX 2E

CORRELATION BETWEEN MINERAL ABUNDANCES AND WHOLE ROCK CHEMISTRY

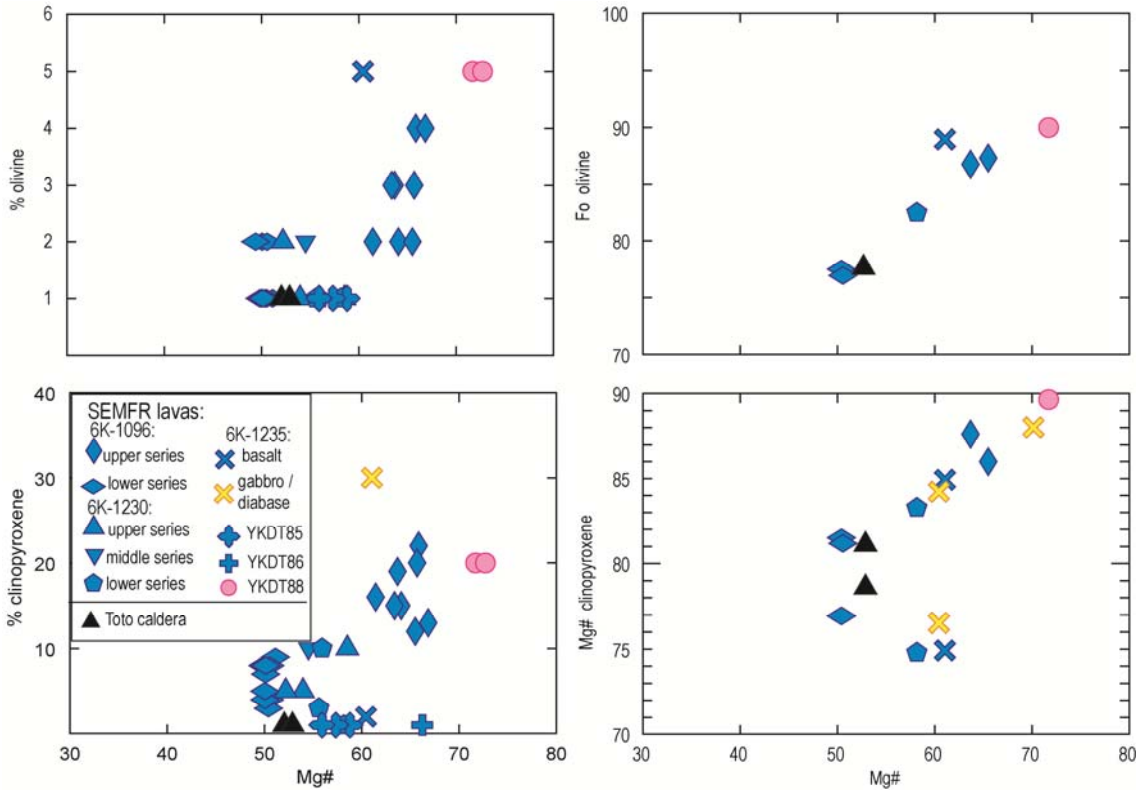

Figure 2E.1. Plot showing the correlation between mineral abundances and whole rock composition. A) The olivine proportions are positively correlated to the whole-rock Mg#. B) The more primitive lavas are richer in Mg-rich olivines. C) Abundances in clinopyroxene increase Mg#, consistent with the more primitive lavas are richer in Mg-rich clinopyroxene (D).

Abundances in minerals are correlated with whole rock composition. Abundances in clinopyroxene generally increase with CaO and Mg# contents (Figure 2E.1C) and decrease with SiO_2 and Al_2O_3 contents, suggesting that the more primitive lavas are more enriched in Mg-rich

(and Ca-rich) clinopyroxenes; while fractionated lavas exhibit lower proportions of clinopyroxenes. Inverse correlations of plagioclase abundances with increasing CaO and MgO contents suggest that the more anorthitic plagioclase mainly occurs in the primitive lavas, generally less enriched in plagioclase. The olivine proportions are positively correlated to the whole-rock Mg# content (Figure 2E.1A) and inversely correlated to the FeO content, reflecting that the more primitive lavas have larger abundances in Mg-rich olivines. These geochemical observations, made within the error range of mineral proportion estimations (± 5%), are consistent with the mineralogical observations outlined in section 5.1 in text.

APPENDIX 2F

EFFECTS OF THE VARIATIONS OF THE FO CONTENT ON THE P-T CONDITIONS OF SEMFR MANTLE MELTING

Assumptions (e.g. Fo content of the mantle source and the water content of the lavas) were made to get the P-T conditions of mantle melting. Varying the mantle source from Fo_{89} (more enriched mantle) to Fo_{92} (more depleted mantle) does not strongly affect the result. In contrast, varying water content from 0 to 6 wt% decreases T and increases P (Figure 2.8B) of mantle melting.

CHAPTER 3

NATURE AND DISTRIBUTION OF SLAB-DERIVED FLUIDS AND MANTLE SOURCES BENEATH THE SE MARIANA FOREARC RIFT

3.1 ABSTRACT

Subduction zone magmas are produced by melting depleted mantle metasomatized by fluids released from the subducted slab. In most subduction zones, formation of backarc basin (BAB) and arc magmas depletes the mantle source towards the trench, resulting in more depleted mantle beneath the forearc. Slab-derived fluids are aqueous beneath the forearc where the slab dehydrates, and the deeper subduction component is increasingly dominated by sediment melt at ≥ 100 km depth. Here, we present new data for the S.E. Mariana forearc rift (SEMFR), an unusual region of forearc igneous activity, where 2.7-3.7 Ma lavas were recovered by Shinkai 6500 diving and dredged during the TN273 Thomas Thompson cruise. SEMFR is divided into SE (near the trench) and NW (near the arc) sectors. NW SEMFR lavas and glass are more depleted in melt-mobile elements (e.g., Nb, Ti, La, Sm) and more enriched in fluid-mobile elements (e.g., Cs, Rb, Ba). SEMFR lavas were produced by partial melting of a BAB-like mantle source, metasomatized by aqueous fluid and sediment melt. Evidence of sediment melt, even in SE SEMFR lavas, could be explained by inheritance of high Th/Nb in the SEMFR mantle source. Geochemical mapping demonstrates that the subduction components increase towards the arc; while mantle depletion increases away from the trench, suggesting (i) input of a

less depleted mantle beneath SE SEMFR flowed towards the arc; and (ii) aqueous slab-derived fluids become increasingly important at ~ 50 – 100 km depth.

3.2 INTRODUCTION

Subduction zones are places where one hydrated oceanic plate goes underneath another plate and releases its fluids more or less continuously down to depths of ~ 200 km or more (Schmidt and Poli, 1998). The subducting slab mostly dehydrates beneath the forearc (Hacker, 2008, Schmidt and Poli, 1998), so the first fluid released is aqueous (1); and as the slab dehydrates with increasing depth (2), the slab-derived liquid progressively evolves into hydrous sediment melts (3) at ≥ 100 km deep (Figure 3.1) (Kimura *et al.*, 2010, Manning, 2004). Fluid-mobile elements (FMEs: Cs, Rb, Ba, Sr, K) are carried down by hydrous minerals (e.g. amphibole, biotite, phengite), and they are released along with hydrous fluids into the mantle wedge during mineral breakdown (Kimura et al., 2010, Schmidt and Poli, 1998, Zack *et al.*, 2001). These fluids rise up to hydrate and serpentinize the mantle wedge beneath the forearc (Van Keken et al., 2002, Wada et al., 2011) but cause mantle melting at depths >100 km beneath the arc and sometimes beneath the backarc basin spreading center (Kelley et al., 2006, Kelley et al., 2010). As subduction proceeds, less FMEs become available in the subducting slab (Elliott, 2003, Manning, 2004, Pearce and Stern, 2006, Pearce et al., 2005), so that aqueous fluids released beneath the forearc should be enriched in FMEs relative to deeper fluids. Studies of serpentinized peridotite clasts from Mariana forearc mud volcanoes and from exposed subduction channel complexes like that of Catalina Island, offshore California, also indicate that shallower fluids are more aqueous (and richer in FMEs; (Bebout *et al.*, 2007, Hulme et al., 2010, Savov et al., 2007, Savov et al., 2005))

than are the deeper fluids (Kimura et al., 2010, Manning, 2004, Pearce et al., 2005). Formation of backarc basin and arc magmas successively depletes the mantle flowing toward the trench (4), resulting in a more depleted mantle beneath the forearc (Woodhead *et al.*, 2012).

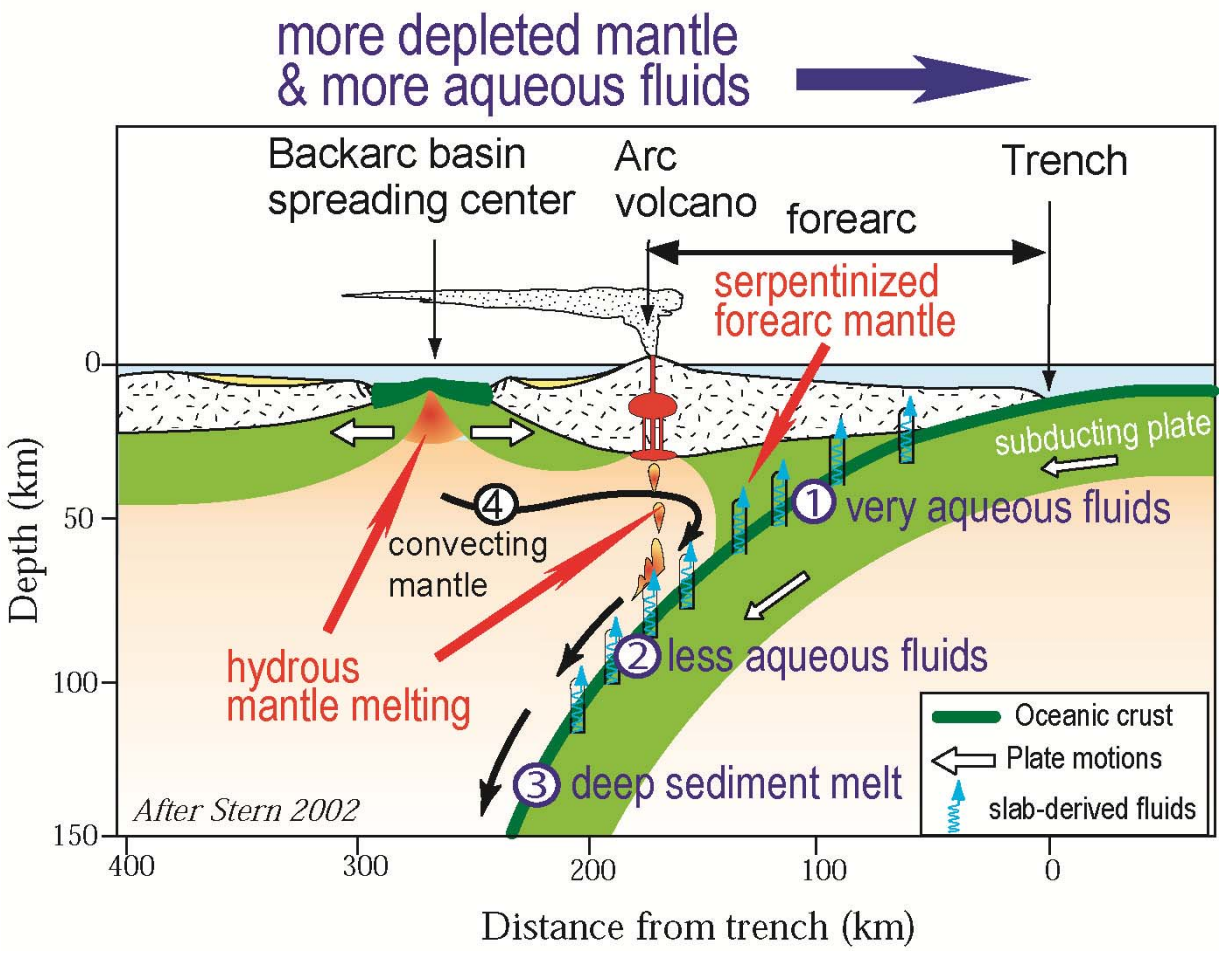

Figure 3.1. Sketch of a typical subduction zone, after (Stern, 2002). The downgoing plate releases its fluids into the mantle wedge as subduction proceeds. The slab-derived fluid is highly aqueous (water-rich) beneath the forearc (1), and the fluid becomes less aqueous with increasing depth (2). The slab-derived fluid becomes a silicate melt from sediment (3) at depth ≥ 100 km. The mantle flows from beneath the backarc basin spreading center towards the trench (4). Beneath the arc, magmas are produced by melting of a depleted mantle metasomatized by aqueous and sediment melt; while BAB lavas formed by adiabatic decompression melting of lherzolitic mantle which interacted with deeper aqueous fluids and hydrous melt from subducted sediment, Formation of magmas beneath the backarc basin, and then beneath the arc, depletes the mantle, resulting in a more depleted mantle towards the trench.

Here, we report the petrography, major and trace element chemistry, and Pb-Nd-Sr radiogenic isotopic compositions for mafic lavas from an unusual volcanic rift in the Mariana forearc, the Southeast Mariana Forearc Rift (SEMFR), which extends from the trench to the southernmost Mariana volcanic arc. Because SEMFR basalts are mantle melts produced beneath the forearc, these potentially provide new insights into the processes and products of shallow subduction zones (Figure 3.1). We use these geochemical and isotopic data to address two major questions: i) what is the composition of the mantle source and the slab-derived fluids beneath SEMFR?; and ii) how do the compositions of the mantle source and the slab-derived fluids vary with slab depth beneath SEMFR?

3.3 GEODYNAMIC SETTING

The southernmost Mariana convergent margin represents the southern end of the Izu-Bonin-Mariana (IBM) intraoceanic arc (Figure 3.2A). Here, the trench curves from N-S to nearly E-W to accommodate collision of the Caroline Ridge, which began in Late Miocene time (Miller et al., 2006a). This E-W trench segment is also the site of the great Challenger Deep. The subducting slab beneath the southernmost Marianas is able to rollback rapidly because it is short and narrow (200 km wide, ~ 250 km deep), which triggers upper plate extension and asthenospheric mantle flow beneath the forearc (Gvirtzman and Stern, 2004). These geodynamic conditions result in a rapidly evolving convergent margin, composed of active submarine arc volcanoes that almost intersect the BAB spreading ridge, the Malaguano-Gadao Ridge (MGR), which lies ~ 110 km from the trench (Figure 3.2A) (Fryer et al., 1998, Stern *et al.*, 2013). This atypical arc – backarc basin configuration allows the backarc mantle of the southernmost

Mariana Trough to capture the slab-derived fluids usually released beneath arc volcanoes, enhancing mantle melting to form the inflated Malaguana-Gadao spreading ridge (Becker et al., 2010, Fryer et al., 1998), in spite of this being a slow-spreading system (~4cm/yr; (Kato et al., 2003)). The Eocene forearc (Ishizuka et al., 2011, Reagan et al., 2010) has been stretching since Late Neogene time to accommodate the opening of the southernmost Mariana Trough, forming SEMFR at 2.7 - 3.7 Ma by seafloor spreading (Ribeiro et al., in press). SEMFR has since evolved into a broadly deformed rift (~ 40 km wide and at least 60 km long) that overlies the shallow part of the subducting slab (≤ 50 km deep) (Becker, 2005). SEMFR is traceable from the trench to a complex volcanic arc chain, the Fina Nagu Volcanic Chain (FNVC). Eastward, the SEMFR is bounded by the W. Santa Rosa Bank fault (WSRBF; Figure 3.2B; (Fryer et al., 2003)), which overlies a tear in the subducting Pacific plate (Fryer et al., 2003, Gvirtzman and Stern, 2004). In the following, we distinguish between NE and SW SEMFR as shown by the dashed white line in Figure 3.2B. SE SEMFR relief (near the trench) is the greatest and most affected by faulting and landsliding whereas NW SEMFR (near FNVC) has smoother relief with better-preserved pillow outcrops (Ribeiro et al., in press).

3.4 METHODS

SEMFR samples were collected in the course of manned submersible (Shinkai 6500) diving (YK08-08 and YK10-12 sites) and dredging (YK 10-12 deep-tow and TN273 sites). Representative fresh samples were selected for petrographic, geochemical, and isotopic studies. Details about the analytical methods are reported in Appendix 3A.. Major and trace element

analyses and isotopic ratios of SEMFR lava whole rocks and glassy rinds are reported in Appendix Tables 3A.1 and 3A.2.

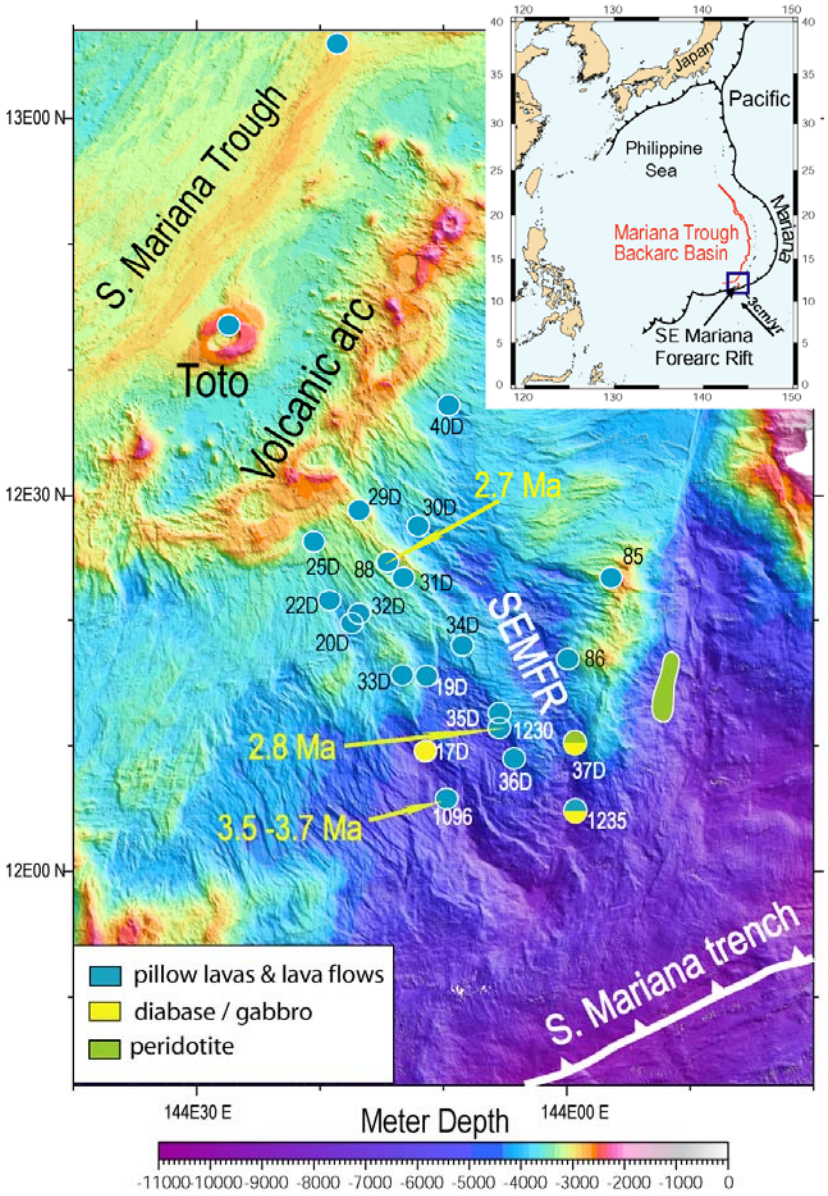

Figure 3.2. Locality maps. A) The Mariana intraoceanic arc system. The arrows represent the convergence rates from (Kato et al., 2003). The box shows the area of B. B) Detailed bathymetric map of the southernmost Mariana intraoceanic arc showing sample sites and their lithologies. The SEMFR is divided in SE and NW sectors, separated by a white dashed line. Map generated with GMT (Smith and Wessel, 1990, Wessel and Smith, 1995b, Wessel and Smith, 1998) using a compilation from the University of New Hampshire / Center for Coastal and

Ocean Mapping / Joint Hydrographic Center (Gardner, 2006, Gardner, 2007, Gardner, 2010). Toto: Toto caldera; FNVC: Fina Nagu volcanic chain. Numbers with D are the indicate TN273 dredging sites; other numbers represent sampling sites performed during JAMSTEC Yokosuka and Karei cruises. The large yellow numbers are ^{40}Ar-^{39}Ar ages for SEMFR lavas. Peridotites (in green) along the W. Santa Rosa Bank Fault (WSRBF) are from (Bloomer and Hawkins, 1983, Michibayashi et al., 2009, Sato and Ishii, 2011).

Samples were also filtered for alteration. Detailed study of the alteration of SEMFR lavas is reported in Appendix 3B. Alteration is not always visible petrographically, and cryptic alteration can affect concentrations of the FMEs in whole rock samples (Hart, 1969, Jochum and Verma, 1996, Kelley et al., 2003). Because the FMEs are of special interest in that manuscript, we selected the freshest whole rock with petrographic alteration ≤ 1%. We also report results from glassy rims to further circumvent problems caused by cryptic alteration of whole-rock samples.

3.5 RESULTS

Detailed petrographic and major element results for SEMFR samples recovered duringYK08-08 and YK10-12 cruises are reported in (Ribeiro et al., in press). In this section we describe the samples recovered from Thomas Thompson TN273 cruise (Figure 3.2B). Locations of the TN273 dredges are reported in Appendix Table 3C.1; and detailed description of TN273 samples is reported in Appendix Table 3C.2.

3.5.1 Petrography:

SEMFR is mostly floored with fresh pillow lavas and lava flows with a thin manganese cover (1 – 2 mm). A few plutonic rocks were also recovered during TN273, including olivine -

clinopyroxene diabase at dredge 17D and amphibole gabbros with peridotite at dredge 37D (not studied here). Plutonic rocks are generally more altered than lavas. Diabase, fine-grained gabbros and peridotites were only recovered in the easternmost SEMFR (Figure 3.2B), demonstrating the importance of faulting and exhumation of the lower crust and upper mantle in that part of the rift (Michibayashi et al., 2009, Ribeiro et al., in press). TN273 lavas are fresh to moderately altered and moderately vesicular basalt and basaltic andesite. Petrography of SEMFR lavas varies along the rift. Lavas from the SE sector are mostly microporphyritic and porphyritic olivine – clinopyroxene - plagioclase basalt, with ≤ 20 % plagioclase and 5 – 10% clinopyroxene. NW SEMFR lavas are mostly diabasic and microporphyritic olivine – clinopyroxene - plagioclase basalts with more plagioclase (> 20%) and clinopyroxene (≥10%; Appendix Table 3C.2). From the trench to the Fina-Nagu Volcanic Chain (FNVC; Figure 3.2), SEMFR lavas contain increasingly more abundant in plagioclase and clinopyroxene; this is also reflected by a change in lava texture from porphyritic to diabasic (≥ 50 % crystals).

3.5.2 Major elements:

SEMFR lavas (bulk samples) are low-K and medium-K basalt, basaltic andesite, and rare andesite (Figure 3.3A) that cluster on the tholeiitic side of the tholeiitic – calc-alkaline boundary of (Miyashiro, 1974) (Figure 3.3B; low-Fe to medium-Fe in the diagram of (Arculus, 2003)). In terms of normative composition, SEMFR lavas are quartz tholeiites (1 – 21 % normative quartz), with no significant difference between NW and SE segments. In Harker variation diagrams, SEMFR lavas define a fractionation trend from the most primitive lavas (olivine-rich basalts with Mg# ~ 0.71 - 0.72 and MgO ≥ 8 wt%) towards MGR andesites (Figure 3.3C-E). SEMFR

lavas have low Mg# (< 0.40) at $SiO_2 \geq 60$ wt% (Figure 3.3C), demonstrating that they are not boninites (Le Bas, 2000). Glassy rinds, which represent the quenched melt of submarine basaltic eruptions, plot along the elemental trends of SEMFR whole rocks (Figure 3.3A-E). However, glassy rinds have lower Mg#, Al_2O_3 and higher FeO*/MgO than their host rocks (Figure 3.3A-C, E), because bulk rocks contain olivine, pyroxene and plagioclase phenocrysts (see also Appendix 3B for more details). Harker variation diagrams (Figure 3.3 C-E) show that major element contents of SEMFR lavas are controlled by crystal fractionation. SE and NW SEMFR lavas define a single liquid line of descent (LLD) in CaO vs MgO diagram (Figure 3.3D); but in Al_2O_3 and FeO* vs MgO diagrams (Figure 3.3E-F), glassy rinds and whole rocks plot along two distinct LLDs: NW SEMFR whole rocks have less Al_2O_3 ($\leq$ 16.5 wt%) and more FeO* than those from SE SEMFR ($\geq$ 16.5 wt% Al_2O_3). Enrichment in Al_2O_3 and depletion in FeO* of SE SEMFR lavas relative to NW lavas, with no corresponding change in CaO, could reflect a slightly more depleted mantle source for NW SEMFR lavas. These geochemical and petrographical variations suggest that regional variations in melting processes and / or mantle source occurred along the rift.

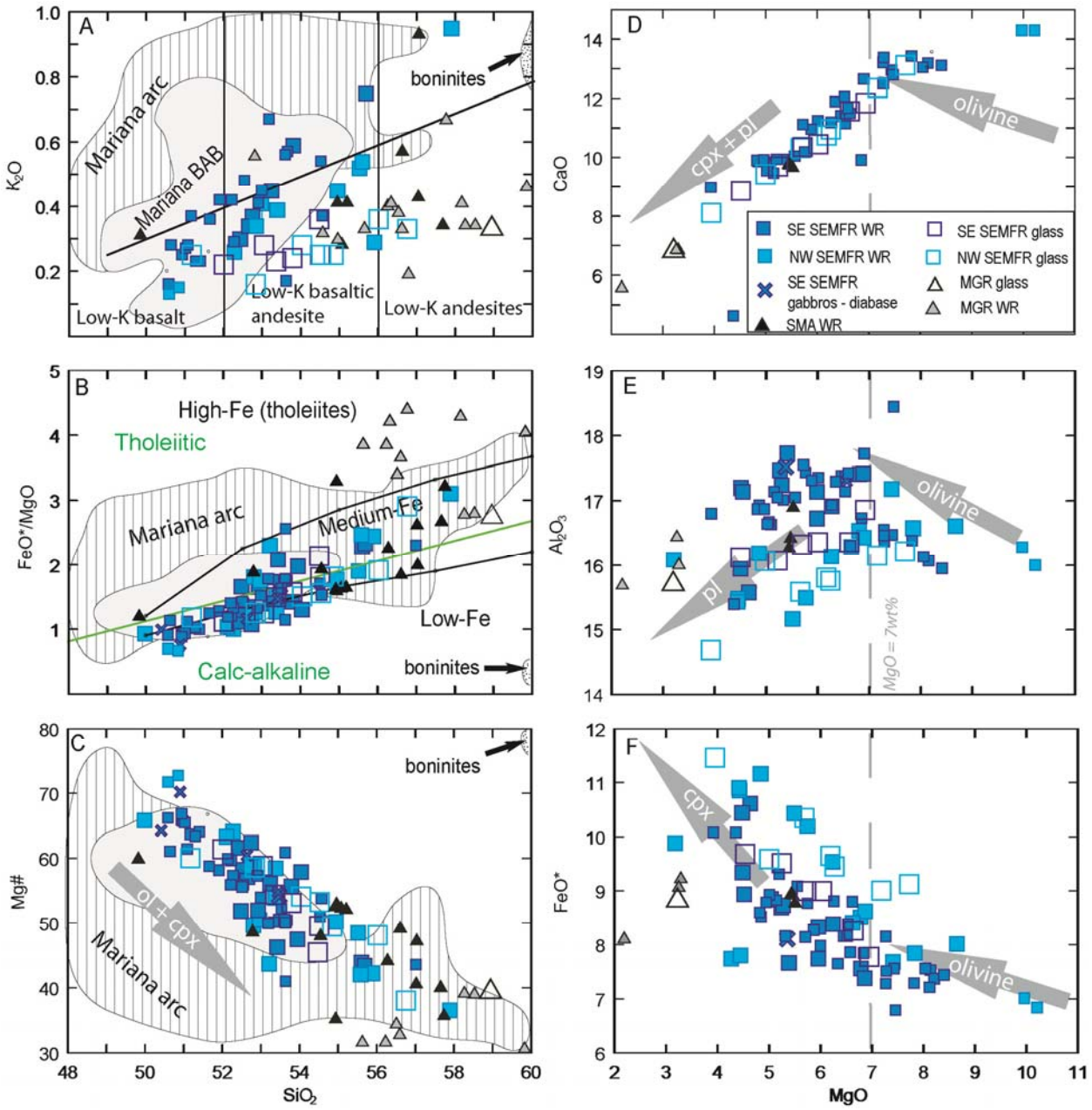

Figure 3.3. Major element variation diagrams (all data recalculated to 100% anhydrous) for SEMFR lavas. A) Potassium – silica diagram, with fields after (Peccerillo and Taylor, 1976). Bulk samples are filtered for alteration using techniques outlined in Appendix 3B. Large blue rectangles represent TN273 whole rock data, and small blue rectangles denote previously analyzed SEMFR samples (Ribeiro et al., in press). Large empty blue rectangles are glassy rinds. The grey field represents Mariana BAB lavas (14°N – 20°N (Gribble et al., 1996, Hawkins et al., 1990, Kelley and Cottrell, 2009, Pearce et al., 2005)). Hatched field represents Mariana Arc lavas (Kakegawa et al., 2008, Kelley and Cottrell, 2009, Kelley et al., 2010, Pearce et al., 2005,

Shaw et al., 2008, Wade et al., 2005). Small grey triangles denote data from the Malaguana-Gadao Ridge (MGR) (Kakegawa et al., 2008, Pearce et al., 2005). Small black triangles are data from S. Mariana arc whole rock (SMA WR) sampled between $13^{o}10'N - 11^{o}N$(Kakegawa et al., 2008, Stern et al., 2013), including Toto caldera samples reported in (Ribeiro et al., in press). The field for boninites is from (Reagan et al., 2010). B) FeO*/MgO vs SiO_2, after (Arculus, 2003); the green line discriminates between tholeiitic and calk-alkaline lavas (Miyashiro, 1974). C) Mg# vs SiO_2; (Mg# = 100Mg/(Mg+Fe); ol: olivine; cpx: clinopyroxene, D) CaO, E) Al_2O_3 and F) FeO* vs MgO diagrams for lavas from SEMFR, MGR, and Toto caldera (black triangles). Arrows represents fractionation trends. The grey dashed line highlights the hinge in CaO, Al_2O_3 and FeO*, resulting from plagioclase and clinopyroxene crystallization starting at MgO = 7 wt%. Pl: plagioclase, cpx: clinopyroxene.

In order to investigate SEMFR magmagenetic processes, lava and glass compositions need to be back-tracked to their compositions as primitive (unfractionated) melts in equilibrium with the mantle (Kelley et al., 2006, Klein and Langmuir, 1987, Langmuir *et al.*, 2006, Taylor and Martinez, 2003). The least fractionated rocks (MgO ≥ 7 wt%; Figure 3.3D-F), which crystallized only olivine, have been corrected to 8 wt% MgO using the equations of (Klein and Langmuir, 1987, Taylor and Martinez, 2003) to calculate the Ti_8, Na_8 and Fe_8 contents. TiO_2 and Na_2O are incompatible elements, so Ti_8 and Na_8 reflect the degrees of mantle depletion and mantle melting; whereas Fe_8 tracks the depth of mantle melting. SE SEMFR lavas and glass have lower Ti_8 and higher Fe_8 contents than NW SEMFR lavas, which cluster between Mariana arc and backarc basin compositional fields (Figure 3.4A). In term of Na_8 and Fe_8, SE SEMFR lavas plot within the BAB compositional field (Figure 3.4B), suggesting that BAB-like decompression melting of asthenospheric mantle dominated that part of SEMFR. In contrast, NW SEMFR lavas and glass have lower Ti_8 and Na_8 at higher Fe_8 contents, similar to Mariana arc lavas, suggesting that NW SEMFR lavas were produced deeper and at higher degrees of hydrous mantle melting than SE SEMFR lavas. This result also suggests that the magmagenetic conditions of SEMFR

lavas evolved from adiabatic decompression melting towards more hydrous mantle melting away from the trench. Differences between the two SEMFR segments are further examined below.

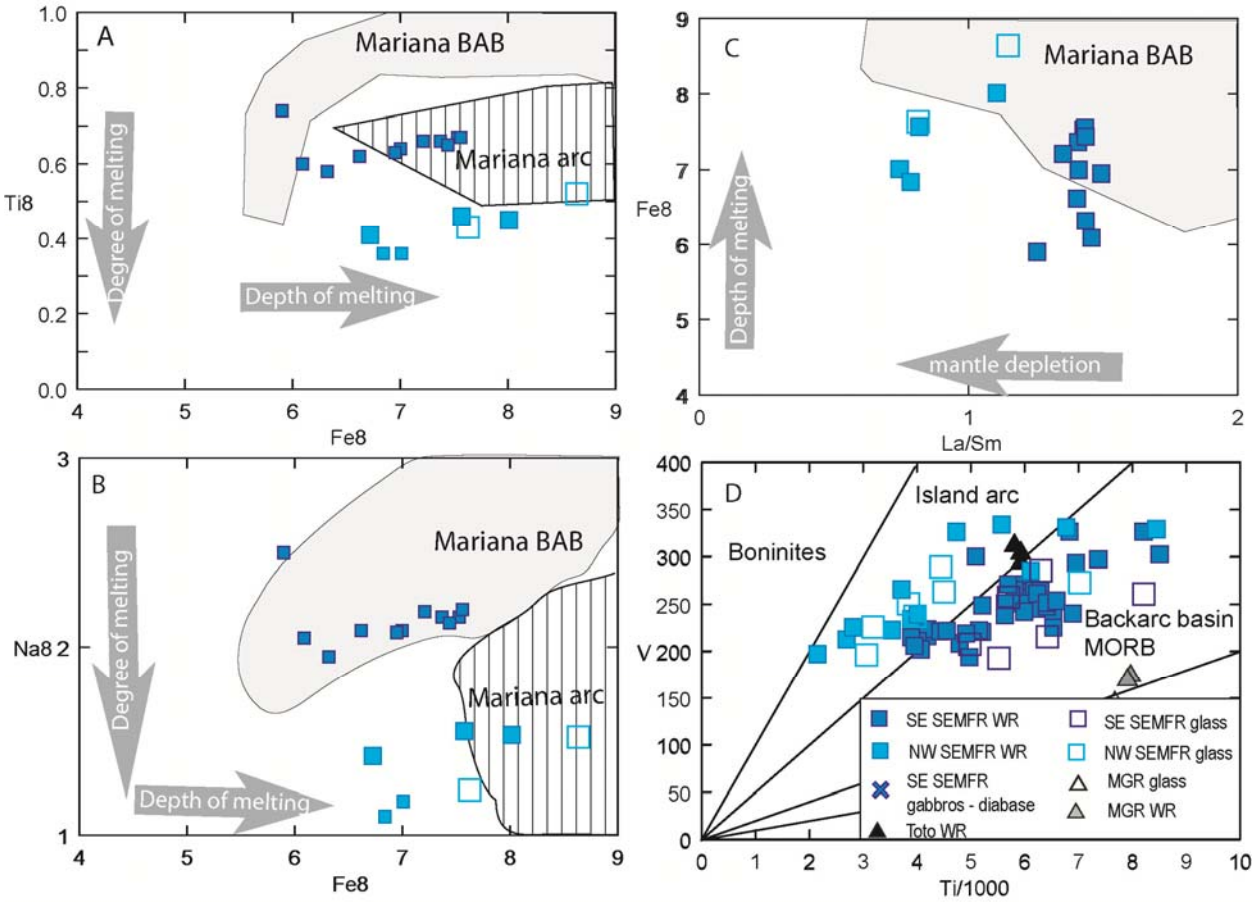

Figure 3.4. Chemical and magmagenetic variations of NW and SE SEMFR lavas, both glass and whole rock (WR). A) Ti_8 vs Fe_8, B) Na_8 vs Fe_8 and B) Fe_8 vs La/Sm diagrams. The composition in Na_2O, TiO_2 and FeO of the least fractionated (MgO ≥ 7 wt%) SEMFR lavas were corrected to MgO = 8 wt%. SE SEMFR lavas have higher Ti_8, Na_8 and La/Sm, and lower Fe_8, demonstrating that they were produced from a more enriched mantle source and / or lower degree of mantle melting at shallower depth than NW lavas. C) Ti-V plot of (Shervais, 1982) illustrating the evolution in magmagenetic conditions in SEMFR lavas, from BAB-like decompression melting to arc-like hydrous mantle melting, along the rift.

3.5.3 Trace elements:

Trace elements also provide petrogenetic information about SEMFR lavas. For example, similar to TiO_2 and Na_2O, La and Sm are melt-mobile elements, with La being more incompatible during mantle melting than Sm; therefore, La/Sm also tracks the degree of mantle depletion and melting. Plotting Fe_8 against La/Sm (Figure 3.4C) also demonstrates that NW SEMFR lavas formed deeper from a more depleted mantle source and / or as a result of higher degree of mantle melting than SE SEMFR lavas. Compositional and magmagenetic differences in SEMFR lavas can also be illustrated using the Ti -V plot of (Shervais, 1982). This diagram uses the melt-mobile behavior of Ti and the sensitivity of V to oxidation state in order to discriminate tectonic settings. Backarc basin lavas were produced by adiabatic decompression of depleted (MORB-like) mantle, so that BAB lavas and MORBs plot within the same Ti-V compositional field. In contrast, arc lavas formed by melting of a more oxidized and depleted mantle source, shifting the arc compositional field towards lower Ti and higher V. In this diagram (Figure 3.4D), SE SEMFR lavas plot within the BAB compositional field, whereas NW lavas mostly plot within the arc compositional field.

Trace element patterns of whole-rock and glass from SEMFR, MGR and Toto caldera are typical of subduction-related lavas, with variable enrichments in FME (Rb, Ba, Cs, Sr, K, U and Pb), and depletion in High Field Strength Elements (HFSE: Nb, Zr, Ta, Ti, Rare Earth element (REE), Y), indicating that these melts were derived from a mantle source that was variably depleted and metasomatized by slab-derived fluids (Figure 3.5A, D). Overall, spider diagrams for SEMFR lavas are similar to those of Mariana arc and backarc basin lavas.

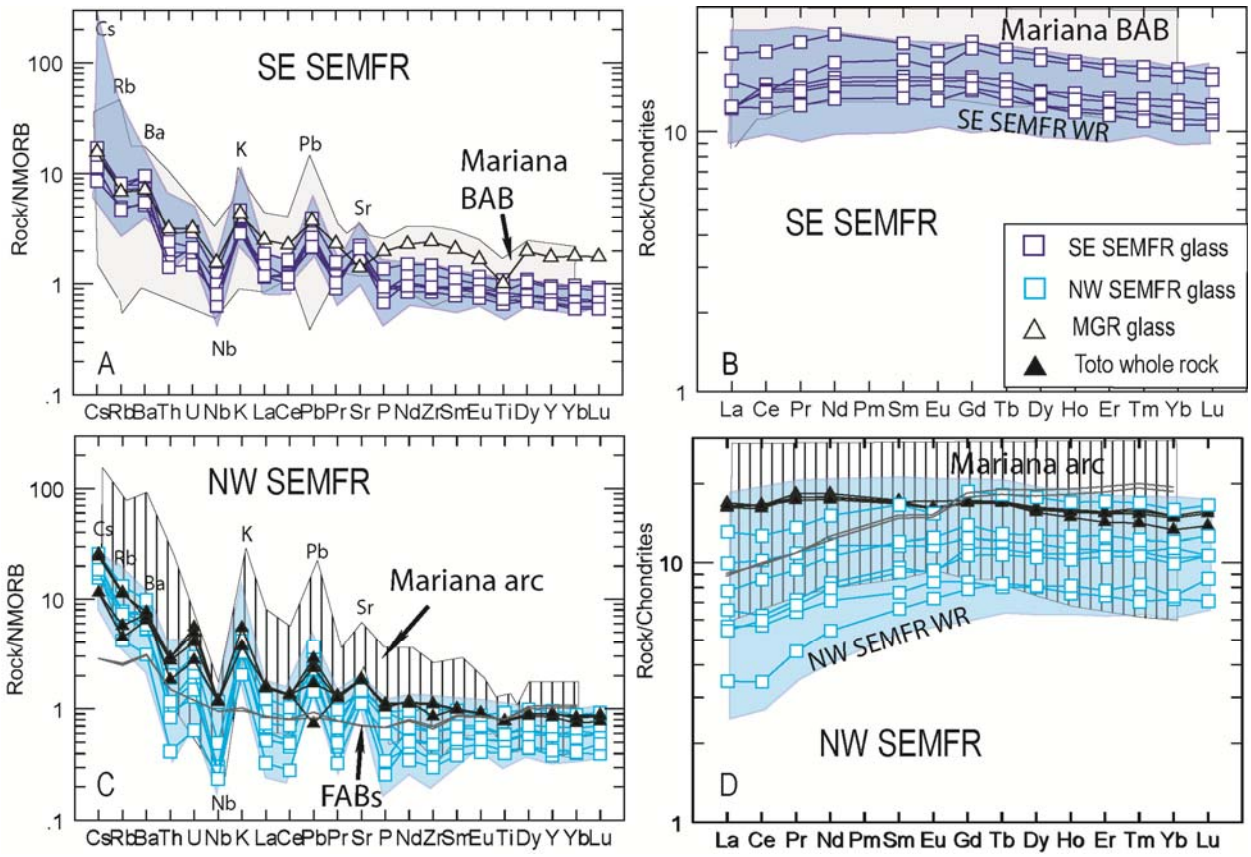

Figure 3.5. N-MORB normalized (Sun and McDonough, 1989) trace element patterns and chondrite-normalized (Sun and McDonough, 1989) Rare Earth element (REE) patterns of MGR and SEMFR lavas from the SE sector (A,B) and the NW sector (C,D). SEMFR whole rock (WR) are blue field and are compared to Mariana arc samples (Fryer, 1993, Kakegawa et al., 2008, Pearce et al., 2005, Stern et al., 2006, Stern et al., 2013), Mariana BAB (Gribble et al., 1996, Gribble *et al.*, 1998, Hawkins et al., 1990, Pearce et al., 2005), and forearc basalt (FABs) glassy rinds (Reagan et al., 2010).

Because FME abundances of whole rock samples are easily affected by low degrees of alteration, the following discussion emphasizes the composition of glassy rinds. Trace element patterns of SEMFR glassy rinds show higher HFSE and Th and lower Cs, Rb and Pb contents toward the SE (Figure 3.5A, D). Trace element patterns of MGR lavas are similar to Mariana BAB basalts; however, their less incompatible elements and REE abundances are elevated relative to those of SE SEMFR lavas. Trace elements patterns of Toto caldera lavas are similar to

those of Mariana arc and NW SEMFR lavas. REE patterns of SE SEMFR whole rock (WR) and glass are nearly flat although slightly humped in MREE ($(La/Yb)_N \sim 1$; $(La/Sm)_N \sim 1$; $(Gd/Yb)_N \sim 1$) with no europium anomaly ($(Eu/Eu^*)_N \sim 1$; Figure 3.5B), similar to REE patterns of Mariana BAB lavas. In contrast, NW SEMFR WR and glass have more strongly LREE-depleted (N-MORB-like) patterns (Figure 3.5D). NW SEMFR lavas and glass have more arc-like trace element patterns; whereas those of SE SEMFR have more BAB-like trace element patterns, consistent with inferences from the Na_8 Ti_8, Fe_8 and Ti-V plots (Figure 3.3F; 3.4A-C). To summarize, SE SEMFR glass is relatively enriched in LREE and HFSE ; whereas NW SEMFR glass is more enriched in FMEs, especially Pb, Rb, Ba, and Cs, and more depleted in HFSE, suggesting that i) the degree of mantle melting and mantle depletion was greater beneath NW than beneath SE SEMFR; and ii) the input of aqueous fluid was greater in the NW than in the SE.

3.5.4 Nd, Sr, and Pb isotopic compositions:

Because radiogenic isotopes are not fractionated during magmatic processes, they are commonly used to identify mantle sources. SE SEMFR lavas show homogeneous Sr and Nd isotopic compositions (Figure 3.6A), with a mean of $^{87}Sr/^{86}Sr = 0.70333 \pm 1$, $^{143}Nd/^{144}Nd = 0.51308 \pm 4$, and $\varepsilon Nd = 8.8 \pm 0.8$. Only NW SEMFR (YKDT-86) samples have Nd-Sr isotopic compositions that differ, with lower $^{87}Sr/^{86}Sr$ (mean $^{87}Sr/^{86}Sr = 0.70306 \pm 1$) and $^{143}Nd/^{144}Nd$ (mean $=0.51300 \pm 1$, $\varepsilon Nd = 7.0 \pm 0.2$) as are MGR lavas (mean $^{87}Sr/^{86}Sr = 0.70293 \pm 0.4$, $^{143}Nd/^{144}Nd = 0.51301 \pm 1$, $\varepsilon Nd = 7.3 \pm 0.2$). SE SEMFR and Toto caldera lavas are offset to higher $^{87}Sr/^{86}Sr$ compared with Mariana BAB lavas (Gribble et al., 1996, Gribble et al., 1998, Volpe *et al.*, 1987, Volpe *et*

al., 1990) (Figure 3.6A). SEMFR lavas plot within the compositional field of Eocene forearc basalts (FABs) of (Reagan et al., 2010), with εNd that is similar to that of Mariana BAB lavas (Stern et al., 2006, Wade et al., 2005, Woodhead, 1989).

Pb isotopic compositions of SEMFR lavas are homogeneous (mean $^{206}Pb/^{204}Pb = 18.67 \pm 0.01$, $^{208}Pb/^{204}Pb = 38.34 \pm 0.01$, $^{207}Pb/^{204}Pb = 15.57 \pm 0.01$) and are remarkably similar to Mariana arc lavas, defining an array from Mariana BABB towards subducted Pacific sediment (Plank and Langmuir, 1998), further demonstrating that sediments are important in the subduction component (Figure 3.5B). MGR lavas are distinctly less radiogenic than those of SEMFR (mean $^{206}Pb/^{204}Pb = 18.32 \pm 0.02$, $^{208}Pb/^{204}Pb = 37.92 \pm 0.01$, $^{207}Pb/^{204}Pb = 15.46 \pm 0.01$), and plot within the BAB compositional field. Toto caldera lavas (mean $^{206}Pb/^{204}Pb = 18.86 \pm 0.01$, $^{208}Pb/^{204}Pb = 38.40 \pm 0.02$, $^{207}Pb/^{204}Pb = 15.56 \pm 0.005$) cluster in the arc compositional field, near SEMFR lavas.

3.6 DISCUSSION

Subduction-related magmas have positive anomalies in FMEs, Th and Pb inherited from their slab-derived fluids, and negative HFSE anomalies inherited from their mantle source. These differences in elemental mobility for aqueous fluids, sediment melts and mantle melts along with the Nd-Sr-Pb isotopic ratios of the lavas can be exploited to examine the nature and the evolution of the mantle and subduction components (Class *et al.*, 2000, Elliott, 2003, Escrig *et al.*, 2009, Pearce, 2008, Plank and Langmuir, 1998, Stern et al., 2006) beneath SEMFR.

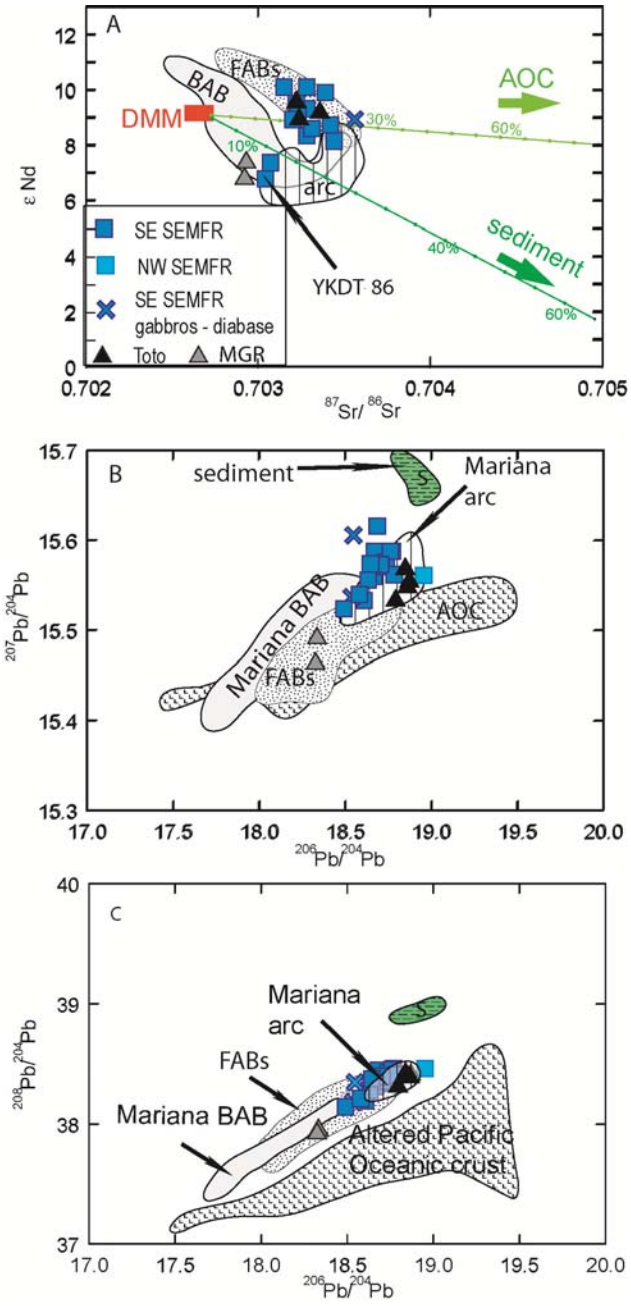

Figure 3.6. Nd-Sr-Pb isotopic compositions of SEMFR lavas. A) εNd vs $^{87}Sr/^{86}Sr$ diagram. The light green and dark green lines are mixing models for SEMFR lavas between a depleted MORB-type mantle (DMM; (Salters and Stracke, 2004)), altered Pacific oceanic crust (AOC; (Hauff *et al.*, 2003)), Pacific sediment (average of ODP site 800 and 801 sediments from (Plank and Langmuir, 1998)). $^{207}Pb/^{204}Pb$ (B) and $^{208}Pb/^{204}Pb$ (C) vs $^{206}Pb/^{204}Pb$ diagrams. NHRL: Northern Hemisphere Reference Line is from (Hart, 1984); S. Mariana arc (SMA; 13°10'N – 11°N; Alphabet Seamount Volcanic Province) and BAB (S-SMT) lavas are from (Stern et al., 2013).

3.6.1 Nature of the mantle and subduction components:

The mantle and subduction components can be tracked by using fluid-mobile and melt-mobile elements normalized to a less incompatible, fluid-immobile element (e.g. Nd, Sm, HFSE, HREE), so that fluid and mantle melt markers are corrected for fractionation and melting processes (Elliott, 2003, Langmuir et al., 2006, McCulloch and Gamble, 1991, Pearce et al., 2005). Ratio of a strongly melt-mobile element over a slightly melt-mobile element (i.e. Nb/Yb) characterizes mantle fertility (Pearce et al., 2005); while ratios of a subduction-mobile element (i.e. Ba, Cs, Rb, Th) over a subduction-immobile element (i.e. Nb, Ta, Yb) are good proxies to track subduction components (Pearce et al., 2005). For example, Ba, Rb, Cs, K, Sr, easily migrate with the aqueous fluids (McCulloch and Gamble, 1991) and with the deeper sediment melt (Manning, 2004, Pearce et al., 2005); while Th is only mobilized with sediment melts (Johnson and Plank, 1999). Therefore, Ba/Yb and Ba/Nb track the total subduction component, Th/Yb and Th/Nb track the deep sediment melt and Ba/Th, Rb/Th and Cs/Th track the shallower aqueous fluids (Pearce et al., 2005).

SEMFR lavas have BAB-like Nb/Yb (~ 1) and Ba/Yb (≤ 70), plotting well above the MORB array (Pearce et al., 2005). This is consistent with the homogeneous Nd isotopic ratios ($\varepsilon Nd = 8.6 \pm 0.7$) of SEMFR lavas and demonstrates that they have a BAB-like mantle source (Figure 3.7A). SEMFR lavas show a gradient in the mantle source: NW lavas have lower Nb/Yb than SE SEMFR lavas, showing that the SEMFR mantle source was more depleted away from the trench. In Ba/Nb vs Th/Nb diagrams (Figure 3.7B) of (Pearce and Stern, 2006), the compositional field of Mariana BAB lavas (Gribble et al., 1996, Gribble et al., 1998, Hawkins et al., 1990, Pearce

and Stern, 2006) reflects the contribution of deep sediment melt; whereas enrichment of Ba without any enrichment in Th defines the shallower aqueous fluid (Pearce and Stern, 2006). Mariana arc lavas (Fryer, 1993, Kakegawa et al., 2008, Stern et al., 2006, Stern et al., 2013, Wade et al., 2005) are enriched in aqueous fluid and deep sediment melt. SE SEMFR lavas plot homogeneously along the Mariana BAB composition field whereas NW SEMFR lavas have higher Ba/Nb (Figure 3.7B), demonstrating that the aqueous fluid signal increases in SEMFR lavas away from the trench. The BAB-like Th/Nb in SEMFR lavas suggests interaction of the mantle source with a sediment melt, perhaps resulting from inheritance of high Th/Nb ratios from the SEMFR mantle source.

Trace element systematics similar to the approach of (Pearce et al., 2005) can be applied by using Cs and Rb in order to investigate the composition of the SEMFR aqueous fluids; for this we must avoid cryptically-altered whole rocks and rely on glassy rims. We use the ratios Cs/Th, Ba/Th and Rb/Th to better distinguish shallow hydrous inputs from the deep sediment melt component. In Figure 3.7C-F, SE SEMFR lavas plot along the arc compositional field, while NW SEMFR lavas have higher Rb/Th and Cs/Th than arc and BAB lavas. These results demonstrate that i) the mantle source of SEMFR lavas captured an aqueous fluid; and ii) the mantle source of NW SEMFR lavas interacted with an aqueous fluid that was richer in Rb and Cs than the fluid released beneath the arc and the backarc basin spreading center.

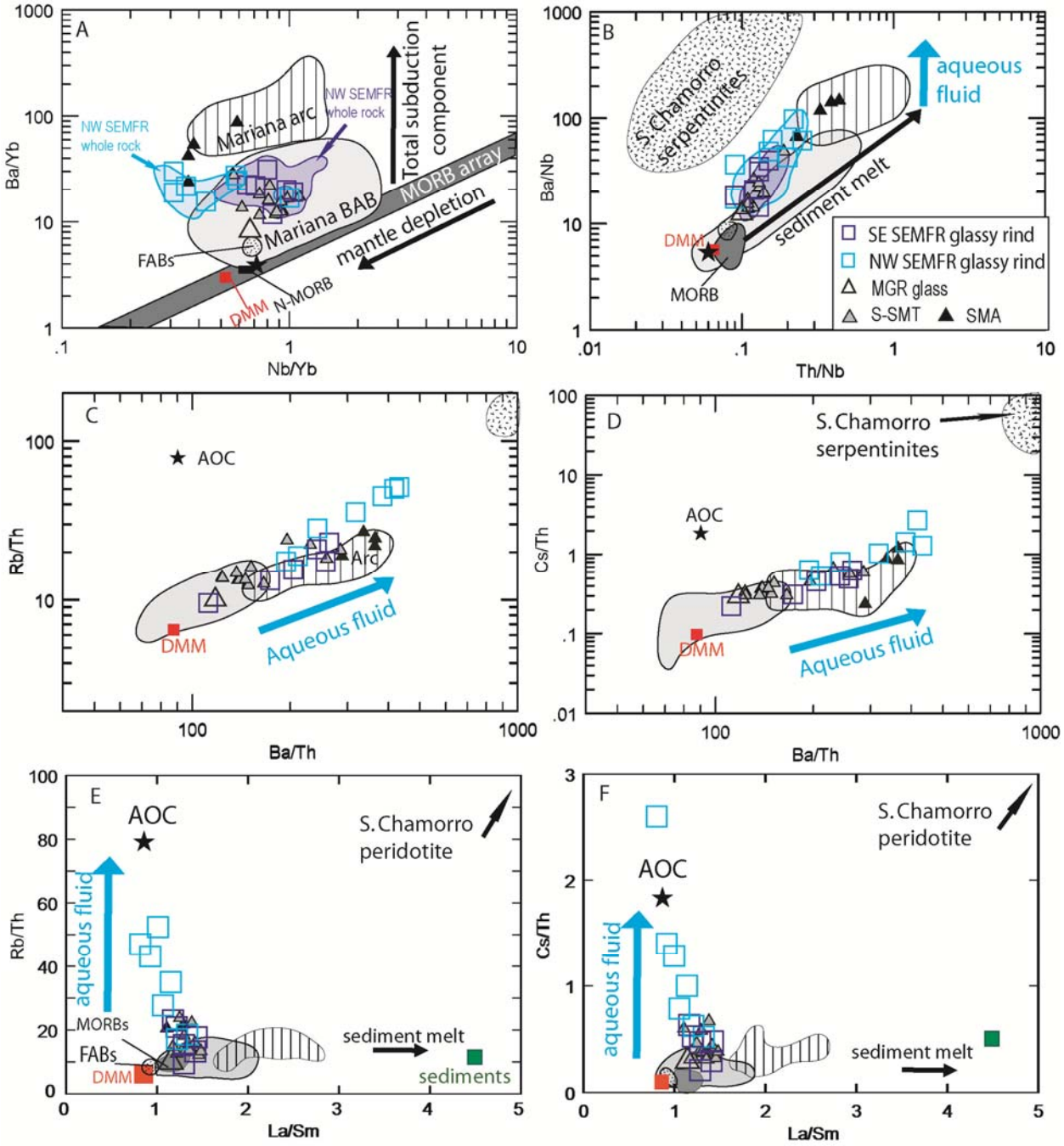

Figure 3.7. Geochemical proxies used to discriminate subduction and mantle components for SEMFR lavas and related rocks, after (Pearce et al., 2005). A) Ba/Yb vs Nb/Yb discriminates the total subduction component (Ba/Yb) from mantle depletion (Nb/Yb) (Pearce et al., 2005). NW SEMFR lavas have lower Nb/Yb and slightly higher Ba/Yb than SE SEMFR lavas. B) Ba/Nb vsTh/Nb diagrams of (Pearce et al., 2005) is used to discriminate the deep sediment melt from the aqueous fluid. Stronger Ba/Nb in NW SEMFR lavas and in the serpentinized peridotites from

S. Chamorro serpentinite mud volcano in the Mariana forearc (Savov et al., 2005) relative to arc lavas and BAB lavas reflect the role of an aqueous fluid released beneath the forearc. Compositions of the whole rock are represented by a light blue field for NW SEMFR and a darker blue field for SE SEMFR. Note that compositions of the NW and SE SEMFR glassy rinds and whole rock match. Rb/Th (C) and Cs/Th (D) vs Ba/Th diagrams used to characterize the composition of the aqueous fluid. NW SEMFR glassy rinds have higher Cs/Th and Rb/Th than arc and BAB lavas. Pacific sediments are an average of the ODP site 800 and 801 from (Plank and Langmuir, 1998). See text for more details. Plots of Rb/Th (E), and Cs/Th (F) vs La/Sm, after (Elliott, 2003), to identify the sources of the aqueous fluid. The altered oceanic crust (AOC) is a mixture of the ODP site 801 tholeiites (Kelley et al., 2003). The depleted mantle source of MORBs (DMM) is from (Salters and Stracke, 2004); the Pacific sediments are an average of ODP site 800 and 801 sediments, from (Plank and Langmuir, 1998); MORB-like BABBs from the central part of the S. Mariana Trough are from (Pearce et al., 2005).

3.6.2 Sources of the slab-derived fluids:

Three sources can be considered for the fluids reflected in the composition of SEMFR lavas: i) subducted altered oceanic crust (AOC) (Elliott, 2003, Langmuir et al., 2006, Pearce and Stern, 2006, Pearce et al., 2005, Plank and Langmuir, 1998); ii) subducted sediments (Elliott, 2003, Langmuir et al., 2006, Pearce and Stern, 2006, Pearce et al., 2005, Plank, 2005, Plank and Langmuir, 1998); and iii) the serpentinized forearc mantle wedge (Hattori and Guillot, 2003, Rüpke et al., 2004, Savov et al., 2007, Scambelluri and Tonarini, 2012, Stern et al., 2006, Straub and Layne, 2003) that captured and stored some of the slab-derived aqueous fluids. Fluid sources can be back-tracked by using elemental ratios and the Pb-Nd-Sr isotopic compositions of the lavas.

Occurrence of a component from subducted Pacific sediments is demonstrated in SEMFR lavas by i) their BAB-like Th/Nb ratios, likely inherited from sediment-melts (Figure 3.7B); and ii) their linear array in Pb isotopic ratios, extending from Mariana BABBs towards Pacific

sediments (Figure 3.5B-C). A subduction component due to altered oceanic crust can also be seen in SEMFR lavas, as demonstrated by their Sr-Nd isotopic composition, plotting near the MORB compositional field (Figure 3.5A); and by their low La/Sm associated with elevated Ba/Th, Rb/Th, and Cs/Th , so that NW SEMFR lavas plot towards AOC (Figure 3.7E-F). Modeling SEMFR Sr-Nd isotopic composition suggests that < 30% fluid from AOC was added to the SEMFR mantle (Figure 3.5A), whereas 10 – 15% fluid from sediments was added to MGR and YKDT-86 mantle source. Finally, Figure 3.7C-D shows that SEMFR lavas plot along an array from the depleted mantle of (Salters and Stracke, 2004) towards S. Chamorro peridotite (Savov et al., 2005), demonstrating that the serpentinized forearc mantle could also be a source of aqueous fluids. In summary, SEMFR budgets for Ba, Cs, Rb were controlled by dehydration of AOC and the serpentinized, mantle wedge; whereas their Th and Pb budgets were controlled by dehydration and melting of subducted sediments.

3.6.3 Tracking mantle and subduction flows:

Geochemical maps help us to track the spatial and compositional evolution of the subduction and mantle source across the SE Mariana forearc (Pearce et al., 2005). In the previous sections (5.1 – 5.2), we showed that SEMFR lavas interacted i) with an aqueous fluid from the subducted altered oceanic crust and serpentinized, upper mantle wedge; and ii) with a sediment-melt. Subduction and mantle components can be mapped by using the Ba/Th, Rb/Th and Cs/Th proxies to illustrate the aqueous fluids, Th/Nb map sediment melt, and Nb/Yb to mantle depletion and from this, to infer mantle flow (Pearce and Stern, 2006, Pearce et al., 2005).

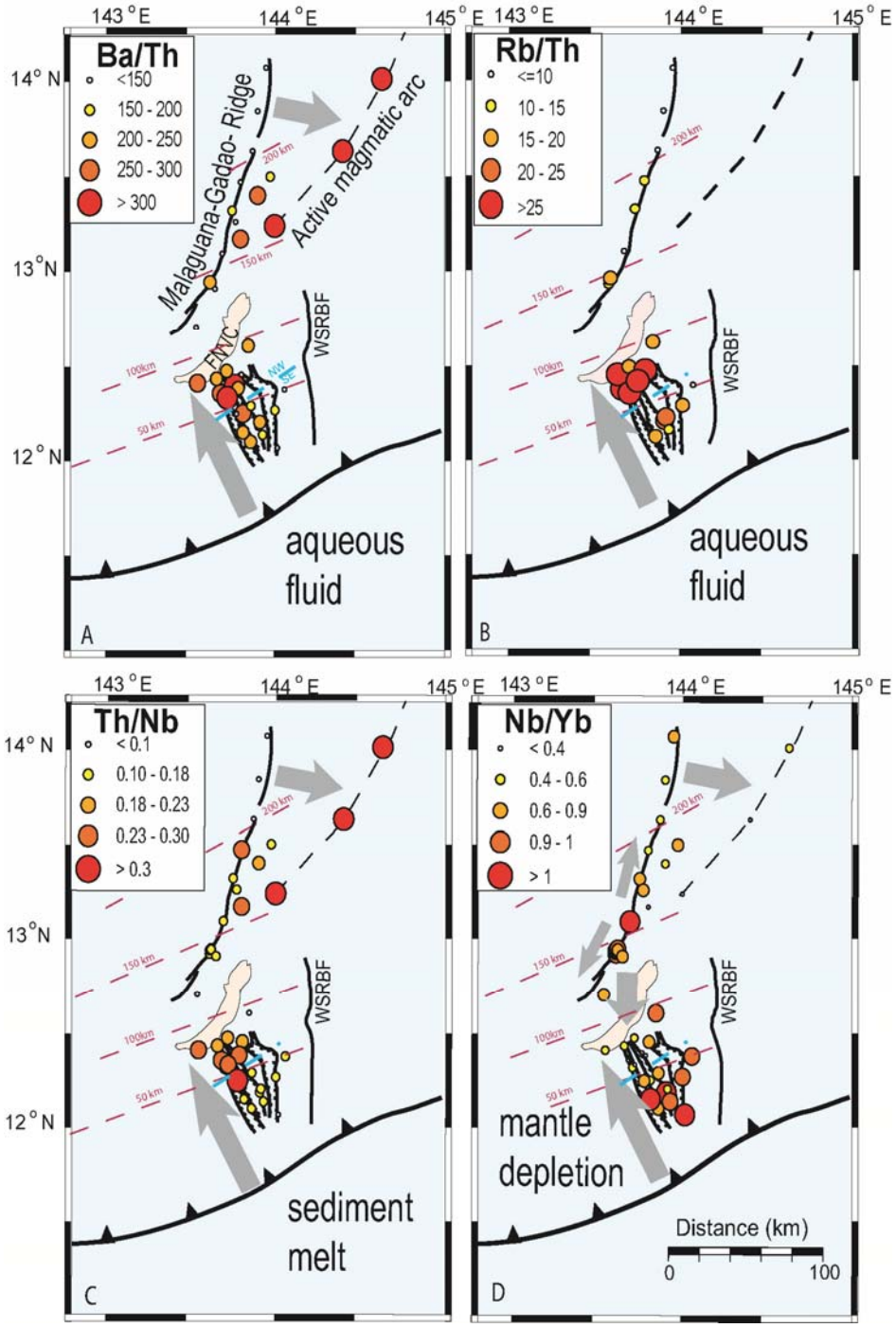

Figure 3.8. Geochemical maps of the subduction and mantle components in the SE Mariana convergent margin, after (Pearce et al., 2005). A) Ba/Th and B) Rb/Th, are proxies mapping the aqueous fluid; and C) Th/Nb ratio maps sediment melt. Cs/Th is not shown but show similar variation as Rb/Th. The subduction components increase toward the Fina-Nagu volcanic arc chain (FNVC), as denoted by the grey arrow. D) Nb/Yb tracks mantle fertility and mantle flow

along SEMFR. Nb/Yb increases toward the trench, indicating that depletion increased away from the trench and suggesting that 3.7 to 2.7 Ma the mantle flowed from the trench toward the arc volcanoes, as illustrated by the long grey arrow. The shorter grey arrows show modern, inferred mantle flow beneath MGR. See text for details.

Ba/Th and Th/Nb in S. Mariana arc-backarc basin lavas increase from the MGR toward the active arc volcanoes (Figure 3.8A-C), demonstrating that aqueous fluid and deep sediment melt are mostly captured by the magmatic arc volcanoes (Pearce et al., 2005). The southern termination of the Mariana Trough, where the spreading center almost intersects with the active arc volcanoes south of 13^{o}N, has intermediate Ba/Th and Th/Nb, between the values of the arc and the backarc basin spreading center. This result is consistent with the interpretations of (Becker et al., 2010, Fryer, 1993, Stern et al., 2013), suggesting that the southernmost part of MGR, localized at ~ 150 km above the Wadati-Benioff zone (Becker, 2005, Fryer et al., 1998), captures the aqueous fluid and sediment melt usually released beneath arc volcanoes (Figure 3.1). Along SEMFR, the proxies Ba/Th, Cs/Th, Rb/Th and Th/Nb increase toward the arc volcanoes, demonstrating that both aqueous fluid and the deep sediment melt increase with slab depth. This observation, in agreement with (Hulme et al., 2010), demonstrates that the composition of the aqueous fluid is controlled by the P-T path of the subducting slab and Rb-Cs-Ba-rich mineral breakdown (such as barite (Plank and Langmuir, 1998), phengite (Zack et al., 2001), and serpentinite (Savov et al., 2007, Savov et al., 2005)). Beneath SEMFR, the slab-derived inputs in Ba, Cs and Rb are the highest between ~ 50 km to 100 km slab depth (Figure 3.8A-C; Figure 3.9), suggesting that Rb-Cs-Ba-rich minerals released their aqueous fluids deeper than beneath the outer forearc (Figure 3.1).

The Nb/Yb ratio (Figure 3.8D) varies along and across the backarc basin spreading center. Along MGR, Nb/Yb is highest around 13°10'N, where a magma chamber was identified (Becker et al., 2010). Nb/Yb decreases away from MGR, suggesting that the mantle is more depleted away from the spreading ridge. Across MGR, Nb/Yb decreases from the backarc basin toward the arc volcanoes, demonstrating that arc mantle is more depleted than the BAB mantle. Such variations in Nb/Yb are consistent with a more depleted mantle flowing towards the trench (Figure3.9) (Pearce and Stern, 2006, Pearce et al., 2005), and suggest that the forearc mantle should be more depleted than the arc mantle (Figure 3.1). However, in SEMFR lavas, Nb/Yb decreases toward the arc volcanoes (FNVC), reflecting a more depleted mantle source away from the trench. This result suggests that new undepleted mantle flowed toward the SE Mariana trench when SEMFR formed. This asthenospheric mantle flow could have been due to N-S southernmost Mariana slab tears (Fryer et al., 2003, Gvirtzman and Stern, 2004), which allowed Pacific asthenospheric mantle to infiltrate beneath the S. Mariana forearc; and Hf isotopic composition of SEMFR need to be analyzed to test that hypothesis.

3.7 CONCLUSIONS

The SE Mariana forearc lithosphere stretched to accommodate opening of the southernmost Mariana Trough, forming SEMFR 3.7 – 2.7 Ma ago. The presence of young basalts in the SE Mariana intraoceanic arc provides an opportunity to investigate compositional evolution of the shallow mantle and subduction processes unusually close to the trench and above a very shallow subduction zone.

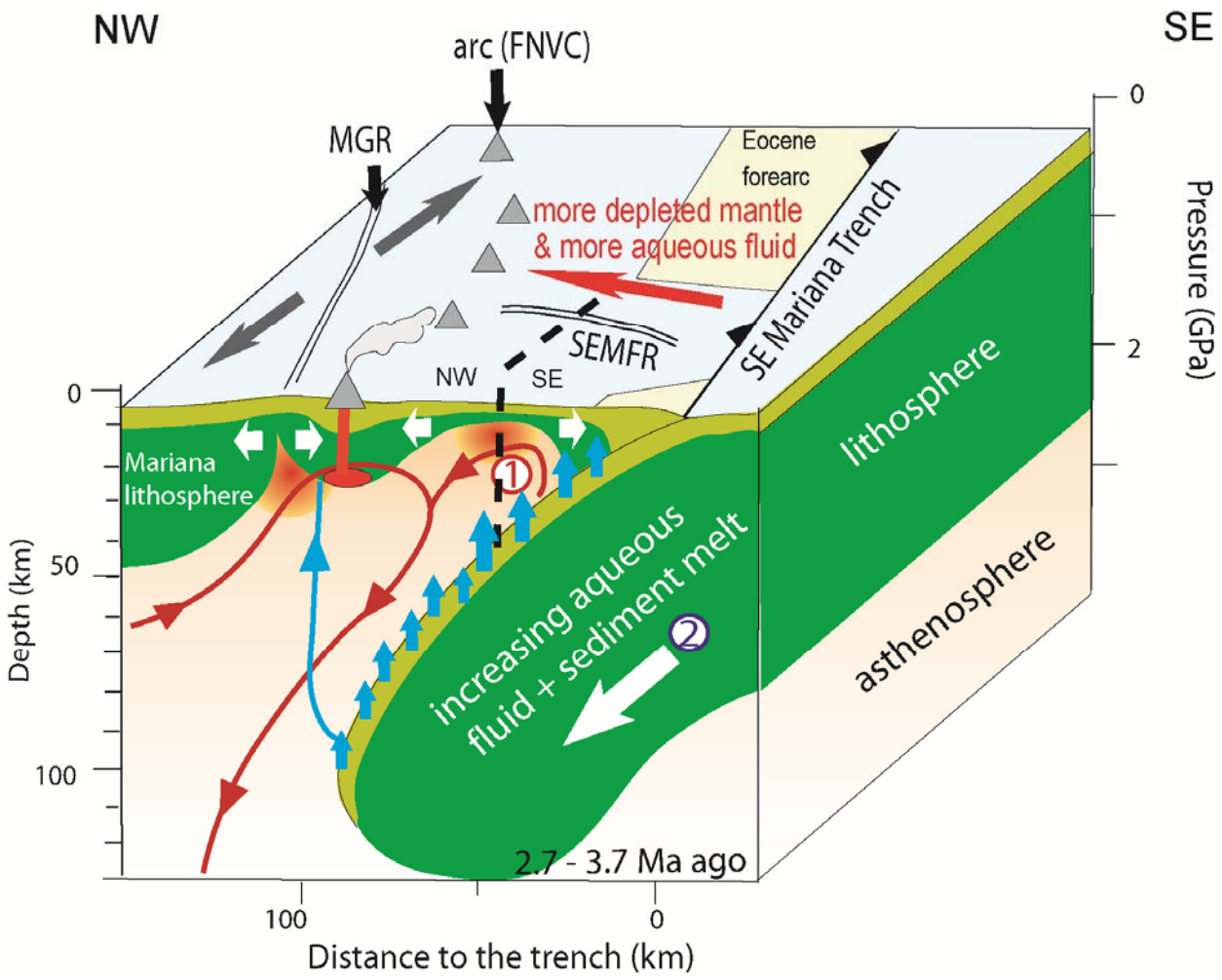

Figure 3.9. 3D model of magmagenesis for SEMFR lavas. Mantle depletion increases away from the trench, suggesting that new mantle input flowed beneath SEMFR toward the arc (1). The Ba, Cs, Rb contents in SEMFR lavas increase toward the arc volcanoes (2), suggesting the Cs-Ba-Rb-rich minerals broke down at ~ 50- 100 km depth, releasing the FME-rich aqueous fluids beneath the forearc – arc. The high Th/Nb ratio in SEMFR lavas, even in SE SEMFR lavas, suggests occurrence of a BAB-like deep sediment melt beneath the forearc. This high Th/Nb ratio could also be inherited from the SEMFR mantle source. The grey arrow shows the opening of MGR. The red arrow along SEMFR shows that mantle depletion and aqueous slab-derived fluids increase away from the trench.

SEMFR lavas did not form from a strongly depleted, forearc mantle source, as expected. Instead they formed from a less depleted, BAB-like mantle source that flowed from the trench toward the arc volcanoes, suggesting a new input of less depleted mantle flowed from near the trench

towards the arc (Figure 3.9), counter to the flow expected beneath convergent plate margins. Mantle beneath SEMFR captured aqueous fluids, and these are reflected in the composition of melts that these generated. These aqueous, slab-derived fluids are more enriched in Cs and Rb, and slightly more enriched in Ba, than the deeper fluids released beneath arc volcanoes and the backarc spreading center, suggesting that SEMFR mantle trapped the aqueous fluids released from the shallow part of the subducting altered oceanic crust and the serpentinized forearc mantle (Figure 3.9). Another surprising result is that SEMFR melts, including SE SEMFR lavas (Figure 3.7B), show a melt component released from subducted sediments (demonstrated by high Th/Nb), which is generally thought to be released much deeper (≥ 100 km) (Johnson and Plank, 1999, Pearce et al., 2005). Occurrence of a deep BAB-like sediment melt component in SEMFR lavas could be inherited from an earlier modification of their mantle source and may not reflect shallow subduction zone processes. Finally, the absence of a strong subduction component in SE SEMFR lavas indicates that aqueous slab-derived fluids and sediment melts are mostly released at 50 – 100 km slab depth, demonstrating that the Cs-Ba-Rb-rich minerals from the subducting slab mostly broke down at this depth to release their aqueous fluid.

3.8 ACKNOWLEDGEMENTS

We would like to thank the R/V Yokosuka and the R/V Thomas Thompson crews for their efforts work during YK08-08, YK10-12 and TN273 cruises. This research was supported by NSF grant 0961352 to RJS. This is UTD Geosciences contribution #12XX

APPENDIX 3A

ANALYTICAL METHODS

During JAMSTEC Yokosuka campaigns in 2008 (YK08-08 Leg 2) and 2010 (YK10-12), 161 mafic samples were collected along SEMFR, including 27 samples during YK08-08 Leg 2 and 134 samples during YK10-12. These samples were collected during one YK08-08 Shinkai 6500 dive (1096), two YK10-12 Shinkai 6500 dives (1230 and 1235) and three YK10-12 deep-tow mini-dredges (YKDT 85,86, 88). During TN273 cruise (21 December 2011 – 22 January 2012), SEMFR was sampled with 19 dredges. From TN273 samples of SEMFR seafloor, we studied 151 mafic. Nine samples from Toto caldera (JAMSTEC Kaiko dive 163R) and the Malaguana-Gadao Ridge (Kaiko dive 164R), sampled during JAMSTEC Karei cruise KR00-03 Leg 2 in 2000, were also studied. General geologic setting for SEMFR, including petrography, mineral chemical, major element, and $^{40}Ar/^{39}Ar$ ages, was reported by (Ribeiro et al., in press); and this manuscript includes mineral chemical and major element compositions for YK08-08 Leg 2 and YK10-12 samples.

Trace element analyses for dive 1096 (YK08-08 Leg 2 cruise) was carried out at the Geological Survey of Japan / AIST (Ishizuka et al., 2009) by ICP-MS (Inductively coupled plasma mass spectrometer) on a VG Platform instrument. Reproducibility is $\leq \pm$ 4% rsd for REE and $\leq \pm$ 6% rsd for other trace elements. TN273 samples were analyzed for major element abundances at Boston University, and for trace elements at the University of Rhode Island (URI), following the

method of (Kelley et al., 2003). Fresh bulk samples were crushed, hand-picked to avoid crystals and alteration, and powdered using a high-purity alumina mill ball. Major elements analyses were conducted on Ultima-C Jobin Yvon Horiba Inductively Coupled Plasma Atomic Emission Spectrometry (ICP-AES) at Boston University. Glass beads were generated by melting 400 ± 5 mg of lithium metaborate (LiBO4) flux with 100 ± 5 mg of ignited sample powder at 1050^{o}C for 10 min. Glass beads were dissolved in 50 mL of 5% HNO_3, and then in 212 mL 5% HNO_3. Trace element analyses were carried out on a Thermo X-series II quadrupole ICP-MS at URI. Whole rock samples were successively dissolved with HF and 8N HNO_3, and solutions were diluted 2500 times. Standards (W2, BIR1, BHVO1, DNC1, JB3) and one blank were prepared following the same procedures as the samples for trace and major analytical works. One set of 10 unknowns, 4 USGS standards, one drift corrector and one blank were analyzed during ICP-MS and ICP-AES analyses. The blank was analyzed at the beginning and the end of each sample set. The drift corrector was analyzed every 3 to 4 samples. Calibration curves yield $r^2 \geq 0.999$ for trace and major elements, but for P_2O_5 ($r^2 \geq 0.997$). Averaged reproducibility of replicate analyses are < 2% rsd for major and trace element analyses, except for P_2O_5 and K_2O (< 4% rsd). Major element oxides sum to 100 ± 1 wt% when measuring Fe_2O_3. Sample replicates analyzed by ICP-MS and ICP-AES agree within < 4% rsd for TiO_2, Sr and K_2O; and trace elements analyzed by ICP-MS in Japan and at URI agree within < 10% (Figure3A.1).

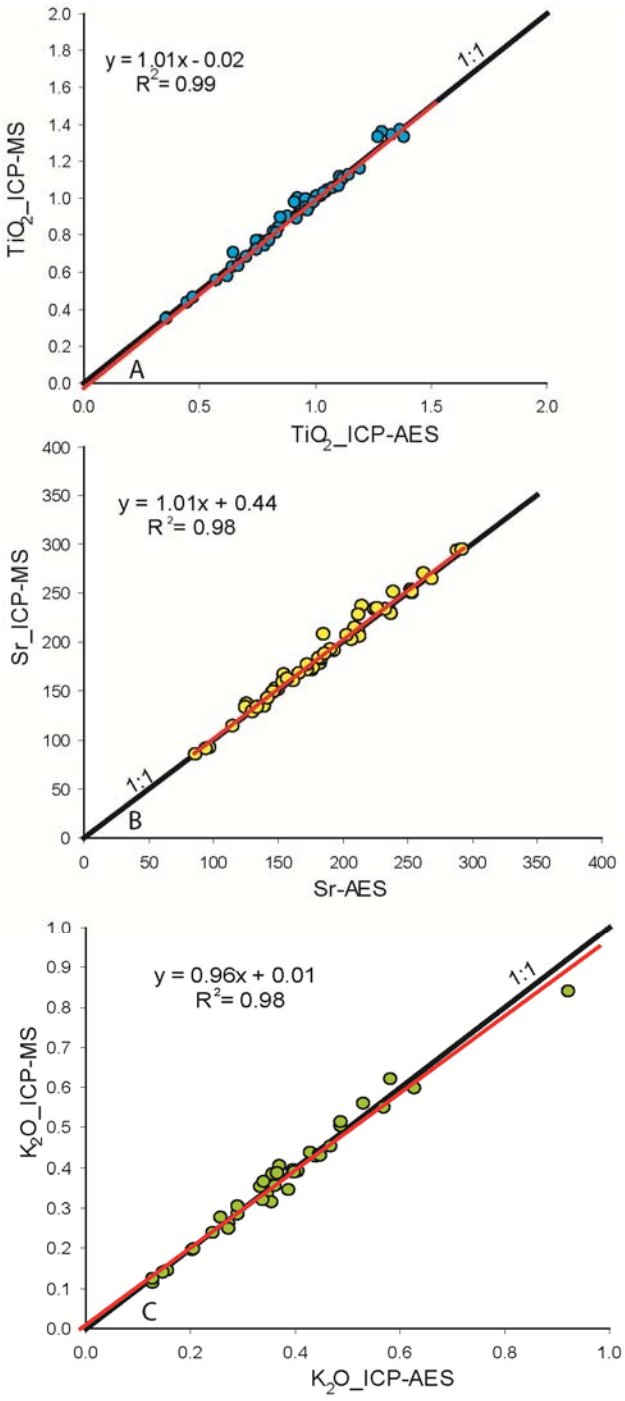

Figure 3A.1. Examples of how major and trace element concentrations of the bulk samples analyzed with ICP-AES and ICP-MS compare for A) % TiO_2, B) ppm Sr and C) % K_2O. The black line denotes the 1:1 line; and the red line is the linear regression for the analyzed samples, for which the equation and correlation coefficient squared are shown. The two techniques agree within < 4% rsd, and the coefficient correlation (r^2) is > 0.970.

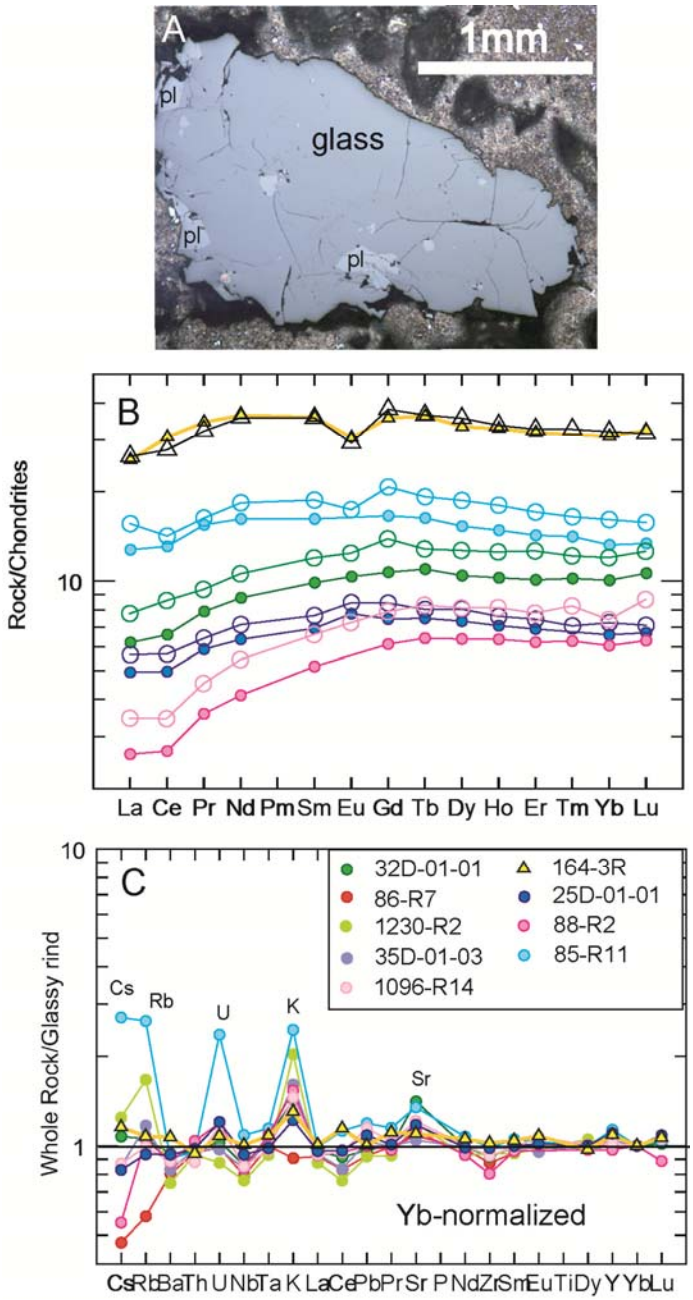

Figure 3A.2. A) Photomicrograph of a glass chip taken under polarized light (sample 36D-01-10). The glass is polished and pushed into Indium (grey material surrounding the glass). The glass contains phenocrysts (in white), such as plagioclase (pl). B) REE patterns of glassy rinds (empty circles) compared with the corresponding whole rock (filled circles) for SEMFR lavas normalized to chondrite abundances (Sun and McDonough, 1989). The REE patterns of the glassy rind - whole rock pairs have the same color, except for sample 164-3R (triangles). MGR glass (sample 164-3R) analyzed by LA-ICP-MS (yellow triangle) and ICP-MS (black triangles) have REE patterns that agree within ≤ 7% rsd. C) Comparison of trace element patterns of the

whole rock with those of the corresponding glassy rind. Spider diagrams are normalized to Yb to remove the effect of crystal fractionation. Agreement between the MGR glass (sample164-3R) analyzed by ICP-MS and LA-ICP-MS is ≤ 8% rsd. Sequence of elements is adopted from (Salters and Stracke, 2004).

Glassy rinds of pillow basalts were also analyzed whenever possible. Fresh, brown and translucent glass chips from the pillow rinds were hand-picked and carefully examined under microscope in polarized and crossed-polarized light to ensure that clean, crystal-free glass was available for analysis. Glass chips were then polished on a single side (with 40 μm, 30 μm, 15 μm and 9 μm aluminum oxide polishing sheets), mounted and polished on Indium (with 6 μm and 3 μm diamond polishing paste, and 1 μm and 0.3 μm alumina polishing paste) prior to analyses (Figure 3A.2A). Glassy rinds were analyzed with the Superprobe JEOL JXA-8200 at MIT for major elements, using a 10 μm defocused beam to minimize alkali loss, a 15 kV accelerating voltage and a 10 nA beam current. The glass standard ALV-1690-20 (Grove *et al.*, 1992) was calibrated daily to monitor precision and accuracy of the unknowns. Repeated analyses of the standard gave a mean CaO = 10.85 wt%, Al_2O_3 = 15.51 wt%, K_2O = 0.15 wt%, MnO = 0.19 wt%, Na_2O = 3.13 wt%, TiO_2 = 1.71wt%, SiO_2 = 49.90 wt%, P_2O_5 = 0.18 wt%, FeO = 9.91 wt%, MgO = 7.68 wt% with a precision < 0.3 %; and mean of repeated analyses of the unknowns has 1 $\sigma \leq 0.5\%$. Trace element analyses were carried out at URI with the UP-213 Laser Ablation System coupled to a Thermo X-series II quadrupole ICP-MS (LA-ICP-MS). Glass chips were ablated using a 10 Hz repeat rate, 60% pulse beam energy and 80 μm spot size (Kelley et al., 2003). Data were background-subtracted, and normalized to ^{43}Ca as internal standard. Concentrations were calculated from calibration curves based on 8 standards (BHVO, BCR, BIR, GOR 132, StHIs, T1, ML-3B, KL2), analyzed under the same conditions as the

unknowns. Calibration curves yield $r^2 \geq 0.999$, but for Li, Be, Y, Lu and Tm ($r^2 \geq 0.996$). Reproducibility of replicate analyses are ≤ 3% rsd for Sr, Nb, Rb, Ba, K2O, ≤ 5% rsd for Y, Li, U, and ≤ 11% rsd for Th and Ni. Some glass chips were also dissolved and analyzed by ICP-MS (i.e. sample 164-3R). Agreement between the LA-ICP-MS and the ICP-MS is ≤ 8% rsd, and agreement between the REE patterns is excellent (≤7% rsd). Trace element and REE patterns of the glassy rinds reproduce those of the whole rock, and differences are related to crystal fractionation and alteration in the whole rock (Figure 3A.2). Major elements analyzed by electron microprobe and by LA-ICP-MS compare well (Figure 3A.3).

Isotopic ratios of Sr, Nd and Pb were determined using a Finnigan MAT 261 multicollector Thermal Ionization Mass Spectrometer (TIMS) at UTD. Sr, Nd and Pb standards were analyzed every 5 samples to check the mass-spectrometer conditions. Repeated analyses (n= 15) of $^{87}Sr/^{86}Sr$ standard (SRM-987) show a mean of 0.71024 ± 3. HDEHP columns were used to separate Nd isotopes. $^{143}Nd/^{144}Nd$ isotopic composition was determined by using dynamic collection mode. Repeated measurement (n = 13) for La Jolla standard yield ($^{143}Nd/^{144}Nd$ = 0.51185 ± 1) for Nd mass calibration. Reproducibility of $^{143}Nd/^{144}Nd$ is better than ± 0.00005. Calculations of εNd use the CHUR value ($^{143}Nd/^{144}Nd = 0.512634$) [Salters and Stracke, 2004]. Pb was separated using the technique of (Manton, 1988); and Pb isotope ratios were measured using the TIMS in static mode. Repeated analyses (n = 11) of the standard NBS-981 gave $^{206}Pb/^{204}Pb = 16.895 \pm 0.01$, $^{207}Pb/^{204}Pb = 15.435 \pm 0.02$, $^{208}Pb/^{204}Pb = 36.515 \pm 0.04$ and were corrected for fractionation (coefficient = 1.48) to the values of (Todt *et al.*, 1996).

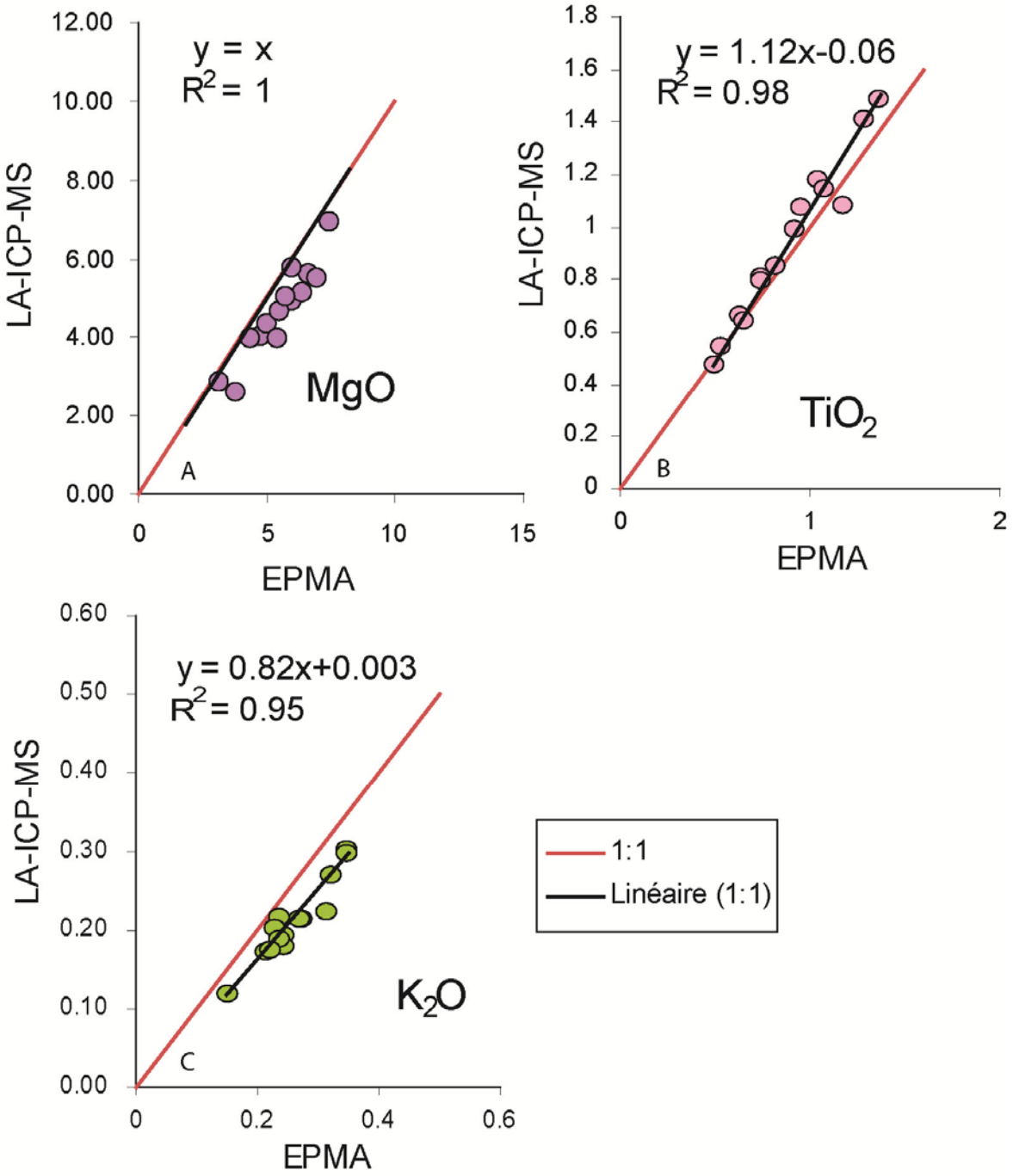

Figure 3A.3. Comparison of major element abundances of the glass analyzed with electron microprobe (EPMA) and LA-ICP-MS for A) MgO, B) TiO_2, C) K_2O. The black line denotes 1:1 line; and the red line is the linear regression for the analyzed samples, for which the equation and correlation coefficient squared are shown. The two datasets compare well.

Table 3A.1. Major, trace element and isotopic compositions of SEMFR, MGR and Toto lavas.

cruise #	YK-10-12	YK-10-12	YK-10-12	YK-10-12	TN273	TN273	TN273	TN273	TN273	TN273	TN273	TN273
Location	SE	SE	NW	NW	SE	SE	SE	NW	NW	NW	NW	NW
	SEMFR	SEMFR	SEMFR	SEMFR	SEMFR	SEMFR	SEMFR	SEMFR	SEMFR	SEMFR	SEMFR	SEMFR
Sample #	YKDT86-R20	YKDT86-R21	YKDT88-R1	YKDT88-R2	17D-01-01	19D-01-01	19D-01-02	20D-01-01	22D-01-01	25D-01-01	25D-01-03	29D-01-06
IGSN	*JMR00002Z	*JMR000030	*JMR000032	*JMR000033	JMR000001	JMR000002	JMR000003	JMR000004	JMR000005	JMR000006	JMR000007	JMR000008
wt%												
SiO2					53.05	54.69	55.35	55.40	52.88	49.78	57.12	52.77
TiO2					0.97	0.84	0.85	0.92	0.61	0.45	1.01	0.64
Al2O3					17.38	15.32	15.85	15.34	15.99	16.55	15.87	16.52
FeO*					8.03	10.44	10.38	10.75	9.45	7.98	9.75	8.50
MnO					0.13	0.18	0.18	0.20	0.18	0.15	0.18	0.17
MgO					5.33	4.58	4.46	4.40	6.19	8.62	3.14	6.78
CaO					10.16	8.98	8.96	8.77	11.38	14.28	7.49	11.95
Na2O					3.58	2.60	2.52	2.94	1.99	1.53	3.04	2.14
K2O					0.45	0.63	0.74	0.29	0.35	0.21	0.94	0.34
P2O5					0.13	0.08	0.08	0.09	0.04	0.03	0.12	0.06
Total					99.19	98.34	99.39	99.10	99.07	99.58	98.66	99.88
Mg#					54.22	43.91	43.40	42.23	53.92	65.86	36.53	58.74
LOI					0.00	0.01	0.01	0.00	-0.02	0.00	0.02	0.01
ppm												
V	223.19	254.16	197.28	197.67	225.44	300.70		334.46	266.06	213.37	285.41	234.77
Cr	74.56	6.95	326.76	352.80	36.20	14.45		2.29	27.94	129.76	0.55	40.14
Ni	42.04	19.27	77.62	74.17	29.35	13.51		22.54	24.09	52.34	6.60	31.35
Rb	7.46	8.17	1.87	2.02	25.59	9.48		4.54	4.92	3.27	11.61	4.85
Sr	224.74	257.81	92.41	91.33	297.28	149.90		155.23	136.74	152.10	158.83	148.75
Y	21.18	25.35	8.73	9.42	21.96	23.91		26.07	15.98	10.76	28.92	17.04
Zr	74.36	98.13	13.53	14.56	87.01	57.53		66.19	32.06	23.01	77.25	45.09
Nb	1.81	2.77	0.40	0.38	2.69	1.35		1.55	0.52	0.60	1.73	0.94
Cs	0.16	0.13	0.06	0.06	1.08	0.22		0.20	0.11	0.08		
Ba	40.17	73.38	12.91	14.03	87.61	58.06		56.83	33.33	28.89	74.56	39.89
La	3.12	4.80	0.58	0.62	4.58	2.42		3.30	1.44	1.17	3.32	1.98
Ce	8.54	12.44	1.60	1.64	12.05	6.56		8.97	3.77	3.04	8.92	5.26
Pr	1.48	2.04	0.33	0.34	1.89	1.16		1.44	0.70	0.56	1.58	0.93

Table 3A.1.continued. Example of major, trace element and Pb-Nd-Sr isotopic compositions of SEMFR lavas. Samples with IGSN numbers with a * have their major element data reported in (Ribeiro et al., in press). Mg# = (Mg^{2+} x 100) / (Mg^{2+} + Fe^{2+}). All the iron is considered as Fe^{2+}. The complete table is provided as a joined excel file.

Sample #	YKDT86-R20	YKDT86-R21	YKDT88-R1	YKDT88-R2	17D-01-01	19D-01-01	19D-01-02	20D-01-01	22D-01-01	25D-01-01	25D-01-03	29D-01-06
Nd	7.34	9.97	1.92	1.93	9.05	6.29		7.50	3.87	2.97	8.14	4.82
Sm	2.29	2.97	0.78	0.79	2.63	2.23		2.55	1.42	1.06	2.76	1.65
Eu	0.88	1.11			0.98	0.82		0.94	0.57	0.45	1.01	0.64
Gd	3.04	3.72	1.25	1.26	3.36	3.27		3.60	2.17	1.53	3.88	2.34
Tb	0.55	0.67	0.24	0.24	0.58	0.58		0.64	0.39	0.28	0.71	0.43
Dy	3.49	4.17	1.62	1.62	3.67	3.92		4.25	2.64	1.86	4.64	2.81
Ho	0.76	0.90	0.36	0.36	0.79	0.86		0.94	0.59	0.40	1.02	0.62
Er	2.13	2.55	1.03	1.03	2.22	2.44		2.64	1.67	1.14	2.94	1.76
Tm	0.32		0.16	0.16	0.32	0.38		0.41	0.26			
Yb	2.05	2.48	1.03	1.03	2.18	2.51		2.70	1.73	1.12	2.95	1.75
Lu	0.31	0.39	0.16	0.16	0.34	0.39		0.42	0.27	0.17	0.46	0.27
Hf	1.78	2.29	0.52	0.50	2.02	1.63		1.84	0.98	0.69	2.14	1.20
Ta	0.13	0.19		0.03	0.17	0.09		0.09	0.04	0.04	0.11	0.06
Pb	0.67	1.13	0.46	0.35	1.84	0.93		1.28	0.63	0.67	1.44	0.82
Th	0.21	0.36	0.04	0.04	0.43	0.22		0.31	0.13	0.10	0.36	0.21
U	0.14	0.24	0.03	0.03	0.18	0.15		0.15	0.11	0.07	0.21	0.13
143Nd/144Nd	0.51298											
2 sigmas	0.00002											
εNd	6.75											
87Sr/86Sr	0.70304		0.70331	0.70331								
2 sigmas	0.00003		0.00004	0.00005								
206/204Pb	18.58			18.95								
2 sigmas	0.00			0.00								
207/204Pb	15.54			15.56								
2 sigmas	0.00			0.00								
208/204Pb	38.21			38.46								
2 sigmas	0.01			0.01								
208/206Pb	2.06			2.03								

Table 3A.2. Example of major and trace element contents of the SEMFR and MGR glassy rinds. Mg# = (Mg^{2+} x 100) / (Mg^{2+} + Fe^{2+}). All the iron is considered as Fe^{2+}. The complete table is provided as a joined excel file.

Location	SE	SE	NW	NW	NW	NW	NW	SE	SE
sample	SEMFR 6K-1096-R14	SEMFR 6K-1230-R2	SEMFR TN273-22D-01-01	SEMFR TN273-25D-01-01	SEMFR TN273-29D-01-06	SEMFR TN273-30D-02-08	SEMFR TN273-32D-01-01	SEMFR TN273-35D-01-03	SEMFR TN273-36D-01-10
material	glass	glass	glass	glass	glass	glass	glass	glass	glass
ISGN	JMR00003D	JMR00003E	JMR00003I	JMR00003J	JMR00003K	JMR00003L	JMR00003M	JMR00003N	JMR00003O
wt%									
SiO2	51.04	52.32	52.79	49.50	52.03	52.85	53.84	51.91	52.38
TiO2	0.83	1.05	0.66	0.53	0.75	0.64	0.74	0.95	1.37
Al2O3	15.75	15.43	15.01	15.69	15.18	15.33	15.45	15.77	15.52
FeO	7.95	9.13	9.96	8.83	9.10	9.36	9.22	8.69	9.31
MnO	0.13	0.15	0.16	0.18	0.17	0.19	0.20	0.14	0.18
MgO	6.38	5.03	5.47	7.46	6.03	5.99	4.80	5.52	4.35
CaO	11.12	9.30	9.93	12.69	10.54	10.42	9.07	9.99	8.52
Na2O	2.66	3.27	1.95	1.58	2.13	1.90	2.43	3.23	4.04
K2O	0.27	0.24	0.24	0.24	0.27	0.24	0.35	0.23	0.35
P2O5	0.11	0.08	0.09	0.04	0.11	0.03	0.04	0.10	0.16
Total	96.22	95.98	96.25	96.72	96.29	96.94	96.12	96.52	96.17
ppm									
Rb	4.07	4.37	3.89	3.85	4.27	4.32	7.35	3.98	4.52
Sr	194.31	167.05	129.61	142.44	139.45	112.63	148.28	172.59	200.96
Y	18.84	21.23	17.07	10.78	16.11	16.13	19.29	20.52	26.66
Zr	62.49	69.62	36.14	25.81	45.39	35.35	45.42	67.02	109.75
Nb	1.53	1.46	0.55	0.71	1.14	0.59	0.64	1.48	2.86
Cs	0.11	0.12	0.11	0.11	0.12	0.14	0.18	0.10	0.10
Ba	59.92	49.83	33.38	34.13	47.80	36.69	61.85	46.17	58.95
La	2.93	2.89	1.55	1.34	2.35	1.29	1.84	2.89	4.71
Ce	7.50	9.24	3.81	3.48	6.24	3.65	5.26	8.80	12.36
Pr	1.19	1.43	0.68	0.61	1.03	0.65	0.89	1.39	2.09
Nd	6.21	7.49	3.90	3.33	5.44	3.71	4.94	7.19	11.02
Sm	2.05	2.47	1.46	1.17	1.77	1.40	1.83	2.39	3.33
Eu	0.76	0.93	0.53	0.49	0.67	0.54	0.72	0.90	1.18
Tb	0.49	0.59	0.42	0.30	0.45	0.40	0.48	0.55	0.77
Gd	2.95	3.30	2.35	1.73	2.54	2.19	2.85	3.22	4.53
Dy	3.18	3.61	2.74	2.04	2.99	2.66	3.22	3.59	5.01
Yb	1.90	2.23	1.76	1.23	1.93	1.68	2.04	2.10	2.94
Lu	0.28	0.32	0.27	0.18	0.27	0.27	0.32	0.31	0.42
Hf	1.52	1.69	1.09	0.76	1.28	1.01	1.29	1.61	2.62
Ta	0.10	0.09	0.04	0.04	0.06	0.04	0.04	0.08	0.18
	0.83	0.87	0.57	0.68	0.98	0.69	1.09	0.79	1.17

APPENDIX 3B

ALTERATION FILTERS

It is important to understand seafloor alteration of basalt because this may affect aspects of rock chemical and isotopic composition. The effects of seafloor alteration can vary tremendously, depending on the nature of original rock, the primary mineral phases (which define the starting composition), texture, fracturing, the processes of alteration _including fluid circulation and microbial action_ and the type of secondary phases, which scavenge elements from seawater and the original rock during their formation. Most studies about seafloor alteration were performed on MORBs (Hart, 1969, Hart *et al.*, 1974, Jochum and Verma, 1996, Staudigel and Hart, 1983), partly because of the importance of characterizing the composition of subduction inputs, such as the altered oceanic crust (Kelley et al., 2003, Plank and Langmuir, 1998). MORB seafloor weathering is a useful model for alteration of SEMFR basalts. Alkali metals (K, Rb, Cs), alkaline earths (Sr, Ba), and easily-complexed trace elements (such as U) are the most affected by alteration (Hart, 1969, Hart et al., 1974, Staudigel and Hart, 1983); whereas Ti, Al, REE, Y and other high field strength elements (HFSE such as Nb, Ta, Zr, Hf) are generally unaffected (Jochum and Verma, 1996). This section addresses the likely effects of SEMFR alteration because i) SEMFR lavas have interacted with seawater for ~ 2.7 – 3.7 Ma; and ii) the purpose of this manuscript is to characterize the composition of the ultra-shallow subduction component by examining the fluid-mobile elements (FME: K, Sr, Rb, Cs, U, Ba), that are also most susceptible to seafloor alteration (Hart, 1969, Hart et al., 1974, Jochum and Verma, 1996, Staudigel and

Hart, 1983). We are particularly interested in very low-temperature alteration (T < 40°C), also known as "seafloor weathering" (Brady and Gíslason, 1997). Understanding how such alteration can alter the chemical composition of SEMFR lavas will help us to discriminate the subduction input into SEMFR magma from element redistribution accompanying post-eruption seafloor weathering of SEMFR lavas.

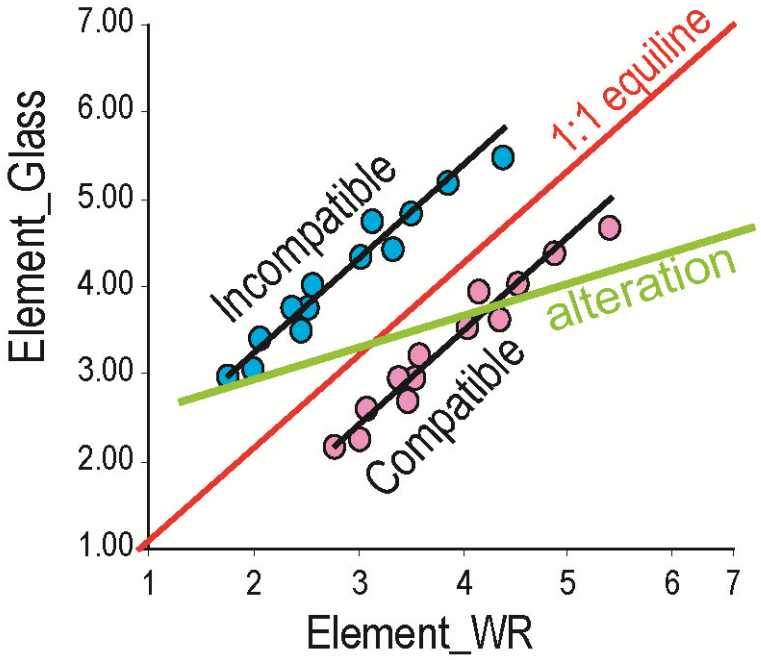

Figure 3B.1. Sketch illustrating the behavior of incompatible and compatible elements during fractionation and alteration. The red line (1:1 equiline) shows where data should plot if abundances of an element are the same in glass and WR. Black lines mark a linear regression for the sample set. WR analyses include phenocrysts and groundmass (melt) whereas glass analyses exclude phenocrysts. Consequently, glass is enriched in incompatible elements so that incompatible element pairs (blue circles) plot on the left side of the equiline. In contrast, the WR is enriched in compatible elements, as they are concentrated in crystals, so that these element (pink circle) plot on the right side of the equiline. In contrast, alteration can reduce or increase the abundances of elements in the WR, so that elements are scattered on both side of the equiline (thick green line).

In order to resolve chemical evidence of weathering, glassy rinds and associated whole rock (WR; interior) pairs were analyzed for major and trace element abundances (see Analytical

Techniques section in Appendix 3A) and these results were compared graphically (Figure 3B.1-3B.3). We build on the knowledge that whole-rock – glass pairs respond differently to seafloor weathering. Specifically, vitreous glass, which represents the quenched melt, best preserves the magmatic signal; whereas alteration cannot be avoided in bulk samples. Fresh and translucent brown glass chips were hand-picked to select the freshest pieces, and carefully examined under a binocular microscope to ensure that crystal-free regions were available for analysis. Because phenocrysts cannot be avoided during bulk rock analysis, while glass analyses exclude phenocrysts, glassy rims are systematically enriched in incompatible elements and depleted in compatible elements, which are concentrated in phenocrysts during fractionation. Due to these different elemental behaviors in glass and WR analyses, incompatible elements will plot to the left of the 1:1 line; and compatible elements will plot to the right of the equiline, generally defining a strongly correlated (r^2>0.7) linear trend (Figure 3B.1). In contrast, significant alteration will redistribute labile elements in the WR so that elements will scatter on either side of the 1:1 equiline (Figure 3B.1). FeO, TiO_2 and Na_2O are incompatible elements enriched into the melt that plot on the left side of the equiline (Figure 3B.2 C-E); and MgO and Al_2O_3 are compatible elements enriched into the WR that plot on the right side of the 1:1 line (Figure 3B.2 A-B). These show that major element contents of SEMFR basalts are mostly affected by magmatic fractionation; only K_2O, an incompatible element, scatters on both sides of the equiline (Figure 3B.1 F) indicating that the distribution of this element in the WR was affected by alteration.

Some trace elements, and especially the fluid-mobile elements of special interest here, are vulnerable to alteration. These abundances need to be carefully scrutinized to discriminate the magmatic subduction-related signal from the effects of alteration. Following the example shown by the major elements, Figure 3B.3 shows the behavior of 8 selected incompatible trace elements: Rb, Sr, Cs, Ba, Nb, U, Th, and Pb. If abundances of these incompatible elements in WR-glass pairs are only controlled by fractionation, they should plot left of the equiline. This is seen for Ba, Th, and Nb (Figure 3B.3 C, F, G); and we conclude these elements are unaffected by alteration. Sr plots to the right of the 1:1 line, because it is fractionated in plagioclase phenocrysts, suggesting that it is also unaffected by alteration. In contrast, WR-glass pairs of Cs, Rb, U, Sr and Pb scatter on either side of the equiline, showing that the distribution of these elements in the WR was affected by alteration (Figure 3B.3 A-B, D-E, H).

These diagrams show that alteration has affected the WR abundances of K, Rb, Cs, U, and Pb in spite of the fact the freshest part of the bulk samples were hand-picked. This demonstrates that i) alteration cannot be avoided during the preparation of the bulk samples, and ii) alteration is not always visible with a binocular microscope (we call this “cryptic alteration”). Alteration mostly affects the K, U, Cs, Rb, and Pb content in SEMFR lavas. Because those elements are of interest in that manuscript, we propose to use a petrographic alteration filter to select the freshest SEMFR WR: samples with petrographic alteration $\leq 1\%$ are selected. 34 samples over 87 passed through the filters and will be further examined carefully. The other samples have their content in Rb, Cs, Pb, U and K_2O reported but ignored.

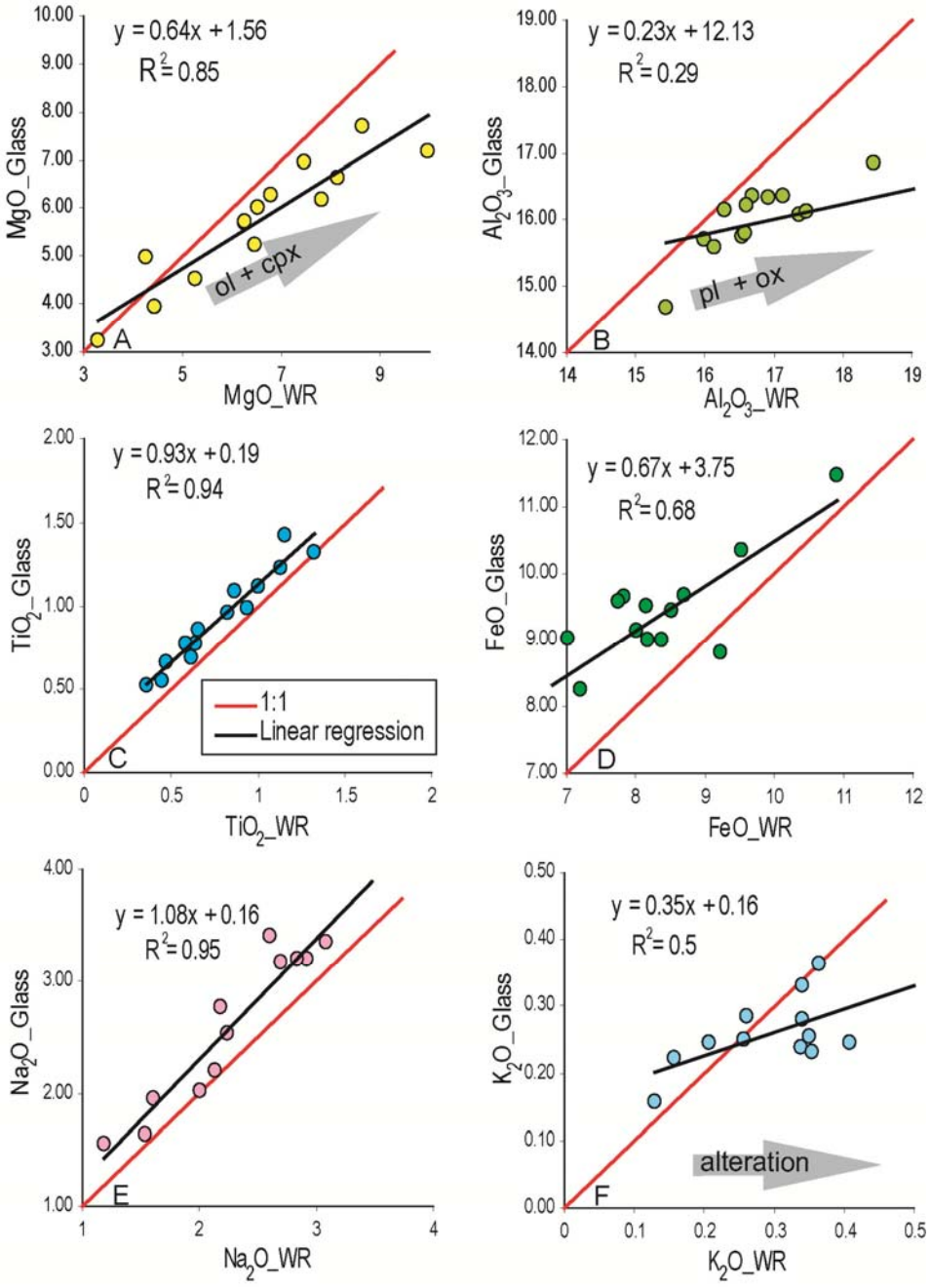

Figure 3B.2. Comparison of abundances in A) MgO, b) Al_2O_3, C) TiO_2, D) FeO*, E) Na_2O and F) K_2O for co-existing whole rocks and glassy rinds. Thick black line denotes 1:1 correlation; thinner red line is a linear regression for the sample set (equation and r^2 given in upper left). Trends mostly reflect fractionation of clinopyroxene (cpx), plagioclase (pl), and olivine (ol), enriching the glass in incompatible elements (FeO, Na_2O, TiO_2), and depleting the glass in compatible elements (MgO, Al_2O_3) in comparison to the whole rock. Behavior of K_2O, an incompatible element, reflects the effect of alteration in WR.

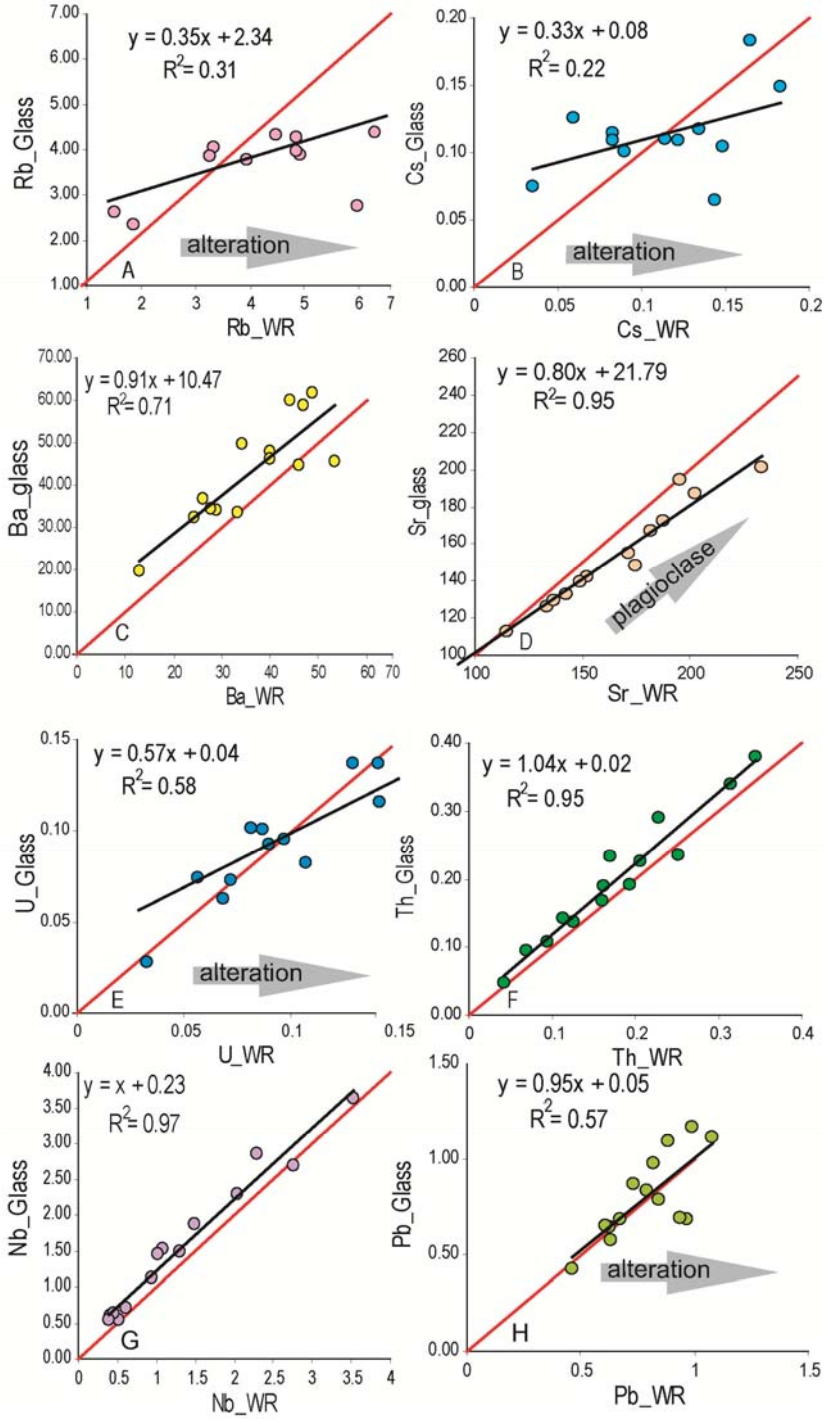

Figure 3B.3. Comparison of selected trace element contents in A) Rb, B) Cs, C) Ba, D) Sr, E) U, F) Th, G) Nb, H) Pb for the whole rock (WR) and the glassy rinds of SEMFR lavas. The red line denotes 1:1 line and the black line is a linear regression for the sample set, for which equation and correlation coefficients are reported on the graph.

APPENDIX 3C

PETROGRAPHY OF SEMFR LAVAS

Table 3C.1 summarizes the latitude, longitude and water depths of the dredging and diving sites performed along SEMFR, the Malaguana-Gadao Ridge (MGR) and Toto caldera. Below, we present a short methodology about rock description used to construct table 3C.2, where a detailed petrography of the SEMFR samples recovered during the TN273 Thomas Thompson cruise is reported. A more detailed methodology is given in (Ribeiro et al., in press). Name of the volcanic and plutonic rocks is based on their mineral abundances. Samples collected during this cruise are mostly pillow basalts and lava flows, with one diabase (sample 17D-01-01). Pillow lavas are identified as dark, basaltic rocks with a curved glassy rind. Whenever the glassy rind was absent, the lava was reported as lava flow.

To a first order, rocks are classified according to:

- Their degree of crystallinity as holohyaline (100% glass), hypocrystalline (glass and minerals) and holocrystalline (100% minerals). Diabase are holocrystalline and lavas are hypocrystalline;
- Their degree of alteration as fresh (<2% alteration minerals), slightly altered (2 – 5 %), moderately altered (5 – 20%), highly altered (> 20%);

- their grain size as coarse grained (cg: 5 – 30 mm), medium grained (mg: 1 – 5 mm), fine grained (fg: 0.5 – 1 mm), microcrystalline (mx: 0.1 – 0.5 mm), cryptocrystalline (cx < 0.1 mm);
- Their vesicle proportions as: not vesicular (< 1% vesicles), sparsely vesicular (1 – 5%), moderately vesicular (5 – 20% vesicles) and highly vesicular (> 20% vesicles). In the table 3C.2, we reported as vesicular samples with ≥ 5% vesicles.
- Their magmatic texture as: diabasic for hypocrystalline, fine-grained to medium-grained rocks sparsely to highly vesicular with mineral abundances ≥ 50%; porphyric (phenocrysts ≥ 1mm) or microporphyric (microphenocrysts range from 0.1 – 1 mm) for hypocrystalline rocks with crystals surrounded by a glassy groundmass and microlites (< 0.1 mm; (Lofgren, 1974)).

To a second order, the texture of the rock was described according to:

- Occurrence of enclosing crystal as ophitic: olivine or pyroxene partially enclosing plagioclase; subophitic: plagioclase partially encloses olivine or pyroxene; and poikilitic: larger crystals totally enclose smaller crystals.
- Their magmatic flow texture as trachytic when plagioclase laths are subparallel, subtrachytic texture is a poorly-defined subparallel arrangement of plagioclase, and felty when the crystals have random orientation.
- The texture of their groundmass for the lavas, as spherulitic: glass with microlites forming spheroidal bodies; and the texture of the phenocrysts : skeletal (crystal showing a high proportion of voids filled with glass or groundmass), dendritic (needle-like crystals),

embayed (holes in crystals filled with glass or groundmass), glomerocryts (clusters of phenocrysts), and diktytaxitic (vesicles in which phenocrysts protrude).

- Segregation vesicles: dark, glassy and microcrystalline to cryptocrystalline groundmass with spherulitic microlites of plagioclase surrounding large vesicles (Smith, 1969).

Table 3C.1. Locations of dives and dredges in Southeast Mariana Forearc Rift, Toto caldera and MGR

Location	Cruise	Dredge / Dive number	Latiitude start of dive	Longitude start of dive	Latiitude end of dive	Longittude end of dive	depth (m) max.	depth (m) min.	Samples collected
SEMFR	YK08-08 Leg 2	Shinkai dive 1096	12°06.2769	143°51.1773	12°06.7278	143°51.8844	6077	5414	pillow lavas / lava flow
SEMFR	YK10-12	Shinkai dive 1230	12°11.3557	143°54.1910	12°11.9046	143°54.6005	4958	4280	pillow lavas / lava flow
SEMFR	YK10-12	Shinkai dive 1235	12°04.2220	144°00.7300	12°04.9072	144°01.1973	6478	5861	lavas & gabbros
SEMFR	YK10-12	YKDT 85	12°23.0000	144°03.0000	12°23.2061	144°03.8340	3090	2577	pillow lavas / lava flow
SEMFR	YK10-12	YKDT 86	12°16.5000	143°59.7000	12°16.6400	144°00.3853	4050	3454	pillow lavas / lava flow
SEMFR	YK10-12	YKDT 88	12°24.2000	143°45.7000	12°24.4536	143°45.9875	3475	3342	pillow lavas / lava flow
SEMFR	TN 273	TN273_17D	12° 09.4211	12° 09.5438	143°48.7162	143°48.8485	5772	5469	diabase
SEMFR	TN 273	TN273_19D	12° 15.4403	12° 15.5162	143° 48.8430	143° 48.7527	4430	4320	pillow lavas / lava flow
SEMFR	TN 273	TN273_20D	12° 19.5058	12° 19.6205	143° 42.3378	143° 42.3689	4131	3959.8	pillow lavas / lava flow
SEMFR	TN 273	TN273_22D	12° 21.7844	12° 21.8858	143° 40.8060	143° 40.9460	3890	3814	pillow lavas / lava flow
SEMFR	TN 273	TN273_25D	12° 26.4083	12° 26.4646	143° 39.3875	143° 39.5992	3495	3437	pillow lavas / lava flow
SEMFR	TN 273	TN273_29D	12° 28.8516	12° 29.0631	143° 42.9691	143° 43.2318	3181	3107	pillow lavas / lava flow
SEMFR	TN 273	TN273_30D	12° 27.6004	12° 27.9534	143° 48.1964	143° 48.3671	3954	3822	pillow lavas / lava flow
SEMFR	TN 273	TN273_31D	12° 23.3280	12° 23.4785	143° 47.0256	143° 47.1621	3524	3434	pillow lavas / lava flow
SEMFR	TN 273	TN273_32D	12° 20.3500	12° 20.5830	143° 43.1034	143° 43.4078	3451	3374	pillow lavas / lava flow
SEMFR	TN 273	TN273_33D	12° 15.3944	12° 15.2629	143° 46.4338	143° 46.6545	3778	3478	pillow lavas / lava flow
SEMFR	TN 273	TN273_34D	12° 17.8033	12° 17.8632	143° 51.4157	143° 51.7196	3945	3766	pillow lavas / lava flow
SEMFR	TN 273	TN273_35D	12° 12.5949	12° 12.8944	143° 54.7966	143° 54.8498	4046	3978	pillow lavas / lava flow
SEMFR	TN 273	TN273_36D	12°08.60114	12° 08.8797	143° 55.6055	143° 55.8981	4545	4472	pillow lavas / lava flow
SEMFR	TN 273	TN273_37D	12° 10.0024	12° 10.0037	144° 00.517	144° 00.9996	4570	4256	peridotite & gabbro
SEMFR	TN 273	TN273_40D	12° 36.7570	12° 37.063	143° 50.5480	143° 50.8090	3983	3735	peridotite & gabbro
MGR	KR00-03 Leg 2	Kaiko dive 164	13°06.1800	143°41.5500	13°06.2700	143°41.4500	2920	2908	basaltic pillow lavas
Toto caldera	KR00-03 Leg 2	Kaiko dive 163	12°42.9154	143°32.1192	12°42.8032	143°32.3786	3044	3006	basalts

Table 3C.2. Example of petrographic description for some of the SEMFR lavas and diabase. The complete table is provided as a joined excel file. Ol: olivine; cpx: clinopyroxene; pl: plagioclase, cx : crysptocrystalline, mx: microcrystalline.

REGION	SAMPLE	LITHOLOGY	TERMINOLOGY	texture	Vesicles (%)	cpx (%)	olivine (%)	plagioclase (%)	Oxides (%)	Phenocrysts (%)	Vesicles (mm)	Cpx (mm)	Ol (mm)
SE SEMFR	17D-01-01	Diabase	ol-cpx diabase	holocrystalline	5%	10%	<1	80%	5.00%	**95%**	≤0.5	≤0.25	≤0.5
SE SEMFR	35D-01-03	pillow lava	ol-cpx basaltic andesite	microporph. / nearly diabasic	30%	10%	≤ 1%	30%		**40%**	3 - 0.25	0.25 - 0.5	0.1 - 0.25
SE SEMFR	36D-01-10	pillow lava	ol-cpx basaltic andesite	microporph.	15%	10%	≤1	15%	1-5%	**25%**	2-0.1	0.25-1	0.1-0.25
SE SEMFR	36D-02-01	lava flow	enclave: pl basaltic andesite	microporph.	20%			10%		**10%**	0.25-0.1		
SE SEMFR	36D-02-02	lava flow	host: ol-cpx basaltic andesite	diabasic	5%	10%	<1	40%	1-5%	**50%**	0.1-1	0.5-0.1	0.1
SE SEMFR	36D-03-01	lava flow	ol-cpx basaltic andesite	diabasic	25%	5%	<1	50%		**55%**	0.25-1	0.25-0.5	0.1
SE SEMFR	36D-04-01	lava flow	altered basaltic andesite	microporph.				15%	5.00%	**20%**			
SE SEMFR	19D-01-01	lava flow	cpx - pl basaltic andesite	porph.	20%	5%		10%	<1	**15%**	3-0.1	2-0.1	
SE SEMFR	33D-01-12	pillow lava	ol-cpx basaltic andesite	microporph.	20%	5%	<1	20%	<1	**25%**	2-0.1	0.25-0.1	<0.1
SE SEMFR	33D-01-25	lava flow	cpx - pl basaltic andesite	microporph.	10.0%	5%		20%	5.00%	**30%**	3 - 0.25	0.1	
SE SEMFR	33D-02-02	lava flow	ol-cpx basaltic andesite	diabasic	15 - 20%	10%	≤1	50%		**60%**	0.1 - 0.5	0.1 - 0.5	0.1
SE SEMFR	34D-01-01	lava flow	host: ol-cpx basaltic andesite	diabasic	5%	20%		50%	5.00%	**75%**	0.25 - 0.5	0.1 - 1	
SE SEMFR	34D-01-01	enclave	enclave: pl basaltic andesite	microporph.	5%			15%	5.00%	**20%**	1.5- 0.1		
SE SEMFR	34D-01-06	lava flow	ol-cpx basaltic andesite	microporph.	20%	10%	<1	15%		**25%**	0.25 - 2	0.25 - 0.5	0.1 - 0.2
NW SEMFR	20D-01-01	lava flow	cpx - pl basaltic andesite	microporph.	20%	1%		20%		**21%**	4.5-0.1	0.75-0.1	
NW SEMFR	31D-01-01	lava flow	cpx - pl basaltic andesite	microporph.	20%	5%		5%	<1	**10%**	1-0.1	0.5-0.1	
NW SEMFR	32D-01-01	lava flow	pl basaltic andesite	porph	20%	<1	<1	10%	<1	**10%**	0.5-0.1	0.5-1	0.5-0.1
NW SEMFR	22D-01-01	pillow lava	ol-cpx basaltic andesite	microporph.	20%	10%	<1	20%		**30%**	1.5-0.1	0.1-0.5	≤0.2
NW SEMFR	25D-01-01	pillow lava	ol-cpx basalt	diabasic	20%	20%	<1	30%	<1	**50%**	2-0.1	0.5-0.1	≤0.25

Table 3C.2. continued. Petrographic description of the SEMFR lavas and diabase.

REGION	SAMPLE	PI (mm)	Oxides (mm)	vesicular (≥ 5% vesicles)	Hypocrystalline	Holocrystalline	Mx	Diabasic	microporphyric (M) / porphyric (P)	Cx	Variolitc	Ophitic	Subophitic
SE SEMFR	17D-01-01	≤1	≤0.1			X		X				X	X
SE SEMFR	35D-01-03	0.5 - 1		X	X			GR	M		GR	X	X
SE SEMFR	36D-01-10	1-0.25	<0.1	X	X			GR	M			X	X
SE SEMFR	36D-02-01	0.75-0.1		X	X				M		X		
SE SEMFR	36D-02-02	0.1-1	<0.1	X	X			X				X	X
SE SEMFR	36D-03-01	0.25-0.5		X	X		X	X				X	X
SE SEMFR	36D-04-01	<0.1	<0.1		X				M	X			
SE SEMFR	19D-01-01	1-0.1	<0.1	X	X				P			X	
SE SEMFR	33D-01-12	0.5-0.1	<0.1	X	X		X		M			X	X
SE SEMFR	33D-01-25	0.25	≤0.1	X	X				M		X	X	
SE SEMFR	33D-02-02	≤ 0.5		X	X		X	X					
SE SEMFR	34D-01-01	0.25- 1	< 0.1	X	X			X				X	X
SE SEMFR	34D-01-01	0.1 - 0.2		X	X		X		M		X		X
SE SEMFR	34D-01-06	0.25 - 1		X	X				M		GR	X	
NW SEMFR	20D-01-01	1-0.1		X	X				M		X		X
NW SEMFR	31D-01-01	1-0.25	<0.1	X	X				M				X
NW SEMFR	32D-01-01	2.5-0.5	≤0.1	X	X				P				X
NW SEMFR	22D-01-01	1-0.1		X	X				M		GR	X	X
NW SEMFR	25D-01-01	1-0.1	<0.1	X	X			X			X	X	X

CHAPTER 4

COMPOSITION OF THE SHALLOW AQUEOUS FLUIDS RELEASED BENEATH FOREARCS: INSIGHTS FROM OLIVINE-HOSTED MELT INCLUSIONS FROM THE SE MARIANA FOREARC RIFT

4.1 ABSTRACT

Shallow aqueous slab-derived fluids released beneath forearcs are important features at subduction zones; however, investigating their composition is challenging as the cold forearc mantle does not melt. Experiments and analyses of arc glass suggest that these shallow fluids are hydrous. Basaltic lavas of the Southeast Mariana forearc rift (SEMFR) provide an unusual opportunity to examine melts that were generated in association with fluids released above a shallow subduction zone. SEMFR extends from arc volcanoes nearly to the Mariana trench and was generated by forearc seafloor spreading ~2.7–3.7 Ma ago. SEMFR olivine-hosted melt inclusions (Ol-MI) are primitive basalts and are the most depleted melts known from the Mariana arc system. These MI are trapped in unusually refractory olivines (Fo_{90-93}) and are interpreted as hydrous melts trapped in the forearc mantle. These OL were entrained with BABB-like basalts and brought to the surface by eruption. SEMFR glassy rinds and Ol-MI contain mean of H_2O = 1.85 ± 0.26 wt%, S = 757 ± 109 ppm, Cl = 334 ± 169 ppm, F = 94 ± 31 ppm, CO_2 = 144 ± 137 ppm. Here, we show that the SEMFR Ol-MI and their host basaltic glassy rinds have the highest subduction-related ratios in volatiles and fluid-mobile elements (FMEs :Ba, Rb, Cs), with a mean of H_2O/Ce = 10096 ± 3901, Cl/Nb = 1238 ± 516, Cs/Th = 6 ± 5, Ba/Th = 523 ± 203, Rb/Th = 79

± 38 for the Ol-MI; and mean H_2O/Ce = 4953, Cl/Nb = 838, Cs/Th = 0.84 ± 0.66, Ba/Th = 265 ± 97, Rb/Th = 27 ± 14 for the glassy rinds ever recorded in the Mariana intraoceanic arc (mean H_2O/Ce = 1705 ± 1125, Cl/Nb = 429 ± 414, Cs/Th = 0.39 ± 0.16, Ba/Th = 264 ± 150, Rb/Th = 15 ± 3 for the Mariana arc Ol-MI), indicating that the shallow fluids released beneath the forearcs have distinctive FMEs/Th and volatile/incompatible ratios. However, SEMFR glassy rinds and OL-MI also show a SE-NW gradient in the volatile and the FME fluxes, demonstrating that the aqueous slab-derived fluids and the volatile fluxes are the highest at ~50–100 km slab depth. These new results suggest that the minerals carrying volatiles and FMEs to depth mostly broke down beneath the arc.

4.2 INTRODUCTION

Aqueous fluids released from dehydrating the subducting oceanic lithosphere play a key role in subduction zone magmatism. They serpentinize the cold forearc mantle wedge (Van Keken et al., 2002, Hyndman and Peacock, 2003, Wada et al., 2011), and they trigger hydrous mantle melting beneath the arc volcanoes, once the plate is ≥ 100 km deep (Grove *et al.*, 2006, Grove *et al.*, 2012, Kelley et al., 2010). Arc lavas inherit the chemical imprints of the aqueous fluids during their magmagenesis, resulting in magmas enriched in fluid-mobile elements (FMEs: Sr, K, Ba, Cs, Rb) and volatiles (H_2O, Cl, CO_2, S, F) relative to the backarc basin (BAB) lavas and mid-oceanic ridge basalts (MORBs) (Elliott, 2003, Pearce et al., 2005, Jenner and O'Neill, 2012, Kelley et al., 2010, Shaw et al., 2008, Wanless and Shaw, 2012). As the subducting plate dehydrates, the aqueous fluids become less hydrous and the concentrations of solutes increase until hydrous sediment melts to supercritical fluids are produced (Kawamoto *et al.*, 2012,

Kimura et al., 2010, Manning, 2004, Pearce et al., 2005). Therefore, the shallow aqueous fluids, released beneath the forearc (≤ 100 km depth), are expected to be more enriched in FMEs and in volatiles than are the deeper aqueous fluids released beneath the arc volcanoes (≥ 100 km depth). In this manuscript, we focus on the shallow aqueous fluids released beneath forearcs, by studying young basalts of the SE Mariana Forearc Rift (SEMFR).

Micro-analytical studies of olivine-hosted melt inclusions and glassy pillow rinds provide a unique perspective on mantle and subduction processes by better preserving the composition of more primitive and unmixed mantle melts than do host lava compositions (Bouvier *et al.*, 2010, Cervantes and Wallace, 2003, Kent and Elliott, 2002, Shaw et al., 2008). Glassy rinds represent melts quenched during submarine eruptions, trapping volatiles before they are lost by degassing accompanying eruption. In contrast, olivines are the first minerals to crystallize from the primary basaltic melt; and they can trap small parcels of their equilibrium melt as they grow (Kent, 2008). Melt inclusions (MI) and glassy rinds both strongly reflect the composition of the subduction components by capturing slab-derived volatiles and FMEs; thus, they provide a better way to investigate the volatile fluxes at subduction zones. Here, we present new major and trace elements, and volatile (H_2O, CO_2, S, Cl, F) contents of olivine-hosted melt inclusions from basalts collected in the SEMFR, and we compare these to the compositions of associated glassy rinds. SEMFR is unique in the Mariana convergent margin, as it is a part of the forearc with young igneous activity (2.7 – 3.7 Ma; (Ribeiro et al., in press)) that extends from the trench to the volcanic arc, allowing us to investigate shallow subduction processes occurring beneath forearcs. Olivine-hosted melt inclusions (Ol-MI) and glassy rinds have systematically different

major and trace element compositions, suggesting that comparing these two types of melts can provide valuable insights on the nature and composition of shallow slab-derived fluids. We use these data to address three questions: (i) what is the origin of the melt inclusions?; (ii) what do SEMFR Ol-MI reveal about the composition of the aqueous fluids released from the shallow subducting slab?; and (iii) how do volatile and FME abundances of these fluids vary with depth to the slab?

4.3 GEOLOGICAL SETTING

The Mariana intraoceanic arc is a convergent margin resulting from the subduction of the old and cold Pacific plate beneath the Philippine Sea plate (Figure 4.1A) that began in Eocene time, ~52 Ma ago (Ishizuka et al., 2011, Reagan et al., 2010). The southernmost Mariana Trench curves from N-S to E-W to accommodate its collision with the Caroline Ridge, which began in Late Miocene time (Fujioka *et al.*, 2002, Miller *et al.*, 2006b, Okino *et al.*, 2009). The southernmost Mariana Trench reaches the deepest point on Earth at the Challenger Deep (10994 m, (Gardner and Armstrong, 2011)), and Pacific-Philippine Sea plate convergence is approximately orthogonal to the southernmost Mariana trench (Bird, 2003). The southernmost Mariana convergent margin ($13^{o}10'$N – 11^{o}N) is deforming rapidly; and the Eocene forearc has been stretched since Late Neogene time to accommodate opening of the southernmost Mariana Trough, with seafloor spreading presently occurring at the Malaguana-Gadao Ridge (MGR; (Becker, 2005)). Stretching of the forearc formed the SE Mariana forearc rift, which was accompanied by abundant magmatic activity 2.7 – 3.7 Ma ago, as demonstrated by the abundant basaltic and basaltic pillow lavas and lava flows (Figure 4.1B; (Ribeiro et al., in press)). SEMFR

has evolved since into a broadly deformed postmagmatic rift (~ 40 km wide and at least 60 km long) that overlies the shallow part of the subducting slab (≤ 100 km deep) (Becker, 2005). SEMFR extends from the trench to a volcanic arc chain, the Fina Nagu Volcanic Chain (FNVC; Figure 4.1B). Near the trench, the SE SEMFR relief is rugged and affected by scarp faulting and landsliding; whereas near FNVC, NW SEMFR has smoother relief with better-preserved pillow outcrops (Ribeiro et al., in press).

4.4 METHODS

SEMFR samples were collected during YK08-08 Leg 2, YK10-12 and TN273 Thomas Thompson cruises (Ribeiro et al., submitted, Ribeiro et al., in press). We measured major elements, trace elements and major volatile concentrations (H_2O, CO_2, F, S, and Cl) on 20 glassy olivine-hosted melt inclusions (4 MI from YK08-08 Leg 2, sample 1096-R14; 7 MI from TN273, sample 30D-02-08; 9 MI from YK10-12, sample 88-R2) and volatile composition of 13 naturally-quenched pillow rinds (one sample from YK08-08 Leg2; 8 samples from TN273; 4 samples from YK10-12). Major elements and trace elements of the glassy rinds are reported by (Ribeiro et al., submitted). We also report the volatile contents of glassy rind for one sample collected along the Malaguana-Gadao Ridge during JAMSTEC Kairei cruise KR00-03 Leg 2 (Kaiko dive 164). These data are reported in Appendix Tables 4A.1 and 4A.2; and detailed methods are reported in Appendix 4A. Major element and volatile contents in melt inclusions were corrected for post-entrapment crystallization (PEC; Appendix Figure 4A.3). Less than 20 % equilibrium olivine was added back to the composition of the melt inclusion (mean = 13.0 ± 5.7% olivine added; Table 4A.2 in Appendix). In the following sections, major and volatile

contents of the Ol-MI are PEC-corrected; and major element contents of the MI and glassy rinds are also reported an anhydrous basis.

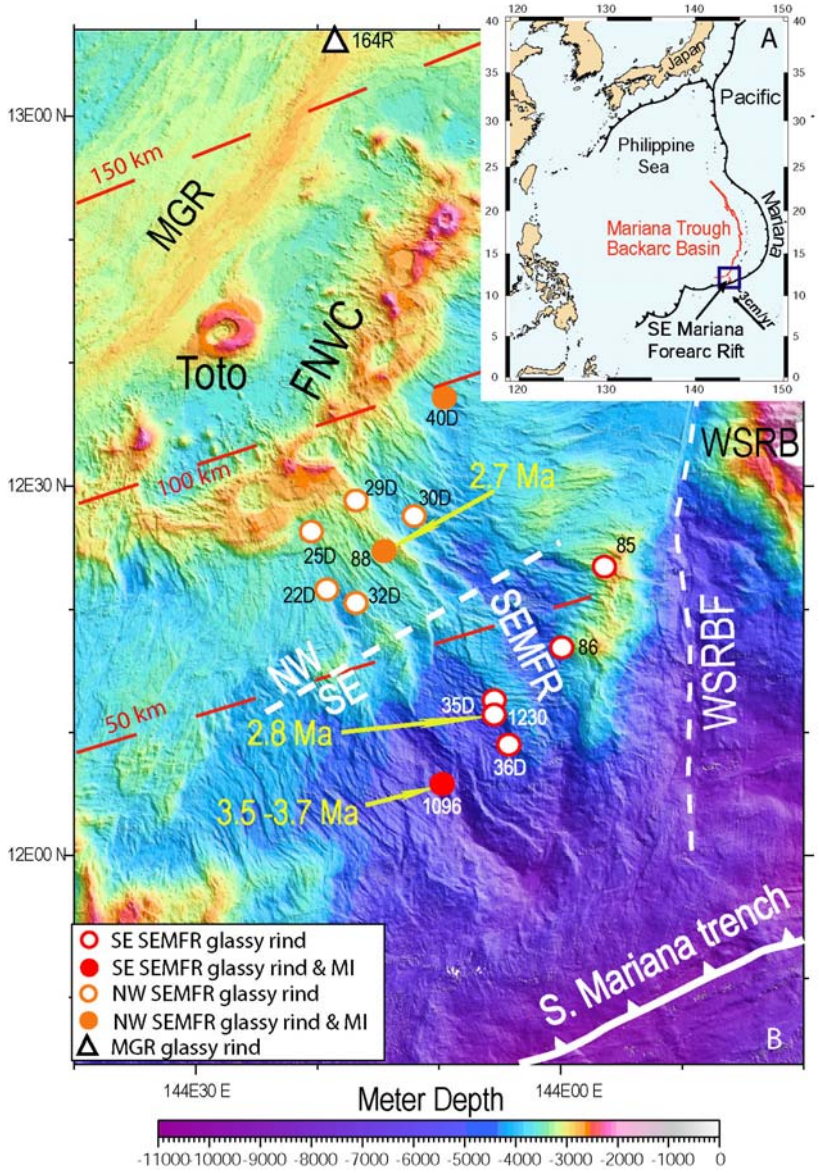

Figure 4.1. Locality maps. A) The Mariana intraoceanic arc system. The arrows represent convergence rates from (Kato et al., 2003). The blue box shows the area of B. B) Detailed bathymetric map of the southernmost Mariana intraoceanic arc. The SEMFR is divided into SE and NW sectors, separated by a white dashed line. The map shows the location of SE and NW SEMFR glassy rinds and melt inclusions. These colors are used in the other figures. Map generated with GMT (Smith and Wessel, 1990, Wessel and Smith, 1995b, Wessel and Smith, 1998) using a compilation from the University of New Hampshire / Center for Coastal and Ocean Mapping / Joint Hydrographic Center (Gardner, 2006, Gardner, 2007, Gardner, 2010).

Toto: Toto caldera; FNVC: Fina Nagu volcanic chain. Numbers with D indicate TN273 dredging sites; other numbers represent sampling sites performed during JAMSTEC Yokosuka (1096: YK08-08 Leg 2 and 1230; 85; 86; 88: YK10-12) and Kairei (164R; KR00-03 Leg 2) cruises. The large yellow numbers are ^{40}Ar-^{39}Ar ages for SEMFR lavas from (Ribeiro et al., in press). WSRBF: W. Santa Rosa Bank Fault, MGR: Malaguana-Gadao Ridge. The red dashed lines denote the slab depths reported by (Becker, 2005).

SEMFR glassy rinds and MI are compared to the Mariana arc olivine-hosted melt inclusions of (Kelley and Cottrell, 2009, Kelley et al., 2010, Kent and Elliott, 2002, Shaw et al., 2008), the Mariana backarc basin (BAB) glass of (Gribble et al., 1996, Gribble et al., 1998, Hawkins et al., 1990, Ikeda *et al.*, 1998, Kelley and Cottrell, 2009, Pearce et al., 2005), and the MORB glass of (Jenner and O'Neill, 2012, Wanless and Shaw, 2012). We used the whole rock and glass data sets for the trace elements of (Gribble et al., 1996, Gribble et al., 1998, Hawkins et al., 1990, Ikeda et al., 1998, Kelley and Cottrell, 2009, Pearce et al., 2005) for the Mariana BAB lavas, of (Kelley and Cottrell, 2009, Kelley et al., 2010, Kent and Elliott, 2002, Pearce et al., 2005, Shaw et al., 2008, Stern et al., 2006, Wade et al., 2005) for the Mariana arc lavas, and of (Jenner and O'Neill, 2012) for the MORBs, as complete trace element datasets in glasses are not always available.

4.5 RESULTS

Uncorrected melt inclusion volatile and major element compositions and compositions of olivine hosts are reported in Appendix Table 4A.1. PEC-corrected volatile, major element and uncorrected trace element compositions for SEMFR melt inclusions are reported in Appendix Table 4A.2, along with the volatile contents of SEMFR and MGR glassy rinds. Olivine hosts are Mg-rich and their Fo contents range from 90 to 93 for SE SEMFR melt inclusions and from 89 - 91 for NW SEMFR melt inclusions. Some of these olivines also host chromium spinel

inclusions, which analyses are reported in (Ribeiro et al., in press). Analyzed Ol-MI are sub-rounded (diameter > 20 μm) and generally associated with a gas bubble (Appendix Figure 4A.1).

4.5.1 Major elements:

SEMFR glassy rinds and host basalts are compositionally similar. SEMFR whole rock compositions are low-K basalts to medium-K andesites (Peccerillo and Taylor, 1976), with a mean of 52.86 ± 1.60 wt% SiO_2 (Ribeiro et al., in press). SEMFR glassy rinds are low-K basalts to basaltic andesites (51.17 – 56.75 wt% SiO_2; Figure 4.2A), with mean SiO_2 = 53.95 ± 1.52 wt% (Ribeiro et al., submitted). PEC-corrected SEMFR melt inclusions are less evolved than the glassy rinds, with a mostly basaltic composition ranging from low-K basalts to low-K basaltic andesites and SiO_2 = 48.94 - 53.11 wt% (mean = 51.46 ± 1.16 wt% SiO_2). SEMFR melt inclusions are consistently more primitive than the glassy rinds (Figure 4.2B), with Mg# = 70.6 – 79.6 for melt inclusions and Mg# = 38.0 – 61.4 for the glassy rinds. These results indicate that the melt inclusions trapped more primitive melts.

SEMFR MI have lower contents of TiO_2, Na_2O and K_2O than their host lavas. Glassy rinds contain 0.52 to 1.42 wt% TiO_2, 1.55 to 4.20 wt % Na_2O and 0.16 to 0.36 wt% K_2O (means = 0.89 ± 0.27 wt% TiO_2 ; 2.71 ± 0.80 wt% Na_2O; 0.27 ± 0.06 wt% K_2O); whereas PEC-corrected MI compositions range from 0.30 to 0.56 wt% TiO_2 , 0.55 to 1.89 wt% Na_2O and 0.04 to 0.21 wt% K_2O (mean = 0.39 ± 0.06 wt% TiO_2; 1.20 ± 0.30 wt% Na_2O; 0.12 ± 0.07 wt% K_2O). The MgO and TiO_2 content of the SEMFR MI plot within the compositional field of boninites (MgO > 8 wt% and $TiO_2 \leq 0.5$ wt%; (Le Bas, 2000)); however, the low SiO_2 content of the SEMFR MI

(< 54 wt%) demonstrates that SEMFR MI are not boninites (Le Bas, 2000). The low TiO_2 and Na_2O contents in SEMFR MI suggest that these melts were derived from a more depleted source than were their host basalt. SEMFR MI have much lower TiO_2, Na_2O, FeO* contents and higher CaO and MgO contents and Mg# than do Mariana arc olivine-hosted melt inclusions, Mariana Trough glassy rinds and MORB glassy rinds (Figure 4.2B-G), indicating that the SEMFR glass inclusions are some of the most primitive and the most depleted melts recorded in the Mariana intraoceanic arc.

The major element contents of SEMFR melt inclusions and glassy rinds plotted against MgO do not overlap (Figure 4.2C-G). Plots of Al_2O_3 and CaO against MgO show that SEMFR melt inclusions plot on the high-MgO side of fractionation-controlled kinks in the data trends, observed at MgO ~ 7 wt% and CaO ≥ 11 wt% (Figure 4.2E-F), demonstrating that the melts sampled by MI have only crystallized olivine. Diagrams of FeO*, Al_2O_3, Na_2O and TiO_2 contents vs. MgO content show that the SE and NW SEMFR melt inclusions and glassy rinds plot along two slightly different liquid lines of descent (LLDs) (Figure 4.2C-D, F-G), reflecting regional variations in the melting processes and / or mantle source along the rift (Ribeiro et al., submitted).

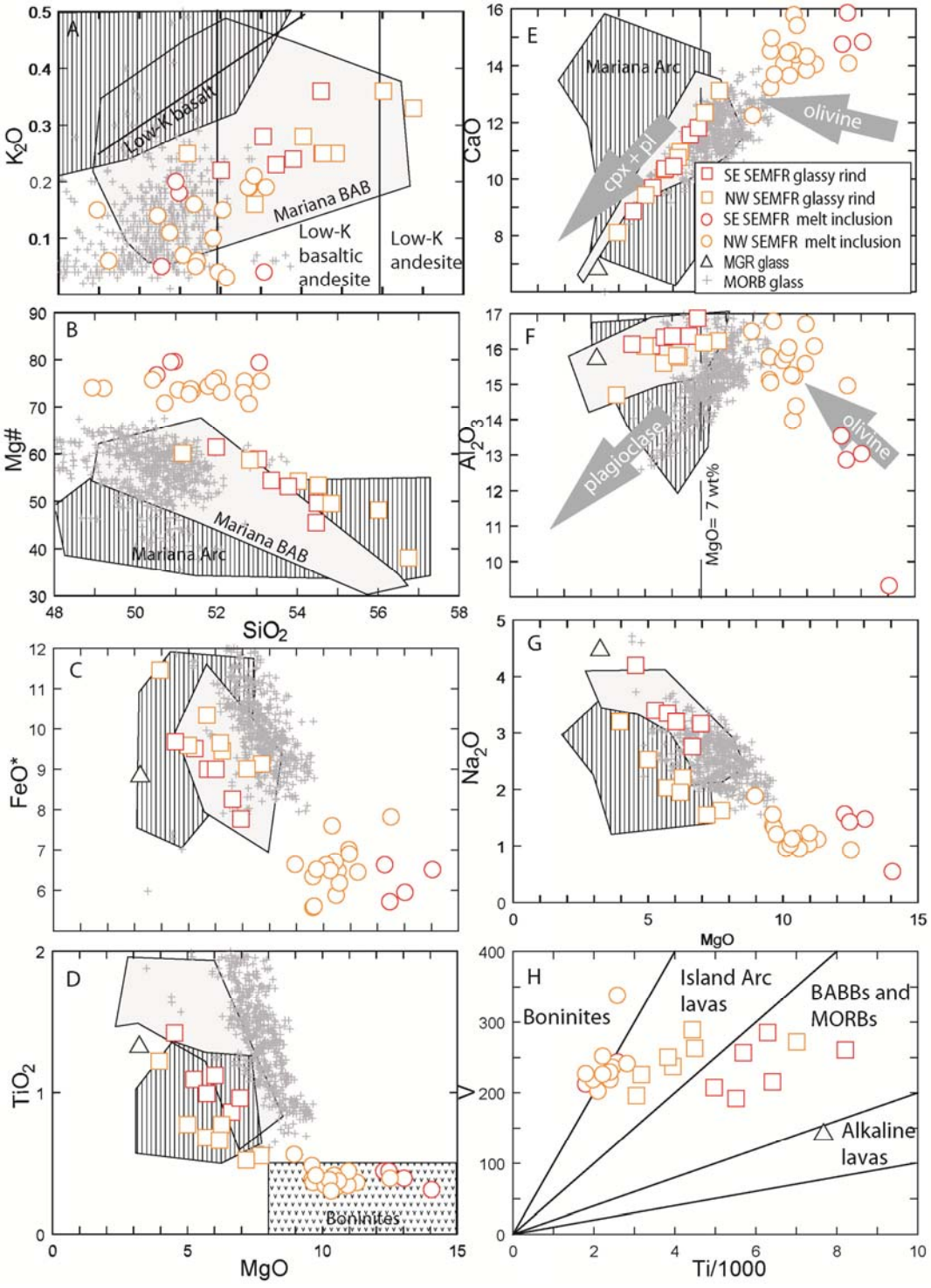

Figure 4.2. Major element variation diagrams (all data recalculated to 100% anhydrous) for SEMFR glassy rinds and melt inclusions. Melt inclusion data are corrected for post-entrapment olivine crystallization. A) Potassium – silica diagram, with fields after (Peccerillo and Taylor,

1976). B) Mg# vs SiO_2; (Mg# = 100Mg/(Mg+Fe)) showing that the melt inclusions are more primitive (Mg# > 70) than glassy rinds (Mg# < 70). C) FeO*, D) TiO_2, E) CaO, F) Al_2O_3 and G) Na_2O vs MgO diagrams for SEMFR glassy rinds and melt inclusions, and MGR glassy rind (black triangles). Arrows represents fractionation trends. The black dashed line highlights the hinge in CaO and Al_2O_3, resulting from plagioclase and clinopyroxene crystallization starting at MgO = 7 wt%. Melt inclusions have MgO > 7 wt% demonstrating that they crystallized olivine only. Cpx: clinopyroxene. The field for boninites is from (Le Bas, 2000). H) Ti-V plot of (Shervais, 1982) illustrating the difference between compositions of SEMFR glassy rinds and melt inclusions. All the melt inclusions have lower Ti contents than the glassy rinds.

4.5.2 Magmatic degassing:

During quenching, glassy rinds of pillow lavas might degas, losing some of their volatiles. Also, while analyzed melt inclusions are fully enclosed by their olivine hosts, preventing them from degassing, olivines might have trapped melt that had already degassed. Therefore, it is important to assess the effect of degassing in glassy rinds and melt inclusions. Because CO_2 and S are less soluble in basaltic magmas than H_2O (Dixon and Stolper, 1995), the effects of degassing can be evaluated by comparing H_2O, S and CO_2 contents of MI and rinds (Kelley et al., 2010, Shaw et al., 2008), as CO_2 and then S will degas before H_2O. We applied two filters for degassing, following the method of (Kelley et al., 2010): samples with PEC-corrected CO_2 > 50 ppm and S ≥ 500 ppm are considered to have retained enough CO_2 and S so that other volatiles were not significantly degassed. Based on these filters, most of the glassy rinds are likely degassed (Figure 4.3A-B), whereas most melt inclusions are undegassed. The Figure 4.3C shows that the most primitive glass (MgO > 8 wt%) are also the least degassed.

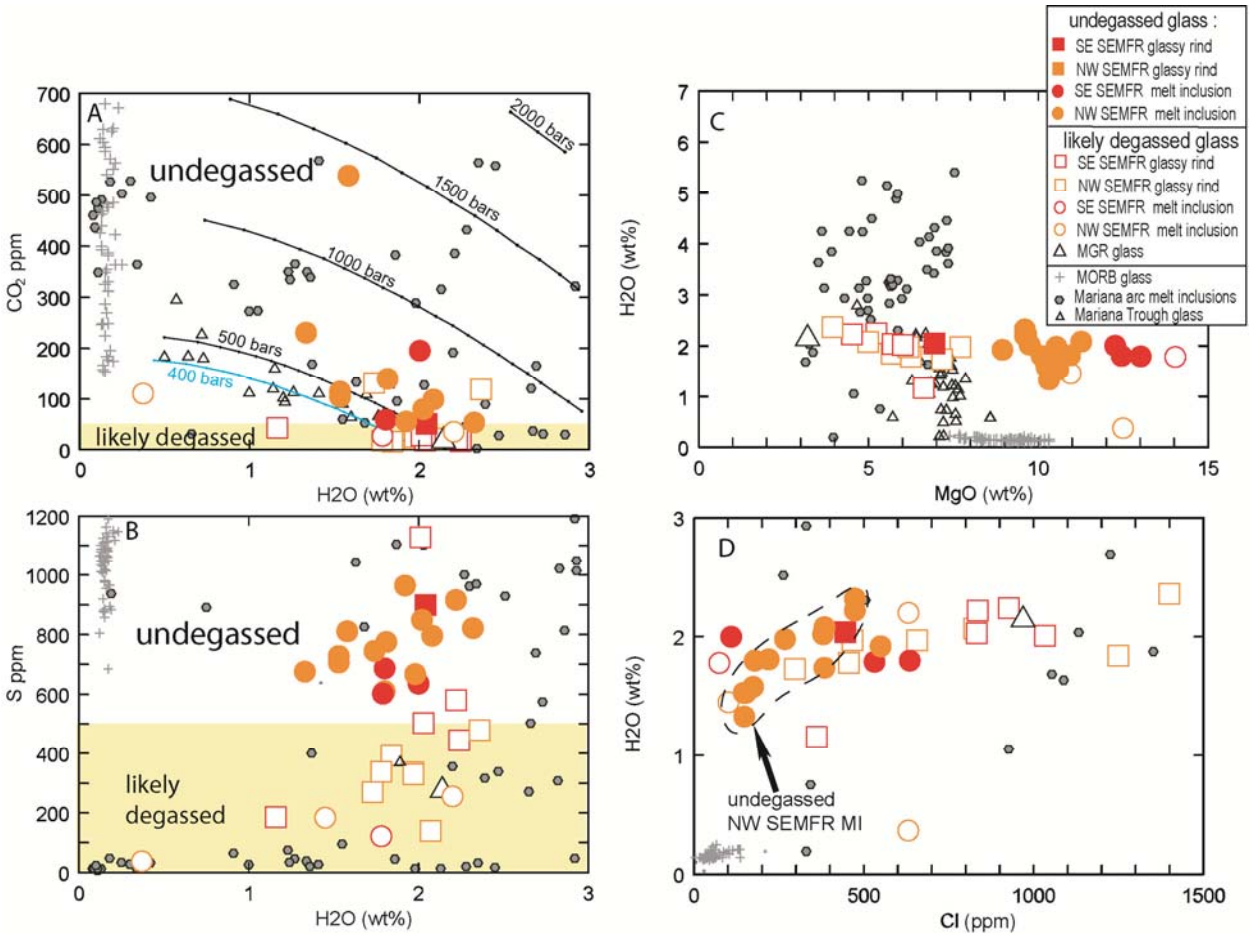

Figure 4.3. Volatile contents of SEMFR glassy rinds and melt inclusions. A) H_2O vs CO_2 diagram. The yellow field identifies samples with $CO_2 < 50$ ppm, which are likely to have degassed some H_2O. Isobars were calculated using the VolatileCalc vapor solubility model for basalt compositions (Newman and Lowenstern, 2002). The blue saturation curve models the approximate depth of the SEMFR seafloor. B) H_2O vs S diagram. The yellow field identifies the likely degassed samples with S < 500 ppm. C) H_2O vs MgO diagram. Melt inclusions have higher water content than MORB glass (Wanless and Shaw, 2012), and intermediate water content between Mariana arc Ol-MI and Mariana Trough glassy rinds. D) H_2O vs Cl diagram. SEMFR melt inclusions have lower contents in Cl than the SEMFR glassy rinds and Mariana arc melt inclusions. In diagrams C and D, we only used undegassed glass for the MORBs and the Mariana arc and BAB glass.

We also calculated the saturation pressures of each sample by using the vapor saturation model of (Newman and Lowenstern, 2002). Glasses with smaller saturation pressures than their collection (eruption) depths probably reached saturation with H_2O and CO_2 vapor, and they

likely degassed. Most SEMFR glassy rinds give saturation pressures (225 – 806 bars; mean = 475 ± 136 bars; Table 4A.2 in Appendix) that approximate their collection depth 3090 – 5737 m (303 – 563 bars) and were vapor-supersaturated when they erupted (Figure 4.3A). In contrast, SEMFR melt inclusions are vapor-undersaturated, as they record deeper saturation pressures from 255 -1389 bars (mean = 607 ± 266 bars; Table 4A.2 in Appendix), so that their volatiles did not exsolve (Figure 4.3A). These results are consistent with the co-variations of CO_2 and S against H_2O outlined previously.

4.5.3 Volatile contents:

SEMFR glassy rinds and melt inclusions show variable range in undegassed volatile compositions (CO_2, H_2O, Cl, F, Cl and S). They span lower volatile abundances in Cl (111 – 637 ppm), F (58 – 186 ppm), S (601 -963 ppm), CO_2 (51 – 539 ppm) and H_2O (1.33 – 2.32 wt%) compared to the Mariana arc Ol-MI (Cl = 209 – 1697 ppm; F = 17 – 1962 ppm; S = 501 – 2153 ppm; CO_2 = 52 – 795 ppm; and H_2O = 0.19 – 5.40 wt%; Figure 4.3). SEMFR glass have similar water contents to those of the undegassed Mariana Trough glass (H_2O = 0.20 – 2.78 wt%). Mariana arc Ol-MI show the highest water content (3.31 ± 1.16 wt% H_2O); while MORB glass have the lowest water (≤ 0.3 wt%) and Cl (< 150 ppm) contents (Figure 4.3). (Ribeiro et al., submitted) noted a SE-NW gradient in the FMEs and High Field Strength Elements (HFSE) abundances in SEMFR lavas; and SE SEMFR glass are slightly more enriched in Cl (Figure 4.3D) and slightly more depleted in S (Figure 4.3B) than NW SEMFR glass. We also observe some differences in F and CO_2 abundances between the undegassed glassy rinds and the melt inclusions. SEMFR MI have similar abundances in H_2O (1.84 ± 0.26 wt%), S (748 ± 106 ppm)

and Cl (327 ± 172 ppm) than their host glass (H_2O = 2.04 wt%; S = 898 ppm and Cl = 447 ppm); but OL-MI have lower contents in F (88 ± 20 ppm) and higher CO_2 abundances (152 ± 141 ppm) than their host (F = 186 ppm; CO_2 = 51 ppm).

4.5.4 Trace elements:

V and Ti can be used as markers of SEMFR lava tectonic settings, as V is sensitive to oxidation state and Ti tracks mantle depletion (Shervais, 1982). BABBs are generally accepted to be produced by adiabatic decompression melting of a depleted, metasomatized mantle source. In contrast, arc basalts are generally accepted to be produced by higher degrees of hydrous melting of a more depleted mantle source, resulting in lower Ti and higher V contents in arc basalts than in BABBs. In the Ti-V plot of (Shervais, 1982), NW SEMFR glassy rinds plot within the arc compositional field; while SE SEMFR glassy rinds plot within the BABB compositional field (Figure 4.2H), reflecting a more depleted mantle towards NW SEMFR (Ribeiro et al., submitted). SE and NW SEMFR melt inclusions do not show a SE-NW gradient as do glassy rinds; instead they cluster tightly along the boundary between boninitic and arc compositional fields, further suggesting that the melt inclusions were produced from a more depleted mantle source than their host basalt.

Rare Earth Element (REE) patterns of the NW and SE SEMFR melt inclusions are depleted in Light REE (LREE; $(La/Yb)_N < 1$; $(La/Sm)_N < 1$; $(Gd/Yb)_N = 1$) with no europium anomaly ($(Eu/Eu^*)_N = 1$; Figure 4.4A-B). Trace element patterns of the melt inclusions have positive

anomalies in FMEs (Ba, Cs, Rb, K, Sr), U and Pb and negative anomalies in HFSE (Nb, Zr, Ti), La, Ce, Th.

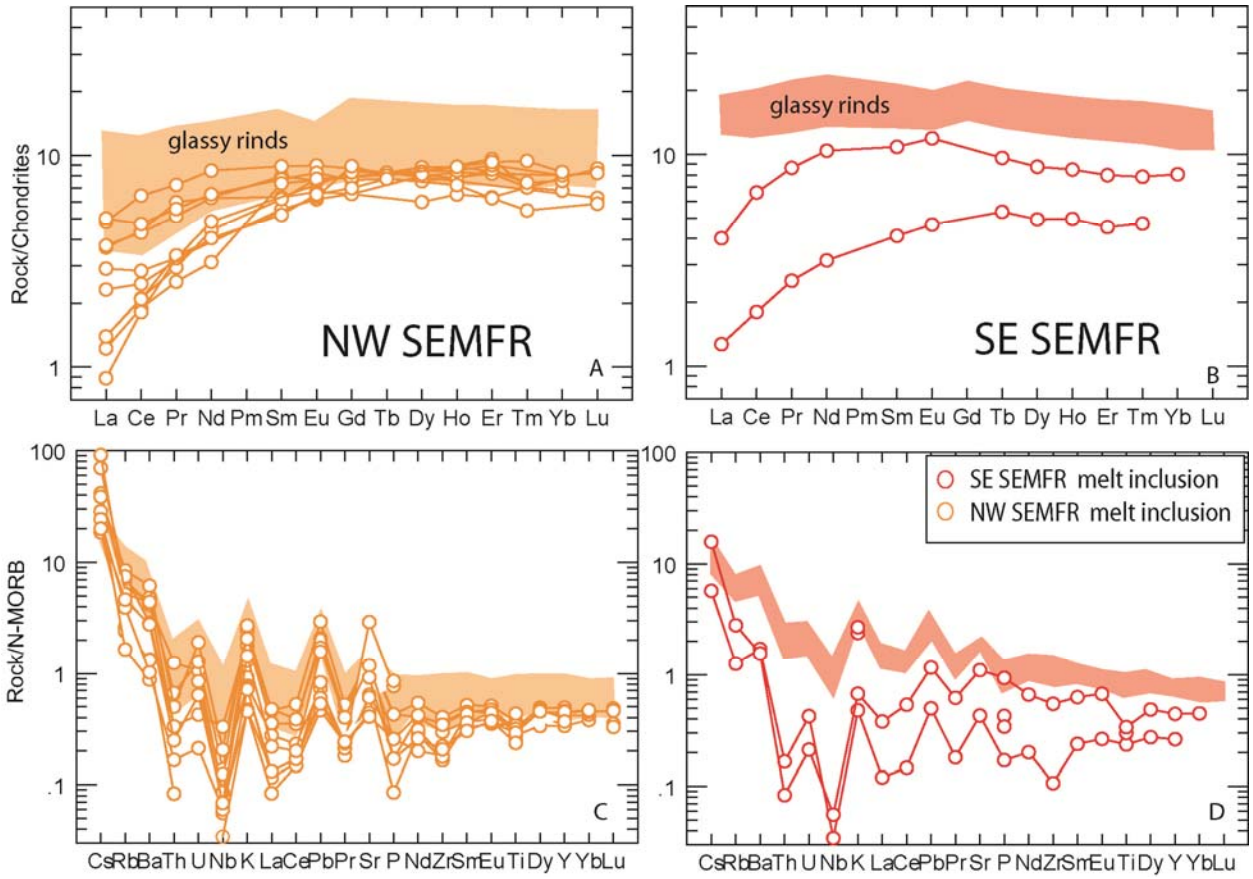

Figure 4.4. Chondrite-normalized (Sun and McDonough, 1989) Rare Earth element (REE) patterns and N-MORB normalized (Sun and McDonough, 1989) trace element patterns of SEMFR lavas from the NW sector (A,C) and the SE sector (B,D). SE SEMFR melt inclusions are more depleted in LREE and in HFSE than their host glass. NW SEMFR melt inclusions are as depleted as to more depleted in HFSE and in LREE than the glassy rinds See text for details.

The least LREE-depleted REE patterns and the least HFSE-depleted trace element patterns of NW SEMFR melt inclusions overlap the most LREE- and HFSE-depleted patterns of glassy rims of their host basalt (Figure 4.4A, C and Figure 4A.2b-c in Appendix); and all the spider diagrams of the NW SEMFR melt inclusions have FME contents that are similar to their host basalt glassy

rim. In contrast, the REE and the trace element patterns of SE SEMFR melt inclusions do not overlap those of their host glass (Figure 4.4B, D and Appendix Figure 4A.2a). The greater LREE and HFSE depletion also suggests that SEMFR melt inclusions were produced from a more depleted mantle source than their host basalt, as reflected by glassy rims. Chemical differences between SE and NW SEMFR lavas are also observed in the trace element patterns of their melt inclusions. SE and NW SEMFR melt inclusions have similar HSFE depletion and their patterns overlap for most trace elements; but NW SEMFR inclusions are enriched in Cs, as also observed for their glassy rinds (Figure 4.4C-D).

4.6 DISCUSSION

Subduction-related magmas are mixing products between mantle melts and slab-derived fluids, and olivine-hosted melt inclusions are key tools to investigate the origin and the composition of the mantle and subduction components (Kent, 2008, Kelley et al., 2010, Kent and Elliott, 2002, Ruscitto *et al.*, 2012, Shaw et al., 2008). Olivines crystallize first in primary basaltic magmas, and they can capture their equilibrium melt as they grow (Kent, 2008). The main advantages of studying Ol-MI are : (i) they are almost unaffected by decompression during magma ascent (Schiano and Bourdon, 1999) ; and (ii) their mineral host protect them from alteration. As a result, Ol-MI can preserve their high-pressure, primitive melt composition with minimal volatile loss (Kent, 2008, Newman *et al.*, 2000). Comparing Ol-MI and their host glassy rinds can provide major insights into volatile fluxes during subduction-related magmatic evolution, as MI should be less degassed relative to glassy rinds. Below, we investigate the compositional differences between the SEMFR Ol-MI and their host basalt glassy rinds, and we discuss these

implications for understanding melt generation in the mantle beneath SEMFR. First, we explore how the SEMFR melt inclusions formed and then, we discuss what SEMFR MI and glassy rinds reveal about the composition of the shallow, aqueous fluids released beneath forearcs.

4.6.1 Origin of the SEMFR olivine-hosted melt inclusions:

PEC-corrected melt inclusions and glassy rinds have distinctive major and trace element compositions. SEMFR MI have the lowest SiO2, TiO2, FeO* and Na2O contents and the highest MgO and CaO contents recorded in the Mariana intraoceanic arc (Figure 4.2B-G), along with a strong depletion in HFSE and LREE relative to their associated glassy rinds (Figure 4.4), suggesting that SEMFR MI sampled more primitive melts that formed deeper from higher degrees of melting or from a more depleted mantle source. We use the water-sensitive geothermobarometer of (Lee et al., 2009) to constrain the P-T conditions of primary melts in equilibrium with the mantle wedge, along with elemental ratios and Fe8, to test the hypothesis that the SEMFR MI were produced deeper from higher degrees of mantle melting or from a more depleted mantle.

P-T conditions estimated by the geothermobarometer of (Lee et al., 2009) are those of the last melt in equilibrium with the mantle or mean P-T conditions of polybaric, fractional pooled melts recorded along a melting column (Kelley et al., 2010); and below, we use the P-T uncertainties of (Lee et al., 2009). Glasses were first filtered to remove those affected by plagioclase and clinopyroxene fractionation and we retained the most primitive samples (MgO $\geq$ 7 wt%, see section 3.1 for details) for which water contents were analyzed. For comparison, we used the

same filters on Mariana arc MI, Mariana Trough glasses and MORB glasses. We used Fe^{3+}/FeT = 0.17 for Mariana BABBs and SEMFR lavas, 0.16 for MORBs and 0.25 for Mariana arc basalts (Kelley and Cottrell, 2009). We assumed that olivine in the mantle source was Fo90 for the host basalts except for the SEMFR MI, as these are mostly in equilibrium with olivine Fo92. Calculated P-T conditions of mantle-melt equilibration of the undegassed, PEC-corrected, SEMFR MI mostly cluster above the subducting beneath SE SEMFR (≤ 50 km depth; (Becker, 2005, Gvirtzman and Stern, 2004); Figure 4.5A). MI yield P-T conditions of 1203 – 1366 ± 40^{o}C and 0.23 – 1.17 ± 0.2 GPa with a mean T = 1258 ± 40^{o}C and P = 0.67 ± 0.2 GPa, i.e. 22.0 ± 6.6 km depth. They overlap the P-T conditions of their host basalt glassy rinds within the uncertainties (1284 – 1291 ± 40^{o}C and 0.78 – 0.98 ± 0.2 GPa with a mean T = 1287 ± 40^{o}C and P = 0.88 ± 0.2 GPa, i.e. 29.1 ± 6.6 km depth). Undegassed SE and NW SEMFR MI show similar P-T conditions (mean T = 1247 ± 40^{o}C and P = 0.54 ± 0.2 GPa for SE SEMFR MI; and mean T = 1260 ± 40oC and P = 0.70 ± 0.2 GPa for NW SEMFR MI). This suggests that the melts sampled by SEMFR MI do not record any SE-NW P-T gradient associated with increasing slab depth (≤ 50 km near the trench vs ~ 100 km near the arc (Becker, 2005, Gvirtzman and Stern, 2004)). In comparison, Mariana arc MI (1240 - 1522 ± 40^{o}C and 1.06 – 2.96 ± 0.2 GPa with a mean T = 1339 ± 40^{o}C and P = 1.65 ± 0.2 GPa) and MORBs (1306 – 1456 ± 40^{o}C and 0.99 -1.91 ± 0.2 GPa with a mean T = 1360 ± 40^{o}C and P = 1.27 ± 0.2 GPa) reflect higher P-T conditions of mantle-melt equilibration than do SEMFR MI (Figure 4.5A). Calculated P-T conditions of Mariana Trough BABB glassy rinds (1214 – 1359 ± 40^{o}C and 0.63 – 1.53 ± 0.2 GPa with a mean T = 1272 ± 40^{o}C and P = 0.96 ± 0.2 GPa) overlap those of SEMFR and (Ribeiro et al., submitted, Ribeiro et al., in press) have commented on the geochemical similarities of SEMFR

and Mariana Trough BAB basalts. Deeper and warmer P-T conditions of mantle-melt equilibration beneath the Mariana arc are consistent with hydrous mantle melting (Kelley et al., 2010). The lower P-T conditions of mantle-melt equilibration recorded by SEMFR glassy rinds suggest that SEMFR lavas formed shallow (29.0 ± 6.6 km depth) by adiabatic decompression mantle melting just on top of the subducting slab (Ribeiro et al., in press). The lower equilibration pressures captured by SEMFR MI suggest that they formed shallower (22.0 ± 6.6 km depth) than did their host glassy rinds.

The shallower melting depth of the SEMFR MI is also illustrated by Fe_8 (Figure 4.5B). Fe_8 is the FeO* content of the lavas corrected to MgO = 8 wt%, using the equation of (Klein and Langmuir, 1987). For this, we used the most primitive glassy rinds and MI (MgO ≥ 7 wt%; see section 4.1 for details) that lie on the olivine LLD (Figure 4.2C-G). We compared SEMFR MI to the associated primitive glassy rinds and bulk rock compositions, which were also filtered for MgO ≥ 7 wt%. SEMFR MI recorded the lowest Fe_8 relative to their host lavas and the Mariana arc lavas (Figure 4.5B), demonstrating that they formed shallower, as shown with the geothermobarometer of (Lee et al., 2009).

We also test if SEMFR MI derive from a more depleted mantle region or from higher degree of mantle melting; and for this, we use Nb/Yb and La/Sm (Elliott, 2003, Pearce et al., 2005), as Nb and La are incompatible elements that concentrate in mantle melts (McCulloch and Gamble, 1991).

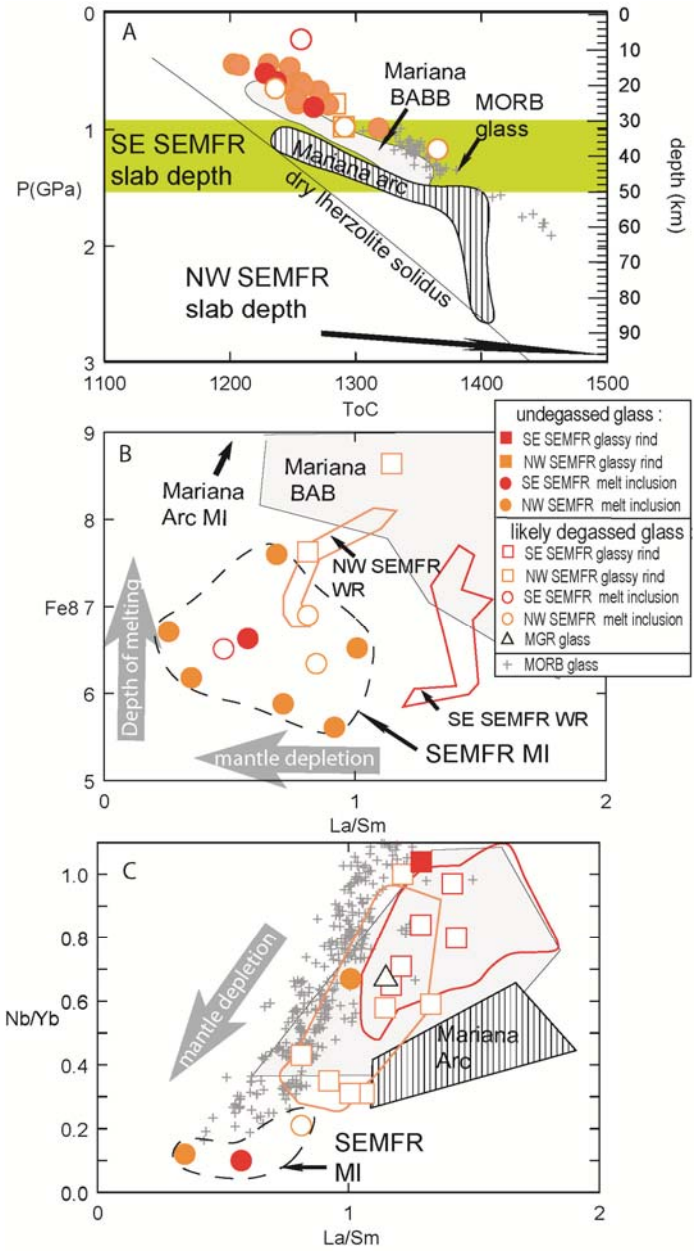

Figure 4.5. A) P-T conditions of mantle-melt equilibration for the SEMFR glassy rinds and melt inclusions estimated by using the geothermobarometer of (Lee et al., 2009). The slab depth is from (Becker, 2005, Gvirtzman and Stern, 2004). SEMFR MI have mostly recorded lower P-T conditions than did the SEMFR glassy rinds, the Mariana arc MI and the MORB glasses. Glass were filtered to retain the primitive glasses (MgO ≥ 7 wt%) with analyzed water contents. Fe_8 (B) and Nb/Yb (C) vs La/Sm diagrams used to track the compositional differences between the SEMFR glassy rims and the OL-MI. MI have much lower Nb/Yb, La/Sm and Fe_8 than the glassy rinds and the Mariana arc lavas, showing that SEMFR MI formed from a shallower and more depleted mantle source. Composition fields of NW and SE SEMFR whole rock (WR) are from (Ribeiro et al., submitted, Ribeiro et al., in press).

Plot of Nb/Yb against La/Sm (Figure 4.5C) shows that SEMFR glassy rinds plot within the Mariana BAB compositional field, with a more depleted mantle source beneath NW SEMFR, as outlined by (Ribeiro et al., submitted). In contrast, no significant difference can be seen between Nb/Yb and La/Sm in NW and SE SEMFR OL-MI. Instead, most MI show significantly lower Nb/Yb and La/Sm than do glassy rinds, indicating that they formed from a more depleted mantle source or from higher degrees of melting than did their host basaltic magmas and Mariana arc lavas.

The Mg-rich olivines (Fo_{89-93}) hosting the SEMFR MI are not in equilibrium with their host rock (in equilibrium with Fo < 85; see Appendix Table 4A.2); and they also host chromium spinel (Cr# = 47 – 73 in (Ribeiro et al., in press) ; Appendix Figure 4A.1). SEMFR olivine – spinel assemblages plot in the mantle array of (Arai, 1994) and they are similar to the SE Mariana forearc mantle peridotite (Ohara and Ishii, 1998). These observations demonstrate that (i) the olivine hosts are forearc mantle xenocrysts (Ribeiro et al., in press) and (ii) SEMFR OL-MI are aqueous silicate melts that metasomatized the SEMFR forearc mantle. Petrographic observations of the olivine xenocrysts show that SEMFR glass inclusions occur as isolated MI (Appendix Figure 4A.1), suggesting that forearc mantle neoblasts trapped MI (Schiano *et al.*, 1995, Andersen and Neumann, 2001). We propose that stretching of the Eocene SE Mariana forearc lithosphere triggered hydrous mantle melting beneath the forearc. The hydrous melts rose into the forearc mantle wedge where formed mantle olivine neoblasts (Figure 4.6). Ol-MI from the upper lithospheric mantle was never sampled before in the Mariana intraoceanic system (Kelley and Cottrell, 2009, Kelley et al., 2010, Shaw et al., 2008). Mantle Ol-MI from other subduction

zones are either silica-rich melts in equilibrium with the lherzolitic subarc mantle (Schiano et al., 1995, Ertan and Leeman, 1999). Therefore, SEMFR Ol-MI are the first record of primitive melts in equilibrium with the forearc mantle that provide new insights into the shallow subduction processes explored below.

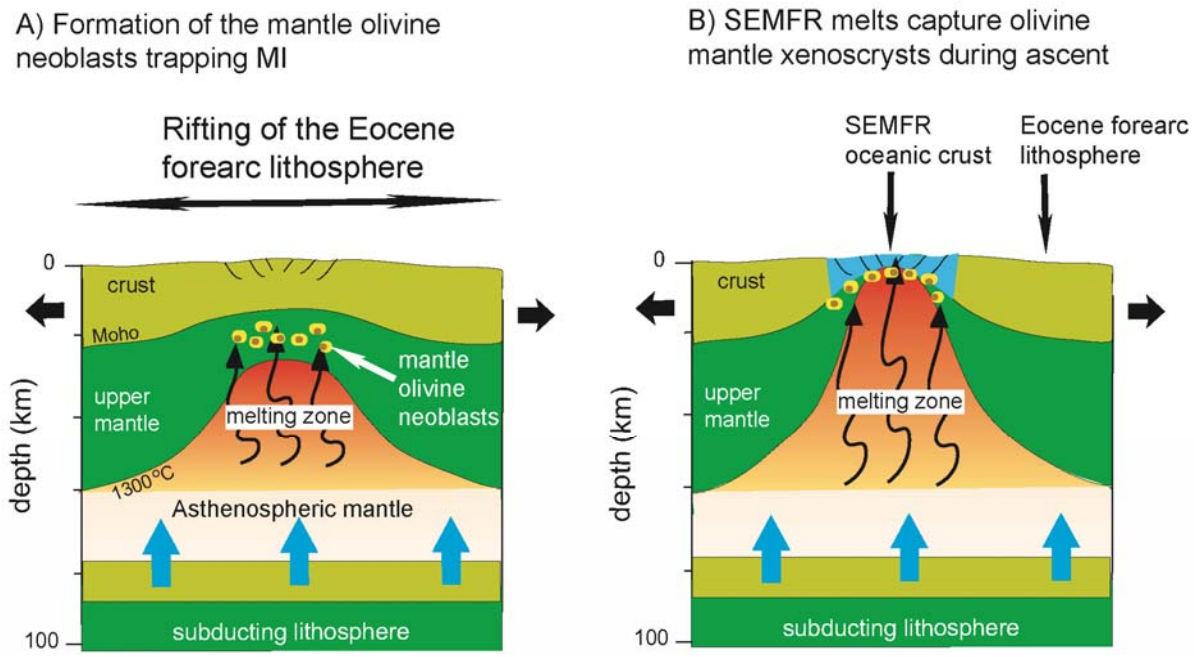

Figure 4.6. Model of formation of the mantle olivine neoblasts and their capture by the SEMFR melts along SSW-NNE cross-sections. A) The forearc lithosphere is serpentinized by the aqueous slab-derived fluids released from the subducting slab (blue arrows). Stretching of the Eocene forearc lithosphere triggers hydrous mantle melting beneath the SE Mariana forearc. Melts rise into the upper mantle wedge (black curved arrows), forming mantle olivine neoblasts that trapped melt inclusions (yellow ellipsoids with a brown circle) during their growth at ~ 22 ± 6.6 km depth. B) Further stretching of the SE Mariana forearc lithosphere opens SEMFR and forms new oceanic crust. Melts are produced by hydrous, adiabatic decompression melting of the asthenospheric mantle at ~ 29 ± 6.6 km depth. SEMFR melts capture some mantle olivine neoblasts during their ascent.

4.6.2 Composition of the shallow aqueous slab-derived fluid:

Recent studies (Elliott, 2003, Pearce and Stern, 2006, Pearce et al., 2005) use incompatible trace element ratios to track mantle and subduction processes, as these ratios are little affected by mantle melting and magmatic fractionation. We follow the approach of (Pearce et al., 2005, Pearce and Stern, 2006) to investigate the shallow subduction processes occurring beneath SEMFR. For this, we propose our own systematics, described in (Ribeiro et al., submitted), to track if SEMFR MI and glassy rinds captured any shallow, aqueous slab-derived fluids. Finally, we investigate correlations between the FME and volatile abundances to constrain the volatile fluxes and the composition of the aqueous fluids released beneath SEMFR.

4.6.2.1 Did SEMFR glass capture the shallow, aqueous slab-derived component?

Trace elements have different mobilities in aqueous fluids and in silicate melts and this difference can be exploited to track subduction fluids. Ba/Nb tracks the total subduction components and Th/Nb tracks contribution from the sediment melts, generally released at depth ≥ 100 km (Pearce et al., 2005, Johnson and Plank, 1999). Similarly, Rb/Th, Ba/Th and Cs/Th track the composition of the slab-derived aqueous fluids, as the effects of sediment melt are minimized by normalizing the FMEs to Th (Pearce et al., 2005). In the diagram Th/Nb vs Ba/Nb (Figure 4.7A), SEMFR glassy rinds and MI cluster slightly above the Mariana BAB compositional field, with higher Ba/Nb, indicating an important role for aqueous slab-derived fluids beneath SEMFR (Pearce et al., 2005, Pearce and Stern, 2006, Ribeiro et al., submitted).

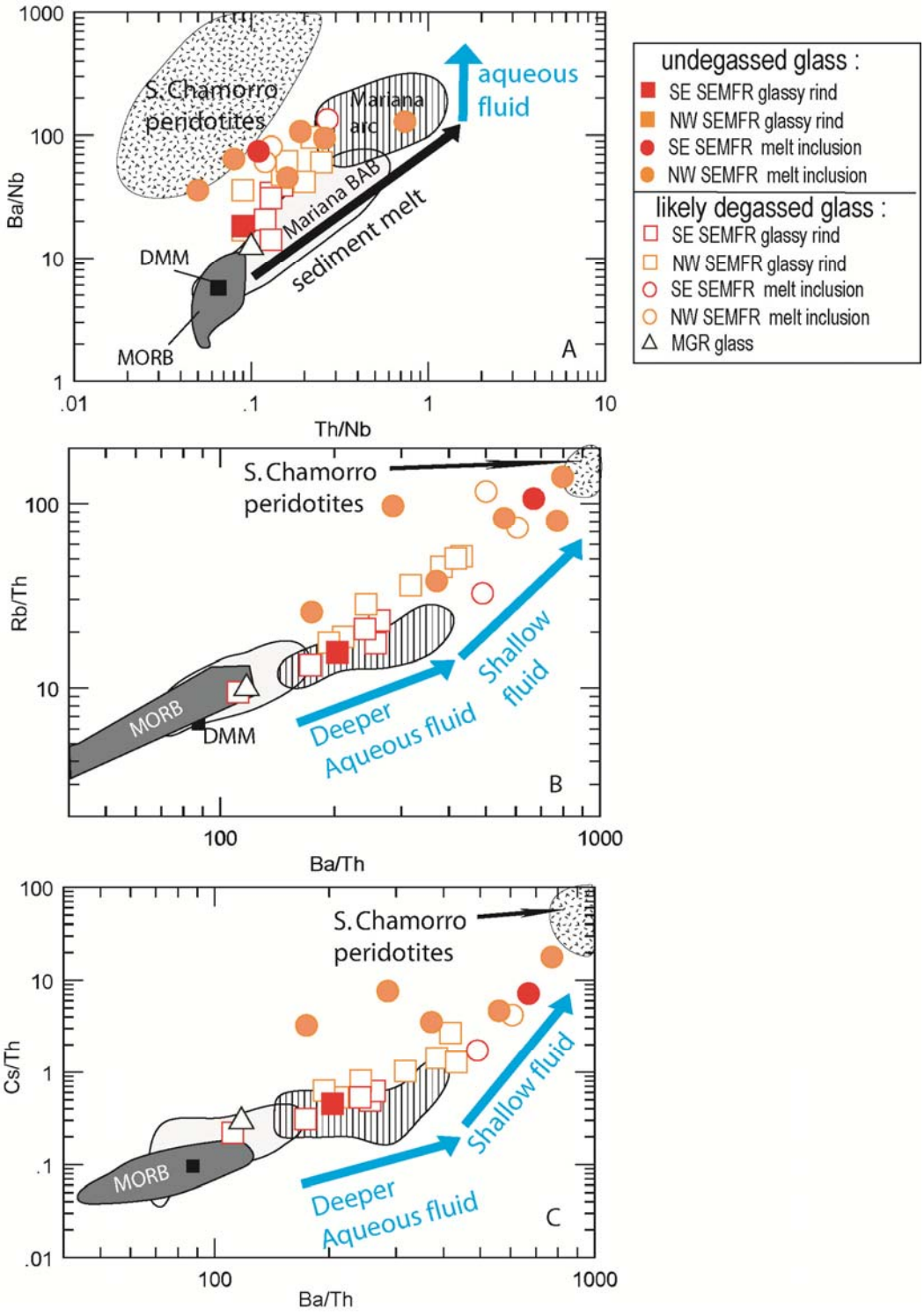

Figure 4.7. A) Pearce's diagrams (Pearce et al., 2005) used to illustrate the subduction components in SEMFR glassy rinds and melt inclusions. Ba/Nb track the total subduction

component; while increasing Th/Nb tracks the sediment melt released deeper. See text for details. B) Rb/Th and C) Cs/Th vs Ba/Th diagrams illustrating the aqueous fluids released beneath arc volcanoes and forearcs. The forearc fluids are characterized by a stronger enrichment in Ba, Rb, Cs than the arc lavas, as demonstrated by higher Rb/Th, Ba/Th and Cs/Th ratios in SEMFR glassy rinds and melt inclusions. We used the depleted MORB-like mantle of (DMM; (Salters and Stracke, 2004)), the S. Chamorro forearc serpentinites of (Savov et al., 2007); and the altered oceanic crust (AOC) of (Kelley et al., 2003).

The unusually high Ba/Nb, Ba/Th, Rb/Th and Cs/Th in SEMFR MI (Figure 4.7) demonstrate that MI captured the shallow aqueous fluids that would have otherwise serpentinized the SEMFR forearc mantle wedge. These fluids are less FME-rich than the fluids captured by the S. Chamorro serpentinites (Figure 4.7; (Savov et al., 2007)); however, exhumed forearc mantle is exposed to seawater alteration that can strongly alter the FME composition (Hart, 1969, Jochum and Verma, 1996, Kelley et al., 2003, Ribeiro et al., submitted). In contrast, olivine hosts protect the enclosed MI from alteration; thus, MI record a more reliable composition of the shallow subduction component. NW and SE SEMFR glassy rinds form a trend from the depleted MORB mantle (DMM) of (Salters and Stracke, 2004) toward the SEMFR MI, with higher Ba/Th, Rb/Th and Cs/Th in the NW SEMFR glassy rinds than in the Mariana arc lavas, demonstrating that SEMFR lavas also interacted with the shallow aqueous fluids (Figure 4.7B-C). However, the fluids preserved in glassy rinds are less enriched in FMEs, indicating that the SEMFR MI captured a more aqueous subduction component, which may have been released earlier, as argued in the previous section (Figure 4.6A).

4.6.2.2 Volatile fluxes and composition of the shallow aqueous fluids beneath SEMFR:

Petrologic experiments and analyses of Ol-MI from arc volcanoes (Cervantes and Wallace, 2003, Grove et al., 2012, Schmidt and Poli, 1998, Sadofsky *et al.*, 2008) show that FME and volatile

abundances decrease with slab depth, especially once the plate is ≥ 100 km depth, suggesting that volatile and FME fluxes are greatest beneath the forearc. In this section, we investigate the correlations between FMEs and volatiles beneath SEMFR to better constrain volatile fluxes and the composition of shallow aqueous fluids. For this, we use the ratios H_2O/Ce and Cl/Nb, as Ce and Nb have similar partition coefficients to those of the volatiles (Dixon *et al.*, 2002), to ensure that the undegassed volatile contents are not fractionation-controlled (Appendix 4B) and reflect subduction processes. These ratios are compared to the shallow subduction proxies Rb/Th and Cs/Th (Figure 4.8). We note that SEMFR MI are the most depleted melts in Nb in the whole Mariana intraoceanic arc (Figure 4.5B-C), which is largely responsible for their extremely high Cl/Nb. However, SEMFR MI also have the highest Cl/Th, and these ratios show similar trends to those seen in Figure 4.8. We prefer to normalize Cl to Nb, as these ratios are largely used in the literature (Cervantes and Wallace, 2003, Rowe and Lassiter, 2009, Ruscitto et al., 2012).

Undegassed SEMFR MI have much higher H_2O/Ce, Cl/Nb, Cs/Th, Ba/Th and Rb/Th (mean H_2O/Ce = 10096 ± 3901, Cl/Nb = 1238 ± 516, Cs/Th = 6 ± 5, Ba/Th = 523 ± 203, Rb/Th = 79 ± 38) relative to their host basaltic glassy rinds (H_2O/Ce = 4953, Cl/Nb = 838, Cs/Th = 0.84 ± 0.66, Ba/Th = 265 ± 97, Rb/Th = 27 ± 14) and the Mariana arc MI (mean H_2O/Ce = 1705 ± 1125, Cl/Nb = 429 ± 414, Cs/Th = 0.39 ± 0.16, Ba/Th = 264 ± 150, Rb/Th = 15 ± 3; Figure 4.7-4.8). NW SEMFR MI have higher H_2O/Ce and Cl/Nb (mean H_2O/Ce = 10527 ± 3412 and Cl/Nb = 1288 ± 528) than does the single undegassed SE SEMFR MI (H_2O/Ce = 4953 and Cl/Nb = 838) and glassy rind (H_2O/Ce = 2366 and Cl/Nb = 239), further indicating occurrence of a SE-NW gradient in the SEMFR volatile fluxes (Figure 4.8).

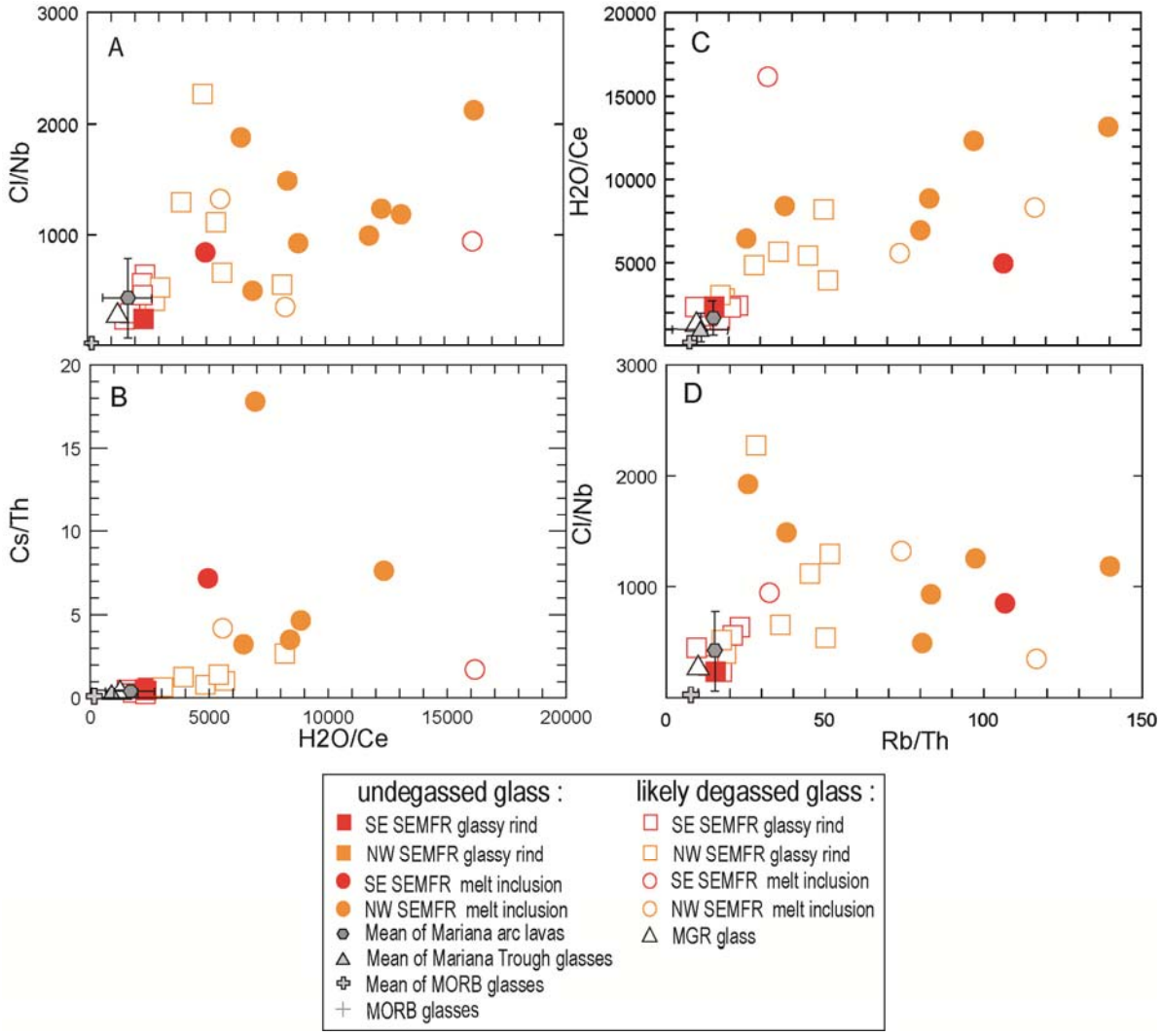

Figure 4.8. Comparison of SEMFR volatile/FME ratios. A) Cl/Nb, and B) Cs/Th vs H_2O/Ce diagrams; and C) H_2O/Ce, and D) Cl/Nb vs Rb/Th diagrams showing that the undegassed SEMFR Ol-MI have the highest volatile and FME ratios relative to the undegassed Mariana arc Ol-MI, Mariana Trough glass and MORB glass. NW SEMFR Ol-MI also have higher Cl/Nb and H_2O/Ce than do SE SEMFR MI, suggesting occurrence of a SE-NW gradient in the volatile abundances along SEMFR. Such compositional trend is also observed in the degassed SEMFR glassy rinds, Rb/Th, Cs/Th of SEMFR glassy rinds decrease toward the trench, but no trenchward gradient is observed in the SEMFR MI. See text for details. We used an average of the whole rock and glass data set for the trace element ratios and an average of the undegassed volatiles (S > 500 ppm and CO_2 > 50 ppm) for the MORB glassy rinds, Mariana arc Ol-MI and Mariana Trough BAB glass (references are reported in the method section), whenever volatile contents and / or Ba, Rb, Th, Ce were not analyzed for each sample. When S and CO_2 were not analyzed for the Mariana BAB glass, we assumed that the volatiles were likely undegassed, as few BAB volatile data are available. Averages are reported with one standard deviation error bar.

A similar gradient has been observed between the SE and the NW SEMFR glassy rinds based on their FME ratios (Figure 4.7), with a mean of Cs/Th = 1.20 ± 0.73, Ba/Th = 314 ± 100, Rb/Th = 35 ± 14 for NW SEMFR glassy rinds and a mean of Cs/Th = 0.44 ± 0.15, Ba/Th = 209 ± 58, Rb/Th = 17 ± 5 for SE SEMFR glassy rinds (Ribeiro et al., submitted). In contrast, SEMFR MI do not show not any clear SE-NW regional variation in Cs/Th, Ba/Th and Rb/Th (mean of Cs/Th = 7 ± 6, Ba/Th = 509 ± 222, Rb/Th = 82 ± 38 for NW Ol-MI and mean of Cs/Th = 4 ± 4, Ba/Th = 581 ± 126, Rb/Th = 70 ± 53 for SE Ol-MI; Figure 4.8B-D and Figure 4.7B-C). H_2O/Ce and Cl/Nb of undegassed SEMFR glass (MI and glassy rinds) are not correlated to Cs/Th and Rb/Th (Figure 4.8). These observations show that (i) the volatile fluxes (Cl and H_2O) might be decoupled from Cs and Rb during shallow subduction processes; (ii) the volatile fluxes and the FME ratios are the highest beneath SEMFR, demonstrating that the shallow slab-derived fluids are the most hydrous beneath forearcs; and (iii) the SEMFR volatile fluxes the FME ratios (Ba/Th, Cs/Th and Rb/Th) increase toward the arc volcanoes, as shown by the SE-NW gradient ,suggesting that the subducted minerals carrying volatiles and FMEs to depth (such as serpentinite, barite, phengite and chlorite; (Grove et al., 2006, Zack et al., 2001, Schmidt and Poli, 1998, Scambelluri and Tonarini, 2012)) mostly broke down at ~ 50 - 100 km depth (Figure 4.9) ; and they decrease once the subducting plate is ≥ ~ 100 km depth (Ruscitto et al., 2012).

4.7 CONCLUSIONS

SEMFR OL-MI trapped melts strongly depleted in HFSE and highly enriched in FMEs and volatiles relative to their host basaltic glassy rinds, the Mariana arc and BAB lavas (Figure 4.5B-C, 4.7 & 4.8). SEMFR MI are the first records of equilibrium melts with olivine xenocrysts from

the forearc mantle, and they thus provide unique insights into volatile fluxes and shallow slab-derived fluids released beneath forearcs.

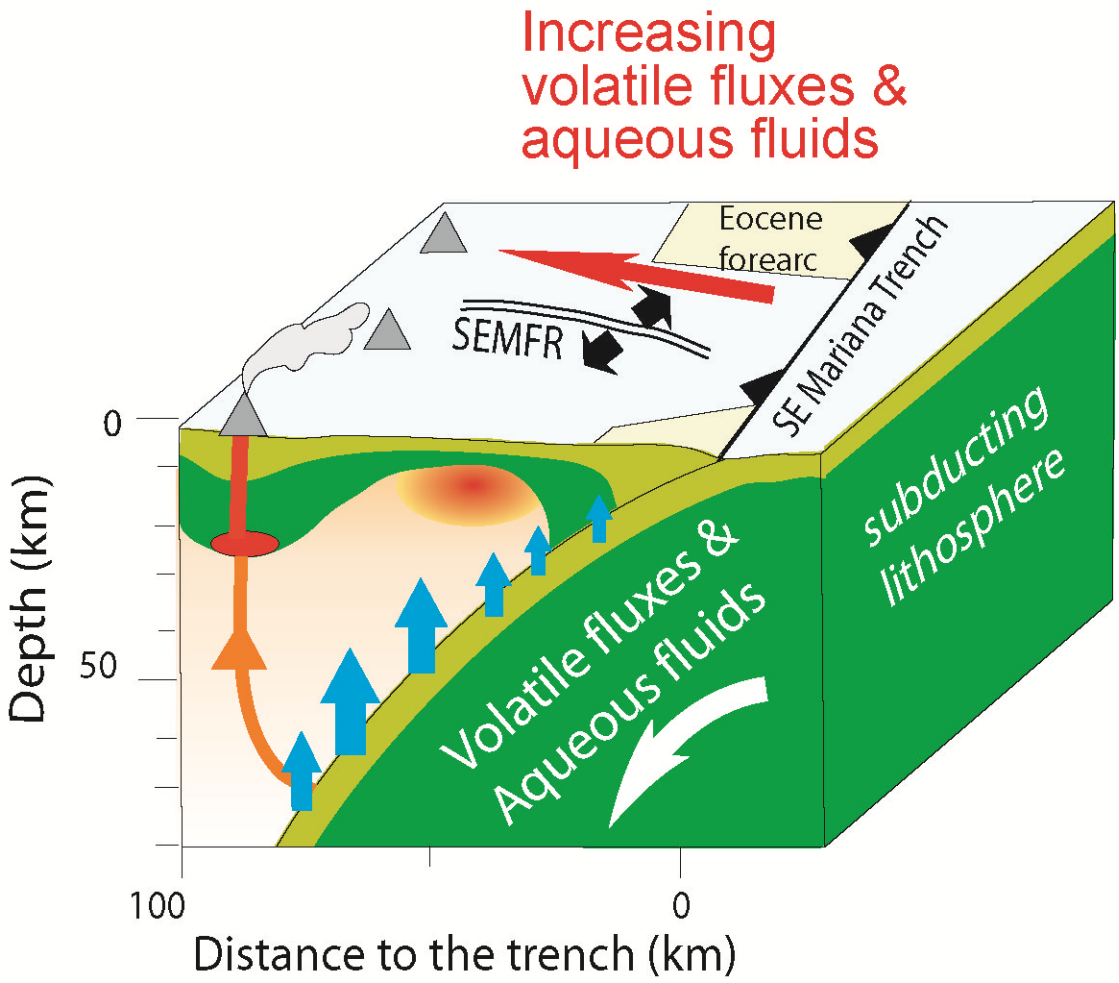

Figure 4.9. 3D model of compositional evolution of the shallow aqueous fluids and volatile fluxes released beneath SEMFR. The subducting slab is mostly dehydrated between ~ 50 and 100 km depth, as shown with the white and the red arrows; and slab dehydration starts decreasing beneath the arc volcanoes (~ 100 km slab depth), as illustrated by the blue arrows. The orange arrows illustrate hydrous mantle melting beneath the arc volcanoes.

Undegassed SEMFR Ol- MI recorded the highest inputs in the volatile ratios (H_2O/Ce and Cl/Nb) and in FME ratios (Ba/Th, Cs/Th, Rb/Th) in the Mariana intraoceanic system, indicating that the shallow slab-derived fluids released beneath forearcs are the most hydrous, consistent

with the previous observations (Grove et al., 2012, Ruscitto et al., 2012, Sadofsky et al., 2008, Schmidt and Poli, 1998). However, volatile ratios in undegassed SEMFR Ol-MI and FME ratios in SEMFR glassy rinds do not increase toward the trench; instead they show a SE-NW compositional gradient, where the aqueous slab-derived fluids and the volatile fluxes are the greatest at ~ 50 – 100 km slab depth, demonstrating that the minerals carrying volatiles and FMEs (serpentinite, chlorite, barite, phengite) mostly released their fluids beneath the arc volcanoes (Figure 4.9).

4.8 ACKNOWLEDGEMENTS

We would like to thank the R/V Yokosuka and the Thomas Thompson crews for their efforts work during YK08-08 Leg 2, YK10-12 and TN273 cruises, the SIMS team at WHOI, the EPMA team at MIT and M. Lytle for their precious help and comments. This research was supported by NSF grant 0961352 to RJS. This is UTD Geosciences contribution # 12XX.

APPENDIX 4A

METHODS

4.A.1 Analytical methods:

We measured major elements, trace elements and major volatile concentrations (H_2O, CO_2, F, S, and Cl) on a total of 20 naturally glassy olivine-hosted melt inclusions and volatile composition of 13 naturally-quenched pillow rinds along the SE Mariana Forearc Rift. We also report the volatile contents of one sample collected along the Malaguana-Gadao Ridge during JAMSTEC Kairei cruise KR00-03 Leg 2, Kaiko dive 164. Details for the major element and trace element analyses of the glassy rinds are reported in (Ribeiro et al., submitted). Samples were crushed and sieved with 2 mm, 1 mm, 0.5 mm mesh screens. Fresh, brown and translucent glass chips from the pillow rinds were hand-picked at the University of Rhode Island (URI) and examined under microscope in polarized and crossed-polarized light to ensure that clean, crystal-free glass was available for analysis. Olivine-hosted melt inclusions were hand-picked at the Woods Hole Oceanographic Institution (WHOI) and at URI, and examined under a microscope to ensure that they were fully enclosed by the olivine host and composed of translucent, brown or clear glass free of secondary crystals (Figure 4A.1A). Glass chips and melt inclusions were then polished on a single side (with 40 μm, 30 μm, 15 μm and 9 μm aluminum oxide polishing sheets), mounted and polished on Indium (with 6 μm and 3 μm diamond polishing paste, and 1 μm and 0.3 μm alumina polishing paste) prior to analyses (Figure 4A.1B).

Volatiles were measured using the CAMECA IMS 1280 Ion probe with a Cs^+ ion beam at WHOI, with a 1.28 nA and 30 μm beam, following the technique outlined in (Hauri *et al.*, 2002). Melt inclusions with smaller region available for analysis (< 30 μm) were measured using a 500 pA and 20 μm beam. Glass standards (519-4-1, 51-3, 46D, 1649-3, D20-3, JD17H, 1654-3, 6001, D52-5, NS-1) were measured prior to analyses for calibrations; and calibration curves yield $r^2 > 0.9$, but for water ($r^2 > 0.8$). Major element were measured at Massachusetts Institute of Technology (MIT) on the Superprobe JEOL JXA-8200, using a 10 μm defocused beam to minimize alkali loss, a 15 kV accelerating voltage and a 10 nA beam current. The glass standard ALV-1690-20 and olivine standard P140 of (Grove et al., 1992) were analyzed daily for calibrations, and to monitor precision and accuracy of the unknowns. Repeated analyses of the glass and olivine standards give a precision ≤ 0.3 %; and repeated analyses of the glass standard gave a mean CaO = 10.85 wt%, Al_2O_3 = 15.51 wt%, K_2O = 0.15 wt%, MnO = 0.19 wt%, Na_2O = 3.13 wt%, TiO_2 = 1.71wt%, SiO_2 = 49.90 wt%, P_2O_5 = 0.18 wt%, FeO = 9.91 wt%, MgO = 7.68 wt%. Mean of repeated analyses of the unknowns has 1 $\sigma \leq 0.5\%$ for the melt inclusions and ≤ 1.1 % for the olivine. Olivine hosts were analyzed 3 – 4 times from the core to the rim, to ensure that no reverse zoning occurred. All analyzed olivines were homogeneous.

Trace element analyses were carried out at URI with the UP-213 Laser Ablation System coupled to a Thermo X-series II quadrupole ICP-MS (LA-ICP-MS). Melt inclusions were ablated using a 5 Hz repeat rate, 60% pulse beam energy and 20 – 80 μm spot size (Kelley et al., 2003). Data were background-subtracted, and normalized to ^{43}Ca as internal standard. Concentrations were calculated from calibration curves based on 8 standards (BHVO, BCR, BIR, GOR 132, StHIs,

T1, ML-3B, KL2), analyzed under the same conditions as the unknowns. Calibration curves yield $r^2 \geq 0.999$, but for Zn, Co, Tb, Yb, U and Lu ($r^2 \geq 0.996$). Reproducibility of replicates analyses are ≤ 3% rsd for Sr, Nb, Rb, Ba, K_2O, ≤ 5% rsd for Y, Li, U, and ≤ 11% rsd for Th and Ni. REE patterns of the melt inclusions are smooth and their HREE patterns are subparallel to the HREE patterns of their host glass (Figure 4A.2).

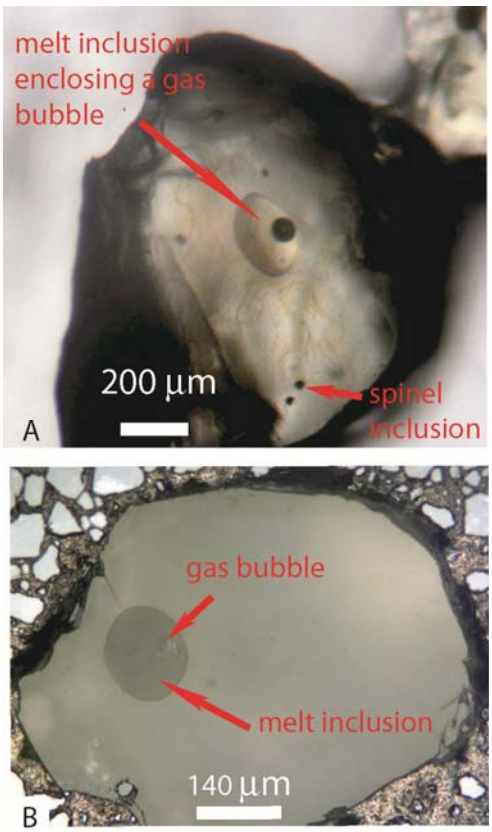

Figure 4A.1. Microphotographs of olivine-hosted melt inclusions (MI). A) Unpolished olivine in a 70% propanol bath. This method allows us to see through the olivine and to look at the melt inclusion. The dark circle inside the melt inclusion is a shrinkage bubble formed in reason of the greater expansion of the silicate melt than the olivine host during cooling (Schiano and Bourdon, 1999). Olivine also encloses some chromium spinel inclusions. No secondary MI occurring as trails along cracks were observed, demonstrating that SEMFR Ol-MI are neoblasts that trapped the MI during OL growth (Andersen and Neumann, 2001). B) Polished olivine with melt inclusion pushed into indium (grey material surrounding the olivine) for SIMS analyses. Microphotograph (A) was taken with a binocular microscope and microphotograph (B) was taken under a polarized microscope.

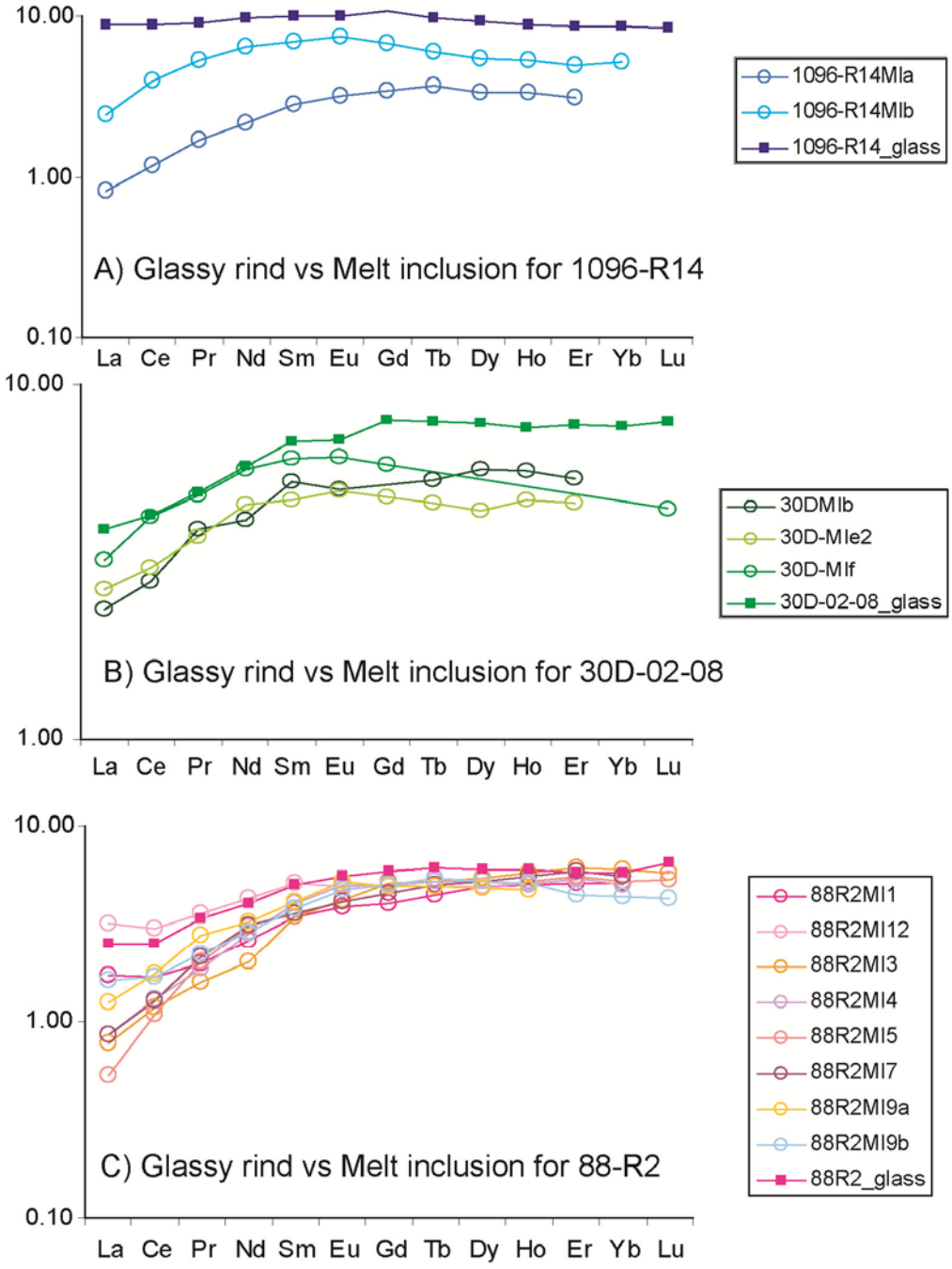

Figure 4A.2. REE patterns of the melt inclusions (MI) compared to the REE patterns of the glassy of their host rock for the samples (A) 1096-R14, (B) 30D-02-08, (C) 88-R2. REE patterns of the MI are smooth.

4.A.2 Correction of melt inclusion composition:

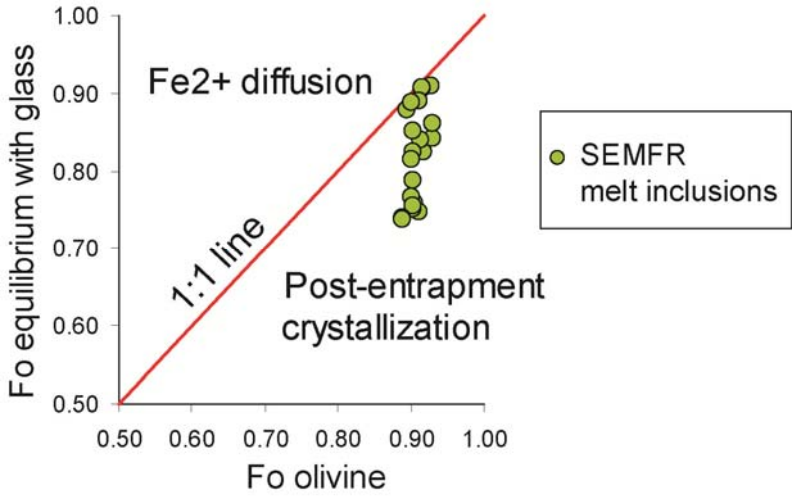

Figure 4A.3. Comparison of calculated equilibrium Fo contents of the olivine-hosted melt inclusion (Y-axis) with the Fo content measured in the olivine host (X-axis). All SEMFR melt inclusions have their Fo equilibrium < Fo olivine, demonstrating that they experienced post-entrapment crystallization.

Melt inclusion compositions were corrected for post-entrapment crystallization. Olivine host can crystallize against the melt inclusion (MI) wall during magmatic processes, depleting the inclusion in Mg and enriching it in Fe and volatiles (Kent, 2008). Post-entrapment crystallization (PEC) can be corrected by calculating the Fo content of the equilibrium olivine that should be in equilibrium with the glass inclusion using a partition coefficient ($K_D^{ol\text{-}liq}$(Fe/Mg)) of 0.33 (Roeder and Emslie, 1970), and by comparing the Fo equilibrium to the measured Fo content of the host olivine. PEC is characterized by Fo equilibrium < Fo measured and can be corrected by adding back equilibrium olivine to the melt inclusion composition in 0.1% increments until the host olivine composition is reached. This correction is sensitive to the ratio Fe^{3+}/Fe_T in the MI; and while this ratio is not known for SEMFR lavas, we used $Fe^{3+}/Fe_T = 0.17$ as determined for BABBs (Kelley and Cottrell, 2009). Major element and volatile contents in all the melt

inclusions were corrected for PEC (Figure 4A.3); and less than 20 % equilibrium olivine was added back to the composition of the melt inclusion (mean = 13.0 ± 5.7%; Table 4A.2).

Table 4A.1. Example of uncorrected volatile and major element contents of the SEMFR melt inclusions. Major element contents of the olivine host are also reported. The complete table is provided in a joined excel file.

Location	SE SEMFR	SE SEMFR	SE SEMFR	SE SEMFR	NW SEMFR	NW SEMFR	NW SEMFR	NW SEMFR	NW SEMFR	NW SEMFR
sample	6K-1096-R14	6K-1096-R14	6K-1096-R14	6K-1096-R14	TN273-30D-02-08	TN273-30D-02-08	TN273-30D-02-08	TN273-30D-02-08	TN273-30D-02-08	TN273-30D-02-08
material	MI-a	MI-b	MI-d1	MI-d2	MI-b	MI-c	MI-d	MI-e1	MI-e2	MI-f
ISGN	JMR000033R	JMR000033S	JMR000033T	JMR000033U	JMR000033V	JMR000033W	JMR000033X	JMR000033Y	JMR000033Z	JMR000040
Melt inclusion										
CO2 ppm	29.53	231.42		68.81			121.41	54.63		38.58
H2O wt%	1.93	2.37	2.13	2.09	1.97	2.33	2.54	2.36	2.25	2.40
F ppm	83.01	109.52	140.11	158.19	95.60	103.26	97.29	81.53	93.93	109.51
S ppm	130.43	750.44	717.63	796.78	843.37	785.06	973.07	835.67	925.92	277.71
Cl ppm	82.09	131.01	636.44	739.63	436.53	317.05	472.16	483.81	480.81	691.52
wt%										
SiO2	52.34	50.42	51.06	50.64	51.90	51.97	50.92	51.46	50.99	51.96
TiO2	0.34	0.52	0.47	0.51	0.47	0.39	0.43	0.38	0.36	0.52
Al2O3	10.11	16.01	15.61	14.97	15.83	17.96	19.53	15.27	15.13	17.09
FeO*	6.21	5.36	4.80	4.78	4.82	4.58	4.44	5.33	5.37	5.55
MnO	0.12	0.11	0.14	0.13	0.11	0.11	0.11	0.10	0.13	0.10
MgO	8.77	3.51	3.58	4.13	3.53	2.02	1.84	7.12	7.29	4.42
CaO	17.43	17.44	17.77	18.46	17.88	16.96	17.05	14.64	15.04	14.34
Na2O	0.60	1.86	1.77	1.66	1.29	1.18	1.36	1.38	1.33	1.69
K2O	0.04	0.06	0.22	0.24	0.18	0.12	0.17	0.19	0.20	0.20
P2O5	0.02	0.13	0.06	0.05	0.05	0.06	0.03	0.03	0.03	0.06
Total	96.15	95.72	95.82	95.85	96.43	95.59	96.11	96.20	96.06	96.03
olivine host										
wt%										
SiO2	40.36	39.42	40.10	40.10	40.34	39.60	39.46	40.24	40.24	39.52
Al2O3	0.06	0.04	0.02	0.02	0.02	0.02	0.03	0.01	0.01	0.03
FeO	7.00	7.92	6.92	6.92	8.42	9.27	8.66	8.38	8.38	9.70
MgO	50.63	49.65	51.26	51.26	50.17	49.34	49.64	50.17	50.17	50.30
Total	98.65	97.62	98.91	98.91	99.50	98.79	98.35	99.38	99.38	100.17
Fo measured	0.93	0.92	0.93	0.93	0.91	0.90	0.91	0.91	0.91	0.90

Table 4A.2. Example of corrected volatile, major and uncorrected trace element contents of the SEMFR melt inclusions (MI). Volatile contents of SEMFR and MGR glassy rinds are also reported. Major and trace elements of the glassy rinds are from (Ribeiro et al., submitted). Mg# = (Mg^{2+} x 100) / (Mg^{2+} + Fe^{2+}). All the iron is considered as Fe^{2+}. P sat. is the saturation pressure calculated by using the vapor saturation model of (Newman and Lowenstern, 2002). P and T are the pressure and the temperature of mantle melting calculated by using the water-sensitive geothermobarometer of (Lee et al., 2009). The complete table is provided in a joined excel file.

Location	SE SEMFR	SE SEMFR	SE SEMFR	SE SEMFR	NW SEMFR	NW SEMFR	NW SEMFR	NW SEMFR	NW SEMFR
sample	6K-1096-R14	6K-1096-R14	6K-1096-R14	6K-1096-R14	TN273-30D-02-08	TN273-30D-02-08	TN273-30D-02-08	TN273-30D-02-08	TN273-30D-02-08
material	MI-a	MI-b	MI-d1	MI-d2	MI-b	MI-c	MI-d	MI-e1	MI-e2
ISGN	JMR00003R	JMR00003S	JMR00003T	JMR00003U	JMR00003V	JMR00003W	JMR00003X	JMR00003Y	JMR00003Z
CO2 ppm	27.22	195.60		59.23			99.19	53.64	
H2O wt%	1.78	2.00	1.79	1.80	1.74	1.98	2.08	2.32	2.22
F ppm	76.51	92.56	117.31	136.15	84.34	87.65	79.47	80.04	92.79
S ppm	120.21	634.16	600.78	685.71	743.98	666.29	794.75	820.40	914.62
Cl ppm	75.65	110.70	532.76	636.47	385.06	269.06	385.60	474.93	474.91
P sat.(Bar)	375.78	820.12		453.03			651.37	659.57	
Collection depth (m)	5737.00	5737.00		5737.00			3888.00	3888.00	
P collection depth (Bar)	562.80	562.80		562.80			381.41	381.41	
wt%									
SiO2	52.07	49.49	50.02	49.93	51.10	50.74	49.36	51.83	51.49
TiO2	0.30	0.43	0.38	0.43	0.41	0.32	0.35	0.37	0.35
Al2O3	9.13	13.26	12.79	12.62	13.72	14.92	15.74	14.77	14.70
FeO*	6.39	6.49	5.84	5.62	5.78	6.35	6.31	5.45	5.48
MnO	0.11	0.09	0.11	0.11	0.10	0.09	0.09	0.10	0.13
MgO	13.77	12.02	12.78	12.23	10.28	10.32	11.03	9.38	9.43
CaO	15.75	14.45	14.56	15.56	15.50	14.09	13.74	14.16	14.61
Na2O	0.54	1.54	1.45	1.40	1.12	0.98	1.10	1.33	1.29
K2O	0.04	0.05	0.18	0.20	0.15	0.10	0.13	0.19	0.19
P2O5	0.02	0.11	0.05	0.04	0.05	0.05	0.02	0.03	0.02
Total	*98.13*	*97.93*	*98.15*	*98.14*	*98.20*	*97.96*	*97.87*	*97.60*	*97.70*
Mg#	79.35	76.74	79.59	79.51	76.03	74.35	75.71	75.43	75.43
Fo equilibrium	0.91	0.82	0.84	0.86	0.84	0.76	0.75	0.91	0.91
Fo measured	0.93	0.92	0.93	0.93	0.91	0.90	0.91	0.91	0.91
% olivine added	9.63	17.17	18.08	15.72	13.31	16.92	19.41	3.28	2.83
ToC	1256.29	1266.48	1236.42	1227.92	1230.39	1248.70	1253.11	1202.62	1207.22
P (GPa)	0.23	0.81	0.59	0.52	0.44	0.61	0.78	0.44	0.45
ppm									
Rb	0.71	1.57			3.87				3.08
Sr	38.70	99.61			134.17				125.13
Nb	0.08	0.13			0.20				0.32
Cs	0.04	0.11			0.49				0.29
Ba	10.78	9.84			26.31				30.35

APPENDIX 4B

CONTROL OF CRYSTAL FRACTIONATION ON VOLATILE TRENDS

During ascent, the melt cools and starts crystallizing. Fractionation shifts the melt composition toward higher silica and lower MgO content; and the melt can become oversaturated in volatiles (Figure 4B.1). As more fractionation occurs, the melt is likely to degas (Schiano and Bourdon, 1999), resulting in volatile loss in the silica-rich melt (Kelley et al., 2010).

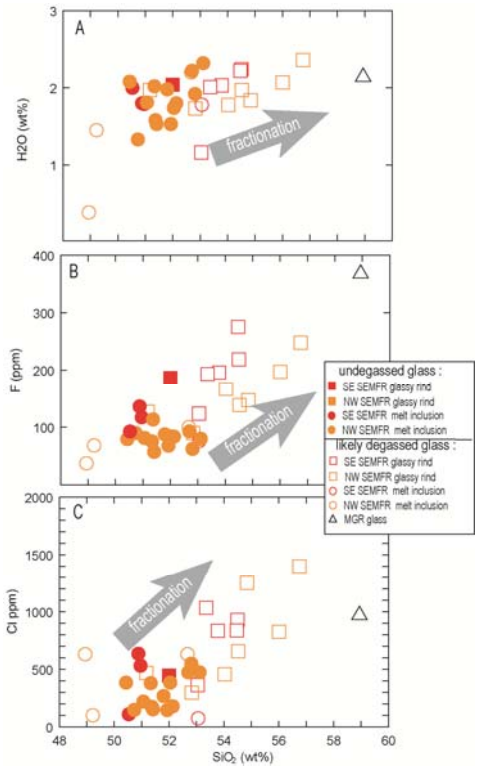

Figure 4B.1. Effect of crystal fractionation on the A) water, B) fluorine and C) chlorine contents of the SEMFR glass. As fractionation occurs, the melt become more silica-rich and volatile-rich. Higher volatile contents in SEMFR glassy rinds relative to the SEMFR MI, suggest that they are undegassed. Filled and unfilled symbols represent that are likely to contain H2O and S contents that are undegassed and degassed, respectively, as identified from Figure 4.3A, B.

REFERENCES

ANDERSEN T. & NEUMANN E.-R. 2001. Fluid inclusions in mantle xenoliths. *Lithos,* 55**,** 301-320.

ARAI S. 1994. Characterization of spinel peridotites by olivine-spinel compositional relationships: Review and interpretation. *Chemical Geology,* 113**,** 191-204.

ARCULUS R. J. 2003. Use and abuse of the terms calcalkaline and calcalkalic. *Journal of Petrology,* 44**,** 929-935.

AREVALO JR. R. & MCDONOUGH W. F. 2010. Chemical variations and regional diversity observed in MORB. *Chemical Geology,* 271**,** 70-85.

BAKER E. T., EMBLEY R. W., WALKER S. L. *et al.* 2008. Hydrothermal activity and volcano distribution along the Mariana arc. *Journal of Geophysical Research,* 113**,** B08S09, DOI: 10.1029/2005GC000948.

BEBOUT G. E., BEBOUT A. E. & GRAHAM C. M. 2007. Cycling of B, Li, and LILE (K, Cs, Rb, Ba, Sr) into subduction zones: SIMS evidence from micas in high-P/T metasedimentary rocks. *Chemical Geology,* 239**,** 284-304.

BECKER N. C. 2005. Recent volcanic and tectonic evolution of the southern Mariana arc. pp. 166, University of Hawai'i, Hawai'i.

BECKER N. C., FRYER P. & MOORE G. F. 2010. Malaguana-Gadao Ridge: Identification and implications of a magma chamber reflector in the southern Mariana Trough. *Geochemistry Geophysics Geosystems,* 11**,** Q04X13, DOI: 10.1029/2009GC002719.

BIRD P. 2003. An updated digital model of plate boundaries. *Geochem. Geophys. Geosyst.,* 4**,** 1027, DOI:10.1029/2001GC000252.

BLOOMER S. H. & HAWKINS J. W. 1983. Gabbroic and ultramafic rocks from the Mariana Trench: An island arc ophiolite. *In* HAYES, D. E. (ed.) *The Tectonic and Geologic Evolution of Southeast Asian Seas and Islands: Part 2.* Vol. 27, Geophysical Monograph Series, Washington, D.C.

BOUVIER A. S., MÉTRICH N. & DELOULE E. 2010. Light elements, volatiles, and stable isotopes in basaltic melt inclusions from Grenada, Lesser Antilles: Inferences for magma genesis. *Geochemistry, Geophysics, Geosystems,* 11**,** DOI:10.1029/2010gc003051.

BRADY P. V. & GÍSLASON S. R. 1997. Seafloor weathering controls on atmospheric CO2 and global climate. *Geochimica et Cosmochimica Acta,* 61**,** 965-973.

CERVANTES P. & WALLACE P. J. 2003. Role of H2O in subduction-zone magmatism: New insights from melt inclusions in high-Mg basalts from central Mexico. *Geology*, 31**,** 235-238.

CLASS C., MILLER D. M., GOLDSTEIN S. L. & LANGMUIR C. H. 2000. Distinguishing melt and fluid subduction components in Umnak Volcanics, Aleutian Arc. *Geochem. Geophys. Geosyst.,* 1**,** 1-30.

CORDIER C., CLEMENT J. P., CAROFF M. *et al.* 2005. Petrogenesis of Coarse-grained Intrusives from Tahiti Nui and Raiatea (Society Islands, French Polynesia). *Journal of Petrology*, 46**,** 2281-2312.

DICKINSON W. R. 1975. Potash-Depth (K-h) Relations in Continental Margin and Intra-Oceanic Magmatic Arcs. *Geology,* 3**,** 53-56.

DIXON J. E., LEIST L., LANGMUIR C. & SCHILLING J.-G. 2002. Recycled dehydrated lithosphere observed in plume-influenced mid-ocean-ridge basalt. *Nature,* 420**,** 385-389.

DIXON J. E. & STOLPER E. M. 1995. An Experimental Study of Water and Carbon Dioxide Solubilities in Mid-Ocean Ridge Basaltic Liquids. Part II: Applications to Degassing. *Journal of petrology,* 36**,** 1633-1646.

ELLIOTT T. R. 2003. Tracers of the slab. *In* EILER, J. (ed.) *Inside the Subduction Factory.* Vol. 138, pp. 23-45, Geophysical Monograph Series, Washington, DC.

ERTAN I. E. & LEEMAN W. P. 1999. Fluid inclusions in mantle and lower crustal xenoliths from the Simcoe volcanic field, Washington. *Chemical Geology,* 154**,** 83-95.

ESCRIG S., BÉZOS A., GOLDSTEIN S. L., LANGMUIR C. H. & MICHAEL P. J. 2009. Mantle source variations beneath the Eastern Lau Spreading Center and the nature of subduction components in the Lau basin–Tonga arc system. *Geochem. Geophys. Geosyst.,* 10**,** Q04014, DOI: 10.1029/2008gc002281.

FLECK R. J., SUTTER J. F. & ELLIOT D. H. 1977. Interpretation of discordant $^{40}Ar/^{39}Ar$ age-spectra of mesozoic tholeiites from antarctica. *Geochimica et Cosmochimica Acta,* 41**,** 15-32.

FRYER P. 1993. The relationship between tectonic deformation, volcanism, and fluid venting in the southeastern Mariana convergent plate margin. *Proceedings of JAMSTEC,* Symposium on Deep Sea Research**,** 161–179.

FRYER P., BECKER N., APPELGATE B., MARTINEZ F., EDWARDS M. & FRYER G. 2003. Why is the Challenger Deep so deep? *Earth and Planetary Science Letters,* 211**,** 259-269.

FRYER P., FUJIMOTO H., SEKINE M. *et al.* 1998. Volcanoes of the southwestern extension of the active Mariana island arc : new swath-mapping and geochemical studies. *Island Arc,* 7**,** 596-607.

FUJIOKA K., OKINO K., KANAMATSU T. & OHARA Y. 2002. Morphology and origin of the Challenger Deep in the Southern Mariana Trench. *Geophys. Res. Lett.,* 29**,** 1372, DOI: 10.1029/2001GL013595.

FUNICIELLO F., FACCENNA C., GIARDINI D. & REGENAUER-LIEB K. 2003. Dynamics of retreating slabs: 2. Insights from three-dimensional laboratory experiments. *Journal of Geophysical Research,* 108**,** 2207, DOI: 10.1029/2001JB000896.

FUNICIELLO F., MORONI M., PIROMALLO C., FACCENNA C., CENEDESE A. & BUI H. A. 2006. Mapping mantle flow during retreating subduction: Laboratory models analyzed by feature tracking. *J. Geophys. Res.,* 111**,** B03402, DOI: 10.1029/2005JB003792.

GAMO T., MASUDA H., YAMANAKA T. *et al.* 2004. Discovery of a new hydrothermal venting site in the southernmost Mariana Arc : Al-rich hydrothermal plumes and white smoker activity associated with biogenic methane. *Geochemical Journal,* 38**,** 527-534.

GARDNER J. V. 2006. Law of the Sea Cruise to Map the Western Insular Margin and 2500-m Isobath of Guam and the Northern Mariana Islands. Cruise Report. *Center for Coastal and Ocean Mapping (CCOM)/Joint Hydrographic Center (JHC).* pp. 37, University of New Hampshire (UNH), Durham, NH.

GARDNER J. V. 2007. U.S. Law of the Sea Cruise to Map the Western Insular Margin and 2500-m Isobath of Guam and the Northern Mariana Islands. Cruise Report. *Center for Coastal and Ocean Mapping (CCOM)/Joint Hydrographic Center (JHC).* pp. 45, University of New Hampshire (UNH), Durham, NH.

GARDNER J. V. 2010. U.S. Law of the Sea cruises to map sections of the Mariana Trench and the eastern and southern insular margins of Guam and the Northern Mariana Islands. Cruise report. *Center for Coastal and Ocean Mapping (CCOM)/Joint Hydrographic Center (JHC).* pp. 82, University of New Hampshire (UNH), Durham, NH.

GARDNER J. V. & ARMSTRONG A. A. 2011. The Mariana Trench: A new view based on multibeam echosounding. *AGU Fall Meeting 2011.* American Geophysical Union.

GRIBBLE R. F., STERN R. J., BLOOMER S. H., STÜBEN D., O'HEARN T. & NEWMAN S. 1996. MORB mantle and subduction components interact to generate basalts in the southern Mariana Trough back-arc basin. *Geochimica et Cosmochimica Acta,* 60**,** 2153-2166.

GRIBBLE R. F., STERN R. J., NEWMAN S., BLOOMER S. H. & O'HEARN T. 1998. Chemical and Isotopic Composition of Lavas from the Northern Mariana Trough: Implications for Magmagenesis in Back-arc Basins. *Journal of Petrology,* 39**,** 125-154.

GROVE T. L., CHATTERJEE N., PARMAN S. W. & MÉDARD E. 2006. The influence of H2O on mantle wedge melting. *Earth and Planetary Science Letters,* 249**,** 74-89.

GROVE T. L., KINZLER R. J. & BRYAN W. B. 1992. Fractionation of mid-ocean ridge basalt (MORB). *In* MORGAN, J. P., BLACKMAN, D. K. & SINTON, J. M. (eds.) *Mantle Flow and Melt Generation at Mid-Ocean Ridges.* Vol. 71, pp. 281-310, Geophysical Monograph Series, Washington, DC.

GROVE T. L., TILL C. B. & KRAWCZYNSKI M. J. 2012. The Role of H_2O in Subduction Zone Magmatism. *Annual Review of Earth and Planetary Sciences,* 40**,** 413-439.

GVIRTZMAN Z. & STERN R. J. 2004. Bathymetry of Mariana trench-arc system and formation of the Challenger Deep as a consequence of weak plate coupling. *Tectonics,* 23**,** TC2011, DOI: 10.1029/2003tc001581.

HACKER B. R. 2008. H2O subduction beyond arcs. *Geochem. Geophys. Geosyst.,* 9**,** Q03001, DOI: 10.1029/2007gc001707.

HART S. R. 1969. K, Rb, Cs contents and K/Rb, K/Cs ratios of fresh and altered submarine basalts. *Earth and Planetary Science Letters,* 6**,** 295-303.

HART S. R. 1984. A large-scale isotope anomaly in the Southern Hemisphere mantle. *Nature,* 309**,** 753-757.

HART S. R., ERLANK A. J. & KABLE E. J. D. 1974. Seafloor basalt alteration: Some chemical and Sr isotopic effects. *Contributions to Mineralogy and Petrology,* 44**,** 219-230.

HATTORI K. H. & GUILLOT S. 2003. Volcanic fronts form as a consequence of serpentinite dehydration in the forearc mantle wedge. *Geology,* 31**,** 525-528.

HAUFF F., HOERNLE K. & SCHMIDT A. 2003. Sr-Nd-Pb composition of Mesozoic Pacific oceanic crust (Site 1149 and 801, ODP Leg 185): Implications for alteration of ocean crust and the input into the Izu-Bonin-Mariana subduction system. *Geochem. Geophys. Geosyst.,* 4**,** 8913, DOI: 10.1029/2002gc000421.

HAURI E., WANG J., DIXON J. E., KING P. L., MANDEVILLE C. & NEWMAN S. 2002. SIMS analysis of volatiles in silicate glasses: 1. Calibration, matrix effects and comparisons with FTIR. *Chemical Geology,* 183**,** 99-114.

HAWKINS J. W., LONSDALE P. F., MACDOUGALL J. D. & VOLPE A. M. 1990. Petrology of the axial ridge of the Mariana Trough backarc spreading center. *Earth and Planetary Science Letters,* 100**,** 226-250.

HULME S. M., WHEAT C. G., FRYER P. & MOTTL M. J. 2010. Pore water chemistry of the Mariana serpentinite mud volcanoes: A window to the seismogenic zone. *Geochem. Geophys. Geosyst.,* 11**,** Q01X09, DOI:10.1029/2009gc002674.

HYNDMAN R. D. & PEACOCK S. M. 2003. Serpentinization of the forearc mantle. *Earth and Planetary Science Letters,* 212**,** 417-432.

IKEDA Y., NAGAO K., STERN R. J., YUASA M. & NEWMAN S. 1998. Noble gases in pillow basalt glasses from the northern Mariana Trough back-arc basin. *Island Arc,* 7**,** 471-478.

ISHIZUKA O., TANI K., REAGAN M. K. *et al.* 2011. The timescales of subduction initiation and subsequent evolution of an oceanic island arc. *Earth and Planetary Science Letters,* 306**,** 229-240.

ISHIZUKA O., YUASA M., TAYLOR R. N. & SAKAMOTO I. 2009. Two contrasting magmatic types coexist after the cessation of back-arc spreading. *Chemical Geology,* 266**,** 274-296.

JENNER F. E. & O'NEILL H. S. C. 2012. Analysis of 60 elements in 616 ocean floor basaltic glasses. *Geochem. Geophys. Geosyst.,* 13**,** Q02005, DOI: 10.1029/2011gc004009.

JOCHUM K. P. & VERMA S. P. 1996. Extreme enrichment of Sb, Tl and other trace elements in altered MORB. *Chemical Geology,* 130**,** 289-299.

JOHNSON M. C. & PLANK T. 1999. Dehydration and melting experiments constrain the fate of subducted sediments. *Geochem. Geophys. Geosyst.,* 1**,** 1-26.

KAKEGAWA T., UTSUMI M. & MARUMO K. 2008. Geochemistry of Sulfide Chimneys and Basement Pillow Lavas at the Southern Mariana Trough (12.55°N and12.58°N). *Resource Geology,* 58**,** 249-266.

KATO T., BEAVAN J., MATSUSHIMA T., KOTAKE Y., CAMACHO J. T. & NAKAO S. 2003. Geodetic evidence of back arc spreading in the Mariana trough. *Geophysical Research Letters,* 30**,** 1625, doi:10.1029/2002GL016757.

KATZ R. F., SPIEGELMAN M. & LANGMUIR C. H. 2003. A new parameterization of hydrous mantle melting. *Geochem. Geophys. Geosyst.,* 4**,** 1073, DOI:10.1029/2002GC000433.

KAWAMOTO T., KANZAKI M., MIBE K., MATSUKAGE K. N. & ONO S. 2012. Separation of supercritical slab-fluids to form aqueous fluid and melt components in subduction zone magmatism. *Proceedings of the National Academy of Sciences,* 109**,** 18695–18700.

KELLEY K. A. & COTTRELL E. 2009. Water and the Oxidation State of Subduction Zone Magmas. *Science,* 325**,** 605-607.

KELLEY K. A., PLANK T., GROVE T. L., STOLPER E. M., NEWMAN S. & HAURI E. 2006. Mantle melting as a function of water content beneath back-arc basins. *Journal of Geophysical Research,* 111**,** B09208, DOI: 10.1029/2005jb003732.

KELLEY K. A., PLANK T., LUDDEN J. & STAUDIGEL H. 2003. Composition of altered oceanic crust at ODP Sites 801 and 1149. *Geochem. Geophys. Geosyst.,* 4**,** 8910, DOI: 10.1029/2002GC000435.

KELLEY K. A., PLANK T., NEWMAN S. *et al.* 2010. Mantle Melting as a Function of Water Content beneath the Mariana Arc. *Journal of Petrology,* 51**,** 1711-1738.

KENT A. J. R. 2008. Melt Inclusions in Basaltic and Related Volcanic Rocks. *Reviews in Mineralogy and Geochemistry,* 69**,** 273-331.

KENT A. J. R. & ELLIOTT T. R. 2002. Melt inclusions from Marianas arc lavas: implications for the composition and formation of island arc magmas. *Chemical Geology,* 183**,** 263-286.

KIMURA J.-I., KENT A., ROWE M. C. *et al.* 2010. Origin of cross-chain geochemical variation in Quaternary lavas from the northern Izu arc: Using a quantitative mass balance approach to identify mantle sources and mantle wedge processes. *Geochem. Geophys. Geosyst.,* 11**,** Q10011, DOI: 10.1029/2010gc003050.

KIMURA J.-I. & STERN R. J. 2008. Neogene Volcanism of the Japan Island Arc: The K-h Relationship Revisited. *In* SPENCER, J. E. & TITLEY, S. R. (eds.) *Ores and orogenesis: Circum-Pacific Tectonics, Geologic Evolution, and Ore Deposits.* Vol. 22, pp. 187-202, Geological Society, Digest, Arizona.

KLEIN E. M. & LANGMUIR C. H. 1987. Global correlations of ocean ridge basalt chemistry with axial depth and crustal thickness. *J. Geophys. Res.*, 92**,** 8089-8115.

LALLEMAND S. 2001. *La subduction océanique,* Gordon and Breach Science Publishers, Amsterdam.

LANGMUIR C. H., BEZOS A., ESCRIG S. & PARMAN S. W. 2006. Chemical systematics and hydrous melting of the mantle in back-arc basins. *In* CHRISTIE, D. M. & AL. (eds.) *Back-Arc Spreading Systems: Geological, Biological, Chemical, and Physical Interactions.* Vol. 166, pp. 87-146, Geophysical Monograph Series, Washington, DC.

LANPHERE M. A. & BAADSGAARD H. 2001. Precise K-Ar, $^{40}Ar/^{39}Ar$, Rb-Sr and U/Pb mineral ages from the 27.5 Ma fish canyon tuff reference standard. *Chemical Geology,* 175**,** 653-671.

LE BAS M. J. 2000. IUGS Reclassification of the High-Mg and Picritic Volcanic Rocks. *Journal of Petrology,* 41**,** 1467-1470.

LE MAITRE R. W., BATEMAN P., DUDEK A. *et al.* 1989. *A Classification of Igneous Rocks and Glossary of terms: Recommendations of the international union of geological sciences subcommission on the systematics of igneous rocks.,* Blackwell Scientific Publications, Oxford, U.K.

LEE C.-T. A., LUFFI P., PLANK T., DALTON H. & LEEMAN W. P. 2009. Constraints on the depths and temperatures of basaltic magma generation on Earth and other terrestrial planets using new thermobarometers for mafic magmas. *Earth and Planetary Science Letters,* 279**,** 20-33.

LOFGREN G. E. 1974. An experimental study of plagioclase crystal morphology; isothermal crystallization. *American Journal of Science,* 274**,** 243-273.

MACKENZIE W. S., DONALDSON C. H. & GUILFORD C. 1982. *Atlas of igneous rocks and their textures,* Longman, London , U.K.

MANNING C. E. 2004. The chemistry of subduction-zone fluids. *Earth and Planetary Science Letters,* 223**,** 1-16.

MANTON W. I. 1988. Separation of Pb from young zircons by single-bead ion exchange. *Chemical Geology: Isotope Geoscience section,* 73**,** 147-152.

MARTINEZ F., FRYER P. & BECKER N. 2000. Geophysical characteristics of the southern Mariana Trough, 11°50'N-13°40'N. *Journal of Geophysical Research,* 105**,** 16,591-16,607.

MARTINEZ F. & STERN R. J. 2009. The Southern Mariana Convergent Margin: A Pre-Ophiolite Analogue. *AGU Fall Meeting 2009.* American Geophysical Union.

MCCULLOCH M. T. & GAMBLE J. A. 1991. Geochemical and geodynamical constraints on subduction zone magmatism. *Earth and Planetary Science Letters,* 102**,** 358-374.

MICHIBAYASHI K., OHARA Y., STERN R. J. *et al.* 2009. Peridotites from a ductile shear zone within back-arc lithospheric mantle, southern Mariana Trench: Results of a Shinkai 6500 dive. *Geochemistry Geophysics Geosystems,* 10**,** Q05X06, DOI: 10.1029/2008GC002197.

MILLER M. S., GORBATOV A. & KENNETT B. L. N. 2006a. Three-dimensional visualization of a near-vertical slab tear beneath the southern Mariana arc. *Geochem. Geophys. Geosyst.,* 7**,** Q06012, DOI:10.1029/2005gc001110.

MILLER M. S., KENNETT B. L. N. & TOY V. G. 2006b. Spatial and temporal evolution of the subducting Pacific plate structure along the western Pacific margin. *Journal of Geophysical Research,* 111**,** B02401, DOI: 10.1029/2005jb003705.

MIYASHIRO A. 1974. Volcanic rock series in island arcs and active continental margins. *American Journal of Science,* 274**,** 321-355.

MOTTL M. J., WHEAT C. G., FRYER P., GHARIB J. & MARTIN J. B. 2004. Chemistry of springs across the Mariana forearc shows progressive devolatilization of the subducting plate. *Geochimica et Cosmochimica Acta,* 68**,** 4915-4933.

NEWMAN S. & LOWENSTERN J. B. 2002. VolatileCalc: a silicate melt–H2O–CO2 solution model written in Visual Basic for excel. *Computers & Geosciences,* 28**,** 597-604.

NEWMAN S., STOLPER E. & STERN R. J. 2000. H2O and CO2 in magmas from the Mariana arc and back arc systems. *Geochemistry Geophysics Geosystems,* 1**,** DOI: 10.1029/1999gc000027.

OHARA Y. & ISHII T. 1998. Peridotites from the southern Mariana forearc: Heterogeneous fluid supply in mantle wedge. *Island Arc,* 7**,** 541-558.

OHARA Y., REAGAN M., ISHII T. *et al.* 2008. R/V Yokosuka YK08-08 LEG 2 cruise report: Structure and origin of the Mariana forearc and implications for the origin of the continental crust : A Shinkai 6500 study of he southern Mariana forearc *In* JAMSTEC (ed.) pp. 90, Jamstec.

OHARA Y., REAGAN M., MICHIBAYASHI K. *et al.* 2010. R/V Yokosuka YK10-12 cruise report: Composition, tectonic and structure of the Mariana forearc. *In* JAMSTEC (ed.) pp. 275, Jamstec.

OHARA Y., STERN R. J., ISHII T., YURIMOTO H. & YAMAZAKI T. 2002. Peridotites from the Mariana Trough: first look at the mantle beneath an active back-arc basin. *Contributions to Mineralogy and Petrology,* 143**,** 1-18.

OKINO K., OHARA Y., FUJIWARA T. *et al.* 2009. Tectonics of the southern tip of the Parece Vela Basin, Philippine Sea Plate. *Tectonophysics,* 466**,** 213-228.

PARKINSON I. J. & PEARCE J. A. 1998. Peridotites from the Izu–Bonin–Mariana Forearc (ODP Leg 125): Evidence for Mantle Melting and Melt–Mantle Interaction in a Supra-Subduction Zone Setting. *Journal of petrology,* 39**,** 1577-1618.

PEARCE J. A. 2008. Geochemical fingerprintring of oceanic basalts with applications to ophiolite classification and the search for Archean oceanic crust. *Lithos,* 100**,** 14-48.

PEARCE J. A. & STERN R. J. 2006. Origin of Back-Arc Basin Magmas: Trace Element and Isotope Perspectives. *In* CHRISTIE, D. M. & AL. (eds.) *Back-Arc Spreading Systems: Geological, Biological, Chemical, and Physical Interactions.* Vol. 166, pp. 63-86, Geophysical Monograph Series, Washington, D. C.

PEARCE J. A., STERN R. J., BLOOMER S. H. & FRYER P. 2005. Geochemical mapping of the Mariana arc-basin system : Implications for the nature and distribution of subduction components. *Geochemistry Geophysics Geosystems,* 6**,** 27, DOI:10.1029/2004GC000895.

PECCERILLO A. & TAYLOR S. R. 1976. Geochemistry of Eocene calcalkaline volcanic rocks from the Kastamonu Area, Northern Turkey. *Contrib. Mineral. Petrol,* 58**,** 63-81.

PLANK T. 2005. Constraints from Thorium/Lanthanum on Sediment Recycling at Subduction Zones and the Evolution of the Continents. *Journal of petrology,* 46**,** 921-944.

PLANK T. & LANGMUIR C. H. 1998. The chemical composition of subducting sediment and its consequences for the crust and mantle. *Chemical Geology,* 145**,** 325-394.

REAGAN M. K., ISHIZUKA O., STERN R. J. *et al.* 2010. Fore-arc basalts and subduction initiation in the Izu-Bonin-Mariana system. *Geochemistry Geophysics Geosystems,* 11**,** Q03X12, DOI: 10.1029/2009GC002871.

RIBEIRO J., STERN R. J., KELLEY K., MARTINEZ F., ISHIZUKA O. & MANTON W. I. submitted. Nature and distribution of the slab-derived fluids and the mantle source along the SE Mariana Forearc Rift. *Geochemistry Geophysics Geosystems*.

RIBEIRO J., STERN R. J., MARTINEZ F. *et al.* in press. Geodynamic evolution of a forearc rift in the southernmost Mariana Arc. *Island Arc*.

ROEDER P. L. & EMSLIE R. F. 1970. Olivine-liquid equilibrium. *Contributions to Mineralogy and Petrology,* 29**,** 275-289.

ROWE M. C. & LASSITER J. C. 2009. Chlorine enrichment in central Rio Grande Rift basaltic melt inclusions: Evidence for subduction modification of the lithospheric mantle. *Geology,* 37**,** 439-442.

RÜPKE L., MORGAN J. P., HORT M. & CONNOLLY J. A. D. 2004. Serpentine and the subduction zone water cycle. *Earth and Planetary Science Letters,* 223**,** 17-34.

RUSCITTO D. M., WALLACE P. J., COOPER L. B. & PLANK T. 2012. Global variations in H2O/Ce: 2. Relationships to arc magma geochemistry and volatile fluxes. *Geochemistry, Geophysics, Geosystems,* 13**,** Q03025, DOI: 10.1029/2011gc003887.

SADOFSKY S., PORTNYAGIN M., HOERNLE K. & BOGAARD P. 2008. Subduction cycling of volatiles and trace elements through the Central American volcanic arc: evidence from melt inclusions. *Contributions to Mineralogy and Petrology,* 155**,** 433-456.

SALTERS V. J. M. & STRACKE A. 2004. Composition of the depleted mantle. *Geochem. Geophys. Geosyst.,* 5**,** DOI:10.1029/2003GC000597.

SATO H. & ISHII T. 2011. Petrology and Mineralogy of Mantle Peridotites from the Southern Marianas. *In* OGAWA, Y., ANMA, R.& DILEK, Y. (ed.) *Accretionary Prisms and Convergent Margin Tectonics in the Northwest Pacific Basin, Modern Approaches in Solid Earth Sciences.* Vol. 8, pp. 129-147, Springer, Houten, Netherland.

SAVOV I. P., RYAN J. G., D'ANTONIO M. & FRYER P. 2007. Shallow slab fluid release across and along the Mariana arc-basin system: Insights from geochemistry of serpentinized peridotites from the Mariana fore arc. *J. Geophys. Res.***,** B09205, DOI: 10.1029/2006JB004749.

SAVOV I. P., RYAN J. G., D'ANTONIO M., KELLEY K. & MATTIE P. 2005. Geochemistry of serpentinized peridotites from the Mariana Forearc Conical Seamount, ODP Leg 125: Implications for the elemental recycling at subduction zones. *Geochem. Geophys. Geosyst.,* 6**,** Q04J15, DOI: 10.1029/2004GC000777.

SCAMBELLURI M. & TONARINI S. 2012. Boron isotope evidence for shallow fluid transfer across subduction zones by serpentinized mantle. *Geology,* 40**,** 907-910.

SCHELLART W. P., FREEMAN J., STEGMAN D. R., MORESI L. & MAY D. 2007. Evolution and diversity of subduction zones controlled by slab width. *Nature,* 446**,** 308-311.

SCHIANO P. & BOURDON B. 1999. On the preservation of mantle information in ultramafic nodules: glass inclusions within minerals versus interstitial glasses. *Earth and Planetary Science Letters,* 169**,** 173-188.

SCHIANO P., CLOCCHIATTI R., SHIMIZU N., MAURY R. C., JOCHUM K. P. & HOFMANN A. W. 1995. Hydrous, silica-rich melts in the sub-arc mantle and their relationship with erupted arc lavas. *Nature,* 377**,** 595-600.

SCHMIDT M. & POLI S. 1998. Experimentally based water budgets for dehydrating slabs and consequences for magma generation. *Earth and Planetary Science Letters,* 163**,** 361-379.

SHAW A. M., HAURI E. H., FISCHER T. P., HILTON D. R. & KELLEY K. A. 2008. Hydrogen isotopes in Mariana arc melt inclusions: Implications for subduction dehydration and the deep-Earth water cycle. *Earth and Planetary Science Letters,* 275**,** 138-145.

SHEN Y. & FORSYTH D. W. 1995. Geochemical constraints on initial and final depths of melting beneath mid-ocean ridges. *Journal of Geophysical Research,* 100**,** 2211-2237.

SHERVAIS J. W. 1982. Ti-V plots and the petrogenesis of modern and ophiolitic lavas. *Earth and Planetary Science Letters,* 59**,** 101-118.

SMITH R. E. 1969. Segregation vesicles in basaltic lava. *American Journal of Science,* 265**,** 696-713

SMITH W. H. F. & WESSEL P. 1990. Gridding with continuous curvature splines in tension. *Geophysics,* 55**,** 293-305.

STAUDIGEL H. & HART S. R. 1983. Alteration of basaltic glass: Mechanisms and significance for the oceanic crust-seawater budget. *Geochimica et Cosmochimica Acta,* 47**,** 337-350.

STERN R. J. 2002. Subduction Zones. *Reviews of Geophysics,* 40**,** 37, DOI:10.1029/2001RG000108.

STERN R. J. 2010. The anatomy and ontogeny of modern intra-oceanic arc systems. *In* KUSKY, T. M., ZHAI, M.-G. & XIAO, W. (eds.) *The Evolving Continents: Understanding Processes of Continental Growth.* Vol. 338, pp. 7-34, Geological Society of London, Special Publications, London, U.K.

STERN R. J. & BLOOMER S. H. 1992. Subduction zone infancy: Examples from the Eocene Izu-Bonin-Mariana and Jurassic California arcs. *Geological Society of America Bulletin,* 104**,** 1621-1636.

STERN R. J., FOUCH M. & KLEMPERER S. L. 2003. An Overview of the Izu-Bonin-Mariana Subduction Factory. *In* EILER, J. & HIRSCHMANN, M. (eds.) *Inside the subduction factory.* Vol. 138, pp. 175-222, Geophysical Monograph Series, Washington, D.C.

STERN R. J., KOHUT E., BLOOMER S. H., LEYBOURNE M., FOUCH M. & VERVOORT J. 2006. Subduction factory processes beneath the Guguan cross-chain, Mariana Arc: no role for sediments, are serpentinites important? *Contribution to Mineralogy and Petrology,* 151**,** 202-221.

STERN R. J., TAMURA Y., MASUDA H. *et al.* in press. How the Mariana Volcanic Arc ends in the south. *Island Arc*.

STERN R. J., TAMURA Y., MASUDA H. *et al.* 2013. How the Mariana Volcanic Arc ends in the south. *Island Arc,* 22**,** 133-148.

STRAUB S. M. & LAYNE G. D. 2003. Decoupling of fluids and fluid-mobile elements during shallow subduction: Evidence from halogen-rich andesite melt inclusions from the Izu arc volcanic front. *Geochem. Geophys. Geosyst.,* 4**,** 9004, DOI:10.1029/2002gc000349.

SUN S. S. & MCDONOUGH W. F. 1989. Chemical and isotopic systemics of ocean basalt: Implications for mantle composition and processes. *In* SAUNDERS, A. D. & NORRY, M. J. (eds.) *Magmatism in the Ocean Basins.* Vol. 42, pp. 313-345, Geological Society of London, Special publications, London.

TAYLOR B. & MARTINEZ F. 2003. Back-arc basin basalt systematics. *Earth and Planetary Science Letters,* 210**,** 481-497.

TEAGLE D. A. H., ALT J. C., UMINO S. *et al.* 2006. *Proceedings of the Integrated Ocean Drilling Program, Volume 309/312,* Integrated Ocean Drilling Program Management International, Inc., for the Integrated Ocean Drilling Program, Washington, DC.

TIBI R., WIENS D. A. & YUAN X. 2008. Seismic evidence for widespread serpentinized forearc mantle along the Mariana convergence margin. *Geophys. Res. Lett.,* 35**,** L13303, DOI: 10.1029/2008gl034163.

TODT W., CLIFF R., HANSER A. & HOFMANN A. 1996. Evaluation of a ^{202}Pb - ^{205}Pb double spike for high - precision lead isotope analysis. *In* BASU, A. & HART, S. (eds.) *Earth Processes: Reading the Isotopic Code.* Vol. 95, pp. 429-437, Geophysical Monograph Series, Washington, DC.

VAN KEKEN P. E., KIEFER B. & PEACOCK S. M. 2002. High-resolution models of subduction zones: Implications for mineral dehydration reactions and the transport of water into the deep mantle. *Geochem. Geophys. Geosyst.,* 3**,** 1056, DOI:10.1029/2001GC000256.

VOLPE A. M., DOUGLAS MACDOUGALL J. & HAWKINS J. W. 1987. Mariana Trough basalts (MTB): trace element and SrNd isotopic evidence for mixing between MORB-like and Arc-like melts. *Earth and Planetary Science Letters,* 82**,** 241-254.

VOLPE A. M., DOUGLAS MACDOUGALL J., LUGMAIR G. W., HAWKINS J. W. & LONSDALE P. 1990. Fine-scale isotopic variation in Mariana Trough basalts: evidence for heterogeneity and a recycled component in backarc basin mantle. *Earth and Planetary Science Letters,* 100**,** 251-264.

WADA I., RYCHERT C. A. & WANG K. 2011. Sharp thermal transition in the forearc mantle wedge as a consequence of nonlinear mantle wedge flow. *Geophys. Res. Lett.,* 38**,** L13308, DOI: 10.1029/2011gl047705.

WADE J. A., PLANK T., STERN R. J. *et al.* 2005. The may 2003 eruption of Anatahan volcano, Mariana Islands: Geochemical evolution of a silicic island-arc volcano. *Journal of Volcanology and Geothermal Research,* 146**,** 139-170.

WALLACE L. M., MC CAFFREY R., BEAVAN J. & ELLIS S. 2005. Rapid microplate rotations and backarc rifting at the transition between collision and subduction. *Geology,* 33**,** 857-860.

WANLESS V. D. & SHAW A. M. 2012. Lower crustal crystallization and melt evolution at mid-ocean ridges. *Nature Geoscience,* 5**,** 651-655.

WESSEL P. & SMITH W. H. F. 1995a. New version of the Generic Mapping Tools released. *EOS Transactions American Geophysical Union,* 76**,** 329, Electromic supplement available from http://www.agu.org/eos_elec/951546.html.

WESSEL P. & SMITH W. H. F. 1995b. New version of the Generic Mapping Tools released. *EOS Transactions American Geophysical Union,* 76**,** 329.

WESSEL P. & SMITH W. H. F. 1998. New, improved version of Generic Mapping Tools released. *EOS Transactions American Geophysical Union.* Vol. 79, pp. 579, Washington, D.C.

WHEAT C. G., FRYER P., FISHER A. T. *et al.* 2008. Borehole observations of fluid flow from South Chamorro Seamount, an active serpentinite mud volcano in the Mariana forearc. *Earth and Planetary Science Letters,* 267**,** 401-409.

WOODHEAD J. D. 1989. Geochemistry of the Mariana arc (Western Pacific) : source composition and processes. *Chemical Geology,* 76**,** 1-24.

WOODHEAD J. D., STERN R. J., PEARCE J. A., HERGT J. M. & VERVOORT J. 2012. Hf-Nd isotope variation in Mariana Trough basalts: The importance of "ambient mantle" in the interpretation of subduction zone magmas. *Geology,* 40**,** 539-542.

YORK D. 1969. Least squares fitting of a straight line with correlated errors. *Earth and Planetary Science Letters,* 5**,** 320–324.

ZACK T. Z., RIVERS T. R. & FOLEY S. F. 2001. Cs-Rb-Ba systematics in phengite and amphibole: an assessment of fluid mobility at 2.0 GPa in eclogites from Trescolmen, Central Alps. *Contributions to Mineralogy and Petrology,* 140**,** 651-669.

VITA

Julia M. Ribeiro was born near Paris, France, where she grew up and spent most of her childhood. After completing her schoolwork, she received her Baccalauréat dilploma, with biology specialty, which allowed her to enter The University Pierre et Marie Curie in Paris, France, where she received a Bachelor of Science and a Master of Science with a major in Geosciences. She entered The Institut Universitaire Européen de la Mer (IUEM) in Plouzané, France to complete her second year of Master Degree in Geology - Geochemistry applied to Oceanography, and she graduated with honor in MSc. research in 2007. In 2008, she entered the Graduate School of The University of Texas at Dallas to start a PhD on subduction-related magmas in Western Pacific.